FACULTAD DE CIENCIAS
Departamento de Química Física Aplicada

STRUCURE AND REACTIVITY OF IRON-BASED CATALYSIS FOR FISCHER-TROPSCH SYNTHESIS

Memoria para aspirar al grado de

DOCTOR EN CIENCIAS QUIMICAS

(con Mención Internacional)

MOHAMMED ALI M. ALDOSSARY

Instituto de Catálisis y Petroleoquímica
Consejo Superior de Investigaciones Científicas

Madrid, 2015

FACULTAD DE CIENCIAS
Departamento de Química Física Aplicada

Memoria para aspirar al grado de
DOCTOR EN CIENCIAS QUIMICAS
(con Mención Internacional)

MOHAMMED ALI M. ALDOSSARY

STRUCURE AND REACTIVITY OF IRON-BASED CATALYSIS FOR FISCHER-TROPSCH SYNTHESIS

Directores:
José Luis G. Fierro
Profesor de Investigación, CSIC

Dr. Manual Ojeda Pineda

Instituto de Catálisis y Petroleoquímica
Consejo Superior de Investigaciones Científicas

Madrid, 2015

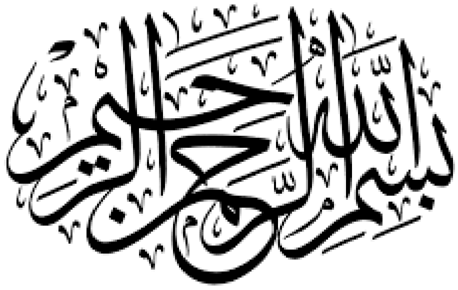

In the Name of Allah, the Most Gracious, the Most Merciful

Dedication

This work is dedicated to my dearly loved
mother and father

Table of Contents

Summary / Resumen

Summary and Concluding Remarks

Nowadays, oil fossil fuel is the main raw materials for producing liquid fuels and feedstock chemicals. Numerous concerns have been raised, however, about the sustainability of its use. Concerning its usage it caused negative environmental impacts due to the crude oil contains sulfur, aromatics and nitrogen-containing compounds which may compromise the development of our society. On the other hand, and due to depleting oil reserves, limited supply and unpredictable price of crude oil are expected to result in negative impacts on our economy. For these reasons, the sustainable production of clean liquid fuels for the transport sector and feedstock chemicals from coal, natural gas and biomass is a social, political and environmental priority.

Accordingly, the production of clean liquid fuels from natural gas, coal and biomass via syngas and Fischer-Tropsch (FT) synthesis has a strong interest. In the last decades, this interest has been focused in the production of diesel from natural gas (Gas-To-Liquid, GTL). In the last decade, however, the scientific community is seriously considering the possibility of producing clean liquid fuels from biomass via gasification and FTS, the so called Biomass-To-Liquid (BTL) processes. Recent studies propose the combined usage of coal and biomass for this matter (CBTL) combining the possibility of having large amounts of raw fossil resource (coal) while balancing CO_2 emissions by using a carbon source decoupled from net CO_2 emissions (biomass).

Compared to other metal catalysts employed for the FT synthesis, the use of iron-based catalyst is more attractive for FTS with low H_2/CO ratio syngas derived from coal or biomass because its higher water-gas shift activity. In principle, Fe-based precursors would be ideal candidates to be used in the FTS. Moreover, Fe catalysts are attractive due to lower cost, favorable engineering characteristics, flexible product distribution and its highly olefinic nature of the obtained products which allows their use as a feedstock for chemical industry. Most of Fe phases such as metallic iron, iron carbides (FeC_x) or oxides (FeO_x) form have been proposed at some point to act as active structures during the FTS steady-state. However, catalysts containing Fe alone have some drawbacks like a general limitation of the FTS process, high selectivity to non-desired products such as methane or rapid deactivation. The addition of promoters can result in an enhancement of the activity of Fe-based FTS catalysis. Therefore, extensive promotion of these catalysts with transition metals have been required to enhance the reducibility and carburization of the iron catalysts to an extent sufficient to improve their structural integrity or catalytic properties in order to achieve acceptable Fischer-Tropsch conversion activities.

The main objectives of this Doctoral Thesis is to understand how parameters such as nature of the promoter, additives, morphology, pre-reduction and reaction conditions affect to the performance of Fe-based catalysts for the production of hydrocarbons from syngas.

First, a thorough discussion about the effect of Zr loading onto Fe-based catalysts for the syngas conversion to hydrocarbons is presented in Chapter 4. A series of Fe_2O_3/ZrO_2 catalysts have been synthesized by the coprecipitation technique. These catalysts, in which the Fe-content varied between 0 and 100%, were tested in the CO hydrogenation reaction under fixed reaction conditions ($H_2/CO = 2$, $T = 250$ ºC, $P = 20$ bar, GHSV = 0.0083 L/g.s.). The resulting activity data indicated that CO conversion is strongly depends on the iron contents of the catalysts. The catalysts have been characterized in detail by a combination of different techniques such as nitrogen adsorption-desorption isotherms, X-ray diffraction (XRD), H_2-temperature-programmed reduction (H_2-TPR), NH_3-temperature-programmed desorption (NH_3-TPD) and X-ray photoelectron spectroscopy (XPS).

It was found that the lowest CO conversion (< 5%) was obtained using Zr-rich catalysts (15Fe and 5Fe), and the highest CO conversion was obtained using Zr-free (100Fe) catalysts. However, the activity profile of this catalyst slightly drops with the time on-stream, indicating that it is progressively deactivated. If the activity is normalized to the iron content, the 95Fe and 85Fe catalysts display better performances and relative stability with the time on-stream.

In Chapter 5, the effect of pre-reduction temperature on the Fischer-Tropsch synthesis on zirconia-iron catalysts is reported. The influence of the H_2 treatment temperature of the Fe_2O_3/ZrO_2 catalysts on the conversion of syngas has been investigated at 300 °C, GHSV = 0.0021 $L/g_{cat}.s$, P = 2.02 MPa. The conversion rate, based on steady-state, increased with the pretreatment temperature up to a maximum and then decreased at higher temperatures. Moreover, methane selectivity was found to decrease slightly from the lowest H_2 treatment temperatures to the highest one, while middle and high molecular weight hydrocarbons followed an opposite trend. Presumably, methane formation takes place on the highly active low coordination sites lying at corners and edges, which are more abundance on small iron carbide particles.

The effect of Cu-promoted onto Fe_2O_3/MgO-based Fischer-Tropsch catalysts for the conversion of biomass-derived syngas to valuable hydrocarbons has been studied thoroughly. Chapter 6 includes the study of the effect of Cu loading on the reducibility and carburization extent of Fe-based catalysts by using X-ray absorption near edge structure (XANES) techniques.

To obtain this study, a series of precipitated Fe_2O_3/MgO catalysts incorporated with the copper promoter were prepared by the combination of coprecipitation and incipient wetness impregnation methods. It was found that Cu increases the rate of Fe_2O_3 reduction by providing H_2 dissociation sites. The content of iron carbide phases during TPR process in the syngas increases with the increase of copper content and reaches a maximum for the Cu/Fe atomic ratio of 0.02. The optimal catalyst composition (Cu/Fe = 0.02) has high activity for the FTS reaction.

Finally, in the last stage of the PhD Thesis, a study of the effect of Mn loading onto MnFeO nanocomposites for the CO_2 hydrogenation reaction is studied in chapter 7. This work describes the preparation of mesoporous xMnFe oxide (x = 0, 0.05, 0.1, 0.2, 0.3 and 0.5 molar ratios) nanocomposites through a one-step sol-gel process in the presence of a triblock copolymer as a structure-directing agent. We have observed that among these catalysts, the 0.05MnFe catalyst performed best under the selected reaction conditions. This catalyst provided a much higher conversion of CO_2 to valuable hydrocarbons and the lowest levels of undesirable products such as methane and CO among the xMnFe series. Moreover, the 0.05MnFe catalyst was the only one with a mesoporous structure, and it had a substantially lower reduction temperature than did the other members of the series. The enhanced catalytic activity of the 0.05MnFe catalyst, which contains only a small amount of Mn, appears to result primarily from its high specific area and relatively easy reduction.

Actualmente, los combustibles de origen fossil son la material prima de fabricación de los combustibles para automoción y compuestos químicos. Aún con un uso muy extendido se han planteado numerosas controversias. Su uso causa impactos negativos en el medio ambiente debido a que el petróleo contiene compuestos de azufre, nitrógeno y aromáticos lo que bien e a comprometer el desarrollo de nuestra. Por otra parte, y debido a la disminución de las reservas, suministro limitado y precios impredecibles del crudo se esperan impactos negativos en nuestra economía. Por estas razones, la producción sostenible de combustible líquidos limpios para el sector del transporte y compuestos químicos a partir del carbón, gas natural y biomasa es una prioridad política y medioambiental.

Conforme a estas premisas, la producción de combustibles líquidos limpios a partir del gas natural, carbón y biomasa mediante la síntesis Fischer-Tropsch (FT) tiene un enorme interés. En las últimas décadas, este interés se ha focalizado en la producción de diésel a partir del gas natural (Gas-To-Liquid, GTL). En la última década, la comunidad científica está considerando seriamente la posibilidad de producción de combustibles líquidos a partir de la biomasa via gasificación y FTS, procesos denominados Biomass-To-Liquid (BTL). Estudios recientes han propuesto el uso combinado de carbón y biomasa (CBTL) combinando la posibilidad de tener grandes cantidades de precursor fósil (carbón) al mismo tiempo que compensar las emisiones de CO_2 del carbón con las de la fuente renovable (biomasa).

Comparados con otros catalizadores metálicos usados en la síntesis FT, los catalizadores de hierro son más atractivos para realizar la síntesis FT debido a que operan con una baja relación H_2/CO obtenida por gasificación de carbón o biomasa debido a la actividad más elevada en la reacción del desplazamiento del gas de agua. En principio, los precursores de hierro son los candidatos ideales a usar en la síntesis FT. Además, los catalizadores de hierro son atractivos debido a su bajo coste, características favorable de ingeniería, distribución flexible de productos y naturaleza altamente olefínica de los productos obtenidos lo que permite su uso como materia prima en la petroquímica. Se han propuesto distintas fases de hierro, tales como hierro, carburos de hierro (FeC_x) u óxidos de hierro (FeO_x) como fases activas en la reacción FTS en estado estacionario. Sin embargo, los catalizadores que solamente contienen Fe tienen algunas limitaciones: alta selectividad a productos no deseados tales como CH4 o desactivación rápida. La incorporación de promotores puede mejorar la actividad de los catalizadores de Fe en la reacción FT. Por esta razón, la promoción de estos catalizadores con metales de transición es una práctica bastante común para mejorar la reducibilidad y carburización de los catalizadores de hierro en una extensión suficiente que venga a mejorar su integridad estructural o propiedades catalíticas de forma que mejoren la actividad FT.

El objetivo principal de esta Tesis Doctoral es entender como parámetros tales como la naturaleza del promotor, aditivos, morfología, pre-reducción y condiciones de reacción afectan el comportamiento de los catalizadores de hierro en la producción de hidrocarburos a partir del gas de síntesis.

En primer lugar, en el Capítulo 4 se presenta una discusión detallada sobre el efecto del contenido de Zr en los catalizadores de hierro para la conversión del gas de síntesis a hidrocarburos. A tal efecto, se preparó una serie de catalizadores Fe_2O_3/ZrO_2 mediante la técnica de coprecipitación. Estos catalizadores en los que el contenido de Fe varió entre 0 y 100% se utilizaron en la reacción de hidrogenación de CO bajo condiciones fijas de reacción ($H_2/CO = 2$, $T = 250$ ºC, $P = 20$ bar, GHSV = 0.0083 L/g.s.). Los datos de actividad resultantes indicaron que la conversión de CO depende marcadamente del contenido de hierro de los catalizadores. Estos catalizadores se caracterizaron en detalle mediante una combinación de diferentes técnicas tales como isotermas de adsorción-desorción de nitrógeno, difracción de rayos X (XRD), reducción a temperatura programada (H_2-TPR), desorción de NH_3 a temperatura-programada (NH_3-TPD) y espectroscopía fotoelectrónica (XPS).

Los catalizadores ricos en Zr (15Fe y 5Fe) mostraron la conversión de CO más baja (< 5%) mientras que la conversión de CO más elevada se obtuvo con el catalizador másico (100Fe). Sin embargo, el perfil de actividad de este catalizador progresivamente decae con el tiempo en reacción como consecuencia de su desactivación. Si la actividad se normaliza por el contenido de hierro, resulta que los catalizadores 95Fe y 85Fe presentan el mejor comportamiento catalítico y estabilidad relativa con el tiempo de reacción.

En el capítulo 5 se presenta el efecto de la temperatura de pre-reducción de los catalizadores Fe_2O_3/ZrO_2 en la síntesis FT. La influencia de la temperatura de pretratamiento en H2 de los catalizadores Fe_2O_3/ZrO_2 sobre la conversión de gas de síntesis se estudió a 300 °C, GHSV = 0.0021 L/g_{cat}.s, P = 2.02 MPa. La velocidad de conversión en estado estacionario aumentó con la temperatura de pretratamiento hasta un máximo y después disminuyo a temperaturas más elevadas. Además, la selectividad a metano disminuyó ligeramente desde la temperatura de tratamiento más baja hasta la más elevada, al mismo tiempo que la selectividad a hidrocarburos de peso molecular medio y elevado siguió una tendencia opuesta. Presumiblemente la formación de metano tiene lugar sobre los centros activos de baja coordinación tales como los situados en vértices y aristas, más abundantes en las partículas de carburo de menor tamaño.

Se estudió el efecto promotor del Cu en los catalizadores Fe_2O_3/MgO utilizados en la reacción de síntesis FT a partir de un gas de síntesis derivado de la biomasa. El Capítulo 6 incluye el estudio del efecto del contenido de Cu como promotor sobre la extensión de la reducción y la carburización de los catalizadores basados en Fe mediante la técnica de absorción de rayos X (XANES).

En este estudio se utilizaron catalizadores Fe_2O_3/MgO preparados por coprecipitación a los que se incorporó cobre como promotor mediante el método de impregnación. Se observe que el Cu aumenta la velocidad de reducción del Fe_2O_3 proporcionando centros de disociación de la molécula H_2. El contenido de las fases carburo en el curso del proceso TPR aumenta conforme lo hace el contenido de Cu y alcanza un máximo para la relación Cu/Fe = 0.02 (atómica). La composición óptima del catalizador (Cu/Fe = 0.02) presenta una elevada actividad en la reacción FTS.

Finalmente, en el Capítulo 7 de esta Tesis se ha realizado un estudio del efecto del contenido de Mn en los nanocompuestos xMnFeO para la reacción de hidrogenación de CO_2. Este trabajo describe la preparación de sistemas mesoporosos xMnFeO (x = 0, 0.05, 0.1, 0.2, 0.3 y 0.5 relación molar) mediante un proceso sol-gel en un solo paso utilizando un copolímero tribloque como agente director de la estructura. Entre los catalizadores, se observe que la composición 0.05MnFepresenta el mayor comportamiento en la reacción FT bajo condiciones de operación prefijadas. Este catalizador proporcionó una conversión de CO_2 más elevada a hidrocarburos y un nivel más bajo de productos indeseables tales como CH_4 y CO entre los catalizadores de la serie xMnFeO. Además, el catalizador 0.05MnFe fue el único que presenta una estructura mesoporosa conjuntamente con una reducción a más baja temperatura que los demás miembros de la serie. La mejora de la actividad de catalizador 0.05MnFe que contiene una pequeña cantidad de Mn es el resultado de su superficie específica elevada y reducción a baja temperatura.

Chapter 1: Introduction

1

Introduction

1.1. Current energy situation. Production of synthetic liquid fuels

The scenario of current energy, and therefore the development model is neither sustainable nor secure, and is conditioned by two factors: (i) natural resources are limited; and (ii) increasing emission of greenhouse gases associated with the current use of these resources. Report just seven years ago [1], just when this Thesis began to be developed, already pointed out that the level of development of society will imply an increase in the use of the energy resources of 50 – 60 % until 2030, based on this increase in the use of fossil fuels (83 % of the total energy consumed). This aspect is even more drastic in the transport sector, where consumption will grow 20 % being associated CO_2 emissions by 33 % of the total emissions [1]. In this sector, the proposal for CO_2 capture is not feasible, which makes it necessary to use renewable and less polluting sources, catalytic processes playing a role in this scenario [2].

Currently the oil is still the main source of obtaining chemicals and fuels, but their use is not sustainable from an environmental point of view. The increasingly stringent environmental laws, the high as well as volatile price of fossil fuels, concern of the states to ensure security of supply of fossil fuels, technological development and perhaps most important, the relevance that being taking renewable fuels in the energy scenario and its implications for sustainable development makes imperative the search for alternative energy sources. These should supply the world's energy consumption, continuously growing due in part of the development of emerging countries such as China (in 2010 it has become the largest consumer of the world energy [3]), and achieving a sustainable development that allows to comply with agreements on emissions of greenhouse gases established several years ago in the United Nations Framework Convention on Climate Change (Kyoto Protocol, 1997 [4]) and which have recently been revised in the United Nations Conference on Climate Change held in December 2009 in Copenhagen [5].

The International Energy Agency has recently presented a report [5] stating that the global economic crisis that destabilized the energy markets since 2008 make the world energy to face unprecedented level of uncertainly. The evolution of the energy sector in the coming years will depend on the pace at which the global economy recovers, governmental actions and the way in which responds to the challenges of climate change and energy security, which will define the future of energy in long term.

As already indicated, one of the main focus of energy demand is the transport sector. Pending sufficient development of alternative technologies such as renewable H_2 production and their use in fuel cells, synthetic liquid fuels are those that will be faced this increase in the energy demand in the transport sector during the present century. The recent Annual Energy Outlook 2011 of the Energy Administration Information (USA) [6] indicates that consumption of liquid fuels for transportation will grow from 13.6 million barrels in 2009 to 14.1 million barrels in 2025, and where the XTL processes take special relevance in the providing of this amount of fuel. The GTL, CTL and BTL processes includes a set of reactions and chemical operations that transform natural gas, coal and biomass preferably in different types of liquid fuels and useful chemicals for the industry. However, should take into account that for these processes to be sustainable, it is necessary to use other technologies such as the capture and storage of CO_2. When synthetic liquids produced from coal without capture and storage of CO_2, the CO_2 emissions are twice the emissions that are derived from petroleum. When captured and/or stored the CO_2, the net emissions are only slightly lower. Regarding to the BTL process, the net CO_2 emissions are lower than those emitted by the conventional processes, being the balance of CO_2 emissions negative if it captures and stores CO_2. However, this process is limited by the amount of biomass that can be stored in a specific place, and also a limited resource, as BTL plants can convert only one third part of carbon contained on the biomass into liquid fuels [7]. Recently, the government of United States is showing some interest in a combined process of production of liquid fuels and electricity from coal and lignocellulosic biomass called Coal/Biomass-to-Liquids (CBTL) [7], whose scheme is shown in Figure 1.

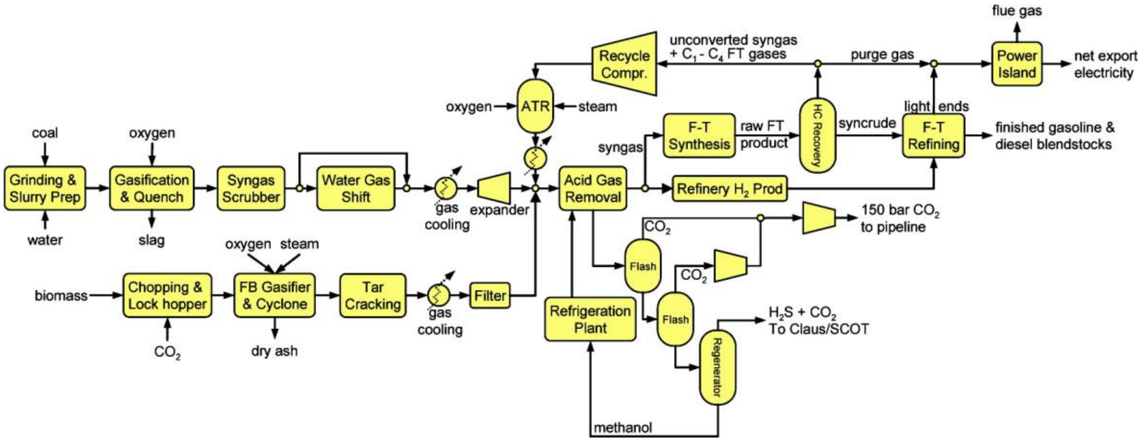

Figure1. CBTL-RC-CCS process configuration for maximize the Fischer-Tropsch liquid fuels production from coal and biomass (CBTL) with capture and storage of CO_2 (-CCS) and recirculation of unconverted synthesis gas (-RC) (extracted from [7]).

The XTL developed processes depends on the following factors:

a) Global reserves of fossil fuels.

b) Location of these reserves.

c) Demand for cleaner fuels.

d) Sustainable development, climate change and reducing CO_2 emissions.

e) Transient energy source to an energy economy based on H_2.

a) <u>Reserves of fossil fuels.</u> The Statistical Review of World Energy 2011 (British Petroleum [8]) estimated that the relationship between the proven reserves and the production by the end of 2010 is almost 3 times greater for coal and twice for natural gas in relation to oil (Figure 2).

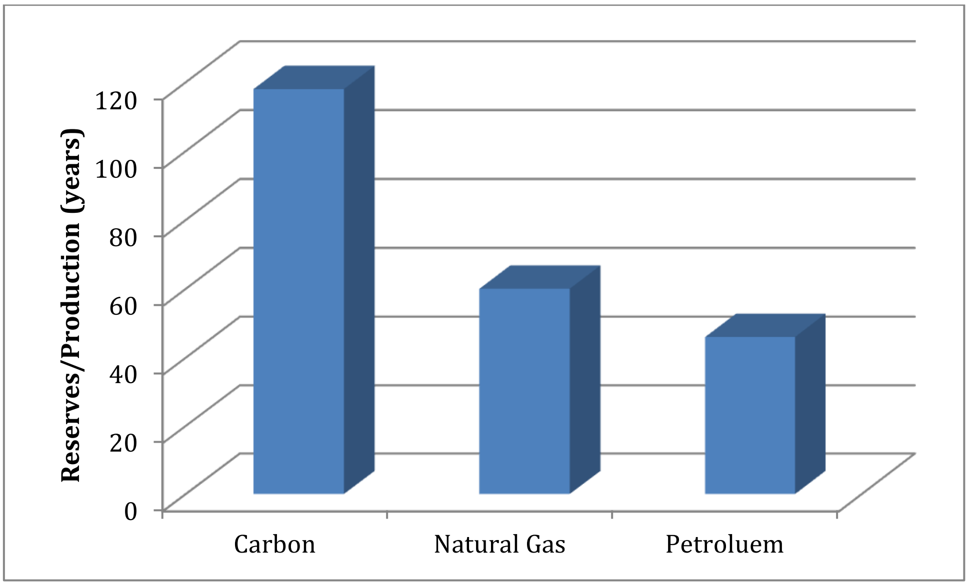

Figure 2. The relationship of the proven reserves versus to the production of fossil fuels (R/P) in the world, by the end of 2010.

As this report reveals, this way of expressing the reserves of fossil fuels gives an estimate of the time it would take to sell out if production is maintained at the same level, so that reserves of coal and natural gas would have a duration of almost 3 or 2 times, respectively, higher than that of petroleum. In the not too distant future it is expected that the use of natural gas acquired great importance in the energy sector as a primary carbon, wherein the GTL technology will be an essential process. Massive emissions of CO_2, SO_2 and NO_x inherent in coal combustion relegate compared to other fuels, unless applied technologies for the capture of these gaseous pollutants in streams afterburner. However, the co-production of liquid fuels using the GTL process and electricity through combined cycle has recently been proposed as a clean and efficient solution [9].

b) Location of the reserves. The major consumer of natural gas are located in Europe and North America, while the world's major natural gas reserves are concentrated in the Middle East, Russia and North Africa [8]. The transportation of natural gas from production area to consumer countries requires a very expensive physical process of liquefaction, which limits this option. In contrast, the chemical liquefaction through the GTL technology dramatically reduces the cost of transportation.

From the point of view of the CTL technology, the fact that large coal reserves are found in eminently consumer countries like the USA, China and Germany [8], makes the development of this technology becoming increasingly more interesting to reduce the strong energy dependence on oil in those countries. In regard to the BTL technology, biomass is a raw material dispersed throughout the world, but has the disadvantage that their treatment is complex [10]. So far, this process has not received much attention compared to GTL or CTL processes [11].

c) Clean fuels. In general, automotive fuels derived from the distillation of petroleum contain high level of aromatic hydrocarbons and hetero-atoms of nitrogen and sulfur compounds. All these compounds are sources of additional pollution to own CO_2 emissions and currently, the environmental laws of some countries are becoming every time less permissive at this point, so it is essential to carry out different processes in the refineries, which are complex and expensive, for elimination (hydro dearomatization, hydro denitrogenation and hydrodesulphurization) [9]. On the other hand, through the GTL, CTL, and BTL processes, clean mixture of hydrocarbons free from aromatic and compounds containing nitrogen or sulfur are obtained.

d) Sustainable development, climate change and reducing of CO_2 emission. Preventing climate change caused by human activity requires a drastic decrease in the emission of greenhouse gases, as has been established in the recent framework agreements [4, 5]. For this reason, renewable energy will play an important role. Among the various alternatives, the biomass generated by the process of photosynthesis from sunlight, CO_2 and H_2O is an extraordinarily attractive alternative to fossil fuels to fix and recycle CO_2 (final product of combustion). Recent studies claim that the use of BTL technology for the production of synthetic fuels is a promising alternative to conventional fuels from petroleum [12]. The World Energy Outlook 2010, which has already been mentioned above, reveals that the use of biofuels derived from biomass will continue to grow rapidly due mainly to the increase in the price of fossil fuels and the government support [5]. Along this line, the European Commission has established that biofuels should account for 20 % of all fuels used in transport by 2020 [13]. This report predicts that the global use of biofuels rise 1 million barrels a day to 4.4 million barrels per day in 2035. It is also expected that the USA, Brazil and the European Union will be the largest producers and consumers of biofuels. Currently, biofuels production costs are higher than the cost of conventional fuels from imported oil, so strong government incentives are needed for biofuels to make them competitive from an economic point of view compared to petroleum fuels.

e) Transient energy source toward an economy based on hydrogen. Current trends indicate that the future of energy use through the use of hydrogen as an energy transfer [14]. However, due to the fact that the current technologies of energy are based on petroleum and its derivatives, a stage of transition is necessary Figure 3.

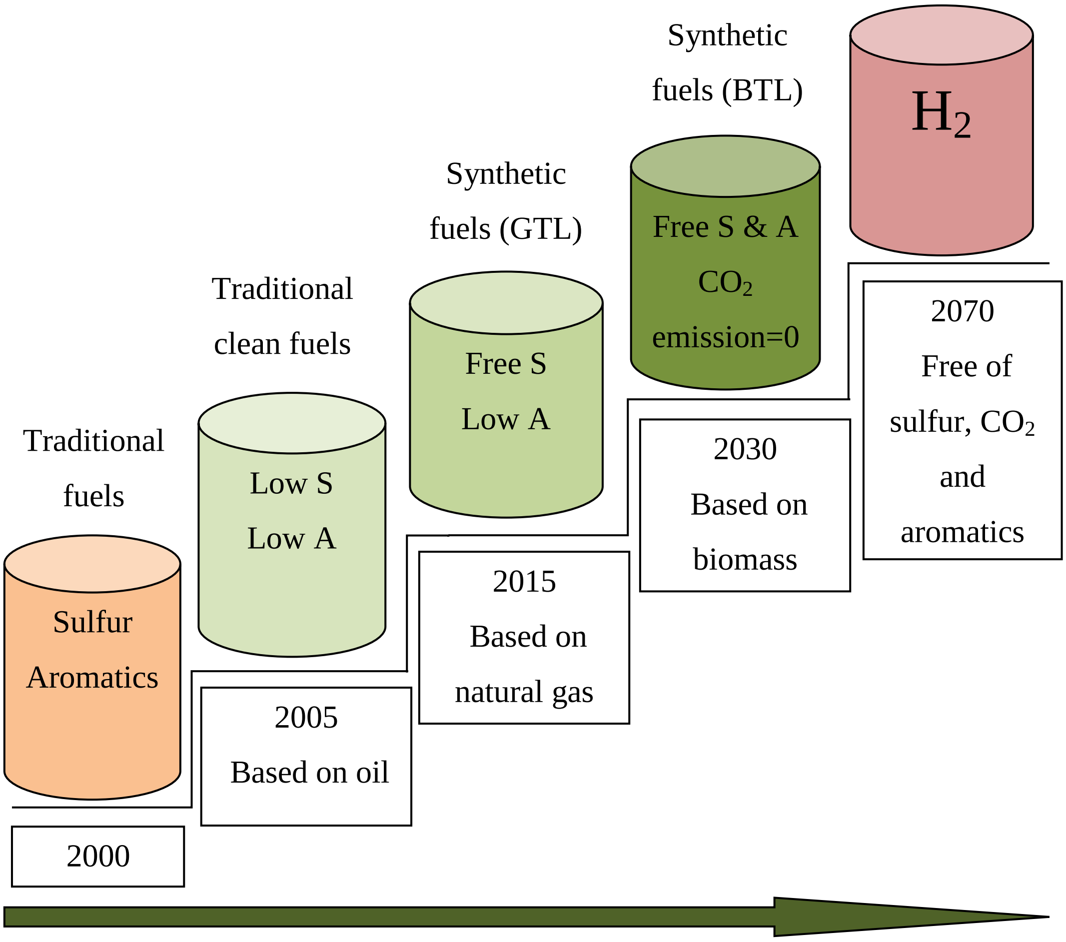

Figure 3. Technological evolution of fuels and prediction for the future (adapted from reference [14]).

Potentially, the production of liquid fuels from biomass or methane substantially reduces pollutant emissions compared to conventional fuels. Furthermore, the fact that automotive engineering developed for diesel engines is almost as efficient as the fuel cells [15], suggests that synthetic fuels from renewable sources and hydrogen could coexist in a "clean" energy market [2, 15, 16]. For this reason, GTL and BTL processes may play a key role in the transition, and even be an alternative to the "era of hydrogen". As discussed above, the need to achieve the objectives of the Framework

Agreements [4, 5] is a factor of pressure toward the interest of the biomass, being considered as the most important source for the renewable energy for the 21st century.

In GTL, CTL and BTL technologies, natural gas, coal and biomass respectively, are transformed into industrially relevant chemicals, including gases (ethylene, propylene, etc.), liquid hydrocarbons, waxes and different oxygenated compounds. Those processes consist of three stages:

a) Production of synthesis gas.

b) Fischer-Tropsch synthesis (FTS).

c) Improvement of the reaction products.

The following briefly discusses various processes for obtaining synthesis gas depending on the starting raw material and subsequently explain in more detail the stage of the synthesis of liquid fuels or Fischer-Tropsch synthesis, as it is the stage that studied in this Doctoral Thesis.

1.2. Background and historical overview

The early 20th century was an exciting period in the development of catalysis. The development of the ammonia synthesis process marked the start of heterogeneous catalysis as a large scale and high pressure continuous processing [17]. Recently, reserves of natural gas, either as such or associated with crude oil, have increased and a significant portion of this gas has been called stranded. The present need to give value for stranded gas is motivate research around the world to develop catalysis and process technology for converting natural gas to chemical and clean fuels. Production of valuable hydrocarbons via Fischer Tropsch reaction is being investigated by many researchers around the world. Although the conversion of synthesis gas to methanol, ethanol and, higher alcohols is also interesting.

For a period of time research concentrated on the production of chemicals from acetylene. Along the chemistry scientific and technological developments, many synthetic compounds can be derived from acetylene, such as acrylonitrile, acids, alcohols, amides, and many other synthetic compounds derived from acetylene. While the cost of intensive production energy of acetylene from calcium carbide appeared too expensive, the development of alternative processes for the production of acetylene, as a main source for production of many organic compounds, is highly challenging for researchers [18-20].

In 1902, Sabatier and Senderens described the catalytic conversion of CO and CO_2 into CH_4 and H_2O with Co and Ni catalysts at 250 °C and atmospheric pressure [21, 22]. After 11 years of that time and in 1913 BASF innovated the production of liquid hydrocarbons from synthesis gas, over a cobalt oxide catalyst in a patent granted [23]. At that time Germany has abundance of coal reserves and research efforts were conducted towards developing a process to obtain valuable products, such as fuels and chemicals, converted from the abundant coal reserves. The research efforts resulted in tremendous and significant discoveries to produced valuable liquid transportation fuels. One of these discoveries was in the decade of 1920's; the conversion of measurable amount of synthesis gas (a mixture of CO and H_2) into mainly hydrocarbons (synthol) via C-C formation is known as the Fischer Tropsch synthesis reaction. This reaction received the names of the engineers Fischer and Tropsch, who were the first to investigate the catalysis of the reaction and built up the first reactors for this purpose to produce hydrocarbons from syngas at the Kaiser-Wilhelm (presently Max Plank) Institute for Coal Research in Mulheim. It was demonstrated just in that time that the cobalt-based catalysts not only can be used for the Fischer Tropsch synthesis reaction but also iron catalysts that are able to work for the FTS reaction in an efficient way. However, Fischer and Tropsch succeeded in producing mainly hydrocarbons over cobalt and iron catalysts at moderate condition (250-300 °C and low pressure) [18-20]. It is worth mentioning that the source of liquid transportation hydrocarbons not only from Fischer Tropsch process but also coal liquefaction participated and contributed efficiently to the liquid fuel production. To produce liquid hydrocarbon fuels from coal gasification, an important work was developed in Germany for the period of time in 1930's. The direct liquefaction of coal with hydrogen at around 500 °C and a hydrogen pressure of no less than 700 bar in the presence of finely divided iron catalysts by Bergius in Rheinau-Mannheim [24]. These two important discoveries process, however complementary in the product, differ significantly in the concept and basic chemistry. Consequently, that's where the FTS generally operated at temperatures in the range between 150 and 300 °C and pressure up to 20 bar, the direct liquefaction of coal with H_2 to liquid transportation fuels was performed in the Bergius process conditions as mentioned above at about 500 ºC and hydrogen pressure up to 700 bar .

For the period of time before the Second World War, the Fischer Tropsch synthesis process industrial commercial plants practically started in Germany and by 1938 up to nine plants were in operation having a combined capacity of about 660.000 tonnes/year [25] . And during the Second World War, Germany were used the liquid transportation fuels that were produced via FT process from these plants. Even though these plants ceased to operate after the Second World War, interest in the Fischer Tropsch process remained because at that stage there was the persistent perception that the reserves of crude oil were very limited. After that time and besides cobalt catalysts, the commercialization of the iron based catalysts predominated.

After Second World War large shale gas reserves were discovered in the USA [26]. Consequently, new possibilities are open for the transformation of natural gas to valuable hydrocarbons. Based on syngas produced from natural gas, an FT plant with a capacity of 360.000 tonnes/year was built and operated in Brownsville, TX (USA), during the 1950s but a sharp increase in the price of methane caused the plant to be shut down [25].

At the same time stage, based on the world-wide prediction of increasing price of crude oil and also due to abundance of coal in South Africa, a Fischer Tropsch plant based on coal came on stream in 1955 in Sasolburg, South Africa with a capacity of about 110.000 tonnes/year, employing iron-based catalyst [27]. Sasol that is operating Fischer Tropsch plant and coal gasification implements two important process such as the Synthoil and Arge process. The Synthoil process produces lower boiling point hydrocarbons, such as gasoline, alcohols and, aldehydes. While the Arge process produces higher boiling point hydrocarbons, such as diesel and waxes. The catalyst mployed in the Synthoil technology process is iron-based catalyst, which is similar to the double promoted iron catalyst used in the ammonia synthesis. The Arge technology process is performed through a supported copper-iron based catalyst in a fixed bed reactor.

Although even before construction of FT plant was completed, the huge oil fields of the Middle East were discovered and consequently the predicted rise in the price of crude oil did not materialize, the interest in the FTS all but disappeared [25].

Table 1 shows the main companies involved currently in the process of production of synthetic fuel through the Fischer-Tropsch synthesis, as well as the production capacity and the expansion plans for the coming years [28, 29].

Table1. Main companies involved in the Fischer-Tropsch synthesis for the production of synthetic fuels and chemicals.

Company	**Country**	**Capacity (barrels/day)**	**Syngas source**
Sasol	South Africa	150.000	Carbon
	China	160.000	Carbon
	Australia	30.000	Natural Gas
	Nigeria	34.000	Natural Gas
	Qatar	34.000	Natural Gas
Shell	Malaysia	12.500	Natural Gas
	Qatar	140.000	Natural Gas
	Indonesia	75.000	Natural Gas
	Iran	70.000	Natural Gas
	Egypt	75.000	Natural Gas
	Argentina	75.000	Natural Gas
	Australia	75.000	Natural Gas
Shell; Choren	Germany	300	Biomass
Mossgas	South Africa	22.500	Natural Gas
Eni Technologie	Italy	20	Natural Gas
BP	USA	300	Natural Gas
Rentech	USA	1.000	Natural Gas
	South Africa	10.000	Natural Gas
	Bolivia	10.000	Natural Gas
Rentech; Pertamina	Indonesia	15.000	
Syntroleum	USA	70	Natural Gas
	Australia	11.500	Natural Gas
	Chile	10.000	Natural Gas
	Peru	5.000	Natural Gas
Gazprom; Syntroleum	Russia	13.500	Natural Gas
Repsol-YPT; Syntroleum	Bolivia	13.500	Natural Gas
	Bolivia	90.000	Natural Gas
ExxonMobil	Qatar	90.000	Natural Gas
Conoco	Qatar	60.000	Natural Gas
	USA	400	Natural Gas

1.3. Light Olefins feed stocks

Ethylene, propylene, and butenes are key building blocks in the petrochemical industry, as these olefins became one of the most important feedstock of choice for a large range of organic chemicals. These fundamental chemicals are among the organic chemicals with the largest production volumes worldwide. Table 2 shows production of organic chemicals worldwide in 2010 in thousands of metric tons [26]. Worldwide petrochemical production, ethylene is the largest-volume produced. The derivatives of these base chemicals result in produced a very different final valuable market products such as, synthetic textiles, solvents, coatings, and packing materials. The C_4 olefins fraction is consisted of *n*-butenes, butadiene, and isobutene which are used in fuel and chemical applications.

Table 2. Production of organic chemicals in 2010 in Thousands of Metric Tons (adapted from reference [26]).

	USA	**Asia**[a]	**China**	**Europe**
Ethylene	23975	18237	14188	19968
Propylene	14085	14295	na[b]	14758
Ethylene dichloride	8810	3222[c]	na	1323
Benzene	6862[d]	10889	5530	5107
Ethyl benzene	4240	na	na	1226
Cumene	3478	na	na	na
Ethylene oxide	2664	845[c]	na	2619
Butadiene	1580[e]	2715	na	2020
Methanol	na	na	15740	na

[a] Japan, South Korea, and Taiwan. [b] Information not available. [c] Japan only. [d] Thousands of liters. [e] 1,3-Butadiene rubber grade.

Ethylene is mainly used by the plastic industries. Ethylene is a versatile petrochemical and industrially used to produce high important intermediate chemicals such as ethylene oxide, ethylene dichloride and ethyl benzene. These derivative chemicals are used in the production of valuable intermediates in industry. For instance but not limited, ethylene oxide is used as a chemical precursor for the synthesis of ethylene glycol and ethyl benzene used to produce styrene via dehydrogenation process. Also ethylene is used as a main feed in the production of other plastics such as polystyrene, polyethylene terephthalate, and polyvinyl chloride, which are widely used in the packing, textile, and construction industries. In 2000 ethylene and its chemical derivatives were listed in the top highest volume chemical products in the United States. In the western European countries and particularly in 2010, the majority of the total consumption of ethylene (accounting for approximately 61%) was dedicated to the production of polyethylene. Propylene is a very important feed-stock hydrocarbon in the petrochemical industry as chemical precursors for many intermediate chemical products. It should be noted that the propylene derivatives more than that for ethylene. The main valuable industrial products can be obtained from propylene is polypropylene. It is worth mentioning that the large increase of the demand of propylene over the past 15 years were due to converted it to polypropylene. In 2010, more than half of the total consumption of propylene was for the production of polypropylene in the Western European countries. Propylene is the second large volume petrochemical produced in the world after ethylene production. Propylene is used to produce intermediate chemicals of high importance in industry such as, propylene oxide, cumene, isopropyl alcohol, acrylonitrile, and other valuable products.

Butenes, *n*-butenes, butadiene, and isobutene are used in fuel and applications of industrially relative chemicals. *n*-Butenes are used as comonomers for polyethylene, which is used for the production of *sec*-butyl alcohol, which in turn is a raw chemical in the production of methyl ethyl ketone (MEK) and is also used for the production of high boiling point olefins.

One of the most important applications of butadiene is manly used as feed stocks for the synthesis of various types of synthetic rubber. Also butadiene is used for the synthesis of acrylonitrile butadiene styrene (ABS), styrene butadiene (SB) copolymer latex and block copolymers, and nitrile rubber (NBR). These synthetic rubbers are in highly demand all over the world, particularly in Asia, for the final goods in the electronic and automotive sectors manufacturing.

Isobutylene is used as raw material for the production of methyl *tert*-butyl ether (MTBE) and ethyl *tert*-butyl ether (ETBE), which are used as octane enhancers, and for the production of isooctane by dimerization and subsequent hydrogenation. Accounting for about 85% of butenes consumption was dedicated to be used in the fuel industry. butenes are used for the synthesis of gasoline blending components such as, gasoline alkylate, polymer gasoline and dimersol.

1.4. Commercially Production of Light Olefins

Traditionally, ethylene is mainly produced from steam cracking process of hydrocarbon feedstocks, such as, naphtha or lower molecular weight paraffins such as, ethane and propane. Widely, naphtha cracking is main source of ethylene production, while recently light molecular weight paraffins has been gaining importance. The low content of higher hydrocarbons of many natural gas deposits in USA is enough to provide the chemical industry in the USA with low cost of feed stocks for the production of light olefins. Also due to the increase consumption of natural gas for raising thermal energy in USA, a huge amount of light hydrocarbons became available.

Thus, thermally steam crackers of light paraffins (ethane and propane) have been installed. While in European countries, where initially the consumption of gasoline for transport purposes was relatively low, since export of gasoline to the USA was legally prohibited, light olefins are obtained mainly from naphtha steam cracking. Furthermore, in Asia ethylene is produced mainly by naphtha steam cracking, while in the Middle East and Canada ethylene is obtained from steam cracking of ethane and propane.

Although propylene can be produced as a byproduct of naphtha steam crackers for ethylene production, it can be recovered from fluid catalytic cracking (FCC), visbreaking/thermal cracking, and coking in the refinery processes. For all of these processes, propylene is obtained as a diluted stream in propane. As well as the abundance of low priced propane in shale gas, the production of propylene via dehydrogenation process of propane (PDH) has grown in the last few years. Accounting for approximately 30% of propylene global supply derived from FCC process and due to the growth of ethylene production from steam cracking of ethane, this percentage tends to increase due to the steam cracking-derived propylene decrease.

The ratio of ethylene/propylene can be directed to desirable ratio during naphtha steam cracking by changing the degree of severity of the cracking process. For instance, the normal conditions of cracking process are moderately high severity cracking to increase cracking process yield to ethylene. While reducing the severity of cracking process lead to increase the production of high value byproducts, such as propylene during short-term optimization.

Traditionally butadiene is recovered from steam cracking of the C_4 fraction by extractive distillation. Other processes for the production of butadiene are as byproducts of the steam cracking of naphtha and gas oil for the production of light olefins such as, ethylene and propylene. An about 95% of the world production of butadiene are obtained via these processes, the steam cracking of naphtha and gas oil for the production of ethylene and propylene.

The demand for light olefins has been grown in the last few years and expecting that the global demand for these important petrochemical products such as ethylene and propylene will be increase in the future. The demand for the feedstocks required in the petrochemical industry will definitely increase as a result of the growth of the demand for light olefins. According to experts, the current production capacity obtain by thermal steam crackers will be insufficient to cover the growing demand for ethylene and propylene. Furthermore to the currently processes for the production of light olefins such as thermal steam crackers insufficient to cover the global demand, these processes have economic and environmental disadvantage. From the economic issue, the currently light olefins derived processes are dependent on the crude oil which is an expensive; moreover the productions of light olefins via thermal steam crackers are consuming energy. From the environmentally side, these conventional oil derived processes involve CO_2 emissions.

1.5. Syngas Production for Fischer Tropsch Synthesis

In the first step, coal, biomass and natural gas is converted to synthesis gas , also known as syngas (“synthesis gas”), which is a gaseous mixture of carbon monoxide and hydrogen ($CO+H_2$), wherein the molar ratio for H_2/CO depends on the carbon source. Usually the molar ratio of H_2/CO reach close to 3 when use natural gas, close to 2 when use biomass and close to 1 when use coal. Throughout the years, the raw material for obtaining synthesis gas has changed depending on several factors. Thus, throughout the decade 1935-1945 in Germany was used coal due to the abundant reserve of this fossil precursor and also to the inaccessibility of the oil. A similar situation occurred in South

Africa since 1955, where it even at the present keeps on applying commercially. The situation has changed in the present so that the synthesis gas is produced from natural gas, due mainly to economic reasons and regulations of CO_2 emissions [30]. The biomass still not used commercially for the production of synthesis gas but has recently been demonstrated in the laboratory scale application [31].

The predominant technology for the production of synthesis gas is the reforming of methane with steam (steam reforming). In this process, a mixture of methane and water vapor is reacted on a Ni catalyst at temperatures in the range 800-900 °C and operating pressure between 10 and 30 bar, and there forms carbon monoxide and hydrogen in accordance with the reaction:

$$CH_4 + H_2O \longrightarrow CO + 3H_2 \qquad (\Delta H = 226\ \text{kJ/mol}) \qquad [1]$$

Even still being the most commercially used option, this way of production of synthesis gas has a series of disadvantages. The reforming of methane with steam is a highly endothermic reaction, that is, it requires the input of large amount of energy, and the rate of the reaction is determined by the rate of heat input from the outside of the tubes in which the catalysts are located and where circulating mixture of CH_4 and H_2O. Furthermore, the molar ratio of H_2/CO obtained via steam reforming is close to 3 and that is too high to be used directly in the conventional Fischer Tropsch Synthesis reactor.

An alternative to this technology is the partial oxidation of methane. In this process, it is made by reacting a mixture of methane and pure oxygen in the molar ratio of CH_4/O_2 equal 2 on a metal catalyst, which is usually nickel or a noble metal such as Rh, in the temperature range from 800 to 900 °C [32, 33]. This reaction can be carried out through a purely thermal, in the absence of catalyst, although the resulting temperatures are much higher (1300–1500 °C).

$$CH_4 + \frac{1}{2} O_2 \longrightarrow CO + 2H_2 \quad (\Delta H = -22\ kJ/mol) \qquad [2]$$

Hot spots in the catalyst bed as a result of the high temperatures used and the exothermic nature of the reaction may occur in the generation of synthesis gas according with the reaction [1.2].

Catalytic reforming of methane and partial oxidation produces synthesis gas of different composition. The methane reforming provides a synthesis gas with a high ratio of H_2/CO. Regardless of the methodology used to prepare the synthesis gas, the H_2/CO ratio can be modified within certain limits by changing the conditions of the process [34]. Neither methane reforming nor partial oxidation produce a synthesis gas of ideal composition for industrial application in the synthesis of hydrocarbons in accordance with the Fischer Tropsch synthesis. The H_2/CO ratio used in the FT industrial reactor is close to 2.15, which is substantially lower than that obtained by steam reforming and slightly higher than that obtained by partial oxidation. A possible solution for this problem consists in coupling the two processes. In this way, the reforming and partial oxidation can be performed in parallel to produce an adjusted composition of synthesis gas, so that the mixing currents generated by each of the two reactors, the desired optimum composition are obtained. Another alternative is the autothermal reforming, wherein the partial oxidation and reforming combined in a single reactor. The term autothermal refers to the fact that the energy required to realizing the endothermic reaction of the steam reforming is supplied by the partial oxidation reaction. Currently, autothermal reforming (with its different variants) appears to be the best alternative to industrial scale for the production of synthesis gas [35].

The reforming process of methane with carbon dioxide, known as dry reforming, is a possibility to produce rich CO synthesis gas (H_2/CO molar ratio = 1) , that it may be advisable to the production of high molecular weight hydrocarbons [36]. The reaction is, like steam reforming, a highly endothermic process:

$$CH_4 + CO_2 \longrightarrow 2\,CO + 2\,H_2 \qquad (\Delta H = 247\ kJ/mol) \qquad [3]$$

This process can also be used to reduce emissions of CO_2 and CH_4, two gases that contribute to the greenhouse effect [37, 38], provided that the CO is used as reactant in another process (carbonylation of organic compounds). However, the molar ratio of H_2/CO obtained via dry reforming process is too low to be able to feed it directly into a conventional Fischer Tropsch synthesis reactor.

Another established process for the production of synthesis gas is the gasification of coal, biomass or any source of carbon, using steam and an oxidant.

$$2\,C + H_2O \longrightarrow 2\,CO + H_2 \qquad (\Delta H = 21.8\ kJ/mol) \qquad [4]$$

Although, in principle, this option is the least desirable environmentally, it can be economically profitable in those areas where there are abundance coal reserves available, as is the case with the three plants that Sasol remains in operation in South Africa [25]. In addition, this technology that historically has been considered as “dirty” is currently emerging as a versatile and efficient process in many areas [39]. Thus, coal gasification, according to equation [1.4], is presented as an ideal process for valuing waste and by-products of other processes and as has already been indicated for the use of renewable sources such as biomass. Beside gasification technology allows the development of energy efficient processes that include the coproduction of hydrogen and electricity as well as the capture of CO_2 emitted, so it is environmentally very attractive one [40].

An important aspect of this technology is that the synthesis gas thus obtained need to be sufficiently pure, free of contaminants such as H_2S, NH_4, CS_2, HCN and particles to prevent the poising of catalysts used in the reactor in which is carried out the Fischer Tropsch synthesis [41]. On the other the H_2/CO molar ratio obtained by this technology is 0.7 when the feedstock is coal [42] and between 0.8 and 1.6 when the synthesis gas is produced from biomass [41]. Therefore, the use of extra flow of hydrogen is needed to obtain the proper H_2/CO molar ratio or the presence of a reactor in which is carried out the water gas shift reaction (WGS) allowing for the H_2/CO molar ratio adequate. Another possibility is the using of iron-based catalysts for Fischer Tropsch synthesis, as a very active in water gas shift reaction (WGS) that allowing in the same way the rise in the ratio of H_2/CO during the reaction itself as will be detailed later. By the water gas shift reaction is converted the CO of synthesis gas in addition hydrogen according to the equation reaction:

$$CO + H_2O \longrightarrow CO_2 + H_2 \qquad (\Delta H = -40.6\ kJ/mol) \qquad [5]$$

1.6. Fischer Tropsch Synthesis Catalysis

The synoptic process in general reaction is a composed of an accompanied of the elementary bond-breaking and bond-formation steps. Here in the Fischer Tropsch Synthesis process, these include dissociation of CO and H_2 (bond-breaking) as well as chain growth (carbon coupling) and hydrogenation process on the metal catalyst surface. The rate of the reactant band dissociation and product formation (bond-formation) processes on the metal catalyst surface dictates the choice of metal.

Transition metals to the right in the periodic table are not active enough to dissociate CO. Furthermore, the transition metals in the left of periodic table are preferably dissociate CO, but do not desirable for FTS applications due to surface carbon and oxygen are too strongly bound to the surface of these metals which in turn leads subsequently to block hydrogenation and carbon coupling reaction to produce hydrocarbon products. The optimal metals for FTS reaction are these located in the middle of the periodic table, that is where these metals can promote CO dissociation, along with a balanced degree of bound the surface carbon and oxygen to the metal surface in order to facilitate hydrogenation and carbon coupling reaction.

1.6.1. Definition and main reactions

The synthesis of hydrocarbons from synthesis gas, known as the Fischer Tropsch (FT) synthesis, is after 70 years of validity [19, 43] a very attractive route for the production of clean fuels as a source of chemicals and, therefore, constitutes the most important step in the GTL, CTL and BTL processes. The FT synthesis is a complex structure of primary and secondary reaction, and can be comparable to a polymerization reaction in which the monomer unit surface -CH_2- is formed *in situ* on the surface of the catalyst from the carbon monoxide and hydrogen.

In the FT synthesis are obtained a complex mixture of hydrocarbons linear and branched chain, and also oxygenates (alcohols, aldehydes and esters), although the majority are linear paraffins and α-olefins. The hydrocarbons obtained, with a boiling point in the range of gasoline and diesel are high quality because they do not have heteroatoms (S, N), do not contain polyaromatic structures and the fraction of middle distillate presents a high cetane index. The reactions involved in the FT synthesis are numerous and complex, the most important are summarized in Table 3 [44].

Table 3. The main and side reaction, including the modification of the catalyst reaction, during the Fischer Tropsch Synthesis.

Main reaction	
Paraffins	$(2n+1)H_2 + nCO \rightarrow C_nH_{2n+2} + nH_2O$
Olefins	$2nH_2 + nCO \rightarrow C_nH_{2n} + nH_2O$
Water gas shift reaction (WGS)	$CO + H_2O \leftrightarrow CO_2 + H_2$
Side reaction	
Alcohols	$2nH_2 + nCO \rightarrow C_nH_{2n+2} + (n-1)H_2O$
Boudouard reaction	$2CO \rightarrow C + CO_2$
Modification of the catalyst	
Oxidation /Reduction catalyst	a. $M_xO_y + y\ H_2 \leftrightarrow xM + y\ H_2O$ b. $M_xO_y + y\ CO \leftrightarrow xM + y\ CO_2$
Carbide formation	$xM + yC \rightarrow M_xC_y$

1.6.2. Products distribution (distribution Schulz-Flory-Anderson)

The products distribution of the Fischer-Tropsch synthesis is described by equations developed originally for polymerization kinetics. According to this model, known as Anderson-Schulz-Flory (ASF), the products distribution in FT synthesis is determined by the expression:

$$Wn = n \cdot (1 - \alpha)^2 \cdot \alpha^{n-1} \qquad (Equation\ 6)$$

where n is the number of carbon atoms in a chain, Wn is the fraction in weight of chains with n carbon atoms, and α is the chain growth probability to pass from n to n+1 carbon atoms. Figure 4 shows the selectivity to the various products according the probability of the chain growth.

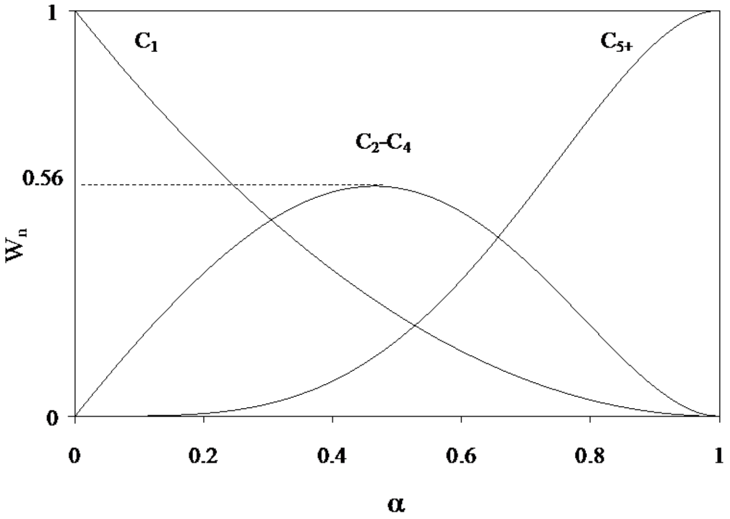

Figure 4. Selectivity of the various products of the FT reaction based on the probability of (α) chain growth.

The probability of the chain growth or α parameter determines the products distribution, depends on the length of the chain and is defined by the following expression:

$$\alpha_n = \frac{\sum_{i=n+1}^{\infty}\phi_i}{\sum_{i=n}^{\infty}\phi_i} = \frac{k_{p,n}}{k_{p,n}+k_{t,n}} \qquad (Equation\ 7)$$

wherein $k_{p,n}$ is the velocity of propagation of the chain growth of n carbon, $k_{t,n}$ is the rate of termination of the chain of n carbon atoms, and ϕ_i is the mole fraction of the products of n carbon atoms. Experimentally, the value of α can be determined from equation 1 as expressed in logarithmic form, plotting log (Wn/n) compared to n according to the following equation:

$$\mathrm{Log}\frac{W_n}{n} = n \cdot (\mathrm{Log}\,\alpha) + \frac{(1-\alpha)^2}{\alpha} \qquad (Equation\ 8)$$

Equation 2 implies that the Fischer-Tropsch synthesis is not selective to a single reaction product or a specific range of carbon numbers, methane being the only exception, which can occur with a selectivity of 100 % ($\alpha = 0$). However, there is the possibility to control, within certain limits, the composition of the products mixture obtained by changing the reaction conditions or the catalysts. Table 4 shows the influence of some experimental variables on conversion and product distribution.

Table 4. Effect of the Fischer-Tropsch synthesis reaction condition on the product distribution.

Variable	***a*** [a]	***Cn=/Cn*** [b]	S_{C1} [c]	X_{CO} [d]
↑Temperature	↓	*	↑	↑
↑Pressure	↑	*	↓	↑
↑H_2/CO molar ratio	↓	↓	↑	↑
↑Residence time	↑	↓	*	↑

[a] Probability of chain growth, [b] relationship *1*-olefins/*n*-paraffins; [c] selectivity to methane; [d] Complex relationship dependent on the catalyst composition

Although it has been indicated that the Fischer-Tropsch synthesis is a reaction of polymerization, this affirmation should not be considered strictly as such. Firstly, the monomer has to be formed *in situ* on the surface of the catalyst from the CO and H_2

molecules. Secondly, the surface reaction rates depend on the size of the chain in the case of C_1-C_4 hydrocarbons. Finally, the reaction products may suffer secondary reactions that affect the overall distribution. These phenomena cause deviation from the ASF distribution and mainly include:

- Selectivity towards CH_4 abnormally high for the vast majority of catalytic systems and reaction conditions [44-47].
- Selectivity towards ethylene and ethane abnormally low and high respectively [48-54].
- Probability of chain growth dependent on the size of the same one, resulting in a higher selectivity than the expected for the heavier hydrocarbons due to the involvement of the secondary reaction [55, 56].

1.6.3. Improving the quality of FT products

The Fischer-Tropsch synthesis produces a mixture of linear high molecular weight and high purity hydrocarbons that may have variety application: pharmaceutical products, cosmetics industry, etc., but this market is very limited and easily saturable. Some of the obtained paraffins can be used as lubricants. However the main application of the wax products in the Fischer-Tropsch synthesis is the production of synthetic fuels such as gasoline and diesel. The ideal gasoline consists of a mixture of C_5-C_{12} alkanes with a high level of branching, while the ideal diesel is formed by alkanes C_{13}-C_{18} linear chain [57].

The paraffin chains (waxes) obtained can be converted into other less length through a hydrocracking process, thereby giving rise to a mixture of lighter hydrocarbons having a boiling point similar to that of petroleum distillates. This mixture is separated in a distillation process in different linear fractions. As mentioned above, linear paraffins constitute a negative aspect for the quality (octane) of gasoline produced. Therefore, the octane number of the hydrocracked wax has to be improved by means of different processes such as isomerization, catalytic reforming, alkylation and oligomerization. However, the linear hydrocarbons obtained in the C_{13}-C_{18} fraction are excellent for use as a diesel fuels because they possess a high cetane number, about 75 (when the minimum requirements are 45-50) [58]. These synthetic fuels are high quality, they do not possess aromatic compounds, nitrogen and/or sulfur. For that reason, they can also be mixed with other fuels of lower quality in order to improve the characteristics of the latter one.

Typically, the processes of improvement type cracking, isomerization and oligomerization of the products obtained in this process accounting for 15 % of the cost of the GTL process [14].

1.6.4. Reactors and operating condition

Typical operation conditions in the Fischer-Tropsch synthesis reaction are between 200 and 360 °C and a total pressure between 20 and 60 bar typically operate in one the following two systems [59]: a low temperature (Low temperature Fischer-Tropsch, LTFT) at temperatures between 200 and 260 °C and with Fe and Co based catalysts to form high molecular weight hydrocarbons; and high temperature (high temperature Fischer-Tropsch, HTFT), between 300 and 360 °C and with Fe-based catalysts to form short-chain hydrocarbons, meanly.

In principle, there are several appropriate technologies to carrying out this highly exothermic process (reaction enthalpy 170 kJ mol^{-1}). The moving bed reactors are normally used in HTFT processes while multitubular fixed bed reactors and Slurry reactors are used in LTFT processes. For example, the Shell Middle Distillate Synthesis Process (SMDS) using tubular reactors of diameter 2.4 cm and a length of 12.2 m. These reactors are easy to manipulate and designed because all the tubes behave similarly. However, they have the disadvantage that they can generate pressure drop and is difficult to eliminate the heat formed during the reaction.

Another example is three-phase bubble columns (slurry bubble column type reactors) developed by Sasol. These reactors are very appropriate for the production of light olefins, gasoline and diesel. However, one of the problems that presented is the separation of the catalysts. Table 5 shows a summary the main advantages and disadvantages of fixed bed reactors and bubble columns.

Table 5. Advantages (+) and disadvantages (-) of the FTS reactors. Adapted from [59].

Type of reactor	**Fixed bed**	**Bubble column**
Diffusion through the pores	-	+
Mass transfer	+	-
Heat removal	-	+
Change of catalyst	-	+
Attrition of the catalyst	+	-
Cost	-	+

Nowadays, attempts have been made to improve the performance of these reactors. Among the different options, one that is being investigated is the variation of the geometry of the catalyst. In this line, the honeycomb monoliths (high number of parallel and identical channels with high cell density) have the advantage of having a high surface area and low probability of creating pressure drops. Also, is significantly improved the mass transfer between the gas, liquid and catalyst. However, the recirculation of the liquid is necessary to maintain a high flow rate and thus maintain Taylor regime inside the capillaries.

Other type of technologies are the so-called microstructured reactor or microchannel, which due to its effectiveness to eliminate the heat produced in the reaction, it is possible to operate isothermally and with more active catalysts.

Finally, membrane reactors are a technological option still underdeveloped but are attracting great interest in recent years. The membranes can have different functions, such as for example one of the reactive fed axially and distributed in the whole reactor, so that the heat produced in the reaction will be more distributed; and also for the eliminating of the H_2O selectivity, which is co-product of reaction and which can transform the active sites of the catalysts into inactive species from the catalytic point of view.

1.6.5. Active Metals for Fischer Tropsch Synthesis Reactions

It is well known that the active metals for FTS reaction are the group eight transition metals. However, the four group VIII metals, Fe, Co, Ni, and Ru have sufficiently high activities for the hydrogenation of carbon monoxide to warrant possible application in the Fischer Tropsch Synthesis [60]. The choice of active metal takes place based on the features of the active metal such as, exhibit CO hydrogenation catalytic activity, products distribution, and cost of the metal. Among these metals only iron, cobalt, and ruthenium are the most active for FTS applications. Being a powerful hydrogenation catalyst consequently it produces excessive amount of methane more than that produced when using Fe or Co catalysts. Nickel is other very active metal for the FTS reaction but nickel has a tendency to form volatile carbonyls and sub carbonyls at temperatures and pressures, at which practical FT plants operate, which cause sintering and loss of the metal via atom migration [61]. In the presence of H_2S, Mo has shown FTS catalytic activity. Rh and Os metals are shows FT activity but the product distribution moving towards oxygenates products when used Rh as active phase catalyst. Cr has also been employed as a catalyst for FTS and showed low CO hydrogenation activity.

The following summarized the main properties of the cobalt and ruthenium based catalysts. The iron metal being the study of this thesis will be discussed in more details in a later section.

1.6.5.1. Ruthenium catalysts

Among all the metals of group 8 in the periodic table, Ru is the most active metal for the CO hydrogenation reaction. Ruthenium produces high molecular weight hydrocarbons working at high pressure and low temperature [62, 63]. The product distribution (length of the chain) depends strongly on the reaction temperature, pressure, and nature of the support. This length of hydrocarbons chain increase as a result of total pressure increase and the reaction temperature decrease.

It was established that the specific activity of Ru for the FT synthesis depends on the particle size. Ru catalysts with a particle size of 3-4 nm tend to agglomerate during the reaction condition, while for large particle sizes, this phenomenon does not occur [64]. Recent studies have pointed out that there is an optimum particle size around 7-8 nm [65, 66].

Ru-based catalysts have the advantage that can operate under conditions of high partial pressure of H_2O. There are studies that confirm that the addition of H_2O into H_2/CO mixture has a positive effect on the catalytic activity and selectivity toward heavy hydrocarbons, since it acts as a source of hydrogen to form reaction intermediates

[67]. Although, the Ru can operate in the presence of other atmospheres of oxygenated compounds, which is vital when working with synthesis gas proceeding from biomass, but the Ru is not active in the reaction of water gas shift, therefore it is used normally with synthesis gas proceeding from natural gas that H_2/CO ratio is equal to 2 [66].

The Ru catalysts are deactivated during the FTS reaction due principally to the deposits of carbonaceous species on the surface of the catalysts. The oxidation of the active phase and/or agglomeration of the particles of ruthenium during the reaction condition do not appear to play an important role in the mechanism of deactivation for these catalysts [68].

As with the Fe and Co-based catalysts, the catalytic performance of the Ru catalysts is modified with the addition of different elements such as Mn [65], which improve the catalytic activity and thermal stability. On the other hand the Ru is also used as promoter of the Fe and Co-based catalysts with the aim of enhancing the reducibility of the corresponding oxides and/or increases the performance of the process [69, 70].

As mentioned previously the most active metal for FTS is ruthenium, which producing high molecular weight products at low reaction temperature about 150 °C, and 20 bar, but it out from large scale applications due to its high cost and low availability [71, 72].

1.6.5.2. Cobalt catalysts

Cobalt based catalysts mainly produce long chain linear alkanes [73]. Typically, Co-based catalysts are activated by a stream of H_2 at 200 - 450 °C to transform cobalt oxide into metallic cobalt, which is the active phase for the FT synthesis [74]. It has recently been demonstrated that the activity per active center, known as turnover frequency (TOF), is not greatly influenced by the particle size when the size of cobalt is bigger than 10 nm [75, 76], but decreases as the particle size decreases from that value.

Typically, the cobalt based catalysts consist of small particles of 10 - 20 nm deposited by means of impregnation with salts of Co^{2+} in inorganic materials (Al_2O_3, SiO_2, or TiO_2). The support provides mechanical resistance and thermal stability against to the agglomeration of particles of cobalt under the reaction condition. Also, the chemical nature of the support determines the reducibility of the cobalt oxide to form metallic particles.

As is the case with the Fe catalysts, different promoters are usually added, such as noble metal (Ru, Pt, or Rh) or metal oxide (MnO_x, ZrO_2, MgO, CeO_2) that enhance the catalytic activity, selectivity and/or stability during the FT reaction [77-79]. On the other hand, the H_2O is the principal product of the reaction has a great influence on the activity of the cobalt based catalysts depending on the partial pressure of the water that in turn depends straight on the conversion level [80-83].

Thus, a low pressure of H_2O has a positive effect on the rate of the FT synthesis and selectivity to C_5^+ products, while a high pressure inhibits the reaction, probably due to the oxidation of Co.

Like ruthenium, the cobalt based catalyst is not active in the reaction of water gas shift and therefore it is used normally with synthesis gas proceeding from natural gas ($H_2/CO = 2$). When using synthesis gas derived from biomass or coal gas ($H_2/CO < 2$), Fe-based catalysts used for FTS, since the iron catalysts are active in the water gas shift reaction and to adjust the H_2/CO ratio to a suitable value for FT synthesis ($H_2/CO \sim 2$).

1.6.5.3. Iron catalysts

Iron catalyst is the first catalyst used in the FT synthesis. The conventional iron catalysts used in the FT synthesis required the involvement of a basic promoter. The basicity of the catalysts surface is a critical to achieve a higher probability of chain growth and catalytic activity, as well as enhance the stability. The promoters used were basic alkaline elements [84], and alkali [85], including potassium, and gave the best catalytic results [86]. It is also often add other components into the catalysts in order to improve the catalytic behavior. For instance, the addition of copper lead to facilitate the reduction of iron oxide precursor [87] and the use of additives such as SiO_2 and Al_2O_3 increase the surface area acting as structural promoters [88]. Furthermore, as promoters, other metal oxides may be added such as Zr [87, 89], Zn [86, 90], Mn [91-93], rare earths, etc, with the aim to improve the catalytic activity and/or modify the product selectivity.

1.7. Fe-based catalysts Active Phase

It is well established that the active phase of the catalysts of Co, Ni, and Ru for the FTS reaction is the metallic phase however there is still no agreement on the type of active phase that forms on the iron catalysts for Fischer-Tropsch synthesis. Even with this shortcoming, which is set is that the iron oxide (hematite) is not active [94] in the reaction, so it is necessary prior reduction pretreatment. This reduction can be performed with a reduction agent such as, hydrogen, carbon monoxide, or a mixture of both of them (syngas). Several authors, particularly Bukur *et al.* [95-97], Datye *et al.* [98] and Davis *et al.* [99] studied the effect of activation on iron catalysts active phase that are formed, as well as on the activity and selectivity of the catalysts.

The transformation that occurred during the pretreatment and FT synthesis reaction in the phases of Fe catalysts play a very important role to explain the effect of each pretreatment and, of course, determine the activity of the catalyst.

Several phases of iron are known to exist when iron-based catalysts are subjected to the FT synthesis conditions. These include metallic iron (α-Fe), iron oxides (hematite, α-Fe_2O_3; magnetite, Fe_3O_4 and Fe_xO), and iron carbide. In general, during the activation of hematite (α-Fe_2O_3), which is the main component of the precursor oxide, under atmospheric pressure of hydrogen is reduced in the first step into magnetite phase (Fe_3O_4) and magnetite finally reduced to Fe metallic. But when the treatment of the hematite is carried out in an atmosphere of carbon monoxide or synthesis gas, iron carbide phase will be obtained. The phase of iron carbide may correspond to O-carbide type, which consist of phases in which the carbon atoms occupy octahedral interstices (ε-Fe_2C, ε'-$Fe_{2.2}C$ and Fe_xC) and carbides type TP that correspond with carbides where the carbon atoms occupy positions interstitial trigonal prismatic (χ–$Fe_{2.5}C$, Hägg carbide and Fe_3C, cementite). In the pretreatment with H_2 is required an induction period of the reaction in order to obtain an active catalyst. In any case, all these changes such as the formation and distribution of these phases depend on many variables such as time of exposure to the reactant gas, activation gas composition (H_2/CO ratio, the concentration of CO or H_2), design of the reactor, the activation conditions such as temperature and pressure and state of the catalyst (reduced/unreduced, supported/unsupported, etc.) [98].

Even with this general knowledge, still remains some controversy about the true nature of the active phase of the Fe catalysts in the FT synthesis. Teichner *et al.* proposed firstly in 1982 and later Kuivila and Butt in 1989 that the magnetite is the active phase in the FTS [100, 101], although in general it is widely accepted that there is a direct relationship between the content of iron carbides in the catalysts and the catalytic activity in the FT synthesis [99, 100, 102, 103]. In this sense, two models have been proposed to explain the role of the metal carbides in the hydrogenation reaction of CO:

(a) Carbides model. The catalytic activity is due to the presence of surface active sites located in the carbide phase and the density of these centers is related to the extent of carburization [104].

(b) Competition model [105]. The activity is due to surface of iron atoms and competition exists between bulk carbidization and the formation of hydrocarbons from CO. This model is based on the observation that the metallic iron is not initially active, but its catalytic activity increases as is carburized, which explains the need for an induction period.

The deactivation of the catalyst is determined by inactive carbon deposition on the active surface of the carbide phase, which progressively blocks more active sites.

1.8. The importance of Fe catalysts in FT synthesis

As already indicated in section 1.1, there is now renewed interest in the synthesis of synthetic fuels from synthesis gas via FT synthesis. In recent decades, this interest has been directed preferentially towards the synthesis of diesel from natural gas (GTL). This approach has limited commercial application of cobalt catalysts, which promote the production of waxes as indicated in paragraph 1.6.5.2. This is due to the ability of cobalt to readsorb olefins formed in the metallic sites, increasing the length of the hydrocarbons chain with the consequent decrease in the hydrogenation reaction and double bond isomerization. Waxes are subsequently divided selectivity in a second stage of hydrocracking to produce high quality diesel [106, 107].

Even considering the performance of the Co catalysts, the Fe catalysts currently have an attractive interest, mainly due to its reactivity. The following are its main advantages that justify their used throughout eight decades of effective and reaffirm its application according to the new trends in the synthesis of synthetic fuels.

(a) High selectivity to light olefins. Fe catalysts are practically the only ones capable of obtaining a high selectivity to olefins. This is due to the ability of metallic iron (α-Fe) to adsorb CO rapidly more than H_2 [44] which causes a low H/C ratio on the surface of the catalyst and therefore a low capacity of hydrogenating.

Light olefins are now one of the most important raw materials in the petrochemical industry. Important examples are polyethylene, polypropylene, and polyvinyl chloride as well as various elastomers, which are manufactured from ethylene and propylene. On the other hand, the acrylonitrile (another important monomer used in polymerization) is produced from propylene and ammonia. Furthermore, deserves special mention production of ethylene oxide, which are obtained numerous chemicals and that, in turn, is obtained from selective oxidation of ethylene.

Ultimately, the production of light olefins is doubtless important in the chemical industry and their alternative production from synthesis gas is a very attractive. In this respect, the fact that Fe catalysts are the only ones capable to obtaining unsaturated hydrocarbons maintains its validity. In the present they are used commercially by Sasol [108, 109] and several research groups have recently worked on the design of the catalysts that can be obtained directly and selectively light olefins from synthesis gas [110].

(b) Activity in the water gas shift reaction (WGS). The most important difference between the Fe and other active metals in the FT synthesis such as Co and Ru is that the Fe shows activity in the WGS reaction [111]. Under the condition in which the FT synthesis is carried out, the WGS reaction is favored thermodynamically. The reverse reaction is slow compared with the direct one in the condition of the FT reaction, and the last one depends on the partial pressure of water vapor in the reaction medium. Taking into account these premises, the Co catalysts produce hydrocarbons and water during the FT synthesis, while the Fe catalysts produce hydrocarbons and carbon dioxide due to the WGS reaction. When the synthesis gas derived from gasification of coal or biomass, the H_2/CO ratio is less than stoichiometric ($H_2/CO = 2$), required to produce hydrocarbons and water by means of the FT synthesis. Thus when using Co catalysts exists a shortage of H_2 for the reaction to take place and will require the involvement of the WGS reaction to convert the addition amount of CO to CO_2 and H_2 and that in turn lead to achieve stoichiometric relationship of the synthesis gas ($H_2/CO = 2$). This is only possible with the Fe catalysts. For this reason, the FT synthesis using a synthesis gas derived from gasification of coal or biomass using Fe catalysts since the reaction of WGS can be carried out in the same reactor in which the FT synthesis is performed. This characteristic prevents the realization of a process prior to the FT synthesis which simplifies and facilitates the operation of the process [111].

(c) Activity in the hydrogenation reaction of CO_2. In the last decades the large increase in energy demand has caused a great increase in the CO_2 emissions of anthropogenic origin. Although their relationship with the global temperature of the planet is not clear, numerous efforts have been conducted with the goal of reduce these emissions, as was established in the Kyoto Protocol. In this context, the chemical utilization of CO_2 via catalytic hydrogenation to produce liquid fuels is presented as an attractive alternative to transform it into useful products. On the other hand, CO_2 is a component present in the synthesis gas produced by gasification of coal, natural gas, or biomass, so that development of catalysts capable of hydrogenated CO and CO_2, avoid the need to purify the synthesis gas and would lower the cost of the process [57, 112].

It has been shown [113, 114] that the iron catalysts promoted with potassium are able to hydrogenate CO_2 to long chain hydrocarbons in conditions of the FT synthesis, through a series of reactions where the WGS reaction is an important intermediate one. That is, the direct hydrogenation reaction of CO_2 is irrelevant while their hydrogenation passes through an intermediate stage of transformation of CO_2 to CO through the WGS reaction. For this reason, the effective hydrogenation of CO_2 necessarily requires catalysts that are active in the water gas reaction, i.e. catalytic converters which are capable of transforming CO_2 to CO.

As outlined in the previous paragraph, that only the Fe catalysts are active in this reaction (CO_2 hydrogenation), so that necessarily for the design of a catalyst to hydrogenate CO_2 to long chain hydrocarbon should be constituted basically by iron phases.

To recapitulate, the Fe catalysts have extraordinary potential, which reaffirms nowadays that the Fe catalysts are preferable compared to those of the Co catalysts due to they are the only ones capable of producing light olefins, working with synthesis gas (H_2/CO ratios less than 2) derived from the gasification of coal or biomass and, furthermore, those catalysts are the most suitable for hydrogenation of CO_2. It should be emphasized also on the fact that the traditional claim that the Co is more active than Fe, it is so vague and ambiguous. It is known that the conversion of CO by using Co catalyst depends on the dispersion of the metallic cobalt [111] and that the fraction of CO and H_2 used to obtain hydrocarbons increase with conversion. In the case of the Fe catalysts, the fraction of synthesis gas converted to hydrocarbons decreases with the conversion to increase the activity in the WGS reaction. Therefore, when comparing the activity of the Co and Fe catalysts to high conversion of CO, the assertion that the Co catalysts are more active is true. On the contrary, when comparing the two catalysts at temperatures at which they produce low levels of CH_4 or CH_4 and CO_2 for Fe catalysts (220 °C for Co and 250-270 °C for Fe), the amount of hydrocarbons produced per gram of catalyst are comparable. Furthermore, considering the higher density of the oxides of Fe-based catalysts with respect to the supported cobalt [90], Fe with volumetric productivities are obtained (g cm^{-3} hydrocarbons/h) much greater than that for Co, which would allow to reduce the volume of the reactor.

In conclusion, if the Fe catalysts are used in several reactors in series, operating with CO conversion close to 60% and recycling unreacted flow of synthesis gas can be obtained much higher yield with the Fe catalysts more that with the Co catalysts, which refutes the claim that the later ones are more active.

Table 6 compares the performance and properties of Fe, Co and Ru catalysts.

Table 6. Comparison of the performance and properties of the Fe, Co, and Ru catalysts

property	**Fe**	**Co**	**Ru**
FT activity	Active	Active	Active
Selectivity	Light hydrocarbons	Heavy hydrocarbons	Heavy hydrocarbons
Syngas	Coal, biomass, natural gas	Natural gas	Natural gas
WGS activity	Active	inactive	Inactive
Poison	H2S	H2S	H2S
Reaction temperature	300-360 °C	200-260 °C	200-260 °C
Cost*	Cheap (1)	Relatively expensive (1000)	Very expensive (5000)

*Assuming the cost of Fe to 1[57]

1.9. References

[1] World Energy Outlook 2006, International Energy Agency, OECD/IEA 2006.

[2] J. R. Rostrup-Nielsen, Catal. Rev.-Sci. Eng. 46 (2004) 247-270.

[3] BP Energy Outlook 2030, www.bp.com, (2010).

[4] United Nations Framework Convention on Climate Change (1997), http://unfccc.int/kyoto_protocol/items/2830.php.

[5] World Energy Outlook 2010, International Energy Agency, OECD/IEA 2010.

[6] Annual Energy Outlook 2011, Energy Administration Information USA, http://www.eia.gov/forecasts/aeo/pdf/0383(2011).pdf.

[7] G. Liu, E. D. Larson, R. H. Williams, T. G. Kreutz,X. Guo, Energy Fuels 25 (2010) 415-437.

[8] BP Statistical Review of World Energy 2011. www.bp.com.

[9] A. P. Steynberg,H. G. Nel, Fuel 83 (2004) 765-770.

[10] K. Okabe, K. Murata, M. Nakanishi, T. Ogi, M. Nurunnabi,Y. Liu, Catal. Lett. 128 (2009) 171-176.

[11] M. J. A. Tijmensen, A. P. C. Faaij, C. N. Hamelinck,M. R. M. van Hardeveld, Biomass Bioenerg. 23 (2002) 129-152.

[12] C. N. Hamelinck, A. P. C. Faaij, H. den Uil,H. Boerrigter, Energy 29 (2004) 1743-1771.

[13] Directiva 2009/28/CE del Parlamento Europeo y del Consejo, http://eur-lex.europa.eu/LexUriServ/LexUriServ.do?uri=OJ:L:2009:140:0016:0062:es:PDF.

[14] E. F. Sousa-Aguiar, L. G. Appel,C. Mota, Catal. Today 101 (2005) 3-7.

[15] J. R. Rostrup-Nielsen, Science 308 (2005) 1421-1422.

[16] G. W. Huber, J. N. Chheda, C. J. Barrett,J. A. Dumesic, Science 308 (2005) 1446-1450.

[17] I. Chorkendroff,J. W. Niemantsverdriet, Concepts of Modern Catalysis and Kinetics, Wiley-VCH, Weinheim. (2007)

[18] F. Fischer,H. Tropsch, Über die Herstellung synthetischer Ölgemische (Synthol) durch Aufbau aus Kohlenoxyd und Wasserstoff. 4 (1923) 276.

[19] F. Fischer,H. Tropsch, The synthesis of petroleum at atmospheric pressures from gasification products of coal. 7 (1926) 97.

[20] F. Fischer,H. Tropsch, Brennstoff-Chem 11 (1926) 489.

[21] J. Soc. Chem. Ind. 21 (1902) 457-507.

[22] P. Sabatier,J. B. Senderens, 134 (1902) 514-516.

[23] A. Mittasch,C. Schneider, German Patent 293 787 (1913).

[24] F. Bergius,J. Billwiller, German Patent 301 231 (1919).

[25] M. E. Dry, Catal. Today 71 (2002) 227-241.

[26] H. M. Torres Galvis,K. P. de Jong, ACS Catal. 3 (2013) 2130-2149.

[27] M. E. Dry, Endeavour 8 (1984) 2-4.

[28] F. J. Pérez-Alonso, PhD Thesis, Universidad Autonoma de Madrid, 2006.

[29] Foc. Catal. 2005, 2005(10), 3.

[30] D. J. Wilhelm, D. R. Simbeck, A. D. Karp,R. L. Dickenson, Fuel Process. Technol. 71 (2001) 139-148.

[31] H. Boerrigter; H. den Uil, Proceedings of the 12th European Biomass Conference 1152. ETA-Florence and WIP-Munich: 2002.

[32] M. A. Pen˜a, J. P. Gómez,J. L. G. Fierro, Appl. Catal. A-Gen. 144 (1996) 7-57.

[33] M. A. Peña; J. L. G. Fierro, Supported metals in the production of hydrogen. In Supported metals in catalysis; M. Fernández-García; J. A. Anderson, Eds.; Chapter 7. Imperial College Press: 2005.

[34] M. E. Dry, J. Chem. Technol. Biotechnol. 77 (2002) 43-50.

[35] J. R. Rostrup-Nielsen, Catal. Today 71 (2002) 243-247.

[36] A. K. Prabhu, R. Radhakrishnan,S. Ted Oyama, Appl. Catal. A-Gen. 183 (1999) 241-252.

[37] J. H. Edwards, Catal. Today 23 (1995) 59-66.

[38] J. Rostrup-Nielsen, Appl. Catal. A-Gen. 255 (2003) 3.

[39] J. C. van Dyk, M. J. Keyser,M. Coertzen, Int. J. Coal Geol. 65 (2006) 243-253.

[40] K. Yamashita,L. Barreto, Energy 30 (2005) 2453-2473.

[41] M. J. Prins, K. J. Ptasinski,F. J. J. G. Janssen, Fuel Process. Technol. 86 (2005) 375-389.

[42] I. Kroschwitz; M. Howe-Grant; Kirk-Othmer, Encyclopedia of Chemical Technology. Wiley & Sons: 4th Ed., New York, 1996.

[43] F. Fischer,H. Tropsch, Brenn. Chem. 11 (1930) 489.

[44] G. P. Van Der Laan,A. A. C. M. Beenackers, Catal. Rev.-Sci. Eng. 41 (1999) 255-318.

[45] H. Schulz, Appl. Catal. A-Gen. 186 (1999) 3-12.

[46] M. E. Dry, J. Mol. Catal. A-Chem. 17 (1982) 133-144.

[47] R. A. Dictor,A. T. Bell, J. Catal. 97 (1986) 121-136.

[48] S. Novak, R. J. Madon,H. Suhl, J. Catal. 77 (1982) 141-151.

[49] S. Novak, R. J. Madon,H. Suhl, J. Chem. Phys. 74 (1981) 6083-6091.

[50] E. W. Kuipers, I. H. Vinkenburg,H. Oosterbeek, J. Catal. 152 (1995) 137-146.

[51] E. W. Kuipers, C. Scheper, J. H. Wilson, I. H. Vinkenburg,H. Oosterbeek, J. Catal. 158 (1996) 288-300.

[52] T. Komaya,A. T. Bell, J. Catal. 146 (1994) 237-248.

[53] D. S. Jordan,A. T. Bell, J. Phys. Chem. A 90 (1986) 4797-4805.

[54] E. Iglesia, S. C. Reyes,R. J. Madon, J. Catal. 129 (1991) 238-256.

[55] D. J. Dwyer,G. A. Somorjai, J. Catal. 56 (1979) 249-257.

[56] H. Schulz, K. Beck,E. Erich, Fuel Process. Technol. 18 (1988) 293-304.

[57] M. E. Dry, J. Chem. Technol. Biotechnol. 77 (2002) 43-50.

[58] M. E. Dry, Appl. Catal. A-Gen. 276 (2004) 1-3.

[59] R. Guettel, U. Kunz,T. Turek, Chem. Eng. Technol. 31 (2008) 746-754.

[60] B. H. Davis, Ind. Eng. Chem. Res. 46 (2007) 8938-8945.

[61] M. Agnelli, M. Kolb,C. Mirodatos, J. Catal. 148 (1994) 9-21.

[62] M. A. Vannice, J. Catal. 37 (1975) 449-461.

[63] J. P. Hindermann, G. J. Hutchings,A. Kiennemann, Catal. Rev.-Sci. Eng. 35 (1993) 1-127.

[64] H. Abrevaya, M. J. Cohn, W. M. Targos,H. J. Robota, Catal. Lett. 7 (1990) 183-195.

[65] M. Nurunnabi, K. Murata, K. Okabe, M. Inaba,I. Takahara, Appl. Catal. A-Gen. 340 (2008) 203-211.

[66] J. Kang, S. Zhang, Q. Zhang,Y. Wang, Angew. Chem.-Int. Edit. 48 (2009) 2565-2568.

[67] M. Claeys,E. van Steen, Catal. Today 71 (2002) 419-427.

[68] K. R. Krishna,A. T. Bell, J. Catal. 130 (1991) 597-610.

[69] G. L. Ott, T. Fleisch,W. N. Delgass, J. Catal. 60 (1979) 394-403.

[70] J. Li, G. Jacobs, Y. Zhang, T. Das,B. H. Davis, Appl. Catal. A-Gen. 223 (2002) 195-203.

[71] M. A. Vannice, J. Catal. 37 (1975) 462-473.

[72] C. X. Xiao, Z. P. Cai, T. Wang, Y. Kou,N. Yan, Angew. Chem.-Int. Edit. 47 (2008) 746-749.

[73] E. Iglesia, Appl. Catal. A-Gen. 161 (1997) 59-78.

[74] R.B. Anderson, P.H. Emmet, The Fischer- Tropsch synthesis, Academic Press Inc., 1956.

[75] J. P. Den Breejen, P. B. Radstake, G. L. Bezemer, J. H. Bitter, V. Frøseth, A. Holmen,K. P. De Jong, J. Am. Chem. Soc. 131 (2009) 7197-7203.

[76] G. Prieto, A. Martínez, P. Concepción,R. Moreno-Tost, J. Catal. 266 (2009) 129-144.

[77] A. Y. Khodakov, W. Chu,P. Fongarland, Chem. Rev 107 (2007) 1692-1744.

[78] S. Sun, K. Fujimoto, Y. Yoneyama,N. Tsubaki, Fuel 81 (2002) 1583-1591.

[79] F. Morales, E. de Smit, F. M. F. de Groot, T. Visser,B. M. Weckhuysen, J. Catal. 246 (2007) 91-99.

[80] M. Ojeda, F. J. Pérez-Alonso, P. Terreros, S. Rojas, T. Herranz, M. López Granados,J. L. G. Fierro, Langmuir 22 (2006) 3131-3137.

[81] S. Storsæter, Ø. Borg, E. A. Blekkan,A. Holmen, J. Catal. 231 (2005) 405-419.

[82] S. Krishnamoorthy, M. Tu, M. P. Ojeda, D. Pinna,E. Iglesia, J. Catal. 211 (2002) 422-433.

[83] G. Kiss, C. E. Kliewer, G. J. DeMartin, C. C. Culross,J. E. Baumgartner, J. Catal. 217 (2003) 127-140.

[84] W. Ngantsoue-Hoc, Y. Zhang, R. J. O'Brien, M. Luo,B. H. Davis, Appl. Catal. A-Gen. 236 (2002) 77-89.

[85] M. Luo,B. H. Davis, Appl. Catal. A-Gen. 246 (2003) 171-181.

[86] S. Li, A. Li, S. Krishnamoorthy,E. Iglesia, Catal. Lett. 77 (2001) 197-205.

[87] K. Chen,Q. Yan, Appl. Catal. A-Gen. 158 (1997) 215-223.

[88] P. Davies, BP statistical Review of World Energy 2005. www.bp.com. 14-6-2005.

[89] K. Chen, Y. Fan, Z. Hu,Q. Yan, Catal. Lett. 36 (1996) 139-144.

[90] S. Li, S. Krishnamoorthy, A. Li, G. D. Meitzner,E. Iglesia, J. Catal. 206 (2002) 202-217.

[91] W. L. van Dijk, J. W. Niemantsverdriet, A. M. van dar Kraan,H. S. van der Baan, Appl. Catal. A-Gen. 2 (1982) 273-288.

[92] G. J. Hutchings,J. C. A. Boeyens, J. Catal. 100 (1986) 507-511.

[93] G. C. Maiti, R. Malessa,M. Baerns, Appl. Catal. A-Gen. 5 (1983) 151-170.

[94] S. Li, W. Ding, G. D. Meitzner,E. Iglesia, J. Phys. Chem. B 106 (2001) 85-91.

[95] D. B. Bukur, M. Koranne, X. Lang, K. R. P. M. Rao,G. P. Huffman, Appl. Catal. A-Gen. 126 (1995) 85-113.

[96] D. B. Bukur, K. Okabe, M. P. Rosynek, C. P. Li, D. J. Wang, K. R. P. M. Rao,G. P. Huffman, J. Catal. 155 (1995) 353-365.

[97] D. B. Bukur, L. Nowicki, R. K. Manne,X. S. Lang, J. Catal. 155 (1995) 366-375.

[98] M. D. Shroff, D. S. Kalakkad, K. E. Coulter, S. D. Kohler, M. S. Harrington, N. B. Jackson, A. G. Sault,A. K. Datye, J. Catal. 156 (1995) 185-207.

[99] R. J. O'Brien, L. Xu, R. L. Spicer,B. H. Davis, Energy Fuels 10 (1996) 921-926.

[100] J. P. Reymond, P. Mériaudeau,S. J. Teichner, J. Catal. 75 (1982) 39-48.

[101] C. S. Kuivila, P. C. Stair,J. B. Butt, J. Catal. 118 (1989) 299-311.

[102] T. Riedel, H. Schulz, G. Schaub, K.-W. Jun, J.-S. Hwang,K.-W. Lee, Top. Catal. 26 (2003) 41-54.

[103] J. A. Amelse, J. B. Butt,L. H. Schwartz, J. Phys. Chem. A 82 (1978) 558-563.

[104] G. B. Raupp,W. N. Delgass, J. Catal. 58 (1979) 361-369.

[105] J. W. Niemantsverdriet, A. M. Van der Kraan, W. L. Van Dijk,H. S. Van der Baan, J. Phys. Chem. A 84 (1980) 3363-3370.

[106] S. T. Sie, M. M. G. Senden,H. M. H. Van Wechem, Catal. Today 8 (1991) 371-394.

[107] M. J.Van der Burgt; C. J. Van Leuween; J. J. del'Amico, Methane Conversion. D. M. Bibby; C. D. Chang; R. F. Howe, Yurchak, S. Eds Elsevier Science Publishers, New York: 1988, p 473.

[108] R. L. Espinoza, A. P. Steynberg, B. Jager,A. C. Vosloo, Appl. Catal. A-Gen. 186 (1999) 13-26.

[109] A. P. Steynberg, R. L. Espinoza, B. Jager,A. C. Vosloo, Appl. Catal. A-Gen. 186 (1999) 41-54.

[110] F. R. van den Berg, M. W. J. Crajé, A. M. van der Kraan,J. W. Geus, Appl. Catal. A-Gen. 242 (2003) 403-416.

[111] I. Kroschwitz; M. Howe-Grant; Kirk-Othmer, Encyclopedia of Chemical Technology. Wiley & Sons: 4th Ed., New York, 1996.

[112] S. Hilaire, X. Wang, T. Luo, R. J. Gorte,J. Wagner, Appl. Catal. A-Gen. 215 (2001) 271-278.

[113] S. Krishnamoorthy, A. Li,E. Iglesia, Catal. Lett. 80 (2002) 77-86.

[114] T. Riedel, G. Schaub, K.-W. Jun,K.-W. Lee, Ind. Eng. Chem. Res. 40 (2001) 1355-1363.

Chapter 2: Objectives

2

Objectives

As explained in the Introduction Chapter, there is currently a growing interest in the production of clean fuels and chemicals feedstock such as ethylene and propylene from synthesis gas through the Fischer-Tropsch synthesis. In the last decades, this interest has been preferably oriented towards the production of diesel from natural gas (GTL process) in order to alleviate the stagnation of proven oil reserves. To this should be added the fact that in recent years there have been new implications in the energy scheme of the developed countries have allowed the development not only the GTL process, but also the CTL and BTL processes, which used coal and biomass as raw materials for obtaining the synthesis gas.

In this scenario, the Fe catalysts are highly attractive and effective mainly because of their reactivity. Thus, when the synthesis gas obtained from coal or biomass, in addition to the lower H_2/CO molar ratio than the stoichiometric ratio, it can contain a large amount of carbon dioxide which would be desirable for development of Fischer-Tropsch catalysts which are also effectively active in the CO_2 hydrogenation reaction. This option would avoid the purification step of the synthesis gas. In this sense, the Fe catalysts have extraordinary potential since they are the only ones capable to work with H_2/CO molar ratios less than stoichiometric and are most suitable for the hydrogenation reaction of CO_2. This is due to the fact that they are active in the water gas shift (WGS) reaction which allows to producing additionally H_2 in the case of the synthesis gas with H_2/CO ratio less than 2. It is also emphasized that in the case of the CO_2 hydrogenation reaction CO is the intermediate molecule implied in the transformation of CO_2. On the other hand, Fe catalysts are the only one capable of inducing a high selectivity to olefins, which are one of the essential raw materials in the chemical industry.

In this study, the impact of adding various different transitions metals (Zr, Mg and Mn) on the catalytic properties of precipitated bulk Fe-based catalysts was investigated. To develop specific targets, the Thesis is structured in several chapters:

Chapter 4 focuses on iron zirconium based catalysts formation during Fischer-Tropsch synthesis. The main objective of this work in this chapter is the development of highly active and stable Fe_2O_3/ZrO_2 catalysts capable to convert syngas ($CO+H_2$) mixtures into the desired fractions such as low molecular weight hydrocarbons, and more specifically C_2-C_4 olefins. This principal objective includes several other objectives. (i), Preparation of an iron oxide-zirconia catalyst series via co-precipitation in which the Fe/Zr atom ratio is varied in a large range of compositions; (ii), testing in the hydrogenation reaction of CO under conditions which approach industrial practice using a fixed-bed catalytic reactor; (iii), Optimization of the conditions employed in both activation and reaction steps as to obtain the maximum yield toward C_2-C_4 olefins (paraffins); (iv), evaluation of catalyst structures and establishment of some kind of correlation between catalyst structure and performance; and (v), in depth discussion of experimental data and redesign catalyst formulations displaying improved performance in the target reaction.

Due to the fact that the Fischer-Tropsch synthesis is a highly structure-sensitive reaction, that is, the crystallite size of the metal catalysts is one of the main factors that controls the FT activity and products selectivity, Chapter 5 sheds light on the effect of the pre-treatment temperature of Fe/ZrO_2 for the Fisher-Tropsch synthesis. It is intended to determine the optimum pre-reduction temperature of Fe/ZrO_2 for the Fischer-Tropsch synthesis reaction in terms of catalytic activity, products selectivity and stability. Therefore between the transitions metals were previously studied above, zirconium oxide was chosen for carrying out this study due to the fact that this structural promoter leads to increase the metal (Fe) dispersion and allow to obtain small crystal size of iron oxide by incorporating it with small zirconium particles (nanoparticles).

To improve catalytic performance iron based catalysts for Fischer-Tropsch synthesis reaction some metal promoters such as magnesium and copper were incorporated into the Fe-based catalyst system. Chapter 6 aims at a systematic understanding of the effect of the copper promoter on the physico-chemical properties of the coprecipitated Fe/Mg catalysts under realistic FTS reaction conditions. The contacting of Fe oxide precursors with synthesis gas (H_2/CO mixtures) leads to structural and chemical changes and to the formation of the active sites required for the FTS. The local structure and oxidation state of the starting Fe_2O_3 precursors promoted by copper were investigated using *in situ* X-ray absorption spectroscopy during activation process.

As the mesoporous substrates are considered promising for highly efficient catalysts due to their high surface areas and large pore sizes, our approach in Chapter 7 consisted in the preparation of mesoporous Mn-Fe nanocomposites through a simple one-step sol-gel process in the presence of a triblock copolymer as a structure-directing agent and their use for the CO_2 hydrogenation reaction via FT synthesis for the production of valuable hydrocarbons. This Chapter presents the results of studies on the effects of manganese addition to MnFeO nanocomposites for the CO_2 hydrogenation reaction. In order to establish the relationship between catalyst structure and performance, the catalysts were investigated using different characterization techniques such as N_2 adsorption-desorption isotherms, high-resolution transmission electron microscopy (HRTEM), X-ray diffraction (XRD) studies, temperature programmed reaction (H_2-TPR) and X-ray photoelectron spectroscopy measurements.

Chapter 3: Experimental Techniques

3

Experimental techniques

In this Chapter the materials, methods and equipment used in the preparation, characterization and evaluation of the catalytic activity of different catalysts used in the development of this Doctoral Thesis are described. The Chapter is divided into three sections: materials and methods for catalyst preparation, techniques used in the characterization of catalyst structures, and description of the equipment used in the evaluation of the catalytic activity.

3.1. Materials and methodology in the catalysts preparation

The catalysts used in the development of this Doctoral Thesis were prepared by different preparation methods such as coprecipitation, incipient wetness impregnation and simple one-step sol-gel processes. Fe/ZrO_2 catalysts were prepared by coprecipitation method in Chapter 4, while prepared by incipient wetness impregnation method in Chapter 5. The catalysts investigated in Chapter 6 (Fe/Mg/Cu) were prepared by a combination of coprecipitation and incipient wetness impregnation techniques. A simple one-step sol-gel process was used to prepare MnFe catalysts in Chapter 7. Table 1 summarizes the precursors used to prepare these catalysts.

Table 1. Catalysts composition and metal precursors used in the development of the Doctoral Thesis

Chapter	**Catalyst composition (atomic ratio)**	**Metal precursor**
4	Fe/ZrO_2 Fe/Zr = (0, 0.05, 0.15, 0.5, 0.85, 0.95 and 1)	-Iron (III) nitrate nonahydrate ($Fe(NO_3)_3.9H_2O$, Aldrich, >= 98%) -Zr(IV) oxynitrate hydrate (Aldrich, 99.99%)
5	Fe/ZrO_2 Fe/Zr = 0.1	-Iron (III) nitrate nonahydrate ($Fe(NO_3)_3.9H_2O$, Aldrich, >= 98%) -zirconium hydroxide (Silica-stabilized) grade XZ0645/01, Magnesium Elektron Ltd.
6	Fe/MgO/CuO Mg/Fe = 0.1	-Iron (III) nitrate nonahydrate ($Fe(NO_3)_3.9H_2O$, Aldrich, >= 98%) -Magnesium(II) nitrate hexahydrate (Aldrich, 99.00%) -Copper(II) nitrate hemipentahydrate (Aldrich, 98%)
7	MnFe Mn/Fe= (0, 0.05, 0.1, 0.2, 0.3 and 0.5)	-Iron(III) acetylacetonate (97%, $Fe(C_5H_7O_2)_3$) -manganese(II) acetate tetrahydrate (99.99%, $(CH_3COO)_2Mn.4H_2O$)

3.2. Characterization techniques

This section briefly describes the fundamentals of experimental procedures and characterization techniques employed along the development of this study. The results obtained from these techniques allow us to relate the catalytic behavior of the catalysts with their physical and chemical properties. All these techniques were employed in this study and the type of information provided by each of them are summarized in Table 2.

Table 2. Characterization techniques employed

Analytical technique	**Information**
Nitrogen adsorption-desorption isotherms	Surface area
Powder X-ray diffraction (XRD)	Crystalline species
In situ X-ray absorption near edge structure (XANES)	Electronic state
Laser Raman spectroscopy (LRS)	Identify phase composition
H_2-Temperature-programmed reduction (H_2-TPR)	Reducibility
CO-Temperature-programmed desorption (CO-TPD)	Adsorption sites
O_2-Temperature-programmed oxidation (O_2-TPO)	Oxidation
X-ray Photoelectron spectroscopy (XPS)	Chemical state and composition of surface atoms
High-resolution transmission electron microscopy (HRTEM)	Distribution and morphology of phases

3.2.1. Textural analysis

3.2.1.1. Nitrogen adsorption-desorption isotherms

Frequently gas adsorption, and particularly physical adsorption at low temperatures, is used for the determination of the specific area and pore distribution of solid materials.

The most extensively used method is based in the determination of nitrogen adsorption-desorption isotherms at the liquid nitrogen temperature (-196 °C). This method consists in representing the volume of adsorbed nitrogen per gram of the solid material, versus the equilibrium pressure, normally expressed as the relative pressure (P/P_0), where P_0 is the pressure of vapour saturation of nitrogen at -196 °C. The amount of adsorbed gas at the equilibrium pressure is given by the difference between the amount of gas introduced and the amount required to fill the space around the adsorbing solid, i.e. the dead volume at the equilibrium pressure. Before determining the adsorption isotherm, the samples are degassed to remove all physisorbed species from their surface.

One of the most common technique of measuring surface area, and widely used in most catalysis characterizations, is that developed by Brunauer, Emmett, and Teller (BET) in the late 1930’s [1]. The pore distribution information determines by the analysis of the shape of the isotherm (adsorption-desorption branches). The BET method consists in calculating the monolayer volume (V_m) of the adsorbed species. With this value, the specific BET surface area can be calculated using the equation:

$$S_{BET} = \left(\frac{V_m}{22414}\right) \cdot N_A \cdot \sigma \qquad (Equation\ 1)$$

where V_m is the monolayer volume; N_A is the Avogadro number ($6.022 \cdot 10^{23}$ atoms/mol), and σ is the cross-sectional area covered by one nitrogen molecule. According to IUPAC, the value of σ in the case of liquid nitrogen is 0.162 nm^2 [2]. The value of V_m is obtained by adjusting the adsorption experimental data to the BET isotherm:

$$\frac{P}{V(P_0 - P)} = \frac{1}{V_m C} + \frac{(C-1)P}{V_m C P_0} \qquad (Equation\ 2)$$

where P is the equilibrium pressure, P_0 is the normal vapour saturation pressure for liquid nitrogen at the experimental temperature (-196 °C), V is the volume of gas adsorbed at pressure P expressed in cm^3, V_m is the volume of gas required to give monolayer coverage of the surface expressed in same unit as V, P an equilibrium pressure and C is a constant related with the condensation heat and adsorption of the adsorbate; the higher the value of C, the stronger is the interaction adsorbate-adsorbing solid.

$$C = e^{(q1-qc)/RT} \qquad (Equation\ 3)$$

Where q_1 is the heat of adsorption on the first layer, q_c is the heat of condensation of adsorbed gas in all other layers, R is the gas constant and T is experimental temperature.

If only the section where the monolayer is formed is considered, representing the experimental data of $P/V_{ads}(P_0-P)$ versus P/P_0, should give a straight line according to the above BET equation; the slope is $(C-1)/V_mC$ and the intercept is $1/V_mC$. These values can be used to determine Vm and C.

The BET model is an extension of the Langmuir theory which considers multilayer adsorption. The application of this method is limited to a reduced range of pressures where the equation adjusts well to the experimental data. Practically, the linearity is maintained for $0.05 < P/P_0 < 0.3$ approximately, and it is in this interval that the BET model can be applied. Below this limit, the micropores are filled and adsorption on the more reactive sites is favoured, while above this limit capillary condensation takes place.

3.2.2. Structural analysis

3.2.2.1. X-ray diffraction (XRD)

The wavelength of X-ray is around the same magnitude as the interatomic distances of solids. X-ray diffraction is based on the reflection of the electromagnetic waves that are irradiated by the successive planes of the crystal atoms. When an X-ray beam reaches a crystal surface under any θ angel (Figure 1), a part of the radiation is reflected, while another part penetrates further. This situation repeats itself in the successive layers. The reflected waves on a crystal plane are in phase concordance, and only under certain conditions they are in phase concordance with waves diffracted by two successive planes. Therefore it is necessary that the difference between the routes of two diffracted waves is an integer number of wavelengths (nλ). In this way, for two waves that are reflected in a point P, the difference in the routes in the two first planes is $\delta = AB + BC$. From the summary of the system, $AB = BC$ and $\delta = 2 * AB$ and therefore $\delta = 2 \sin(\theta)$. The reflection condition elaborated by Bragg and Bragg indicates that the difference in the routes followed must be an integer number of the wavelength [3]. The wavelength is given by the following equation:

$$n\lambda = 2d\sin(\theta) \qquad (Equation\ 4)$$

where d is the distance between two consecutive planes.

According to this equation, different reflections orders are given by the value of n = 1, 2, 3 … this equation indicates that for any wavelength, there is a limit in the spacing which can give place to a diffraction spectrum. This limit is carried out according to the following equation:

$$d_{min} = \frac{2\lambda}{2(\sin(\theta))_{max}} = \frac{2\lambda}{2} \qquad (Equation\ 5)$$

The distance between the different planes of the crystal lattice determines the value of the Bragg angle, which is considered as a fingerprint of the crystalline solid. According to this way, the diffraction patterns provide unmistakable information about the crystalline structure. The angular position of the maximum points of the diffraction patterns are related with the parameters of the unit cell (repeated cell in the crystal), while their intensities reflect the symmetry of the lattice and the electronic density in the unit cell. Almost every crystalline substance has a unique powder X-ray diffraction pattern in terms of the location of the observed peaks and its intensities. If there is a mixture of different components, each phase produces its own diffraction pattern independently of the other phases; therefore this technique can be used to identify phases in such mixtures by comparison with patterns stored in the Joint Committee on Powder Diffraction Standards (JCPDS) databases.

A diffraction setup consists in an X-ray tube, a plane cell where the samples in powder form are positioned in the optical center of a goniometer and a detector (radiation counter) is situated on the edge of the angular system. The number of counts obtained per unit of time is proportional to the intensity of the radiation that reaches the detector. This intensity is represented graphically as a function of the angel (2θ) and thus, the diffraction pattern is represented.

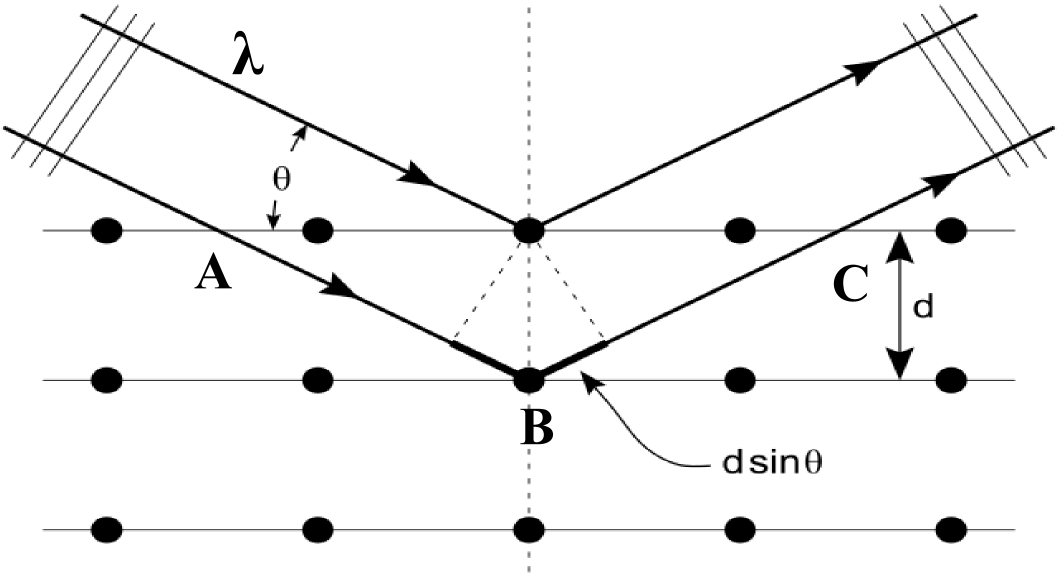

Figure 1. Derivation of Bragg's law.

3.2.2.2. X-ray Absorption Spectroscopy (XAS)

X-ray absorption Spectroscopy technique (XAS) is a technique commonly used for chemical and structural characterization of materials. This technique provides information about the valance states. The technique is based on the interaction of material with an electromagnetic radiation in the energy range of keV. As shown in Figure 2, when the light beam in the correct energy range strikes on atom, this is absorbed by exciting an electron in the process. For X-ray, the incident energy corresponds to excitation of electrons in the internal layers of the atom (core electrons). The energy is so high, and the electrons are ejected above the Fermi level, leaving ionized atom. This fact makes absorption can be called photoelectric absorption. Therefore, for this process to take place, the incident energy should be close to the binding energy of electrons in the atom, which are exciting. In the internal levels, these energies are very different for each type of atom, making the technique of *XAS* specifically for each element.

Experimentally the absorption coefficient, μ, is measured as a function of the incident photon energy, and the edge or leap absorption at the equal energy to the ligation of the excited electron level is observed (Figure 3).

Examining a range of specific energy can have specific information of a single element of the sample, being this technique especially sensitive to the oxidation state, chemical coordination, bond distances, coordination numbers and species of the selected adjacent atoms [4, 5].

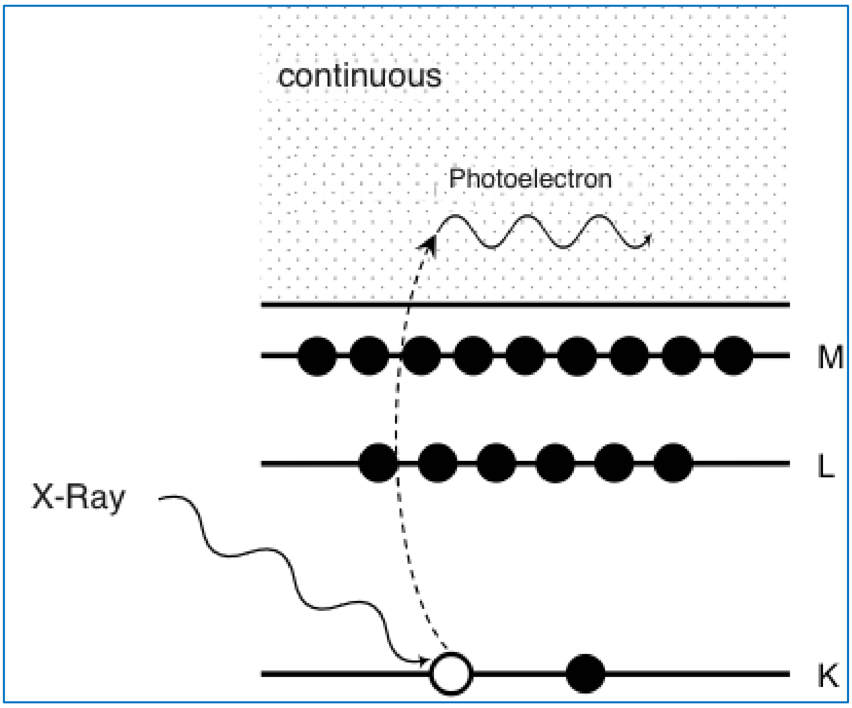

Figure 2. X-ray process absorption adapted from [15].

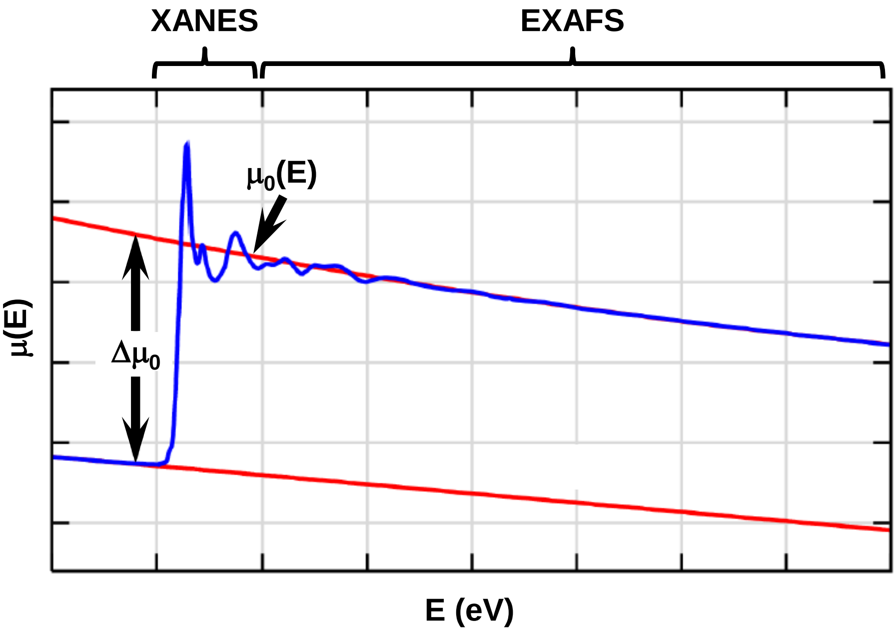

Figure 3. Regions in a spectrum of X-ray absorption. Adapted from [4].

The absorption coefficient μ (E) is determined from the intensity of X-rays transmitted through the sample, according to the equation:

$$I = I_0 \cdot e^{-\mu(E)t} \qquad (Equation\ 6)$$

where "I_0" is the intensity of incident X-ray, "t" is the thickness of the sample, "I" is the intensity transmitted through the sample and "μ" (E) is the absorption coefficient, as shown in Figure 4.

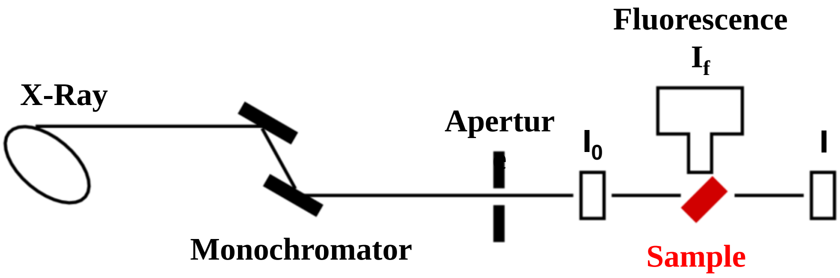

Figure 4. Measurement of X-ray absorption. Adapted from [4].

Within the absorption spectra of X rays are distinguished several zones, as shown in Figure 3. The previous absorption edge area is dominated by a decreasing function corresponding to the inelastic losses from lower ionization energy, while the post-absorption edge area is divided into two regions: (i), framework region near the edge X-ray absorption (XANES), and (ii), fine structure extended region of X-ray absorption (EXAFS)[4, 5].

The XANES region is the closest to absorption edge and extends up to 50-100 eV. This region is extremely sensitive to the formal oxidation state and coordination chemistry (e.g., octahedral, tetrahedral coordination) of the absorbing atom[4, 6].

An important and common application of XANES is to use the shift of the edge position to determine the valence state. Figure 5 shows the valence dependence of Fe metal and oxides of Fe^{2+} and Fe^{3+} (and a mixture of these two phases). With good model spectra, Fe^{3+}/Fe^{2+} ratios can be determined with very good precision and reliability. Similar ratios can be made for many other ions. The highest and positions of pre-edge peaks can also be reliably used to empirically determine oxidation states and coordination chemistry. These approaches of assigning formal valence state based on edge features and as a fingerprinting technique make XANES somewhat easier to crudely interpret than EXAFS, even if a complete physical understanding of all spectral features is not available.

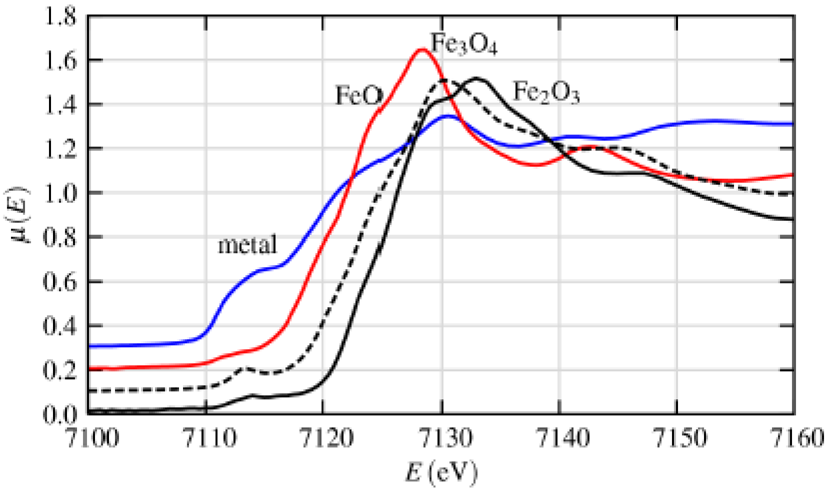

Figure 5. Fe K-edge XANES of Fe metal and several Fe oxides, showing a clear relationship between edge position and formal valence state. In addition, the shapes, positions, and intensities of pre-edge peaks can often be correlated to oxidation state.

For many systems, XANES analysis based on linear combinations of known spectra form “model compounds” is sufficient to tell ratios of valence states and/or phases. More sophisticated linear algebra techniques such as Principle Component Analysis and Factor Analysis can (and are) also be applied to XANES spectra.

3.2.2.3. Laser Raman spectroscopy (LRS)

Raman spectroscopy is a powerful technique for the determination of the internal structure of molecules and crystals. The physicist Raman discovered, in 1928, that the wavenumber of a small fraction of the dispersed radiation by certain molecules is different from the wavenumber of the incident light and the shift observed in the wavelength depends on the chemical structure of the molecules that cause the dispersion [7].

The Raman effect occurs when the sample is irradiated with a powerful laser source of visible or near infrared monochromatic radiation. When a sample is irradiated with photons, it is excited and it can relax in two ways: returning to its original energetic state or end up in a different energetic state. Usually it returns to its initial state liberating an amount of energy equal to the energy absorbed, constituting the elastic or Rayleigh scattering. But there are occasions in which the molecule does not return to its initial state, giving an inelastic scattering that characterizes the Raman scattering. In Rayleigh scattering, the emitted photon has the same wavelength as the incident photon. Due to the inelastic collision between the incident photon and the molecule, the rotational or vibrational energy of the molecule is changed by an amount of ΔE_m.

$$\Delta E_m = h\upsilon_i - h\upsilon_s \qquad (Equation\ 7)$$

where $h\upsilon_i$ is energy of the incident photon, and $h\upsilon_s$ is the energy of the scattered photon.

The Raman Stokes takes place when the energy of the scattered photons is less than the incident photons whilst the Raman anti-Stokes occurs when the energy of the scattering photons is more than the incident photons. The energy increase or decrease from the excitation is associated to the vibrational energy spacing in the ground electronic state of the molecule and as a result the wavenumber of the Stokes and anti-Stokes lines are a direct measure of the vibrational energies of the molecule. Usually, anti-Stokes lines are considerably less intense that the corresponding Stokes lines. Hence, only the Stokes part of a spectrum is commonly used.

Figure 6 shows a diagrammatic explanation of Rayleigh, Raman Stokes and Raman anti-Stokes scattering.

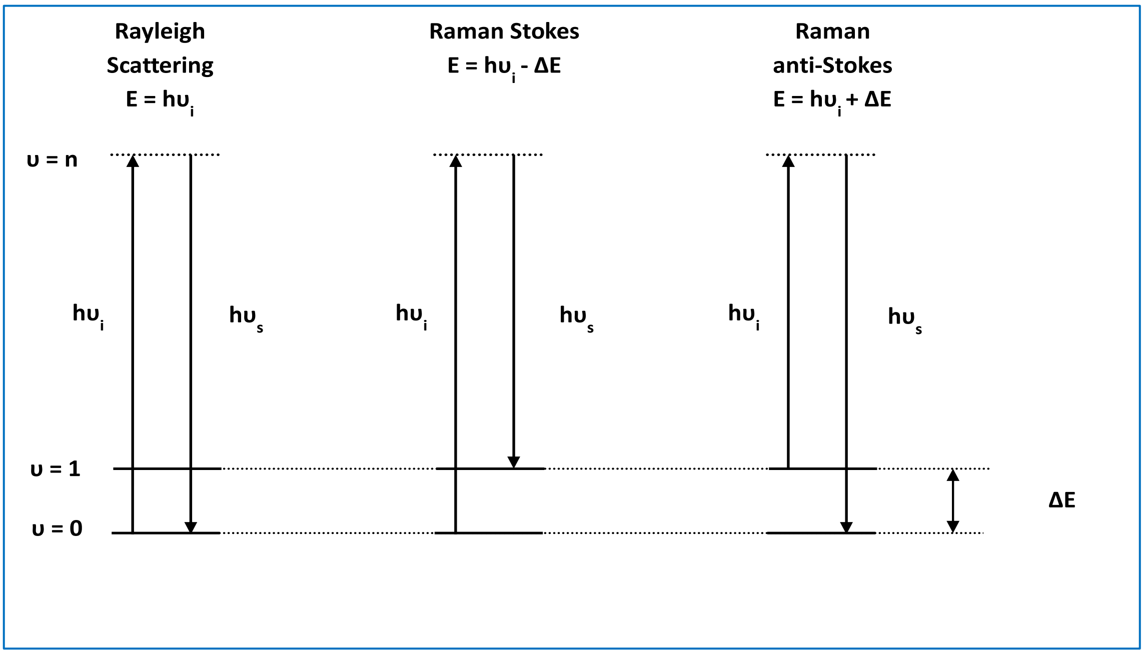

Figure 6. Origin Rayleigh and Raman scattering.

The difference between the Stokes and anti-Stokes bands with respect to the Rayleigh scattering corresponds to the difference between two energy levels in one direction or the other. These transitions between energy levels correspond to the transitions between vibrational states. To obtain a Raman spectrum, the sample is irradiated with a laser beam and the dispersed radiation is studied. In this way, Raman spectroscopy measures the vibrational frequencies as a shift between the energy of the incident and dispersed light. During the irradiation, the spectrum radiation at a certain angle (normally 90°) is registered. Due to the intensity of the Raman lines mostly is 0.001% of the intensity of the source, the Raman equipment usually has a device that removes the elastic scattering, allowing the use of very sensitive detectors.

However Raman spectroscopy measurements are the same type of transitions as infrared (IR) spectroscopy, it follows different selection rules which have certain advantages compared to IR: (i), the design of the cells is easier since quartz or glass may be used, allowing to carry out experiments in extreme temperature conditions; (ii), the presence of a microscope allows the use of minimum quantities of sample; (iii), it is possible to register spectra of the samples under hydrated and dehydrated conditions, since in this case water absorption is not a problem (unlike IR); (iv), Raman spectroscopy is very sensitive to microcrystallites (< 4 nm) and amorphous phase, and therefore is able to detect phases that other techniques cannot detect them such as X-ray diffraction (XRD). Also Raman spectroscopy is especially useful technique to study the structure of supported oxides samples because it can study the vibrations of the terminal M=O bonds, the M-O-M bonds between the supported metal oxides, and the metal-support bonds, M-O-support, under different temperature and atmospheric conditions [8].

3.2.3. Temperature programmed Analysis

Temperature programmed analysis (TPA) techniques are often used for the characterization of heterogeneous catalysts. The transient nature of the TPA techniques, in which the temperature and surface covering change over time, has the advantage to providing different information than that obtained in the stationary state.

Among the various modalities, in this Doctoral Thesis were used: (i), Reduction (Temperature Programmed Reduction, TPR), (ii), Desorption (Temperature Programmed Desorption, TPD), and (iii), Oxidation (Temperature Programmed Oxidation, TPO). The detection and analysis system are constituted by a thermal conductivity detector (TCD) and a mass spectrometer.

3.2.3.1. H_2-Temperature-programmed reduction (H_2-TPR)

Temperature programmed reduction (TPR) has been proved as a powerful technique to analyse the kinetic reduction process of metal oxide precursors. Since hydrogen consumption is proportional to the amount of reducible material, TPR is a valid technique to determine the amount of reducible species in a catalyst sample. This technique can be also used to study the effect of the support and promoters on the extent of reduction. Reduction of an oxide material can take place by dissolution of the reactant into the lattice or by elimination of lattice oxygen. The latter is common to all oxides, while the former occurs in very selected systems.

In the TPR technique a reducing gas mixture is flowed over an oxidized catalyst, while it is subjected to a programmed linear temperature ramp. Usually diluted hydrogen in an inert gas such as argon is used as a reducing agent gas. Room temperature is more often than not the initial temperature. The sample temperature is increased at a constant ramping rate and hydrogen is consumed from the gas mixture as the reduction takes place at certain temperatures. As function of the sample temperature increased, the rate of reduction process will be increased. The hydrogen consumed is measured by detecting the change in the thermal conductivity of the gas mixture by means of a thermal conductivity detector (TCD). The hydrogen consumption is recorded as a function of the reaction temperature. When the reduction is completed, there will be no more consumption of hydrogen, and the proportion of the gas mixture components will return to the initial composition which in turn leads to return the TCD signal to the baseline.

3.2.3.2. Temperature programmed desorption (TPD), oxidation (O_2-TPO) and reduction (H_2-TPR) followed by mass spectrometry

Temperature programmed analysis was used to characterize the carbon monoxide adsorption and carbonaceous deposits formed on the catalysts. For this, four consecutive thermal treatments are performed under different conditions: (inert (I), reducing (H_2/Ar), adsorption/desorption (CO/He) and oxidant (O_2/He), using as detection system a thermal conductivity detector (TCD) and a mass spectrometer for analyzing gaseous emissions generated.

The fundamental principle of mass spectrometry consists in the generation of ions from the test compound and then separated according to the mass/charge ratio (m/z), which allows detecting them qualitatively and quantitatively. A mass spectrometer consists of a sample introduction system, an ion source, a mass analyzer and ion detector. The purpose of the sample introduction system is to enable the entry of a representative quantity of the sample with the minimum possible loss of vacuum. In the ion source, ionization of the sample happens, which can be carried out by different methods: thermally, using electrical fields or by the impact of electrons, ions or photons. Once generated ions, these are separated according to their m/z ratio in the mass analyzer, usually using magnetic or electric fields. Finally, the separated ion analyzer are identified and recorded in the ion detector [9, 10].

3.2.4. Surface analysis

3.2.4.1. X-ray photoelectron spectroscopy (XPS)

The X-ray photoelectron spectroscopy is a technique of electron spectroscopy for chemical analysis that is used to determine the surface composition of the sample, the oxidation state of the atoms and their chemical environment in the sample. This technique is based on the photoelectric effect represented in figure 7. When a sample is irradiated with a beam of high energy X-rays (hυ), an emission of electrons, from the internal levels of the atoms of the samples, takes place. A hemispherical detector detects the electrons emitted and records their energy to obtain the X-ray photoelectron emission spectrum. The electrons that possess a binding energy lower than the energy of the exciting X-rays, are emitted with a certain kinetic energy that must fulfill the equation of the photoelectric effect:

$$E_C = h\upsilon - E_b - \Phi \qquad \text{(Equation 8)}$$

where E_C is the kinetic energy of the emitted electron, $h\upsilon$ is the exciting energy, E_b is the binding energy of the excited electron, and Φ is the work function of the spectrometer.

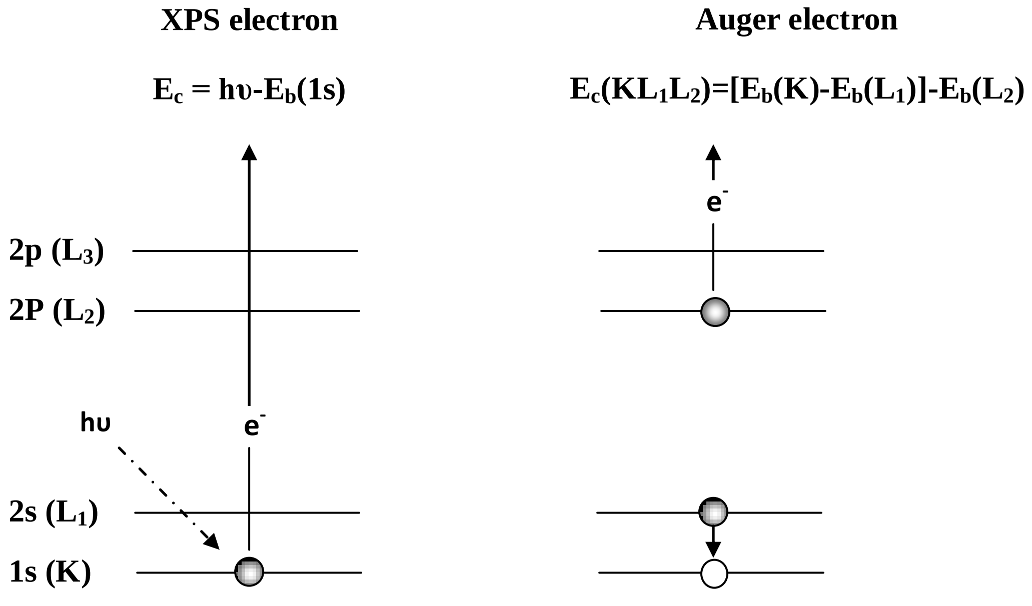

Figure 7. Photoelectric effect and Auger processes.

In an XPS spectrum, the intensity of the flow of emitted electrons by the sample is represented as a function of their kinetic energy or more frequently as a function of their binding energy. The kinetic energy of the emitted electrons is related to their binding energy (BE), which is characteristic of the elements present in the sample and the electronic interactions between them [11].

X-ray photoelectron spectroscopy (XPS) employs photons within the 100-10000 eV energy range, belonging to the X-ray region of the electromagnetic spectrum. At these high energy values, the photons pull out the electrons of the deep levels of the atoms.

Although an X-ray photon can penetrate and excite the photoelectrons that are at various hundred nanometers from the surface, only the photoelectrons that proceed from the most external layers actually have the opportunity to escape from the material and eventually reach the detector and be measured. The majority of XPS determinations of solid samples generate useful information only to a depth of about 2 nm from the surface of the catalytic systems.

The usefulness of the XPS technique is a result of the chemical shifts observed for the different binding energies of the electrons of the internal levels of the atoms. The binding energies of the internal electrons are affected by the valence electrons and, consequently, by the chemical surrounding of the atoms. When the atomic distribution that surrounds an excited atom is changes, the local charge of the environment also changes in this atomic site. At the same time, this change is reflected as a variation in the binding energy of all electrons of that particular atom. In this way, not only the valence electrons, but also the binding energies of the internal electrons undergo a characteristic shift. These shifts are inherent to the chemical species implicated and constitute the base of the chemical-analytical application of the XPS technique. In a simplified manner, the shifts observed in the photoelectronic lines of the XPS spectra reflect the rise in the values of the binding energies when the oxidation state becomes more positive. From a quantitative point of view, the intensity of the photoelectronic lines is proportional not only to the efficient photoelectronic section of a particular element, but also to the number of atoms of that element that are present in the sample.

The conventional XPS equipment possesses a monochromatic X-ray source. The most commonly sources are Mg ($h\upsilon$ = 1253.6 eV) and Al ($h\upsilon$ = 1486.6 eV).

A system of electrostatic lenses guides the electrons that proceed from the sample towards the energy analyzer. In this analyzer, the electrons are directed by a potential difference applied on deviation electrostatic plates. For every potential difference applied, the electrons with a determined kinetic energy go through the exit gap of the analyzer and reach the detector. Practically, the potential difference is varied so as to cover the kinetic energy of all electrons. That's required to have high vacuum conditions in all the system to avoid the attenuation of the electron beam as a consequence of inelastic collisions; thus, the apparatus disposes of a system of pumps in series (rotatory, turbomolecular and ionic).

3.2.5. Morphological analysis

3.2.5.1. Transmission electron microscopy (TEM)

Transmission electron microscopy is a technique commonly used for chemical and structural characterization of materials. This technique provides information about morphology, particle size distribution, chemical composition, degree of crystallinity and identification of crystal phases [12]. The technique is based on the interaction of the material with an electron beam accelerated under a differential electric potential of several hundred kilovolts, which is collimated, focused and guided by several electromagnetic lenses. The electron emission source may be thermionic (W or LaB_6 filament) or field emission (FEG) and the electrons generated are accelerated when are passed through a large potential difference. Before reaching the sample, the electron beam is modified by the condenser lenses to improve coherence. When this beam interacts with a sample of low thickness (0.1-0.5 microns) leads to: (i), elastic processes, in which the incident electrons are dispersed without energy losses; and (ii), inelastic, where the incident electrons give up some of his energy to the internal electrons of the material. The objective lens, which are located below and around the sample, concentered the scattered beams and forming the first intermediate image. The fact that it electrons are fully charged allows that dispersed electrons can be focused to form an image. The first intermediate picture is then increased by a set of project lenses to reach become visible in a fluorescent screen, and then collect these electrons on photographic film or by digital CCD camera.

3.3. Measurements of catalytic activity

3.3.1. Description of the reaction equipment

The catalytic activity measurements were conducted in a fixed bed reactor. This equipment has a gas supplier system and an analysis of products system by means of gas chromatography. The catalysts were tested in the CO hydrogenation reaction using a fixed-bed microreactor. The fixed bed reactor is a tube of stainless steel (165 mm long, 8.5 mm internal diameter and 10.5 mm outer diameter). The sketch diagram is displayed in Figure 8. The gas flow rates were controlled using Bronkhorst High-Tech Series mass flow controllers. The equipment has three mass flow controllers (MFC), one for inert gas (N_2), the second for H_2 and the third for reactant gases (synthesis gas mixture ($CO/H_2/N_2$)). The reactor was held within a furnace equipped with a temperature controller. The reaction temperature was measured with a K-type thermocouple inserted directly in the catalytic bed. The gas mixing zone, the reactor furnace and the high pressure post reaction zone are contained within a box heated at 110 °C. The pressure is regulated by a valve (pressure controller (PC)) located at the exit of the reactor. From the reactor outlet until the inlet of the analytical system, all lines are heated at 130 °C to prevent condensation of the products. Furthermore, the reaction system was equipped with a stainless steel hot trap in the reactor exit set at 110 °C in order to collect the heavier products (C_m hydrocarbons).

Analysis of reactant gases and products was performed on-line with a gas chromatograph (HP 6890 Plus). The gas chromatograph was connected on line to the reactor and the injection of sample was performed automatically by means of a six-way valve. The chromatograph equipped with two columns in parallel, the first one is a Porapak Q (1/8" × 3 m)-packed column connected to a thermal conductivity detector (TCD) was used to analyze the inorganic gases (H_2, N_2, CO, and CO_2) and water. While the second column is a DB-1 capillary column (60 m × 0.25 mm × 0.25 μm) connected to a flame ionization detector (FID) for the analysis of hydrocarbons and various oxygenated compounds. The equipment configuration allowed the analysis of C_1 -C_{16} hydrocarbons, C_1 - C_{10} alcohols and other oxygenated compounds. The carbon balance was always higher than 95%, indicating that the yield to hydrocarbons larger than C_{16+} is small (< 5%). Different catalytic tests were carried out on the same sample to check the results reproducibility. The experimental error was always lower than 1% (absolute values). The chromatograph has a cryogenic system supplied with liquid N_2 which allows to lowering the oven temperature of the column up to -50 °C. The sample injection is carried out simultaneously in both columns. The following temperature program was used: -50 °C for 10 min, then a ramping of 10 °C. min^{-1} up to 230 °C, and then keep at this temperature for 20 min. Nitrogen was used as internal standard for chromatographic analyses.

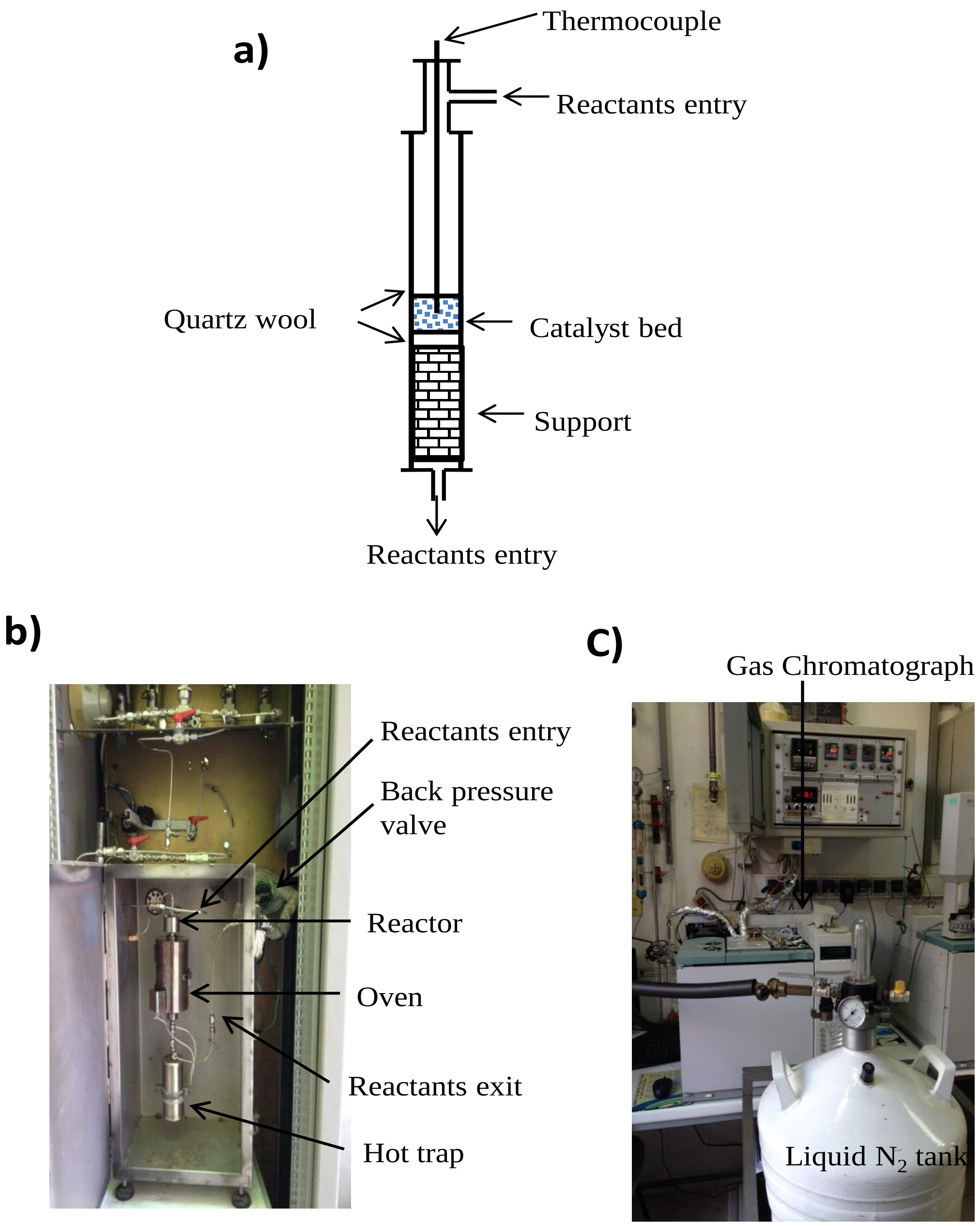

Figure 8. a) Scheme of the fixed bed reactor, b) inside the hot box, c) products analysis system.

3.3.2. Experimental methodology

3.3.2.1. Method of activity measurement in the fixed bed reactor

The catalyst bed was prepared by dilution of the catalysts (particle size between 0.25-0.30 mm) with an inert material (particle size between 0.25-0.30 mm) with the aim of preventing the presence of hot spots in the interior, as well as to reduce the axial dispersion to increase the length of the bed.

Subsequently, the mixture of catalyst and diluents was placed between two pieces of quartz wool in the reactor. Subsequently, the catalysts were activated under suitable conditions at atmospheric pressure. The reactor was then cooled to the reaction temperature and pressurized at 20 bar. CO hydrogenation was then followed and catalysts performance was tested under steady-state conditions.

3.3.2.2. Data analysis

The results obtained from the integration of the areas of the recorded peaks in the chromatogram are introduced in an Excel worksheet that was designed with the aim to obtain the kinetic parameters (conversion and selectivity) in a quick and easy way. These calculations were carried out according to the following expressions:

1) CO conversion

$$X_{CO_i} = \frac{\left(\frac{CO}{N_2}\right)_0 - \left(\frac{CO}{N_2}\right)_i}{\left(\frac{CO}{N_2}\right)_0} \cdot 100 \qquad (Equation\ 9)$$

where the X_{COi} is the conversion (%) of CO measured in the analysis experiment i, $\left(\frac{CO}{N_2}\right)_0$ is the relationship of CO/N_2 areas in the feed and $\left(\frac{CO}{N_2}\right)_i$ is the relationship of CO/N_2 in the analysis experiment i.

2) The selectivity toward a product *i* (S_i) is calculated based on the number of carbon atoms of that product.

$$S_i = \frac{n_i M_i}{\sum_{i=1} n_i M_i} \cdot 100 \qquad (Equation\ 10)$$

where n_i is the number of carbon atoms in the product i and M_i is the number of moles of this same product. For the selectivity toward deferent hydrocarbons, this is expressed based on the carbon atoms not counting the CO_2 produced (free CO_2).

3) **The calculation of carbon balance (% C)** for a test *i* was performed according to the formula:

$$\%C_i = \frac{\sum_{i=1} n_i M_i + n_{CO_i}}{n_{CO_a}} \cdot 100 \qquad (Equation\ 11)$$

Where n_i is the number of carbon atoms in the product i, M_i is the number of moles obtained of the same product, n_{COa} is the moles of CO fed to the reactor and n_{COi} establishes the moles of unreacted CO and is given by the below equation:

$$n_{CO_i} = \left(\frac{(A_{CO})_i}{fr_{CO}}\right) \qquad (Equation\ 12)$$

where $(A_{CO})_i$ is the area of the chromatographic peak of the CO reactant in the TCD signal in a test i, and fr_{CO} is the response factor of the CO reactant in the TCD detector that establishes the relationship between area and moles of CO that were fed and given by below equation:

$$n_{CO_a} = \left(\frac{\left(A_{N_2}\right)_i \cdot \left(\frac{CO}{N_2}\right)_0}{fr_{CO}}\right) \qquad (Equation\ 13)$$

where $(A_{N2})_i$ is the area of the chromatographic peak of N_2 in the TCD detector in a test i.

3.4. References

[1] S. Brunauer, P. H. Emmett,E. Teller, J. Am. Chem. Soc. 60 (1938) 309-319.

[2] K. S. W. Sing, D. H. Everett, R. A. W. Haul, L. Moscou, R. A. Pierotti, J. Rouquerol,T. Siemieniewska, Pure Appl. Chem. 57 (1985) 603-619.

[3] R. Jenkins,R. L. Snyder, Diffraction Theory. (1996).47-95.

[4] M. Newville, Fundamentals of XAFS, Consortium for Advanced Radiation Sources, University of Chicago, Chicago (2004).

[5] M. Faraldos, C. Goberna, Eds., Técnicas de Análisis y Caracterización de Materiales, CSIC, Madrid (2011).

[6] V.L. Aksenov, A.Y. Kuzmin, J. Purans, S.I. Tyutyunnikov, EXAFS spectroscopy at synchrotron-radiation beams, Phys. Part. Nucl. 32 (2001) 675-707.

[7] J. R. Ferraro, K. Nakamoto, Introductory Raman Spectroscopy, Academia Press: 1994.

[8] M. A. Bañares, I. E. Wachs, J. Raman Spectrosc. 33 (2002) 359-380.

[9] D. A. Skoog, F. J. Holler, T. A. Nieman, Principles of Instrumental Analysis, T homson Brooks/Cole, Belmont (2007).

[10] J. H. Gross, Mass Spectrometry: A Textbook, Springer, Co., Berlin (2004).

[11] C. D. Wagner, L. E. Davis, M. V. Zeller, J. A. Taylor, R. H. Raymond, L. H. Gale, Surf. Interface Anal. 3 (1981) 211-225.

[12] D. B. Williams, C. B. Carter., Transmission Electron Microscopy. Part 1: Basics, Springer, Co., New York and London (2009).

Chapter 4: Syngas Conversion to Hydrocarbons on Zirconia-Supported Iron Catalysts

4

Syngas Conversion to Hydrocarbons on Zirconia-Supported Iron Catalysts

M. Al-Dossary*, M. Ojeda, J.L.G. Fierro
Institute of Catalysis and Petrochemistry, CSIC, Marie Curie 2, Cantoblanco, 28049 Madrid, Spain
E-mail address: ma99sa@hotmail.com

Abstract

The hydrogenation of CO to hydrocarbons is investigated over zirconia iron-based catalysts prepared by co-precipitation. These catalysts, in which the Fe-content varied between 0 and 100%, were tested in the CO hydrogenation reaction under fixed reaction conditions (H_2/ CO = 2, T = 250 ºC, P = 20 bar, GHSV = 0.0083 L/g.s.). The resulting activity data indicated that CO conversion is strongly dependent on the iron contents of the catalysts. The lowest CO conversion (< 5%) was obtained using Zr-rich catalysts (15Fe and 5Fe), and the highest CO conversion was obtained using Zr-free (100Fe) catalysts. For this catalyst, the CO conversion level reaches 38.5%, with selectivities for the C_2-C_4 and C_{5+} hydrocarbons of 49.7 and 27.7%, respectively. However, the activity profile of this catalyst slightly decreases with the time on-stream, indicating that it is progressively deactivated. If the activity is normalized to the iron content, the 95Fe and 85Fe catalysts display slightly better performances and are relatively stable for on stream periods of at least 48 h.

Keywords: iron catalysts, zirconia, hydrocarbons synthesis, CO hydrogenation

4.1. Introduction

Fischer Tropsch synthesis (FTS) evolves the conversion of syngas (H_2 and CO) derived from carbon sources, such as coal, peat, biomass, and natural gas, into a product spectrum consisting of complex multi component mixtures of linear and branched hydrocarbons and oxygenated products [1]. The production of liquid fuels and chemicals from syngas has received significantly increasing interest due to limited petroleum reserves [2, 3]. In recent years, Fischer Tropsch synthesis (FTS) has been an important topic. Currently, FTS is attracting more interest as an important technology for producing clean transportation fuels and chemicals, especially for the selective production of petrochemical feed-stocks, such as ethylene, propylene and butylene (C_2-C_4 olefins), directly from synthesis gas. The products derived from Fischer Tropsch Synthesis are endowed with tremendous environmental value due to their lack of harmful contaminants, such as sulphur, nitrogen and aromatic compounds [4].

One approach for improving the selectivity in this process for the conversion of synthesis gas to hydrocarbons involves the use of a bimetallic catalyst system that contains metal catalysts combined with a support [5]. Iron and cobalt catalysts have been commercially used in Fischer Tropsch Synthesis in the last 90 years [6-12]. Compared with Co-based catalysts, iron-based catalysts have greater potential for converting synthesis gas to fuels via FTS due to their low cost, adjustable selectivity (Fe-based catalysts lead to more olefinic products and lower CH_4 selectivity than Co-based catalysts), and reasonable water-gas shift (WGS) activity. Thus, iron-based catalysts allow for more flexible operations in industrial processes and are suitable for low H_2/CO ratio syngas derived from biomass or coal gasification [13-16]. However, pure iron catalysts are not suitable for large-scale commercial application. Therefore, commercial FTS Fe catalysts, which are mainly composed of Fe oxides, are often used with transition metal oxides, alkali salts and structural promoters to improve their physico-chemical performance [17]. The development of Fe catalysts with high FTS activity, low methane selectivity, and long term stability is very important. The addition of some transition metals to Fe-based catalysts improves their activity and selectivity. Commercial grade Fe-based catalysts for FTS generally consist of bulk Fe oxides with Cu (Cu facilitates the reduction of α-Fe_2O_3 to Fe_3O_4 or metallic Fe), potassium (mainly added to enhance the dissociative adsorption of CO, which could improve the carburization and suppress the methane formation of the catalyst) and SiO_2 (as a structure promoter, to improve the stability of the catalyst) [18, 19].

Several research groups have suggested that Fe carbides rather than metallic Fe play a critical role in the activity of Fe-based catalysts for FTS [20-22]. If this suggestion is true, then the active sites of the Fe-based FTS catalysts should exist in a carburized state on the surface. Therefore, the ability of the Fe catalyst to maintain a carburized surface may be important for increasing and maintaining its long-term activity. The addition of another transition metal to bulk Fe catalysts could improve the catalyst activity if it helps maintain or promotes the formation of more active carbide species.

However, the effects of added Zr on Fe FTS catalysts have only been studied modestly [23, 24], and most of these studies have focused on catalyst systems in which Zr was used as a support (ZrO_2) [25]. However, numerous studies have been performed to improve the performance of Co catalysts, in which the Co-structure is modified via the incorporation of ZrO_2 [26-30]. Ali *et al.* [26] studied the influence of ZrO_2 on the performance of FTS over sequentially impregnated Co-Zr-Si-oxide catalysts and concluded that the activity and selectivity were both improved because the active interface between Zr and Co facilitates CO dissociation. Jongsomjit *et al.* [28] investigated Co dispersed on a mixed SiO_2-ZrO_2 support and found that the number of active Co metal atoms increased due to the weakened Co-support interaction. Additionally, Moradi *et al*. [29] studied the effect of Zr loading (0-10 wt%) on the Co/SiO_2 catalysis for the FTS reaction. Their results indicated that the FTS activity and selectivity toward the higher hydrocarbons of the Co-Zr-promoted catalysts increased with increased ZrO_2 content. Also their results showed that with increasing zirconia, Co-SiO_2 interaction was decreased and replaced by Co-zirconia interaction which in turn led to increase extent of reduction degree of cobalt and increase the metallic atoms on the surface.

The impacts of adding various transition metals, such as Cr, Mn and Zr, on the catalytic properties of precipitated bulk Fe-based catalysts in FTS were investigated by Lohitharn *et al.* [24]. These authors found that the addition of a third transition metal (Cr, Mn, and Zr) to FeCu-based catalysts enhanced the Fe dispersion on the catalyst's surface, increasing the FTS activity by varying degrees. In addition, these authors used BET to determine the surface area of the FeCu-based catalysts and observed that the surface area increased when Zr was incorporated in the catalyst structure.

In line with the above study, this work was undertaken to develop highly active and stable Fe/ZrO_2 catalysts capable of converting syngas ($CO+H_2$) mixtures into hydrocarbons. A series of Fe-Zr-oxide catalysts in which the Fe/Zr atom ratio was varied over a large range were designed and prepared using a co-precipitation method. To evaluate the catalyst structures and establish some type of correlation between the catalyst structure and performance, various characterization techniques were employed, including N_2 adsorption-desorption, powder X-ray diffraction (XRD), H_2 temperature-programmed reduction (H_2-TPR) and X-ray photoelectron spectroscopy (XPS). The FTS performance of catalysts was tested under conditions that were similar to industrial conditions using a fixed-bed catalytic reactor.

4.2. Experimental

4.2.1. Catalyst preparation

For comparison, the catalysts used in this study were prepared using the co-precipitation method for rich iron and rich zirconium catalysts. To prepare catalyst precursors using the co-precipitation method, appropriate amounts of iron(III) nitrate nonahydrate (Aldrich, >= 98%) and zirconium(IV) oxynitrate hydrate (Aldrich, 99.99%) with the different Fe/Zr ratios (see Table 1) were dissolved in deionized water and mixed thoroughly at room temperature. Then, a 10 wt% of ammonia solution was added dropwise to the above mixture under continuous stirring until the solution pH reached a 8.0-8.5. The as-prepared precipitates were then filtered out and washed several time with deionized water. The precipitates were dried overnight in ambient air at 120 °C. Finally, aliquots of each dried precipitate were calcined in ambient air at 450 °C for 6 h [31]. The nominal compositions of the Fe-Zr-O catalysts, which were prepared as described, and simplified codes are included in Table 1.

Table 1. Nominal composition, preparation method and Fe/ZrO_2 catalyst codes

Catalyst composition	**Fe/(Fe+Zr) atomic ratio**	**Code**	**Method**
100 % Fe	100	100Fe	co-precipitation
95 % Fe + 5 % Zr	95	95Fe	co-precipitation
85 % Fe + 15 % Zr	85	85Fe	co-precipitation
50 % Fe + 50 % Zr	50	50Fe	co-precipitation
15 % Fe + 85 % Zr	15	15Fe	co-precipitation
5 % Fe + 95 % Zr	5	5Fe	co-precipitation
100 % Zr	0	0Fe	co-precipitation

4.2.2. Characterization techniques

4.2.2.1. Nitrogen adsorption-desorption isotherms

Nitrogen adsorption isotherms were recorded at the temperature of liquid nitrogen (-196 °C) using a Micromeritics ASAP 2000 apparatus. The samples were degassed at 140 °C for 16 h before determining the adsorption isotherm. The specific areas were calculated using BET, and the adsorption data were recorded over a relative pressure range of 0.05 to 0.25 and by using a value of 0.162 nm^2 for the cross section of adsorbed N_2 molecules at -196 ºC. The pore size distributions were determined from the desorption branch of the isotherms by using the Barrett–Joiner–Halenda (BJH) method.

4.2.2.2. Powder X-ray diffraction (XRD)

Powder X-ray diffraction (XRD) patterns of the precursor and calcined samples were recorded using a Seifert 3000 XRD diffractometer equipped with a PW goniometer with Bragg-Brentano θ/2θ geometry, an automatic slit, a bent graphite monochromator and nickel-filtered Cu Kα1 (λ = 0.15406 nm) radiation. A scanning step of 0.02° was used between Bragg' angles of 5 and 90° in scan mode (0.05°, 2 s).

4.2.2.3. H_2-Temperature-programmed reduction (TPR)

Temperature-programmed reduction (TPR) experiments were carried out using a Micrometrics 3000 apparatus. Approximately 30 mg of sample was pretreated under dried air at 110 °C for 1 h. The TPR profiles were recorded by heating the sample from room temperature to 900 °C at a rate of 10 °C/min under a 10 vol. % H_2/Ar flow. The H_2 consumption was monitored using a thermal conductivity detector (TCD). To avoid water condensation from the exit stream, the effluent gas was passed through a cold trap placed before the TCD.

4.2.2.4. X-ray Photoelectron spectroscopy (XPS)

X-ray photoelectron spectra (XPS) were acquired with a VG Escalab 200R spectrometer in the pulse-count mode at a pass energy of 50 eV using an Mg Kα (hv = 1253.6) X-ray source. The kinetic energies of the photoelectrons were measured using a hemispherical electron analyzer operating in the constant pass energy mode. The background pressure in the analysis chamber was maintained at less than 8×10^{-9} mbar during data acquisition. The powder samples were pressed into small stainless steel holders and mounted on a support rod that was placed in the pretreatment chamber. The XPS data were signal averaged for a number of scans and were taken in increments of 0.1 eV with dwell times of 50 ms. The binding energies were calibrated relative to the C 1s peak from the carbon contamination of the samples at 284.8 eV to correct the contact potential differences between the sample and the spectrometer. High-resolution spectral envelopes were obtained by curve fitting synthetic peak components using the "*XPS peak*" software. The raw data were used with no preliminary smoothing. Symmetric Gaussian–Lorentzian product functions were used to approximate the line shapes of the fitting components [32, 33].

4.2.3. Catalytic Performance

The catalysts were tested in the CO hydrogenation reaction using a fixed-bed microreactor (stainless steel, 165 mm long and 8.5 mm ID). The reaction temperature was measured with a K-type thermocouple buried in the catalytic bed. The reactor was held within a furnace equipped with a temperature controller. All pipes after the reactor outlet were kept at 130 °C. The reaction system was equipped with a stainless steel hot trap set at 110 °C to collect heavier products (C_m hydrocarbons). The flow rates were controlled using Bronkhorst High-Tech Series mass flow controllers. The calcined samples (100 mg, 0.25–0.30 mm particle size) were diluted with SiC (ca. 1.5 g, 0.25–0.30 mm particle size) to avoid hot spots. First, the catalysts were activated *in situ* at 450 °C (heating rate of 5 °C/min) for 1 h in syngas (31%CO/62%H_2/7%N_2, GHSV = 0.0083 L/g.s) at atmospheric pressure. Then, the reactor was cooled under the synthesis gas atmosphere to the reaction temperature (250 °C) and pressurized at 20 bar. Next, CO hydrogenation was conducted and the performances of the catalysts were tested under steady-state conditions. The reactant gases and products were analyzed on-line using a gas chromatograph (HP 6890 Plus). A Porapak Q (1/8" * 3 m)-packed column connected to a thermal conductivity detector (TCD) was used to analyze the inorganic gases (H_2, N_2, CO, and CO_2) and water. The hydrocarbons and oxygenated compounds were analyzed using a DB-1 capillary column (60 m *0.25 mm*0.25 µm) connected to a flame ionization detector (FID). The equipment configuration allowed for analysis of the C_1-C_{16} hydrocarbons, C_1- C_{10} alcohols and other oxygenated compounds. The carbon balance was always greater than 95%, indicating that the hydrocarbons yield was large and the C_{16+} yield was small (< 5%). Different catalytic tests were carried out on the same sample to determine the reproducibility of the results. The experimental error was always less than 1% (absolute values). The following temperature program was used: -50 °C for 10 min then ramping to 230 °C at 10 °C/min and maintaining this temperature for 20 min. Nitrogen was used as an internal standard for chromatographic analyses.

4.3. Results and Discussion

4.3.1. Textural Analysis

The nitrogen adsorption-desorption isotherms of all of the samples, including the dried precipitates, and after calcination at 450 °C are shown in Figures 1A and 1B, respectively. All samples displayed type IV isotherms, that were characteristic of mesoporous materials, in accordance with the IUPAC classification system [34]. The specific surface area values of the calcined samples are presented in Table 2. The BET surface area values for the iron zirconium catalysts vary between 70 and 180 m^2/g. Adding zirconium oxide to the catalysts affects their BET area and pore diameter. When considering the *x*Fe series calcined at 450 °C, the adding of small amount of zirconium (5%) leads to increase the BET surface area from 22.2 to 70 m^2/g for 100Fe and 95Fe, respectively. The BET values increased with increasing Zr content in the samples from 70 up to 180 m^2/g for 95Fe and 50Fe, respectively and then progressively decreased with increasing Zr-loading. In contrast, the pore size was higher for the 95Fe sample and decreased with decreasing Fe-loading (15Fe). Finally, a slight increasing tendency was observed, but not when the values of the highest Fe-loaded sample are reached (95Fe).

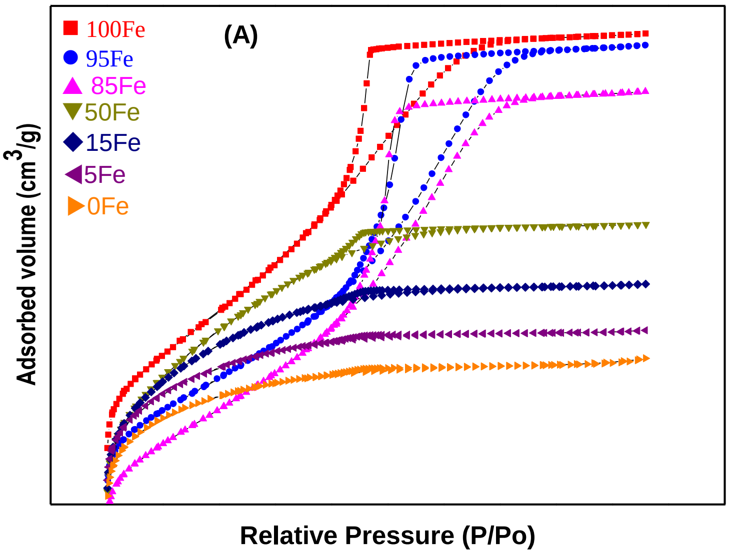

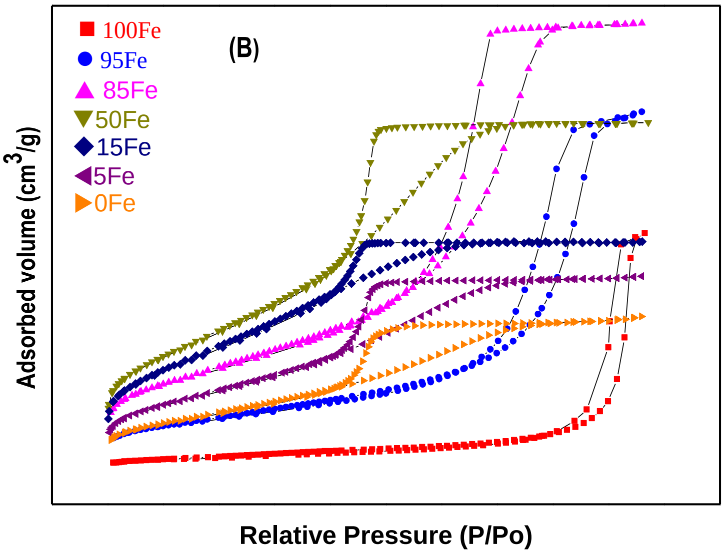

Figure 1. Nitrogen adsorption-desorption isotherms of the dried *x*Fe precursors (A) and the samples calcined at 450 °C (B).

Table 2. Specific BET areas and pore diameters of the catalysts

Catalysts	T_{calc} (ºC)	BET (m^2/g)	Pore diameter (nm)
100Fe	450	22.2	22.9
95Fe	450	70	10.9
85Fe	450	133	7.2
50Fe	450	180	4.1
15Fe	450	161	3
5Fe	450	105	4
0Fe	450	77	4.3

4.3.2. Crystalline structures

The crystalline structure of the *x*Fe (*x* = 100, 95, 85, 50, 15, 5, 0) samples was revealed by X-ray diffraction. The XRD patterns of the non-calcined samples (95Fe-85Fe-50Fe-15Fe-5Fe) (data not shown) displayed broad peaks indicative of amorphous solids resembling ferrihydrite [35]. Upon calcination of the *x*Fe precursors at higher temperatures, diffraction peaks appeared that reflected the appearance of crystalline phases. Figure 2 shows the XRD patterns of the calcined samples at 450 °C. The 95Fe, 85Fe and 50Fe precursors exhibited relatively narrow diffraction peaks that were indicative of crystalline solids. In all cases, the reflections ascribed to the hematite α-Fe_2O_3 structure (JCPDS 84-307) were the only reflections observed for iron. The XRD diffraction peaks of hematite α-Fe_2O_3 had a high intensity for the Fe-rich sample (95Fe) and became broader as the iron content in the sample decreased. Of particular interest is the fact that the two Zr-rich samples (15Fe and 5Fe) did not show any iron oxide diffraction lines. This observation indicates that the iron oxides particles are amorphous or are smaller than the detection limit of this technique (i.e., below 4 nm) [36].

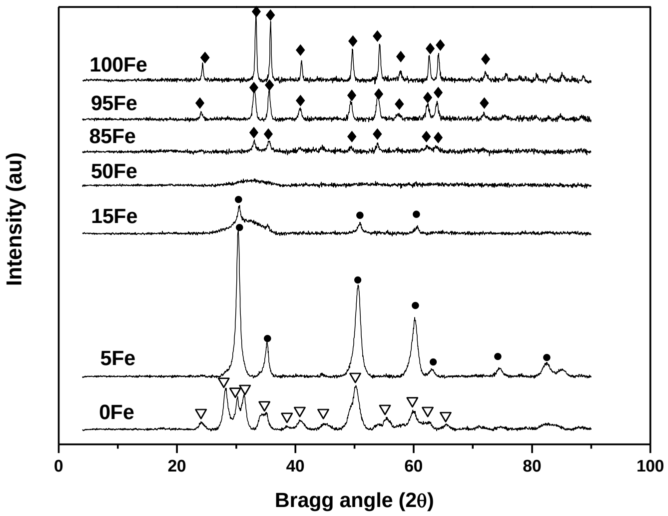

Figure 2. XRD of the Fe/Zr samples with different Zr contents calcined at 450 °C: diamond (♦): α-Fe_2O_3; circles (●): cubic-ZrO_2; triangle (▽): orthorhombic-ZrO_2.

A similar trend was observed for the diffraction peaks of ZrO_2, but contrasting results were observed regarding appearance of the hematite α-Fe_2O_3 diffraction peaks. The ZrO_2 diffraction peaks were very intense when a high zirconium loading (5Fe) was used, indicating that the zirconium oxides are crystalline. The intensities of these peaks decreased as the zirconium content in the samples decreased and disappear completely in the Fe-rich samples (95Fe, 85Fe and 50Fe). The catalyst containing similar amounts of iron and zirconium (50Fe) is amorphous. Although the diffraction peaks of the pure zirconium (0Fe) showed an orthorhombic crystallite structure, a cubic-ZrO_2 crystallite was found for the Fe-containing catalysts. This finding indicated that the addition of a small amount of iron is enough to change the crystalline structure of the ZrO_2 from orthorhombic to cubic.

The effects of ZrO_2 on the dispersion of iron oxides are important because they allow us to follow the direct influence of particle size on catalyst performance. Table 3 shows the effects of adding zirconium on the Fe particle size. The main particle size of each sample was calculated by applying the Scherrer equation. The particle size of the pure calcined Fe was approximately 27 nm and decreased following the addition of zirconium to 14 and 9.4 nm in the 95Fe and 85Fe samples, respectively. Thus, the catalytic performance of the Fe-rich catalysts will be compared with the performance obtained by Zr-rich systems, in which the particle size of the Fe_2O_3 particles deposited on the ZrO_2 phase is less than 4 nm. The incorporation of ZrO_2 as a promoter or as support for the Fe-phase plays an important role in the texture and architecture of the iron phase of this type of catalysts [37].

Table 3. Fe particle size of the H_2-reduced Fe/ZrO_2 catalysts

Catalyst	**Fe Particle size (nm)**	
	Calcined catalyst at 450 °C	Reduced catalyst after TPR experiment
100Fe	27.1	84.6
95Fe	14.0	69.9
85Fe	9.4	52.9
50Fe	-	27.7
15Fe	-	8.5
5Fe	-	8.8

The XRD diffraction patterns of the reduced samples under flowing hydrogen at 900 °C (the sample was collected following the TPR experiments) are displayed in Figure 3. Three main diffraction peaks are observed for the Fe-rich samples (95Fe, 85Fe and 50Fe) with angles of 44.7, 65.1 and 82.4 2θ ascribed to the metallic species (Fe^0). Moreover, these diffraction lines became weaker as the zirconium content in the samples increased and completely disappeared in the Zr-rich catalysts (5Fe), most likely because the metallic Fe particles were covered by ZrO_2 oxides or were deposited on ZrO_2 particles because it was observed for the calcined samples. In addition, the incorporation of zirconium in the catalyst had some effect on the iron particle size. The iron particle size decreased as the zirconium content increased from 84.6 nm to 8.8 nm in the pure iron oxide and rich zirconium samples (5Fe), respectively. The particle sizes of the iron oxides in all of the samples are summarized in Table 3. In the 85Fe catalysts, the peaks of metallic iron (Fe^0) are broad and intense, indicating that the Fe-particles are small and a large proportion of them have developed on its precursor.

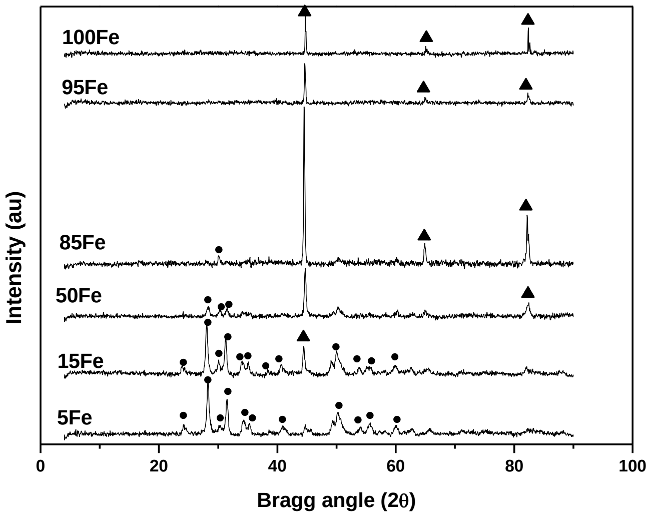

Figure 3. Crystalline structures for the reduced catalysts after the TPR experiment at 900 °C: triangle (▲): metallic iron (Fe^0); circles (●): ZrO_2.

4.3.3. Reducibility of calcined oxide precursors

Figure 4 shows the H_2-consumption profiles recorded during the H_2-TPR experiments of the samples that were calcined at 450 °C. The TPR profile of the pure iron oxide (100Fe) shows two distinct reduction peaks, one centered at 390 °C that results from the reduction of α-Fe_2O_3 to Fe_3O_4 and one with a peak maximum at 580 °C that results from the reduction of Fe_3O_4 to metallic iron (α-Fe). However, the formation of FeO was not observed because FeO is a metastable phase below 570 °C. The TPR profile of pure ZrO_2 (0Fe) is flat, with no H_2-consumption peak due to the high stability of this oxide under the conditions employed in this study (data not shown).

The TPR profiles of the Fe-rich iron samples (95Fe, 85Fe and 50Fe) had reduction peaks that were similar to those of 100Fe. For the Zr-rich samples (15Fe and 5Fe), the Fe^{x+} ($x = 2$ or 3) cations were more stabilized in the zirconia lattice. Thus, the FeO phase can be observed during the reduction process, making further reductions of the Fe^{2+} cations to Fe^o very difficult and shifting the second peak to higher temperatures.

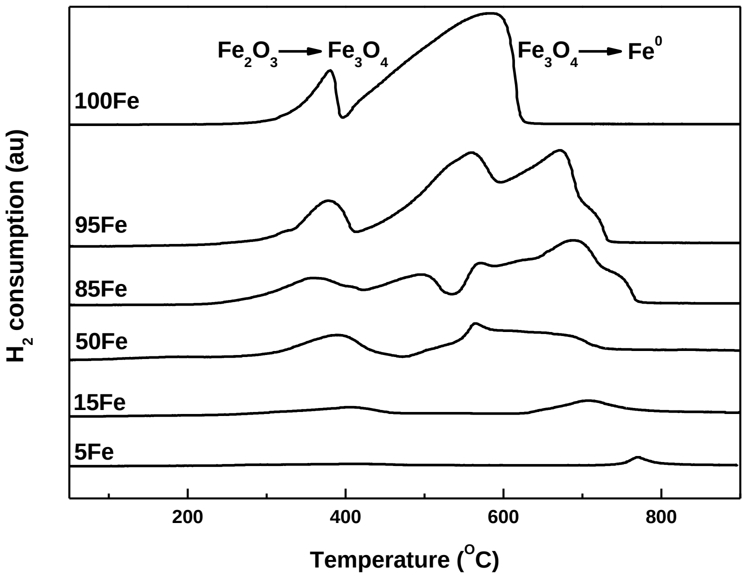

Figure 4.TPR profiles of the catalysts calcined at 450 °C.

4.3.4. Surface analysis

The photoelectron spectroscopy technique was used to determine the nature of the surface species and the relative amount of iron oxides brought about by thermal treatment. Accordingly, all calcined precursors were analyzed using this technique. For each sample, the Fe 2p, Zr 3d and O 1s core-level spectra were recorded. The Zr 3d spectra at approximately 182.2 eV in all samples was characteristic of the ZrO_2 species [38]. The Fe 2p spectra for the catalysts calcined at temperatures of 450 ºC are displayed in Figure 5, and Table 4 presents the binding energies of the Fe $2p_{3/2}$ and Zr $3d_{5/2}$ core-levels and the surface atomic ratios. The binding energy of the Fe $2p_{3/2}$ level falls in the between 710.2 and 711.8 eV and appears to be influenced by Fe-loading. However, the binding energy of the Fe $2p_{3/2}$ increases when the amount of ZrO_2 in the catalyst increases from 710.2 to 711.2 eV in the pure iron oxide and 95Fe, respectively. In addition, the binding energy gradually increases as the zirconia content increases from 711.2 to 711.8 eV in the 95Fe and 5Fe catalysts, respectively. This finding indicates that an interaction between iron and zirconia oxides likely developed Furthermore, these values are characteristic of Fe_2O_3 species [38]. This assignment is also consistent with the observation of a satellite line that is placed on the high binding energy side of the principal Fe 2p peaks.

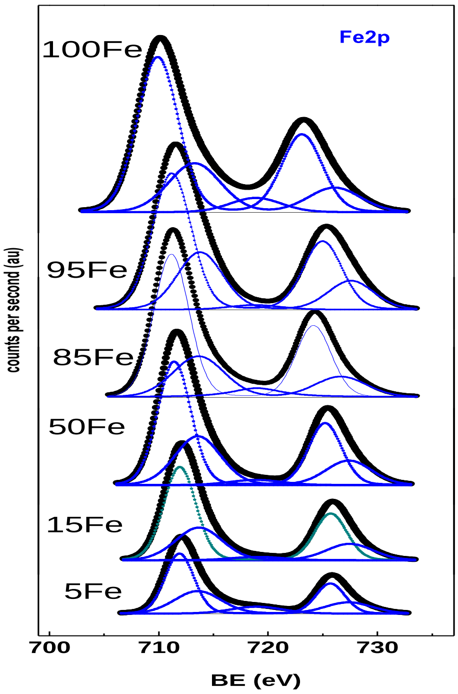

Figure 5. Fe 2p core-level spectra of the *x*Fe catalyst calcined at 450 ºC.

Table 4. Binding energy (eV) of the core-electrons of the calcined Fe/ZrO_2 catalysts

Sample	**Zr3d5/2**	**Fe2p3/2**	**O1s**	**Fe/(Fe+Zr)**
100Fe	-	710.2	530.1	1.000
95Fe	182.2	711.2	530.3	0.914
85Fe	182.2	711.1	530.2	0.821
50Fe	182.1	711.3	530.3	0.390
15Fe	182.1	711.8	530.1	0.099
5Fe	182.1	711.8	530.1	0.016
0Fe	182.2	-	530.2	0.000

In addition, the surface atomic ratios were calculated. In this calculation, the normalized intensities of the peaks using a tabulated atomic sensitivity factor were considered [39]. The resulting Fe/(Fe+Zr) ratios determined by the XPS measurements were compared with the corresponding nominal Fe/(Fe+Zr) ratios. This comparison is given in Figure 6. The deviation from linearity in this plot clearly indicates that the Fe and Zr distributions in the catalyst particles were not uniform. Moreover, the surface Fe/(Fe+Zr) ratios found in all of the compositions that were lower than the nominal ones clearly indicated that zirconia tends to be segregated towards the surface and is more marked in the Zr-rich composition range.

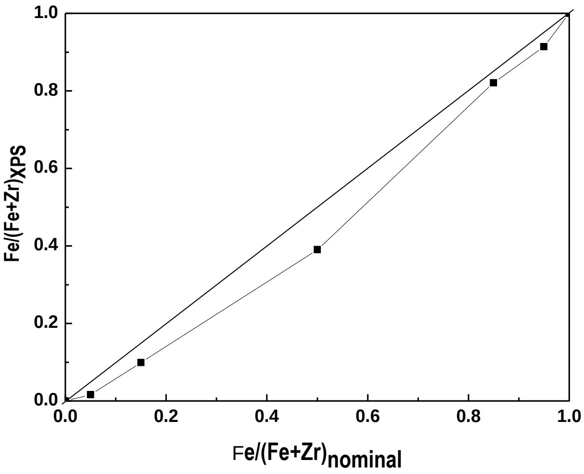

Figure 6. Comparison of surface and nominal Fe/(Fe+Zr) ratios for samples calcined at 450 ºC.

Figure 7 displays the Fe 2p profiles of the reduced precursors (samples taken at the end of the TPR experiments). The doublet placed on the higher binding energy is shifted to a lower binding energy, which means that the Fe^{3+} species is reduced to Fe^{2+}. The presence of Fe^{3+} satellite peaks on the high binding energy side of the peaks in this reduced sample likely resulted from the oxidation of some exposed Fe atoms in the reduced iron phases during the transfer of the sample from the TPR reactor to the analysis chamber of the XPS instrument.

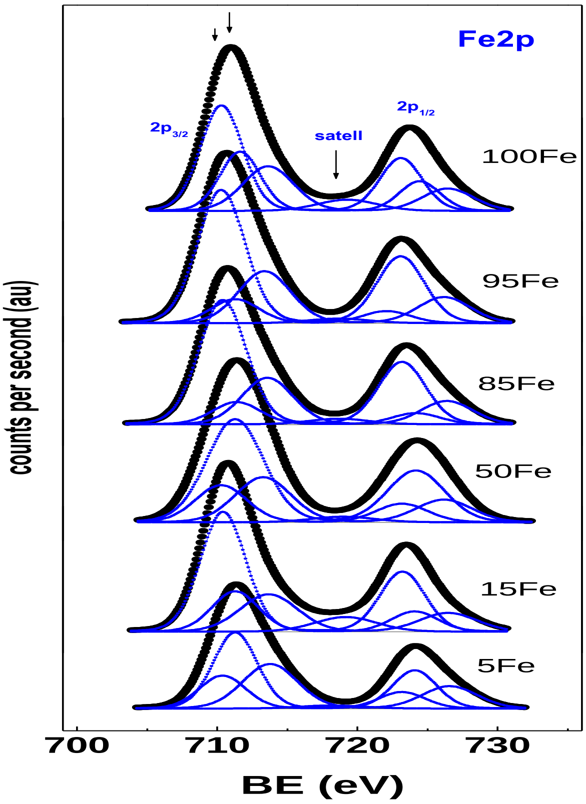

Figure 7. Fe 2p core-level spectra of the *x*Fe reduced catalyst after the TPR experiment at 900 °C.

Next, the surface atomic ratios Fe/(Fe+Zr) for the calcined precursors that were determined by XPS measurements were compared with the corresponding Fe/(Fe+Zr) ratios of the reduced samples. Figure 8 illustrates this comparison. From this figure, a clear deviation from the expected linearity is observed for the Fe-rich precursors. Such a deviation indicates that the Fe particles agglomerate during reduction and that more agglomeration occurs for the Fe-rich catalysts.

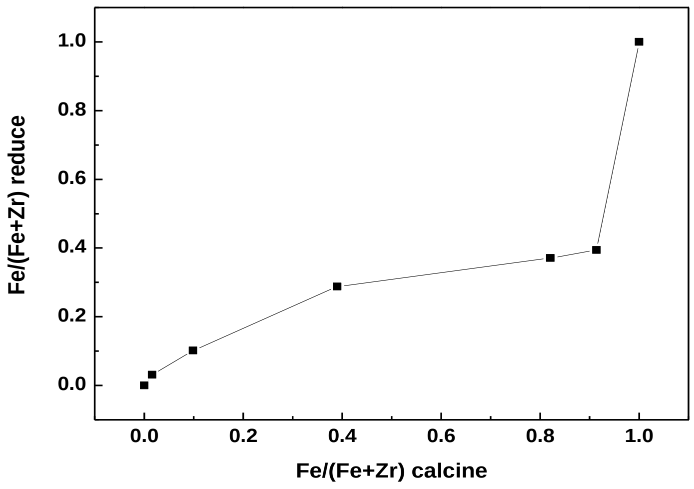

Figure 8. Comparison of the Fe/(Fe+Zr) surface atomic ratios for the calcined and reduced samples.

Finally, the surface atomic ratios of the Fe/Zr for the calcined catalysts that were determined using XPS were compared with the corresponding bulk Fe/Zr ratios. The plot in Figure 9 indicates a deviation from linearity, especially for the Fe-rich precursors. This result indicates that the free Fe and Zr are not more prevalent on the surface. However, large Fe particles are present, and the presence of free Fe and Zr increases as the zirconia content increases in the precursor composition and as the iron particle size decreases.

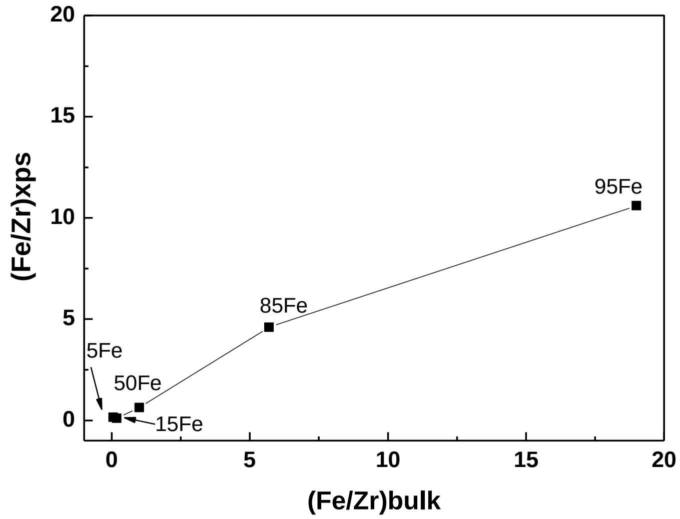

Figure 9. Comparison of the surface and bulk Fe/Zr ratios for the samples calcined at 450 ºC

4.3.5. Catalytic performance

All of the synthesized catalysts were tested in the CO hydrogenation reaction using a catalytic fixed-bed reactor. The calcined samples (100 mg, 0.25–0.30 mm particle size) were diluted using SiC (ca. 1.5 g, 0.25–0.30 mm particle size) to avoid hot spots. First, the catalysts were activated in situ at 450 ºC (at a heating rate of 10 ºC/min) for 1 h in syngas ($31CO/62H_2/7N_2$, GHSV = 0.0083 L/g.s) at atmospheric pressure. Next, the reactor was cooled down in the synthesis gas to the reaction temperature (250 ºC) and pressurized at 20 bar. Then, the performance of CO hydrogenation was investigated for on-stream periods of up to 48 h.

The influence of the zirconia content on the CO conversion of the representative catalyst series *x*Fe calcined at 450 ºC is displayed in Figure 10. The activity increased quickly over a short reaction period and then became stabilize as the on-stream time reached 48 h. The data displayed in this figure indicate that the CO conversion is strongly dependent on the zirconia contents of the catalysts. Under the experimental reaction conditions selected in this study, the lowest CO conversion was attained using a Zr-rich catalyst (15Fe and 5Fe), with activities of less than 5 % (CO conversion). In contrast, the highest CO conversion occurred for the Zr-free (100Fe) catalyst. Because the active phases of these catalysts in the target reaction are iron carbides, we normalized the CO conversion levels to the iron content (Fe at.g). According to this calculation, we noted that the 95Fe and 85Fe catalysts displayed better performance. Indeed, the performance of the pure iron oxide appeared greater, but its activity profile decreased slightly with the time on-stream, indicating that this catalyst is progressively deactivated.

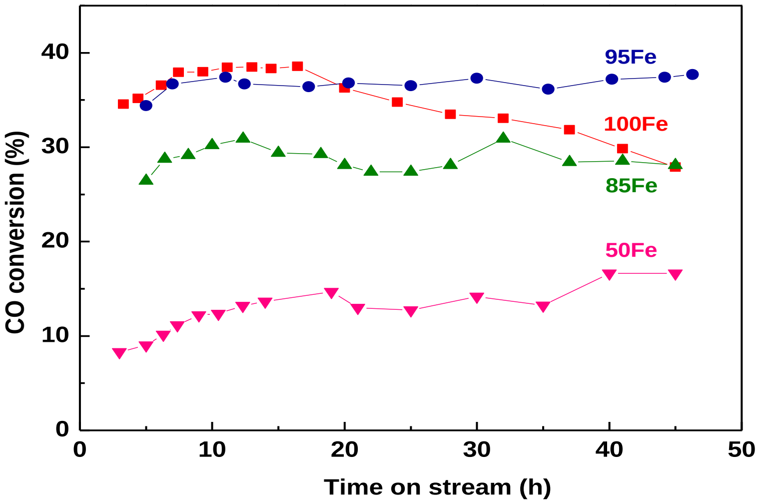

Figure 10. CO conversion as a function of the time on-stream for the *x*Fe catalysts derived from the precursor oxides calcined at 450 ºC. Reaction conditions: H_2/ CO = 2, T = 250 ºC, P = 20 bar, GHSV = 0.0083 L/g.s.

The rather low performance of the other Zr-rich catalysts (15Fe and 5Fe) can be explained as follows: (i) because iron oxide is a minor phase, it is likely that small Fe_2O_3 crystallites interact strongly with the zirconia surface and make the carburization process more difficult relative to the Fe-rich compositions; and (ii), because zirconia is a major phase in this Zr-rich composition region, partial coverage of the Fe_2O_3 crystallites by zirconia is expected. This effect may result in a loss of active iron sites with a subsequent decrease in performance.

Table 5 contains the product selectivity for different hydrocarbons (CH_4, C_2-C_4 and C_{5+}) and for CO_2 at on-stream reaction times of 12 h. In general, the CO_2 selectivity was low and below 10 %. . However, the CO_2 selectivity was nearly constant (8.53 – 8.43%)

for a catalyst composition of 100Fe-95Fe and slightly decreased to 7.3 % for 85Fe and to approximately 5% for 50Fe. This is likely due to the ability of the iron catalysts to perform the water gas-shift reaction ($CO + H_2O \rightarrow CO_2 + H_2$) in which water comes from the main FT reaction. As 50Fe catalyst displays a very low amount of exposed iron sites (cf. Figure 6) its CO conversion rate is rather low.

Table 5. Catalytic performance of the Fe-Zr catalysts in CO hydrogenation recorded at 12h on-stream. Reaction conditions: H_2/ CO = 2, *T* = 250 ºC, *P* = 20 bar, GHSV = 0.0083 L/g.s

Catalyst	**CO Conv. (%)**	**CO Rate (molCO/molFe/h)**	**Selectivity (%)**				**O/P ratio**
			CO_2	**CH_4(*)**	**C_2-C_4(*)**	**C_{5+}(*)**	
100 Fe	38.5	11.7	8.53	19.2	49.7	27.7	1
95Fe	36.7	12	8.43	19.9	45.4	31.9	0.98
85Fe	30.9	11.9	7.31	20.8	45.1	31.4	0.97
50Fe	13.2	10.2	5.17	28	39.4	30.8	0.71

(*) hydrocarbon selectivity calculated based on free CO_2.

The hydrocarbon production trend is best illustrated by plotting the CO_2-free hydrocarbon selectivity for different catalysts as performed in Figure 11. From this figure, it is clear that the CH_4 selectivity is less than 20 % for the 100Fe catalyst. The methanation tends to increase when Zr is incorporated with Fe, and the methane selectivities increased to 19.9, 20.8 and 28 for the 95Fe, 85Fe and 50Fe catalysts, respectively. Similarly, for these catalysts, the C_{5+} selectivity increased when Zr was added from 27.7 to 31.9 for 100Fe and 95Fe, respectively, and remained nearly constant with increasing Zr content at approximately 31% for 95Fe, 85Fe and 50Fe. In contrast, the C_2-C_4 selectivity followed an opposite trend. The high selectivity to CH_4 recorded for the catalysts with small iron particle size suggests that dissociated hydrogen is present on the catalyst surface, because the catalyst with smaller cluster dimensions favor hydrogen adsorption rather than to facilitate dissociative adsorbed CO molecules.

The huge amount of dissociated hydrogen present on the catalyst surface leads, in turn, to hydrogenation of carbon into methane [40-43]. Finally, the olefin/paraffin ratio was nearly constant at approximately 1 for the Fe- rich samples (100Fe, 95Fe and 85Fe) and decreases in the olefin/paraffin ratio were observed for the Zr-rich sample (50Fe). This finding also suggests that the hydrogenation capability is promoted by small Fe particle size as a result of the increasing Zr-loading. This peculiarity must be considered in the next step to drive selectivity towards lower olefin contents.

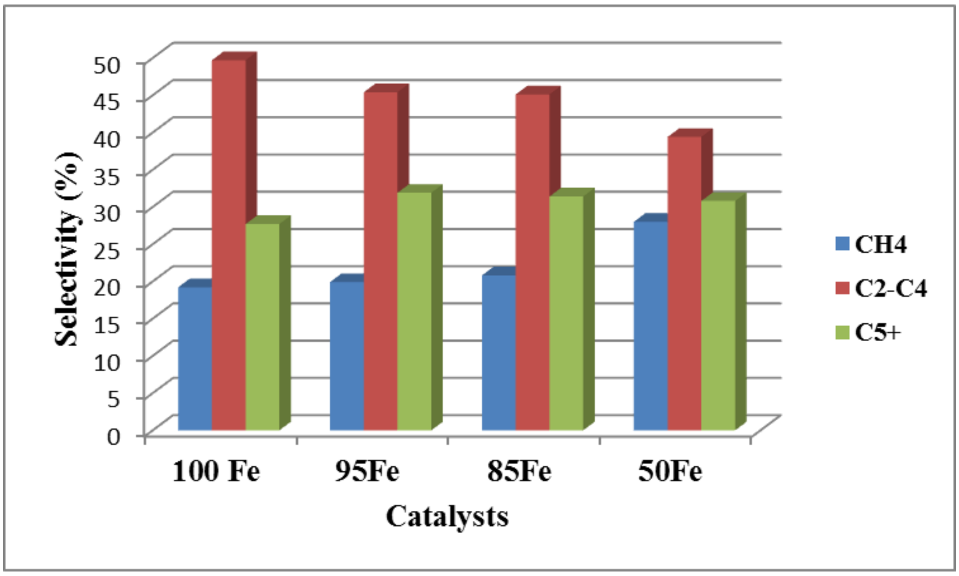

Figure 11. Hydrocarbons selectivity (CO_2 free) at TOS = 12 h.

4.4. General Discussion

In this study, we demonstrated that ZrO_2 influences the activity, hydrocarbon selectivity and stability of Fe/ZrO_2 catalysts for FT synthesis. However, the primary effect of zirconia is to modify the textural properties, the chemical nature of the surface species and the reduced behavior of these catalysts. The BET specific area was greatly enhanced by adding zirconium oxide to the catalysts, especially for the catalysts with similar amounts of iron and zirconium (50Fe). At these compositions, the stability of the catalysts improved, at least for a period of 48 h. Moreover, the 50Fe catalyst displayed the largest methanation rate and the lowest olefin-to-paraffin ratio relative to the other members of the series. This result is likely linked to the higher ability of the smaller iron particles to adsorb and dissociate hydrogen more than the CO species. In addition, this process increases the availability of active H^* atoms on the catalyst surface to hydrogenate surface carbon (C*) and other partially hydrogenated moieties (CH^*, CH_2^* and CH_3^*) but also increases the rate of secondary hydrogenation reactions of olefins to paraffins. However, the hydrogenation capability of the catalysts was acceptable because no K promoter was introduced in this study [44].

The reduction profiles of the Fe/ZrO_2 oxide precursors displayed in Figure 4 revealed that the reduction of iron oxides to metallic iron is difficult. This difficulty could result from the stabilization of the Fe^{3+}/Fe^{2+} cations and the interactions between the Fe-oxides and Zr-oxides [45]. As a consequence of this interaction, the agglomeration of particles to form large iron oxides was restrained, which resulted in the high dispersion of the iron oxides. Furthermore, this was considered to be the origin of the strong dispersion effect of the ZrO_2 matrix.

The product selectivity of the Fe-based catalysts that were promoted by various amounts of Zr clearly affected the particle size of the iron. From the data collected in Table 5, it is evident that both the CO conversion and CO_2 selectivity of the catalysts follow the same increasing trends with increasing iron oxide particle size. The selectivity of the molecular weight hydrocarbons (C_{5+}) slightly increased as the Fe_2O_3 particle size increased from 9.4 to 14 nm, and the CH_4 selectivity decreased as the iron particle size increased. This result agrees with the results of several previous studies [40, 46]. The increase of C_5^+ selectivity with increasing Fe-oxide cluster size could be attributed to easy activation and fast movement, which results in an easy reaction between the adsorbed CO molecules and the iron oxides due to the large particle size. The tendency of catalysts with small iron particle sizes to increase methane selectivity indicates that dissociated hydrogen is present on the surfaces of the catalysts because the catalysts with smaller cluster dimensions have a greater tendency to form atomically adsorbed hydrogen (H*) than the dissociative adsorbed CO molecules, increasing the population of hydrogen species on the surface. The large amount of H* present on the catalyst surface results in the formation of hydrogenate C* and CH_x^* moieties in the CH_4 [41-43].

4.5. Conclusions

The Zr-Fe-O catalyst precursors that were prepared using Fe-loadings of 0 to 100% were calcined at 450 °C to obtain well-crystallites of Fe_2O_3. Then, these precursors were activated in the H_2/CO mixture and tested using Fischer Tropsch Synthesis. The main conclusions of this study include the following: (i) CO conversion was strongly dependent on the surface iron concentration, in agreement with the XPS measurements; (ii) CO_2 selectivity was lower than 10% and nearly constant in the Fe-rich catalysts but decreased as a function of increasing zirconium, which agreed with the expected influences of the water gas-shift reaction on iron sites; (iii), for the Fe-poor catalysts (15Fe and 5Fe) in which no crystalline iron phases were observed by XRD and a strong Zr-enrichment was revealed by XPS, the lowest CO conversion was attained by the Zr-rich catalyst (15Fe and 5Fe) with activities of less than 5% (CO conversion), indicating that the reaction mechanism is different from the reactions involving the Fe-rich catalysts; and (iv) the highest CO conversion occurred in the Zr-free (100Fe) catalyst. Because the active phases of these catalysts in the target reaction are iron carbides, we normalized the CO conversion levels to the iron content (Fe at.g). Based on this calculation, we noted that the 95Fe and 85Fe catalysts displayed better performance. Indeed, the performance of the pure iron oxide appeared to be better but its activity profile decreased slightly with time on-stream, which indicated that this catalyst becomes progressively deactivated. The rather low performance of the other Zr-rich catalysts (15Fe and 5Fe) can be explained as follows: (i) when iron oxides are the minor phase, the small Fe_2O_3 crystallites likely interact strongly with the zirconia surface and make the carburization process more difficult relative to the Fe-rich compositions; and (ii) when zirconia is the major phase in this Zr-rich composition region, partial coverage of Fe_2O_3 crystallites by zirconia is expected, which may induce a loss of active iron sites and a subsequent drop in performance.

Acknowledgments

M. Al-Dossary gratefully acknowledges financial support from SABIC-Saudi Arabia for PhD program.

4.6. References

[1] Pour AN, Shahri SMK, Zamani Y, Zamanian A. Promoter effect on the CO2-H2O formation during Fischer-Tropsch synthesis on iron-based catalysts. Journal of Natural Gas Chemistry 2010;19:193-197.

[2] Lohitharn N, Goodwin Jr JG. An investigation using SSITKA of Chain growth on Fe and FeMnK Fischer–Tropsch synthesis catalysts. Catalysis Communications 2009;10:758-762.

[3] Khodakov AY, Chu W, Fongarland P. Advances in the Development of Novel Cobalt Fischer−Tropsch Catalysts for Synthesis of Long-Chain Hydrocarbons and Clean Fuels. Chemical Reviews 2007;107:1692-1744.

[4] Herranz T, Rojas S, Pérez-Alonso FJ, Ojeda M, Terreros P, Fierro JLG. Hydrogenation of carbon oxides over promoted Fe-Mn catalysts prepared by the microemulsion methodology. Applied Catalysis A: General 2006;311:66-75.

[5] Feyzi M, Mirzaei AA. Performance and characterization of iron-nickel catalysts for light olefin production. Journal of Natural Gas Chemistry 2010;19:422-430.

[6] Ma X, Sun Q, Cao F, Ying W, Fang D. Effects of the Different Supports on the Activity and Selectivity of Iron-Cobalt Bimetallic Catalyst for Fischer-Tropsch Synthesis. Journal of Natural Gas Chemistry 2006;15:335-339.

[7] Panpranot J, Goodwin Jr JG, Sayari A. CO Hydrogenation on Ru-Promoted Co/MCM-41 Catalysts. Journal of Catalysis 2002;211:530-539.

[8] Dutta P, Elbashir NO, Manivannan A, Seehra MS,Roberts CB. Characterization of Fischer–Tropsch Cobalt-Based Catalytic Systems (Co/SiO2 and Co/Al2O3) by X-ray Diffraction and Magnetic Measurements. Catalysis Letters 2004;98:203-210.

[9] Sun S, Fujimoto K, Zhang Y, Tsubaki N. A highly active and stable Fischer–Tropsch synthesis cobalt/silica catalyst with bimodal cobalt particle distribution. Catalysis Communications 2003;4:361-364.

[10] Wu B, Tian L, Xiang H, Zhang Z,Li Y-W. Novel precipitated iron Fischer–Tropsch catalysts with Fe3O4 coexisting with α-Fe2O3. Catalysis Letters 2005;102:211-218.

[11] Xu J, Bartholomew C, Sudweeks J, Eggett D. Design, Synthesis and Catalytic Properties of Silica-Supported Pt-Promoted Iron Fischer–Tropsch Catalysts. Topics in Catalysis 2003;26:55-71.

[12] Curtis V, Nicolaides CP, Coville NJ, Hildebrandt D, Glasser D. The effect of sulfur on supported cobalt Fischer–Tropsch catalysts. Catalysis Today 1999;49:33-40.

[13] Jothimurugesan K, Goodwin Jr JG, Gangwal SK,Spivey JJ. Development of Fe Fischer–Tropsch catalysts for slurry bubble column reactors. Catalysis Today 2000;58:335-344.

[14] Dry ME. The Fischer–Tropsch process: 1950–2000. Catalysis Today 2002;71:227-241.

[15] De Smit E, Weckhuysen BM. The renaissance of iron-based Fischer-Tropsch synthesis: on the multifaceted catalyst deactivation behaviour. Chemical Society Reviews 2008;37:2758-2781.

[16] Davis BH. Fischer-Tropsch synthesis: relationship between iron catalyst composition and process variables. Catalysis Today 2003;84:83-98.

[17] Bukur DB, Lang X, Mukesh D, Zimmerman WH, Rosynek MP,Li C. Binder/support effects on the activity and selectivity of iron catalysts in the Fischer-Tropsch synthesis. Industrial & Engineering Chemistry Research 1990;29:1588-1599.

[18] Wang H, Yang Y, Xu J, Wang H, Ding M,Li Y. Study of bimetallic interactions and promoter effects of FeZn, FeMn and FeCr Fischer–Tropsch synthesis catalysts. Journal of Molecular Catalysis A: Chemical 2010;326:29-40.

[19] Lohitharn N, Goodwin Jr JG. Impact of Cr, Mn and Zr addition on Fe Fischer–Tropsch synthesis catalysis: Investigation at the active site level using SSITKA. Journal of Catalysis 2008;257:142-151.

[20] Al-Dossary M, Fierro JLG, Spivey JJ. Cu-Promoted Fe2O3/MgO-Based Fischer–Tropsch Catalysts of Biomass-Derived Syngas. Industrial & Engineering Chemistry Research 2014;54:911-921.

[21] Campos A, Lohitharn N, Roy A, Lotero E, Goodwin Jr JG,Spivey JJ. An activity and XANES study of Mn-promoted, Fe-based Fischer-Tropsch catalysts. Applied Catalysis A: General 2010;375:12-16.

[22] Li S, Meitzner GD, Iglesia E. Structure and site evolution of iron oxide catalyst precursors during the fischer-tropsch synthesis. Journal of Physical Chemistry B 2001;105:5743-5750.

[23] Zhang H, Yang X, Zhou L, Su Y,Liu Z. Conversion of syngas to higher alcohols over Cu-Fe-Zr catalysts induced by ethanol. Journal of Natural Gas Chemistry 2009;18:337-340.

[24] Lohitharn N, Goodwin Jr JG, Lotero E. Fe-based Fischer–Tropsch synthesis catalysts containing carbide-forming transition metal promoters. Journal of Catalysis 2008;255:104-113.

[25] Qing M, Yang Y, Wu B, Xu J, Zhang C, Gao P,Li Y. Modification of Fe–SiO2 interaction with zirconia for iron-based Fischer–Tropsch catalysts. Journal of Catalysis 2011;279:111-122.

[26] All S, Chen B, Goodwin JG. Zr Promotion of Co/SiO2 for Fischer-Tropsch Synthesis. Journal of Catalysis 1995;157:35-41.

[27] Hong J, Chu W, Chernavskii PA, Khodakov AY. Effects of zirconia promotion on the structure and performance of smaller and larger pore silica-supported cobalt catalysts for Fischer–Tropsch synthesis. Applied Catalysis A: General 2010;382:28-35.

[28] Jongsomjit B, Kittiruangrayub S, Praserthdam P. Study of cobalt dispersion onto the mixed nano-SiO2–ZrO2 supports and its application as a catalytic phase. Materials Chemistry and Physics 2007;105:14-19.

[29] Moradi GR, Basir MM, Taeb A, Kiennemann A. Promotion of Co/SiO2 Fischer–Tropsch catalysts with zirconium. Catalysis Communications 2003;4:27-32.

[30] Ma X, Sun Q, Ying W, Fang D. Effects of promoters on catalytic performance of Fe-Co/SiO2 catalyst for Fischer-Tropsch synthesis. Journal of Natural Gas Chemistry 2009;18:354-358.

[31] Yang J, Sun Y, Tang Y, Liu Y, Wang H, Tian L, Wang H, Zhang Z, Xiang H, Li Y. Effect of magnesium promoter on iron-based catalyst for Fischer–Tropsch synthesis. Journal of Molecular Catalysis A: Chemical 2006;245:26-36.

[32] Herranz T, Rojas S, Pérez-Alonso FJ, Ojeda M, Terreros P, Fierro JLG. Carbon oxide hydrogenation over silica-supported iron-based catalysts: Influence of the preparation route. Applied Catalysis A: General 2006;308:19-30.

[33] Pérez-Alonso FJ, Granados ML, Ojeda M, Herranz T, Rojas S, Terreros P, Fierro JLG, Gracia M, Gancedo JR. Relevance in the fischer-tropsch synthesis of the formation of Fe-O-Ce interactions on iron-cerium mixed oxide systems. Journal of Physical Chemistry B 2006;110:23870-23880.

[34] Fischer F, Tropsch H. Über die Entwicklung unserer Benzinsynthese aus Kohlenoxyd und Wasserstoff bei gewöhnlichem Druck. Brennstoff – Chemie 1930;11:489

[35] R. M. Cornell, U. Schwertmann, The Iron Oxides: Structures, Properties, Reactions and Uses, VCH Publishers, New York, 1996.

[36] Fischer F, Tropsch H. Über die Herstellung synthetischer Ölgemische (Synthol) durch Aufbau aus Kohlenoxyd und Wasserstoff. Brennstoff – Chemie 1923;4:276

[37] Fischer F, Tropsch H. The synthesis of petroleum at atmospheric pressures from gasification products of coal. Brennstoff – Chemie 1926;7:97

[38] Practical Surface Analysis: Auger and X-Ray Photoelectron Spectroscopy, D. Briggs and M.P. Seah, Eds., John Wiley & Sons, Chichester, New York, 1990.

[39] Wagner CD, Davis LE, Zeller MV, Taylor JA, Raymond RH, Gale LH. Empirical atomic sensitivity factors for quantitative analysis by electron spectroscopy for chemical analysis. Surface and Interface Analysis 1981;3:211-225.

[40] Park J-Y, Lee Y-J, Khanna PK, Jun K-W, Bae JW, Kim YH. Alumina-supported iron oxide nanoparticles as Fischer–Tropsch catalysts: Effect of particle size of iron oxide. Journal of Molecular Catalysis A: Chemical 2010;323:84-90.

[41] Gallegos NG, Alvarez AM, Cagnoli MV, Bengoa JF, Marchetti SG, Mercader RC, Yeramian AA. Selectivity to Olefins of Fe/SiO2–MgO Catalysts in the Fischer–Tropsch Reaction. Journal of Catalysis 1996;161:132-142.

[42] Den Breejen JP, Radstake PB, Bezemer GL, Bitter JH, Frøseth V, Holmen A, De Jong KP. On the origin of the cobalt particle size effects in Fischer-Tropsch catalysis. Journal of the American Chemical Society 2009;131:7197-7203.

[43] Bezemer GL, Bitter JH, Kuipers HPCE, Oosterbeek H, Holewijn JE, Xu X, Kapteijn F, Van Diilen AJ, De Jong KP. Cobalt particle size effects in the Fischer-Tropsch reaction studied with carbon nanofiber supported catalysts. Journal of the American Chemical Society 2006;128:3956-3964.

[44] Li S, Li A, Krishnamoorthy S, Iglesia E. Effects of Zn, Cu, and K Promoters on the Structure and on the Reduction, Carburization, and Catalytic Behavior of Iron-Based Fischer–Tropsch Synthesis Catalysts. Catalysis Letters 2001;77:197-205.

[45] Zhang H, Ma H, Zhang H, Ying W, Fang D. Effects of Zr and K Promoters on Precipitated Iron-Based Catalysts for Fischer–Tropsch Synthesis. Catalysis Letters 2012;142:131-137.

[46] Torres Galvis HM, Bitter JH, Davidian T, Ruitenbeek M, Dugulan AI, De Jong KP. Iron Particle Size Effects for Direct Production of Lower Olefins from Synthesis Gas. Journal of the American Chemical Society 2012;134:16207-16215.

Chapter 5: Effect of high-temperature pre-reduction in Fischer-Tropsch synthesis on Fe/ZrO$_2$ catalysts

5

Effect of high-temperature pre-reduction in Fischer-Tropsch synthesis on Fe/ZrO$_2$ catalysts

M. Al-Dossary* and J.L.G. Fierro
Institute of Catalysis and Petrochemistry, CSIC, Marie Curie 2, Cantoblanco, 28049 Madrid, Spain
E-mail: ma99sa@hotmail.com; Fax: +34 91 585 4760

Abstract

Fischer-Tropsch synthesis of low molecular weight (C_2-C_4) olefins is a valuable alternative process for the production of key chemicals from non-petroleum precursors such as a renewable C source like biomass. The influence of the H_2 treatment temperature of zirconia-supported iron catalysts on the conversion of synthesis gas has been investigated. The CO conversion rate, based on steady-state, increased with the pretreatment temperature up to a maximum and then decreased at higher temperatures. Moreover, methane selectivity was found to decrease slightly from the lowest H_2 treatment temperatures (46%) to the highest ones (34%), while C_2-C_4 and C_5^+ hydrocarbons followed an opposite trend. Presumably, methane formation takes place at highly active low coordination sites residing at corners and edges, which are more abundant on small iron carbide particles. Lower hydrocarbons are mainly produced at terrace sites that are available and active, quite independent of the iron crystallite size.

Keywords: iron catalysts, Fischer-Tropsch synthesis, zirconia, low molecular weight olefins

5.1. Introduction

The production of transportation fuels and chemicals by Fischer-Tropsch synthesis (FTS) is currently gaining greater importance fostered by environmental concerns and the necessity of many countries to reduce their reliance on oil imports. The catalytic production of hydrocarbons via FTS reaction from syngas mixtures involves a number of consecutive reactions resulting in a broad spectrum of linear and branched hydrocarbons, olefins and oxygenated products [1-3] with the simultaneous production of water according to the following simplified reactions:

paraffins: $(2n+1)H_2 + nCO \rightarrow C_nH_{2n+2} + nH2O$ [1]
olefins: $nCO + 2nH_2 \rightarrow C_nH_{2n} + nH_2O$ [2]
oxygenates: $H_2 + CO \rightarrow CH_xO_y + H_2O$ [3]

Other parallel reactions such as: (i) Water Gas-Shift (WGS): $CO + H_2O \rightarrow CO_2 + H_2$; (ii) Methanation: $CO + 3H_2 \rightarrow CH_4 + H_2O$; and (iii) Boudouard reaction: $2CO \rightarrow C + CO_2$ occur simultaneously.

It is established that the nature and composition of catalysts control the selectivity of products from FT reactions; therefore, proper catalyst selection as well as optimization of the reaction parameters are of prime importance in FT process. The active and selective catalysts for the FT reaction are mainly based on cobalt or iron. Cobalt-based catalysts have been widely investigated since they favour the formation of long-chain hydrocarbons [4, 5]. As opposed to cobalt-based catalysts, iron-based ones are highly attractive not only because of their relatively low cost but also due to their broad operation conditions and high product selectivity toward light olefins [6]. In addition, iron disfavors the competing formation of methane, and furthermore catalyzes the WGS reaction, enabling the direct processing of synthesis gas with a low H_2/CO ratio derived from modern energy-efficient coal gasifiers without an additional WGS reactor [2, 7, 8].

Despite these promising features, however, Fe-based catalysts for FTS are often used as unsupported catalysts. One of the major drawbacks related to the use of massive unsupported catalysts is physical degradation, producing catalyst fines as a consequence of the volume changes that occur during the FTS reaction. These fines will either plug the fixed-bed reactors, generating a large pressure drop, or will hinder catalyst separation in slurry reactors [9]. The development of appropriate supports and/or binders, which increase attrition resistance of the samples, improves the catalyst life-time. High surface area oxides like silica (SiO_2), alumina (Al_2O_3), titania (TiO_2), magnesia (MgO), manganese oxide (MnO) and zirconia (ZrO_2) are among the supports most frequently used. Several advantages of supported iron catalysts, such as an improved catalytic stability and lower deactivation rate, have been reported [10].

In addition, the FTS is a structure-sensitive reaction [11], which means that the crystallite size of the iron phase plays an important role in FTS activity and product selectivity. It is emphasized that whereas these size effects of cobalt metal catalysts and ruthenium-based catalysts in CO hydrogenation reactions [1, 12-22], the number of researches focused on the effect of iron cluster size in FTS reaction is limited. To the best of our knowledge, the performance of the ZrO_2-supported iron catalysts and the crystallite size effects of the activity and selectivity in FTS reactions have been scarcely investigated. Therefore, this work was undertaken with the aim to investigate the relationship between cluster size of iron oxide and its FT performance. For this purpose, Fe/ZrO_2 catalysts were prepared with different crystallite sizes and their performance evaluated in FTS performed with a laboratory-scale fixed bed reactor.

5.2. Experimental Section

5.2.1. Catalysts preparation

The catalysts used in this study were prepared by the conventional incipient wetness impregnation methods. Zirconia-supported iron catalysts were impregnated on a high surface area of silica-stabilized zirconium hydroxide (zirconium hydroxide (stabilized with 4% silica) grade XZ0645/01, Magnesium Elektron Ltd) with ($Fe(NO_3)_3.9H_2O$) (Iron (III) nitrate nonahydrate (Aldrich, >= 98%)) aqueous solution. Zirconia-supported iron catalysts were prepared with appropriate amount of 10 wt. % metal loading. $Fe(NO_3)_3.9H_2O$ (Aldrich) was dissolved in appropriate deionized water and were added into the support drop by drop. The slurry was then kept at room temperature for overnight in ambient air then dried at 110°C for 3 h. In order to obtain different particles size of metallic iron, aliquots of Fe/ZrO_2 precursor were treated under flowing of pure hydrogen (50 cm^3 min^{-1}). Based on the treatment temperature and period of the treatment under hydrogen environment the catalysts are referred to hereafter as Fe_x and $Fe_{x(yh)}$, where x in Fe_x denotes the pretreatment temperature for 1 h and both *x* and y in $Fe_{x(yh)}$ denote the pretreatment temperature and period of the pretreatment in hours, respectively.

5.2.2. Catalysts characterization

5.2.2.1. Nitrogen adsorption-desorption isotherms

Nitrogen adsorption-desorption isotherms were recorded at the temperature of liquid nitrogen (-196°C), using a Micromeritics ASAP 2000 apparatus. The samples were degassed at 140 °C for 16 h prior to the determination of the adsorption isotherm [2]. Specific areas were calculated by the BET method applied to the region of relative pressure $0.05 < P/P^0 < 0.30$ and taking a value of 0.162 nm^2 for the cross-section of adsorbed N_2 at -196ºC.

5.2.2.2. Hydrogen Temperature programmed reduction (H_2-TPR)

Hydrogen temperature programmed reduction (H_2-TPR) experiments were carried out in a Micrometrics 3000 equipment interfaced to a data station. About 30 mg of the catalyst were pretreated under dry helium at 180°C for 0.5 h. The TPR profile was recorded by heating the sample from room temperature (around 30°C) to 950°C at a rate of 10°C/min under a flowing of 10 vol% of H_2/Ar. The hydrogen consumption was monitored with a thermal conductivity detector (TCD). The effluent gas was passed through a cold trap placed before the TCD to avoid water condensation from the exit stream. More details of the procedure can be found elsewhere [2].

5.2.2.3. Powder X-ray diffraction (PXRD)

Powder X-ray diffraction (XRD) patterns of the precursor and calcined sample were recorded using a Seifert 3000 XRD diffractometer equipped with a PW goniometer with Bragg-Brentano $\theta/2\theta$ geometry, an automatic slit, and a bent graphite monochromator [2]. Using nickel-filtered Cu $K\alpha_1$ (λ = 0.15406 nm) radiation. A scanning step of 0.02° was taken between 5° and 90° Bragg' angles in the scan mode (0.05°, 2 s).

5.2.2.4. Laser Raman Spectroscopy

Raman spectra were recorded with a Renishaw in Via Raman Microscope spectrometer equipped with a laser beam emitting at 532 nm, and a 100 mW output power. The photon scattered by the sample were dispersed by an 1800 lines/mm grating monochromator and simultaneously collected on a CCD camera. The collection optic was set at 50x objective. The samples selected to be studied by Raman Microscope spectrometer were both the pretreated catalysts under hydrogen environment and used samples after FTS reaction. Both samples were directly mounted into the analysis chamber of the Raman Microscope spectrometer without further treatment.

5.2.2.5. X-ray Photoelectron spectroscopy (XPS)

X-ray photoelectron spectra (XPS) were acquired with a VG Escalab 200R spectrometer in the pulse-count mode at a pass energy of 50 eV using an Mg Kα ($h\nu$ = 1253.6) X-ray source. Kinetic energies of photoelectrons were measured using a hemispherical electron analyser working in the constant pass (20 eV) energy mode. The background pressure in the analysis chamber was kept below 3×10^{-8} mbar during data acquisition. The powder samples were pressed into copper holders and then mounted on a support rod placed in the pretreatment chamber. The XPS data were signal averaged for at least 200 scans and were taken in increments of 0.1 eV with dwell times of 50 ms.

Binding energies were calibrated relative to the C 1s peak from adventitious carbon of the samples at 284.6 eV to correct the potential contact differences between the sample and spectrometer. Both binding energy (BE) values and peak areas were computed by fitting the experimental spectra to Gaussian/Lorentzian lines after removing the S-shaped background. The samples were exposed to a synthesis gas stream (62.0 % H_2, 31.0 % CO, and balance N_2, Air Liquid) at room temperature and then the temperature was increased from room temperature until reach 150°C under heating rate of 10°C/min then decrease heating rate from 10°C into 1°C/ min beyond 150 °C until reach the activation temperature (300°C) and keep it for 1 h under following of the syngas at atmospheric pressure. Finally the sample was cooled to ambient temperature and degassed (residual pressure about 10^{-6} mbar) before passing it to the analysis chamber.

5.2.3. Catalytic performance

The catalysts were tested in the CO hydrogenation reaction using a fixed-bed microreactor (stainless steel 316, 165 mm long and 8.5 mm ID. The reaction temperature was measured with a K-type thermocouple buried in the catalytic bed. The reactor was held within a furnace equipped with a temperature controller. All pipes after reactor outlet were kept at 130°C. The reaction system was provided with a stainless steel hot trap set at 110°C to collect the heavier products (waxes). Flow rates were controlled using Bronkhorst High-Tech Series mass flow controllers. The calcined catalyst precursors (200 mg, 0.212–0.315 mm particle size) were diluted with 1.5 g of silicon dioxide (sand SiO_2, Sigma Aldrich) to avoid hot spots owing to the exothermal character of the reaction, and also to facilitate the heat transfer. First, the catalysts were activated *in situ* at 300°C (the temperature was increased from room temperature until reach 150°C under heating rate of 10°C/min, then heating rate was decreased to 1°C/min beyond 150 °C until reach the activation temperature (300°C) and keep it for 1 h in syngas ($31CO/62H_2/7N_2$, GHSV = 0.0042 $L/g_{cat}.s$) at atmospheric pressure. The reactor was then pressurized under synthesis gas at the same temperature (300°C) until 2.02 MPa. Once the reactor reached this pressure, the flow rate of synthesis gas was decreased to GHSV = 0.0021 $L/g_{cat}.s$. CO hydrogenation was then followed and catalysts performance was tested under steady-state conditions.

Analysis of reactant gases and products was performed on-line with a gas chromatograph (HP 6890 Plus). A Porapak Q (1/8" x 3 m)-packed column connected to a thermal conductivity detector (TCD) was used to analyse the inorganic gases (H_2, N_2, CO, and CO_2) and water. Hydrocarbons and oxygenated compounds were analysed with a DB-1 capillary column (60 m x 0.25 mm x 0.25 μm) connected to a flame ionization detector (FID). The equipment configuration allowed the analysis of C_1-C_{16} hydrocarbons, C_1-C_{10} alcohols and other oxygenated compounds. To check the results reproducibility, different catalytic tests were carried out on the same catalyst. The experimental error was always lower than 1% (absolute value). The following temperature program was used: -50°C hold for 10 min, then a ramping of 10°C/min up to 230°C, and then keep at this temperature for 20 min. Nitrogen was used as internal standard for chromatographic analyses, Detailed procedure can be found elsewhere [23].

5.3. Results and discussion

5.3.1. Textural analysis

Figure 1 shows the nitrogen adsorption-desorption isotherm of a representative zirconia-supported iron catalyst ($10Fe/ZrO_2$). This catalyst displayed type IV isotherm, which is characteristic of mesoporous samples, in accordance with the IUPAC classification [24, 25]. The BET surface area, pore volume and pore diameter of the silica-stabilized $Zr(OH)_4$ substrate and the representative iron-supported $10Fe/ZrO_2$ catalyst are shown in Table 1. It can be seen that impregnation of the substrate with the iron salt and pretreatment in ambient air at 110°C for 3 h lead to a decrease in the BET surface area from 292 m^2/g for $Zr(OH)_4$ to 239 m^2/g for the $10Fe/ZrO_2$ catalysts precursor. Similarly, the pore volume also decreased upon substrate impregnation with the iron salt. This fact indicates a partial blocking of the $Zr(OH)_4$ pores by the iron entities incorporated. Also, the effects of pre-reduction temperature on the properties of the catalyst $10Fe/ZrO_2$ were studied and their results listed in Table 1. These data indicate a significant difference in the catalyst properties: as the calcination temperature is increased, the specific BET surface area decreases, while the pore size increases.

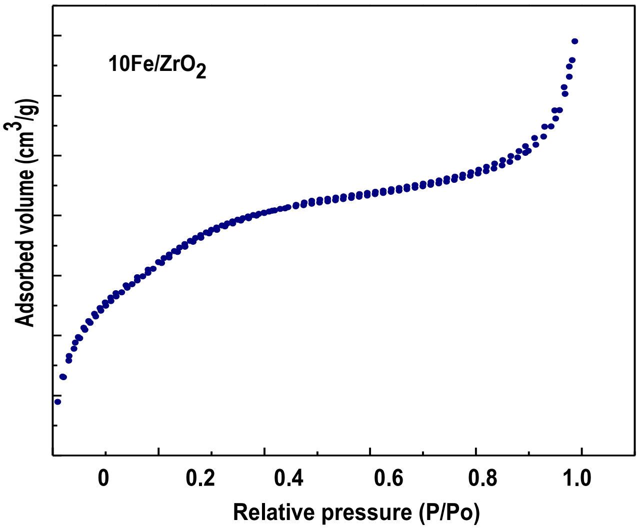

Figure 1. Nitrogen adsorption-desorption isotherms of the zirconia-supported iron catalyst.

Table 1. Textural properties of the support material and iron supported catalyst and Fe crystallite size calculated by Scherrer equation.

Catalyst	**BET specific area (m^2/g)**	**pore volume[a] (cm^3/g)**	**pore diameter (nm)**	**Fe crystallite size (nm)**
$Zr(OH)_4$	292	0.177	26.2	-
Fe/ZrO_2	239	0.135	26.7	-
Fe600	97.4	0.1	3.84	ND
Fe700	72.3	0.089	4.67	ND
Fe800	48.9	0.073	6.46	5.3
Fe900	26.4	0.056	8.24	7
Fe900(3h)	25.7	0.055	8.26	5.5
Fe930	20.6	0.049	9.16	6

[a] values of pore volume were calculated by BJH method from desorption isotherm

5.3.2. TPR of catalyst precursors

The reduction behavior of the oxide precursor provides useful information about the metal oxide-support interaction and on the dispersion of the supported iron oxide phases. The hydrogen consumption profiles for the 10Fe/ZrO$_2$ catalyst whose Fe crystallite size was modified by thermal treatments are shown in Figure 2. All samples show a first hydrogen consumption peak around 400ºC and a second one at temperatures somewhat above 800ºC. This second peak is only visible in samples Fe600, F700 and Fe800 but shifts to substantially higher temperatures in the other samples. It has been reported that both bulk and supported iron oxide catalysts usually show one H$_2$-consumption peak at temperatures of 400-540ºC, and a broad reduction feature at temperatures above 600ºC, suggesting that reduction of Fe$_2$O$_3$ occurs in two stages. The peaks situation in the region 600-800ºC indicates that the reduction process could occur in two or even in three stages according to sequence [2, 26-31]:

$$Fe_2O_3 \rightarrow Fe_3O_4 \rightarrow [FeO] \rightarrow Fe^0 \qquad [1]$$

The first reduction step at temperatures around 400ºC is usually ascribed to reduction of Fe$_2$O$_3$ (hematite) into Fe$_3$O$_4$ (magnetite). To be sure of this assignment, the H$_2$-consumption in this reduction peak was quantified. For all catalysts the H$_2$ consumption, expressed as the number of O-atoms removed per Fe-atom, was in the range 0.14-0.17. Taking into account that during the complete reduction of Fe$_2$O$_3$ into Fe$_3$O$_4$ 0.17 O-atoms per each Fe-atom are eliminated, it can be unambiguously stated that the H$_2$-consumption peak situated at temperatures around 400ºC belongs to reduction of hematite into magnetite phase.

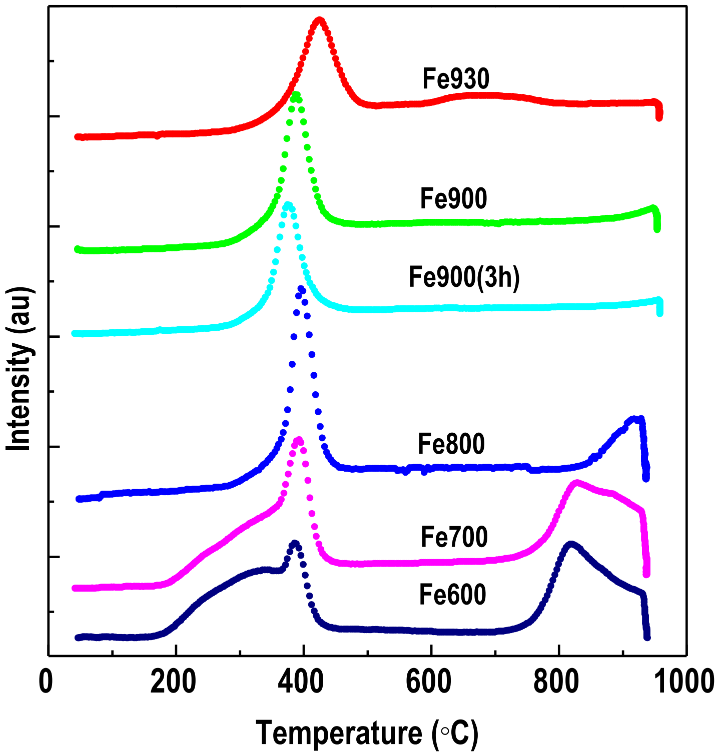

Figure 2. Temperature programmed reduction profiles of the catalysts.

Looking at the TPR profiles in Figure 2, it is clear that the second reduction peak appears at temperatures above 800ºC in samples Fe600, Fe700 and F800 but is not observed for samples Fe900 and Fe930, probably because it shifts at temperatures higher than the maximum permitted by the TPR equipment (950ºC). Quantification of the H_2-concumption of the peak at about 800ºC for samples Fe600, F700 and Fe800 indicates that the O-atoms removed are 1.12, 1.02 and 0.94 for samples Fe600, F700 and Fe800, respectively, which are below the theoretical value of 1.33 required for the complete reduction into metallic Fe^0. This finding would suggest that the reduction into metallic iron is not quantitative or even that FeO and Fe^0 phases might coexist. It has been suggested that FeO (wurzite) is unstable and decomposes into metallic Fe and magnetite. Perhaps the most relevant aspect of these profiles is the shift of this second temperature reduction process in Fe900 and Fe930 towards higher temperatures. Indeed. it has been reported that either $Fe_{1-x}ZrO_3$ (perovskite- or ilmenite-related phase) with Fe mostly in the ferrous state, or $Fe_{2-x}Zr_2O_7$ (pyrochlore-type compound) with Fe predominantly in the ferric state could be developed at such high temperatures [32]. The latter is more likely in view of the valence state of iron in the Fe_2O_3-ZrO_2 solid solution according to Mössbauer spectroscopy [33]. Thus, the $Fe^{3+/}Fe^{2+}$ ions located at the interface of ZrO_2 and Fe oxides in Fe900 and Fe930 samples might well be strongly stabilized by forming certain mixed oxides (pyrochlore or defective perovskite) which are more difficult to reduce.

5.3.3. XRD of catalyst precursors

The crystalline structure of the Fe/ZrO_2 catalysts pretreated in a hydrogen atmosphere was revealed by X-ray diffraction. In order to study the thermal stability of the support, pure ZrO_2 (substrate) was also pretreated under similar conditions to those employed with Fe/ZrO_2 catalysts at different calcination temperatures in the range between 600 and 930°C at different periods of pretreatment under a hydrogen environment. The zirconium oxide phase composition obtained from the X-ray diffraction patterns of all series pretreated with hydrogen at different pretreatment temperatures was the cubic-ZrO_2 crystalline phase, and it was found that the cubic-ZrO_2 crystalline phase once formed is stable in the thermal pretreatment range of this study (results not shown).

The X-ray diffraction patterns for the reduced Fe/ZrO_2 catalysts as a function of the reduction temperature and duration of the reduction treatment are shown in Figure 3. The X-ray diffraction patterns of all Fe-supported catalysts revealed no discernible diffraction peaks for hematite iron oxide phase or magnetite phase. Diffraction lines of cubic-ZrO_2 and metallic (Fe^0) crystalline phases were detected. This finding indicates that all iron oxide phases reduced into metallic phase during the treatment under a hydrogen environment. It is worth mentioning that for the Fe-supported catalysts pretreated at low temperature (below 800°C), no diffraction peaks originated from any oxide or metal phase were recorded. This observation indicates that the samples pretreated at low temperature contain essentially amorphous iron phases. Presumably, the crystallite size is below the detection limit of the XRD technique, whereas in the same samples pretreated at high temperature (higher than 800°C), a new intermetallic phase is observed comprising hexagonal $ZrFe_2$ phase and tetragonal Zr_2Fe phase [34, 35].

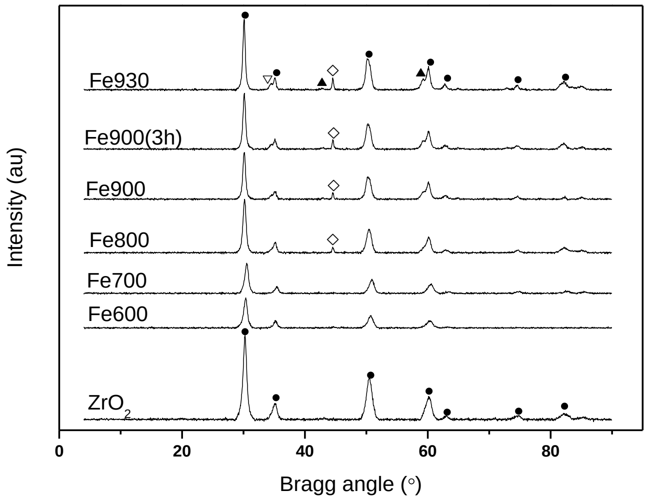

Figure 3. X-ray diffraction profiles of the catalysts. (◊) Fe; (●) ZrO_2; (▽) $ZrFe_2$ (hexagonal) and (▲) Zr_2Fe (tetragonal).

5.3.4. Laser Raman spectroscopy

Laser Raman spectroscopy (LRS) is an extremely sensitive technique to identify phase composition in many transition metal oxides. Therefore, identification of phases present in reduced Fe/ZrO_2 catalysts and used catalysts was carried out by LRS. The normalized Raman spectra of pretreated catalysts in hydrogen environment are shown in Figure 4. It can be seen that the Raman spectrum of fresh samples consisted of peaks located at 147, 270, 317, 461 and 660 cm^{-1}. The first three of these bands are characteristic of the ZrO_2 [36, 37], while the peak at 660 cm^{-1} belongs to the magnetite phase (Fe_3O_4) [38, 39]. It is worth mentioning that in the Raman line located at 461 cm^{-1} are overlapping contributions of both ZrO_2 and Fe_3O_4 phases [37, 40]. It is worth mentioning here that all the catalysts were passivated (by ~ 1% O_2/He in ambient conditions) after the pre-treatment in H_2 at relative high temperatures. While passivation preserves the bulk structure of the catalyst as stated that according to XRD metallic iron is present, the surface layer that contains the active catalyst would be oxidized during the transfer of the sample from the pre-reduction reactor to the characterization instruments, as proved by TPR and Raman results.

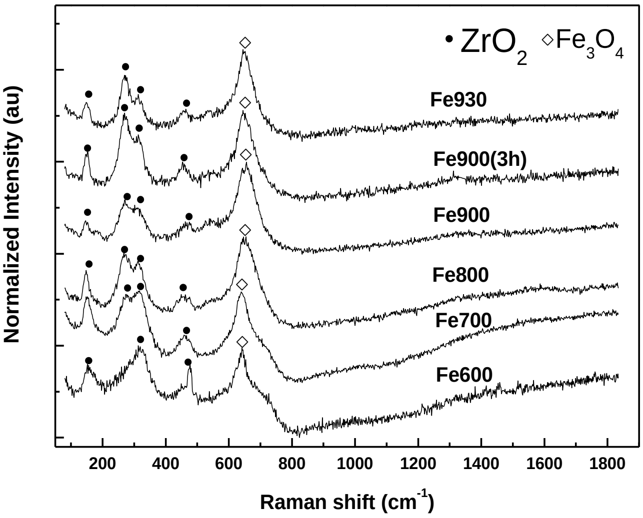

Figure 4. Raman spectrum normalized of the calcined catalysts in pure hydrogen at different calcination temperatures. (◊) Fe_3O_4 and (●) ZrO_2.

The used catalysts via Fischer-Tropsch synthesis reaction were further characterized by Laser Raman spectroscopy with the aim of gaining information about possible changes in catalyst structure and also on the formation of graphite carbonaceous structures formed on the Fe/ZrO$_2$ catalysts during on stream operation. From the Raman spectra for the used catalysts (spectra not shown), there is no spectra corresponding to oxide phases were detected. Apparently, exposure of the Fe/ZrO$_2$ catalysts to the reaction mixture for long periods on stream resulted in a change not only of the supported phases but also to carbide formation. Reduction and carburization of the iron phases during reaction gave rise to an amorphous carbon phase.

Besides the identification of metal oxide phases present on the catalyst surface, Raman spectroscopy has often been used to monitor the appearance of graphitic structures in the region 1330-1600 cm^{-1} [38, 41-43]. From the Raman spectra of catalysts maintained for 60 h on stream (data not shown), there is no bands belonging to graphitic structures were detected for each catalyst. This observation indicates that coke, if present, must be present in an amorphous state. As can be seen in the section on catalytic activity below, these catalysts are highly stable within the explored time on-stream of 60 h; consequently, no carbon deposits have been observed.

5.3.5. X-ray Photoelectron Spectroscopy (XPS)

X-ray photoelectron spectroscopy has been used with the aim to determine the nature of surface species, relative concentration of the reduced Fe/ZrO_2 catalysts and changes in dispersion of the iron oxides brought about by thermal treatments. Catalyst precursors Fe600 and Fe900 were selected to monitor the carburization process of oxide iron species. For each sample, the Fe 2p, Zr 3d and O 1s core-level spectra were recorded. In order to have clear picture of the catalysts' surfaces in the state before starting the FTS reaction and after activation pretreatment process, the XPS experiment was obtained under similar pretreatment conditions.

The Fe 2p and C 1s core-level spectra of samples Fe600 and Fe900 are displayed in Figures 5 and the corresponding binding energy values are compiled in Table 2. As both Fe2$p_{3/2}$ and Fe2$p_{1/2}$ components of the Fe 2p are a little asymmetrical, a peak deconvolution procedure using two doublets was applied. On looking only at the most intense peak (Fe 2$p_{3/2}$), two components are observed whose maximums appear at a binding energy of 707.2 eV and 710.4 eV. The minor component located at 707.2 eV has often been assigned to iron carbide species [44] whereas the major component positioned at 710.4 eV comes from oxidic Fe^{3+}/Fe^{2+} species. It is also observed that the intensity of the doublet placed at the lower binding energy (707.2 eV) is rather low in the sample Fe600 (Figure 5A) and rises with increasing temperature (Fe 900) (Figure 5B). This finding indicates that the extent of iron carbidation in sample Fe900 with respect its Fe600 counterpart increases with greater iron crystallite size. This result indicates that the extent of the reduction and carburization steps increases with an increase of crystallite (Fe900). Further support in favor of the enhancement of reduction and carburization steps in catalyst F900 with respect to Fe600 comes from the C 1s line. The C 1s spectra of carburized Fe600 and F900 catalysts are displayed in Figure 5 C and D, respectively. The C1s profiles of both samples were fitted into two components:

a major component at 284.8 eV and a minor one at 282.7 eV. The component at 284.8 eV is also observed on the non-activated samples and accounts for the adventitious carbon (C-C/C-H) present on the sample as a consequence of sample handling and storage. However, the component at 282.7 eV, which is only detected in activated samples, is characteristic of reduced/carbided C-Fe structures [44]. Consistently with what was observed in the Fe $2p_{3/2}$ emission, the intensity of the component at 282.7 eV increased in sample Fe900 with respect to its Fe600 counterpart.

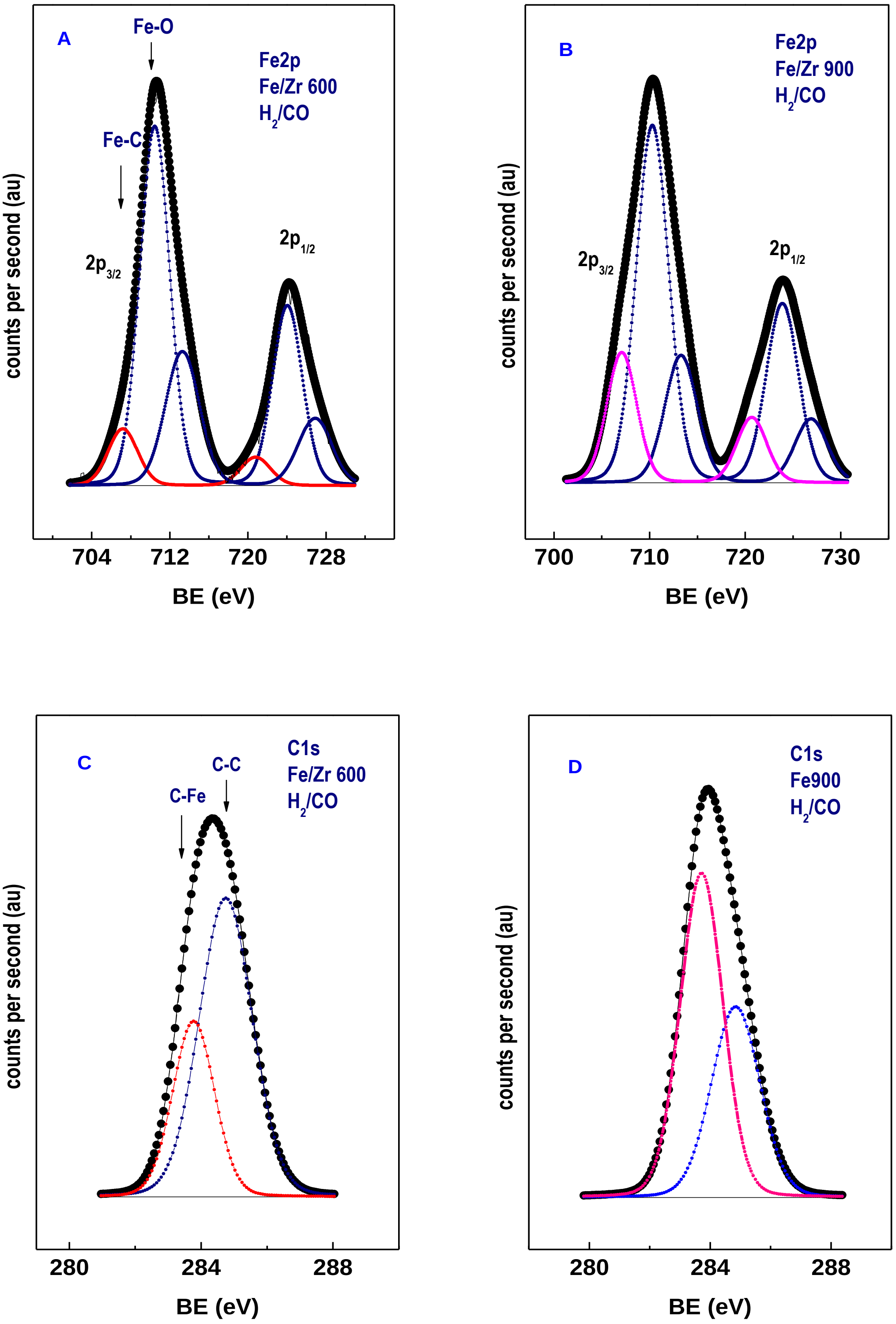

Figure 5. Fe2p and C1s core-level spectra of (A) Fe2p spectra for Fe600, (B) Fe2p spectra for Fe900, (C) C1s spectra for Fe600 and (D) C1s spectra for Fe900. These samples activated under a syngas mixture $H_2/CO/N_2$ = 62/31/6 (molar) mixture at 300 °C for 1h.

Table 2. Binding energies (eV) of core levels of Fe/ZrO$_2$ catalysts thermal treated at 600 ºC or 900 ºC and under exposed to syngas mixture (H_2/CO = 2)

	Zr3d$_{5/2}$	**O1s**	**Fe2p$_{3/2}$**	**C1s**	**Fe/Zr at**	**Fe/C at****
Fe600 (H_2/CO)	182.2	529.9	707.2 (10) 710.4 (90)	282.7 (14)* 284.8 (86)	0.123	1.52
Fe900 (H_2/CO)	182.2	529.9	707.1 (20) 710.3 (80)	282.6 (63)* 284.8 (37)	0.126	1.98

Fe600 and Fe900 catalyst precursors were exposed to a H_2/CO = 2 mixture (1 bar) within the pretreatment chamber of XPS machine; * carbide carbon ; ** only C species belonging to carbide carbon and Fe atoms in a carbide environment were considered

An estimate of the relative dispersion of iron species on the ZrO$_2$ surface was obtained by calculating the atomic Fe/Zr ratio for Fe600 and Fe900 catalysts pretreated under the H_2/CO = 2:1 (molar) within the XPS pretreatment chamber (Table 2). The surface Fe/Zr ratios recorded for Fe600 and F900 samples are 0.123 and 0.126, respectively. The similar values of the Fe/Zr ratio for the two samples suggest that the dispersion of iron/carbide phases does not appear to be altered upon increasing pretreatment temperature from 600ºC to 900ºC. Besides, the atomic Fe_{car}/C_{car} ratio was also computed. In this calculation only the C species belonging to carbide carbon and Fe atoms in a carbide environment were considered. The value of Fe_{car}/C_{car} ratio reached 1.52 for Fe600 and increased up to 1.98. As these values reflect the stoichiometry of surface carbides developed during activation step [45, 46], it is clear that the two catalysts became carbided during the activation pretreatment. Finally, it can be said that, under the activation conditions selected in this work, carbidation is only partial. Thus, magnetite (Fe_3O_4) and some form(s) of iron carbides (Fe_xC) were developed during activation. Most of them have been proposed at some time as the active Fe structure for FTS [47].

5.3.6. Catalytic performance

The FTS performance of the Fe/ZrO_2 catalysts was evaluated in a fixed bed reactor at 300°C, 20 bar under synthesis gas (H_2/CO = 2) and GHSV = 0.0021 L/g_{cat}.s. The effects of H_2 treatment temperatures and duration of the treatment on CO conversion rate and product selectivity are summarized in Table 3. The FTS catalytic activity, expressed as the rate CO conversion of Fe/ZrO_2 catalysts is clearly dependent on the pre-reduction temperature. Steady-state CO conversion rates increase on raising pre-reduction temperature from 600°C up to 900°C and then drop at higher treatment temperature and exposure time. These results unambiguously confirm a definite size-dependent FTS reaction; the optimum performance is attained with the Fe/ZrO_2 catalyst whose iron crystallite size is 7 nm. Iron clusters smaller than 7 nm in size show low CO conversion due to the fact that metal-support interaction is so strong, leading to inhibition of the reduction and carburization degree of the iron oxide precursor. This means that a fraction of iron still remains in the oxide state on the support surface while the rest is in the metallic and carbide phases. Moreover, smaller particles with high surface area are susceptible to being oxidized by water produced during the FTS reaction, and thus eventually losing these active sites [48]. Due to water gas shift (WGS) reaction, both the CO_2 selectivity and CO conversion follow the same trend as shown in Table 3. It is worth mentioning that due to disparity in the catalytic performance activity between different iron particle sizes, the cluster size of iron oxide has a significant impact on catalytic activity, on the interaction between iron oxide and support, and on the extent of reduction and carburization in iron oxide species.

Table 3. CO conversion and selectivity of hydrocarbons including oxygenated, CO_2 and olefins to paraffins ratio during FTS reaction

Catalyst	x_{CO} **(%)**	**Products selectivity %**					**C=C/C-C ratio**
		CO_2	**CH_4**	**C_2-C_4**	**C_5^+**	**Oxy**	
Fe600	6	10	45.9	44.1	7.1	2.9	0.1
Fe700	13	13	41.5	47.2	8.7	2.6	0.1
Fe800	32	16.7	32.8	50.4	13.7	3.1	0.1
Fe900	36	19.7	34.3	50.3	12.3	3.2	0.2
Fe900(3h)	30	16.4	32.5	51.9	12.9	2.7	0.1
Fe930	19	12	35.7	49.6	12.7	2	0.1

Reaction conditions: T = 300 °C; P = 20 bar; GHSV = 0.0021 (L/g_{cat}.s); feed composition (H_2/CO/N_2) = 62/31/7; mol %)

Normalized CO conversion rates during FTS reaction as a function of the calcination temperature of Fe/ZrO$_2$ catalysts are illustrated in Figure 6. Also, Table 3 shows the products' selectivity including oxygenated components and the $C^=$/C ratio. The data displayed in Figure 6 reveal that CO conversion rates increase from 0.05 (Fe600) to 0.35 molCO/g_{Fe}/h (Fe900) when the iron particle size increases due to improved reduction and carburization degree for iron oxide species. Furthermore, on increasing the treatment temperature or exposure period, a decrease of the CO conversion rates was observed, probably due to the appearance of a new intermetallic phase such as $ZrFe_2$ and Zr_2Fe phase, as shown by XRD, with a subsequent drop in the number of active sites.

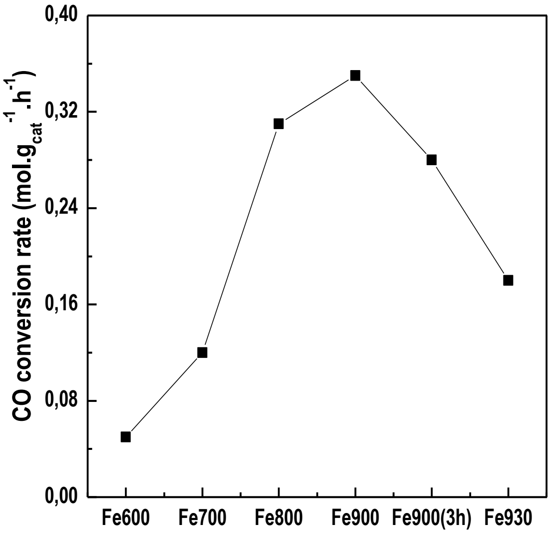

Figure 6. CO conversion rate of catalysts. Reaction conditions: T = 300 °C; P = 20 bar; GHSV = 0.0021 (L/gcat.s); feed composition (H_2/CO/N_2) = 62/31/7; mol %)

Figure 7 shows the hydrocarbons formation selectivity (C_1, C_2-C_4, and C_5^+) during FTS reaction for Fe/ZrO_2 catalysts as a function of the H_2 treatment temperature and the duration of the treatment. It can be seen that methane selectivity of Fe/ZrO_2 catalyst decreases with an increase in the H_2 treatment temperature from 600 to 930°C, which is opposed to the trend observed in higher hydrocarbons selectivity (C_5^+). There is no significant effect of the H_2 treatment temperature on the light chain hydrocarbon selectivity (C_2-C_4), and more specifically for the higher pretreatment and duration of the treatment, while the major impact for the particles dimension on C_2-C_4 selectivity seems clearly to be on the small cluster dimension, which is where the C_2-C_4 selectivity increases with larger Fe particle size. It is worth mentioning that the light hydrocarbons (C_2-C_4) are the majority of hydrocarbons selectivity. The increase in high molecular weight hydrocarbon selectivity by increasing the iron oxide cluster size could be attributed to easy activation and rapid movement leading to easy reaction with the adsorbed CO molecules on high particle size iron oxide. The high selectivity to CH_4 recorded in the tendency of catalysts with small iron particle size to increase methane selectivity indicates that dissociated hydrogen is present on the catalyst surface, due to the catalyst with smaller cluster dimension having a higher penchant for hydrogen adsorption rather than dissociative adsorbed CO molecules and a greater population of hydrogen species on the surface. The huge amount of dissociative hydrogen present on the catalyst surface is led, in turn, to hydrogenate into methane [12, 13, 49, 50]. Our results are consistent with a recent report that shows that very small particle size iron oxide <6.1 nm (5 wt.% Fe/Al_2O_3 catalysts, 280°C, 10 bar, H_2/CO/Ar = 63.2/31.3/5.5; mol%) displays high methane selectivity and low FTS activity per unit metal site due to structure sensitive FTS reaction [50]. Also, a similar behavior for Co particle size was found by other authors [13], who have shown that the small Co particles (1-22 wt.% Co/carbon nanofibers catalyst, 210°C, 35 bar, H_2/CO=2) have low FTS activity and high CH_4 selectivity.

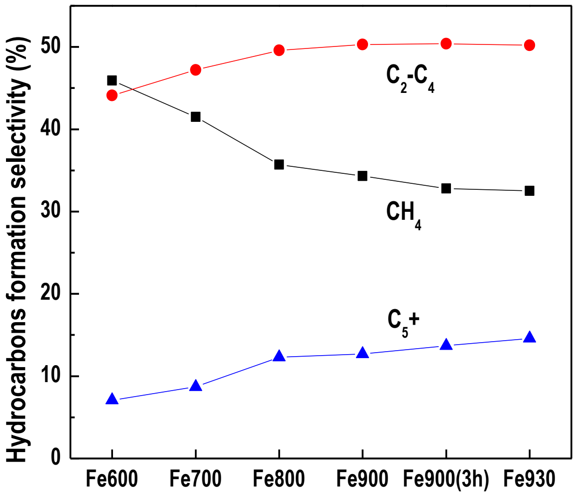

Figure 7. Hydrocarbons selectivity during FTS reaction for all catalysts. Reaction conditions: T = 300 °C; P = 20 bar; GHSV = 0.0021 (L/gcat.s); feed composition (H_2/CO/N_2) = 62/31/7 mol %

It is established that FTS catalysts are deactivated during on-stream operation. This is due to the fact that different phenomena, such as sintering of iron particles, coke formation, poison deposition and distribution of iron phases of the iron-based catalysts, take place during on-stream operation [41, 51, 52]. Thus, the CO conversion of all samples with different H_2 treatment and duration of the treatment was monitored as a function of the time on-stream. The activity profiles of all catalysts are displayed in

Figure 8. Although the active phase for the FTS reaction using iron catalysts is still under debate, it has been argued that the oxidation of the metallic Fe and/or the Fe carbide phases is one of the principal factors responsible for catalyst deactivation [41, 53]. The results reported in Figure 8 indicate clearly that the catalysts containing intermetallic $ZrFe_2$ and Zr_2Fe phases are more active than those in which these phases are not detected. The increase in activity of these catalysts containing $ZrFe_2$ and Zr_2Fe phases is suggested to be associated to development of another highly active phase during on-stream operation.

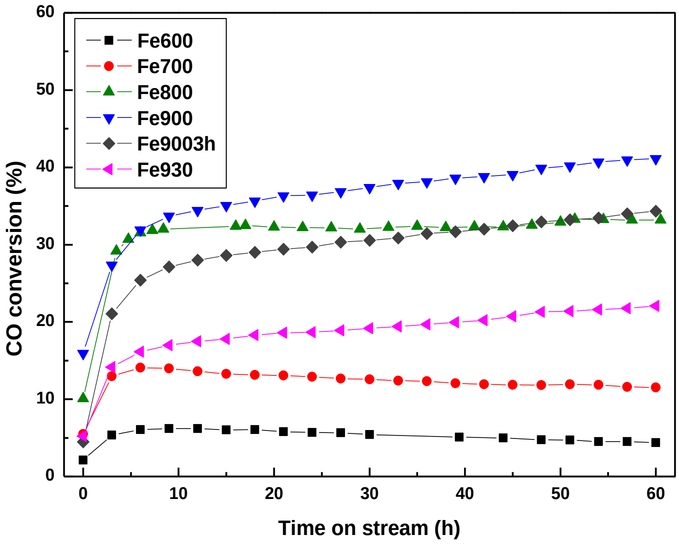

Figure 8. Normalized CO conversion rates during FTS reaction for all catalysts. Reaction conditions: T = 300 °C; P = 20 bar; GHSV = 0.0021 (L/gcat.s); feed composition ($H_2/CO/N_2$) = 62/31/7; mol %)

The continuous increase of CO conversion rate is probably attributed to the appearance of some layers of the intermetallic phase on the surface of the catalysts. This led to covering and isolating the active phase of iron species which detract from the chance of contact by the reactant material with the active phase compounds of the reaction. The XRD patterns of some representative used catalysts are showed in Figure 9. These patterns show diffraction peaks at 30.2°, 35°, 50.4°, 60°, 62.7°, 74°, 82.4° and 85° assigned to ZrO2, which are in good agreement with the recorded values of JCPDS

File No. 00-003-0640. The other intensive diffraction peaks at 20.9° and 26.7° and small traces peaks at relatively high 2 theta characteristic to Hexagonal Quartz (SiO_2) are in agreement with the reference pattern: 01-085-0930. No diffraction patterns were detected for iron oxides or iron carbides as the active sites for FT reaction, which is apparently due to the iron species being amorphous and highly dispersed on the nano zirconia oxide particles or smaller than the detection limit of this technique (i.e., below 4 nm) [54].

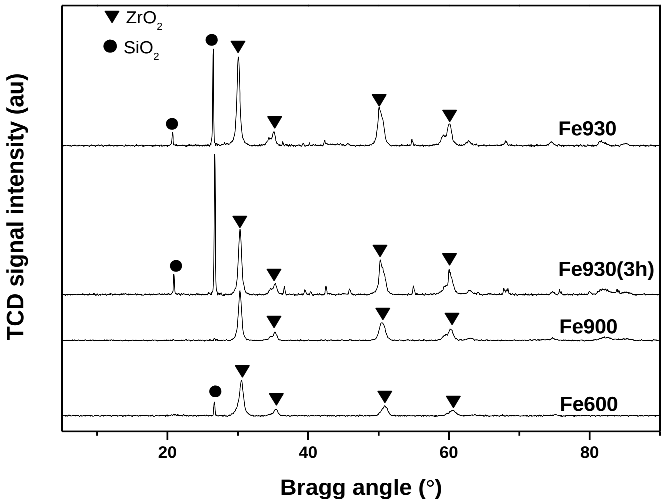

Figure 9. XRD patterns for the used catalysts for FTS reaction. Reaction conditions: *T* = 300 °C; P = 20 bar; GHSV = 0.0021 (L/g_{cat}.s); feed composition ($H_2/CO/N_2$) = 62/31/7; mol %) for 72h. (▼) ZrO_2; (● and all small traces peaks) SiO_2.

5.4. Conclusion

The Fe/ZrO_2 catalysts prepared by conventional incipient wetness impregnation method were investigated for the FTS. It is noticed that size of iron oxide particles play an important role in the catalyst reduction degree due to the effect that particle size of iron oxide has on the interaction strength between the support and iron catalyst. We have found that Fischer-Tropsch synthesis reaction with Fe-based catalysts is very significantly affected by iron oxide particle size. In the range of iron particle size in this study, the CO conversion rate during FTS increases as a function of the increase in particle size, reaching a maximum value for mean Fe particle size of approximately 7 nm.

Acknowledgments

M. Al-Dossary acknowledges gratefully financial support from SABIC, PhD student Program, Saudi Arabia). This research was supported by the Ministry of Science and Innovation (Spain) under grant ENE2010-21198-C04-01) and the Autonomous Government of Madrid, Madrid (Spain) under grant S2009ENE-1743 and S2013/MAE-2882.

5.5. References

[1] Q. Zhang, J. Kang,Y. Wang, ChemCatChem 2 (2010) 1030-1058.

[2] T. Herranz, S. Rojas, F. J. Pérez-Alonso, M. Ojeda, P. Terreros, J. L. G. Fierro, Appl. Catal. A: Gen. 308 (2006) 19-30.

[3] A.P. Steynberg, M.E. Dry, Eds., Fischer-Tropsch Technology, Stud. Surface Sci. Catal. 152, Elsevier, Amsterdam, 2004.

[4] E. L. Kunkes, D. A. Simonetti, R. M. West, J. C. Serrano-Ruiz, C. A. Gärtner, J. A. Dumesic, Science 322 (2008) 417-421.

[5] T. P. Vispute, H. Zhang, A. Sanna, R. Xiao,G. W. Huber, Science 330 (2010) 1222-1227.

[6] C. Wang, L. Xu,Q. Wang, J. Nat. Gas Chem. 12 (2003) 10-16.

[7] Y. Yang, H.-W. Xiang, L. Tian, H. Wang, C.-H. Zhang, Z.-C. Tao, Y.-Y. Xu, B. Zhong,Y.-W. Li, Appl. Catal. A: Gen. 284 (2005) 105-122.

[8] A. N. Pour, S. M. K. Shahri, Y. Zamani,A. Zamanian, J. Nat. Gas Chem. 19 (2010) 193-197.

[9] R. J. O'Brien, L. Xu, S. Bao, A. Raje, B. H. Davis, Appl. Catal. A: Gen. 196 (2000) 173-178.

[10] H. N. Pham, L. Nowicki, J. Xu, A. K. Datye, D. B. Bukur, C. Bartholomew, Ind. Eng. Chem. Res. 42 (2003) 4001-4008.

[11] R. A. van Santen, Acc. Chem. Res. 42 (2009) 57-66.

[12] G. L. Bezemer, J. H. Bitter, H. P. C. E. Kuipers, H. Oosterbeek, J. E. Holewijn, X. Xu, F. Kapteijn, A. J. van Dillen, K. P. de Jong, J. Am. Chem. Soc. 128 (2006) 3956-3964.

[13] J. P. den Breejen, P. B. Radstake, G. L. Bezemer, J. H. Bitter, V. Frøseth, A. Holmen, K. P. de Jong, J. Am. Chem. Soc. 131 (2009) 7197-7203.

[14] G. Prieto, A. Martínez, P. Concepción,R. Moreno-Tost, J. Catal. 266 (2009) 129-144.

[15] J. Gaube,H. F. Klein, J. Mol. Catal. A: Chem. 283 (2008) 60-68.

[16] E. Iglesia, S. L. Soled, R. A. Fiato, J. Catal. 137 (1992) 212-224.

[17] R. Oukaci, A. H. Singleton, J. G. Goodwin. Jr. Appl. Catal. A: Gen. 186 (1999) 129-144.

[18] A. M. Saib, M. Claeys, E. van Steen, Catal. Today 71 (2002) 395-402.

[19] A. N. Martínez, C. López, F. Márquez, I. Díaz, J. Catal. 220 (2003) 486-499.

[20] R. C. Reuel, C. H. Bartholomew, J. Catal. 85 (1984) 78-88.

[21] C. X. Xiao, Z. P. Cai, T. Wang, Y. Kou,N. Yan, Angew. Chem.-Int. Ed. 47 (2008) 746-749.

[22] J. Kang, S. Zhang, Q. Zhang,Y. Wang, Angew. Chem.-Int. Ed. 48 (2009) 2565-2568.

[23] F. J. Pérez-Alonso, M. L. Granados, M. Ojeda, T. Herranz, S. Rojas, P. Terreros, J. L. G. Fierro, M. Gracia, J. R. Gancedo, J. Phys. Chem. B 110 (2006) 23870-23880.

[24] F. Fischer,H. Tropsch, Brennstoff. Chem. 11 (1926) 489.

[25] F. R. van der Berg, PhD Thesis, Utrecht University, 2001.

[26] T. Herranz, S. Rojas, F. J. Pérez-Alonso, M. Ojeda, P. Terreros, J. L. G. Fierro, Appl. Catal. A: Gen. 311 (2006) 66-75.

[27] M. Qing, Y. Yang, B. Wu, H. Wang, H. Wang, J. Xu, C. Zhang, H. Xiang, Y. Li, Catal. Today 183 (2012) 79-87.

[28] C.-H. Zhang, H.-J. Wan, Y. Yang, H.-W. Xiang,Y.-W. Li, Catal. Commun. 7 (2006) 733-738.

[29] H.-J. Wan, B.-S. Wu, C.-H. Zhang, H.-W. Xiang, Y.-W. Li, B.-F. Xu,F. Yi, Catal. Commun. 8 (2007) 1538-1545.

[30] S.-H. Kang, J. Bae, P. S. Sai Prasad, K.-W. Jun, Catal. Lett. 125 (2008) 264-270.

[31] J. F. Bengoa, A. M. Alvarez, M. V. Cagnoli, N. G. Gallegos, S. G. Marchetti, Appl. Catal. A: Gen. 325 (2007) 68-75.

[32] M. L. Wu, D. Gan,P. Shen, Mater. Sci. Eng. A-Struct. Mater. Prop. Microstruct. Process. 297 (2001) 119-123.

[33] S. Popović, B. Grzˇeta, I. Czakó-Nagy, S. Musić, J. Alloy. Compd. 241 (1996) 10-15.

[34] S. F. Tikhov, A. E. Kuz'min, Y. N. Bespalko, V. I. Kurkin, V. A. Sadykov, E. I. Bogolepova, S. V. Tsybulya, A. V. Kalinkin, V. P. Mordovin, A. N. Salanov, V. I. Zaikovskii, A. A. Shavorsky, Stud. Surface Sci. Catal. 163 (2007) 153-175.

[35] A. E. Kuz'min, Y. N. Dyatlova, S. F. Tikhov, V. I. Kurkin, V. A. Sadykov, E. V. Slivinskii, E. I. Bogolepova, S. V. Tsybulya, V. B. Fenelonov, V. P. Mordovin, G. S. Litvak,A. N. Salanov, Kinet. Catal. 46 (2005) 743-751.

[36] C. Gionco, A. Battiato, E. Vittone, M. C. Paganini,E. Giamello, J. Solid State Chem. 201 (2013) 222-228.

[37] G. Štefanić, I. I. Štefanić, S. Musić,M. Ivanda, J. Mol. Struct. 993 (2011) 277-286.

[38] M. Ding, Y. Yang, B. Wu, J. Xu, C. Zhang, H. Xiang,Y. Li, J. Mol. Catal. A: Chem. 303 (2009) 65-71.

[39] M. Ding, Y. Yang, B. Wu, T. Wang, H. Xiang,Y. Li, Fuel Process. Technol. 92 (2011) 2353-2359.

[40] M. Ramalakshmi, P. Shakkthivel, M. Sundrarajan, S. M. Chen, Mater. Res. Bull. 48 (2013) 2758-2765.

[41] W. Ning, N. Koizumi, H. Chang, T. Mochizuki, T. Itoh, M. Yamada, Appl. Catal. A: Gen. 312 (2006) 35-44.

[42] C. Zhang, G. Zhao, K. Liu, Y. Yang, H. Xiang,Y. Li, J. Mol. Catal. A: Chem. 328 (2010) 35-43.

[43] S. Urbonaite, L. Hälldahl,G. Svensson, Carbon 46 (2008) 1942-1947.

[44] M. Al-Dossary, A. A. Ismail, J. L. G. Fierro, H. Bouzid,S. A. Al-Sayari, Appl. Catal. B: Environ. 165 (2015) 651-660.

[45] S. Li, G. D. Meitzner, E. Iglesia, J. Phys. Chem. B 105 (2001) 5743-5750.

[46] F. J. Perez-Alonso, T. Herranz, S. Rojas, M. Ojeda, M. Lopez Granados, P. Terreros, J. L. G. Fierro, M. Gracia, J. R. Gancedo, Green Chem. 9 (2007) 663-670.

[47] G. P. van der Laan, A. A. C. M. Beenackers, Catal. Rev.-Sci. Eng. 41 (1999) 255-318.

[48] E. van Steen, M. Claeys, M. E. Dry, J. van der Loosdrecht, E. L. Viljoen,J. L. Visagie, J. Phys. Chem. B 109 (2005) 3575-3577.

[49] N. G. Gallegos, A. M. Alvarez, M. V. Cagnoli, J. F. Bengoa, S. G. Marchetti, R. C. Mercader,A. A. Yeramian, J. Catal. 161 (1996) 132-142.

[50] J.-Y. Park, Y.-J. Lee, P. K. Khanna, K.-W. Jun, J. W. Bae,Y. H. Kim, J. Mol. Catal. A: Chem. 323 (2010) 84-90.

[51] S. A. Eliason,C. H. Bartholomew, Appl. Catal. A: Gen. 186 (1999) 229-243.

[52] A. Nakhaei Pour, M. R. Housaindokht, S. F. Tayyari, J. Zarkesh, M. R. Alaei, J. Mol. Catal. A: Chem. 330 (2010) 112-120.

[53] S. Li, R. J. O'Brien, G. D. Meitzner, H. Hamdeh, B. H. Davis,E. Iglesia, Appl. Catal. A: Gen. 219 (2001) 215-222.

[54] F. Fischer, H. Tropsch, Über die Herstellung synthetischer Ölgemische (Synthol) durch Aufbau aus Kohlenoxyd und Wasserstoff. 4 (1923) 276.

Chapter 6: Cu-Promoted Fe_2O_3/MgO-Based Fischer-Tropsch Catalysts of Biomass-Derived Syngas

6

Cu-Promoted Fe_2O_3/MgO-Based Fischer-Tropsch Catalysts of Biomass-Derived Syngas

M. Al-Dossary1*, J.L.G. Fierro1, and J.J. Spivey2
1Institute of Catalysis and Petrochemistry, CSIC, Marie Curie 2, Cantoblanco, 28049 Madrid, Spain
2Department of Chemical Engineering, Louisiana State University, Baton Rouge, LA 70803, United State

E-mail address: ma99sa@hotmail.com

Abstract

A series of precipitated Fe_2O_3/MgO catalysts incorporated with the copper promoter were prepared by the combination of coprecipitation and incipient witness impregnation methods. The catalysts were characterized by N_2-adsorption-desorption isotherms, X-ray diffraction (XRD), H_2 temperature programmed reduction (H_2-TPR), CO temperature programmed desorption (CO-TPD), O_2 temperature programmed oxidation (O_2-TPO), laser Raman spectroscopy (LRS), and X-ray absorption near edge structure (XANES). The Fischer-Tropsch (FT) synthesis reaction of the catalysts was also performed in a fixed bed reactor using different H_2/CO ratios (H_2/CO = 1 or 2). The characterization results indicated that Mg increases the BET surface area of precipitated oxide precursors by inhibiting sintering during thermal treatment, and leads to the formation of the relatively smaller iron crystallite size. Cu increases the rate of Fe_2O_3 reduction by providing H_2 dissociation sites. The content of iron carbide phases during TPR process in the synthesis gas increases with the increase of copper content and reaches a maximum for the Cu/Fe atom ratio of 0.02. The optimal catalyst with Cu/Fe = 0.02 has high activity. A maximum in the catalytic activity and methane selectivity was obtained for the synthesis gas ratio of 2 (H_2/CO = 2).

Keywords: Fischer-Tropsch synthesis; iron-based catalysts; promoters; magnesium; copper

6.1. Introduction

Fischer-Tropsch synthesis (FTS) has been widely practiced for the conversion of CO-rich syngas based on various Fe-based catalysts to produce liquid fuels.[1-3] Like biomass, coal produces syngas with a comparable H_2/CO ratio of ~0.7/1.[4] However, there are two differences between air-blown gasification of biomass and coal. First, despite their similar H_2/CO concentrations, air-blown gasified biomass-derived syngas is greatly diluted by nitrogen. Second, biomass-derived syngas is often rich in CO_2, typically in concentrations of 10-20%. High levels of both nitrogen and CO_2 can affect the activity and selectivity of Fe-based FTS conventional catalysts.[5, 6]

Specifically, Mg promoters have been found to increase FTS activity, stability, and particularly to increase the C_5-C_{11} chain selectivity. Further Mg promoters suppress methane formation, facilitate the reduction and carburization extent and increase BET specific area.[7, 8] However, there is little work reported on adding magnesium as a promoter to improve the catalytic performance of iron-based catalysts. It has been shown by Yang *et al.* [7] that adding an appropriate amount of magnesium to an iron-based FTS catalyst can improve the activity and stability of the catalysts, enhance the selectivity to C5-C11 and increase the space time yield of C5+ hydrocarbon. The magnesium promoter can also slightly inhibit the activity of water gas shift reaction, resulting in a drop of CO_2 selectivity and therefore increase of carbon utilization. Gallegos *et al.* [9] studied the Fe/SiO_2-MgO catalysts for FTS reaction. The results showed that the rate of total hydrocarbon formation increased with the increase of the MgO content. They also stated that the addition of MgO increases the selectivity to olefins and suppresses the formation of methane.

In the presence of high levels of CO_2 in biomass-derived syngas, the Fe-based catalysts used in FTS may be exposed to deactivation by oxidation of the active iron carbide phase. [10, 11] So in order to form the active reduced iron carbide catalyst, in this study we used the well-documented Cu as promoter to increase the extent of the reduction and carburization of the iron oxide precursors to these catalysts.[12, 13]

In light of the above, the present work was undertaken with the aim to study the effect of Cu promotion on the physical and chemical properties of Fe-Mg-based catalysts to convert biomass-derived syngas from wood chips produced in an air-blown down-draft gasifier. [6, 14] To achieve this objective, a series of iron-magnesium catalysts promoted with copper have been prepared by means of coprecipitation and incipient wetness impregnation techniques. Various characterization techniques were used, such as nitrogen physisorption, TPR, XRD, CO-TPD, O_2-TPO, laser Raman spectroscopy, and in situ XANES. The FTS catalytic performance of catalysts was measured in a fixed bed reactor under typical FTS reaction conditions.

6.2. Catalyst preparation

The catalysts used in this study were prepared by the coprecipitated and incipient wetness impregnation methods. Fe_2O_3-MgO oxide catalysts were prepared by coprecipitation of oxyhydroxides from a mixed solution of Fe and Mg nitrates using ammonium carbonate as a precipitating agent. A solution of iron(III) nitrate nonahydrate (Aldrich, > = 98%, 3.0 M) and magnesium(II) nitrate hexahydrate (Aldrich, 99.00%, 1.4 M) at a Mg/Fe atomic ratio of 0.1 was added into a large flask containing deionized water (ca. 100 cm^3) at 80°C at a rate of 120 cm^3/h using a liquid pump. A solution of $(NH_4)_2CO_3$ (Aldrich, 99.9%, 1.0 M) was introduced simultaneously into this flask and its rate was controlled in order to keep the pH of the slurry at a constant value of 7.0 ± 0.1, measured by a pH meter (Oakton, EUTECH Instruments). The precipitate (about 10 g) was washed with deionized water several times. Samples were treated in stagnant ambient air at 120°C overnight. The dried precursors were then calcined in ambient air at 350°C for periods of time of 1 h. The copper was introduced onto these Fe_2O_3-MgO oxide powders by the incipient wetness impregnation method with aqueous solutions of copper(II) nitrate hemipentahydrate (Aldrich, 98%) at the concentrations required to obtain the desired Cu/Fe atomic ratios (Cu/Fe = 0.01, 0.02, and 0.03). These impregnate precursors were then treated in stagnant ambient air at 120°C. Finally, aliquots of each dried precipitate were calcined in ambient air at temperatures of 400°C for time periods of 4 h.

These samples are referred to as Fe/Mg, Fe/Mg/Cu1, Fe/Mg/Cu2, and Fe/Mg/Cu3. All samples were pressed into pellets, crushed, and sieved to retain 212 - 315 μm particles.

6.3. Characterization Techniques

6.3.1. Nitrogen adsorption-desorption isotherms

Nitrogen adsorption isotherms were recorded at the temperature of liquid nitrogen (-196°C), using a Micromeritics ASAP 2000 apparatus. The samples were degassed at 140°C for 16 h prior to the determination of the adsorption isotherm.[15]

6.3.2. Temperature Programmed Reduction (TPR)

TPR experiments were carried out on an Altamira AMI-200 reactor. 30 mg of freshly calcined catalysts was first dried in 30 cm^3/min He flow up to 300℃ for 30 min at a ramping rate of 10°C/min. After cooling down to room temperature the catalyst was exposed to 30 cm^3/min of 10% H_2/Ar flow, and the data were recorded in a temperature range of 100-950°C with a ramp rate of 10°C/min for all samples. The consumption of H_2 was monitored by a thermal conductivity detector (TCD). To enable quantitative H_2 consumption measurement, the TCD signal was calibrated with a silver oxide standard.

6.3.3. X-ray Diffraction (XRD)

XRD experiments were carried out using a Bruker/Siemens D5000 system for fresh synthesized Fe-based catalysts. The system had a ceramic X-ray tube with Cu Kα radiation operating at a wavelength of 1.54184 Å. The tube operated at a voltage of 40 kV with a current of 30 mA. The angle of divergence slit for the incident X-ray beam was set to 1° and the antiscatter slit was set at 0.5°. XRD experiments were conducted *ex situ* and four different diffractogram sets were obtained using 2θ variation from 4º to 90º and at a constant sweep rate of 0.02º/min. All the spectra were analyzed by Jade (v. 9) software.

6.3.4. Temperature Programmed Desorption (TPD)

CO-TPD was used to measure the behavior of CO adsorption and desorption on carburized catalysts. CO-TPD experiments were carried out on an Altamira AMI-200 reactor. First, 150 mg of freshly calcined catalysts was dried in 50 cm^3/min of helium at up to 300°C for 30 min with a ramping rate of 10°C/min. After cooling down to room temperature, the catalyst was reduced and carburized by 50 cm^3/min of 5% CO/95% He at 300°C with a ramping rate of 5°C/min for 5 h. After reduction, the catalysts were cooled down to room temperature with 50 cm^3/min of 5% CO/95% He and switched to 50 cm^3/min of pure helium until the CO signal baseline leveled off. Then, the temperature was increased up to 950°C as the temperature ramped at 5°C/min for all samples. All the TPD profiles were recorded in an on-line mass spectrometer (MS, Dycor ProMaxion, Ametek Process Instruments) located down-stream of the reactor. The TPD patterns were recorded by following the mass signal of 28 for CO in the outlet gas. To enable quantitative measurements, the CO mass signal intensities were calibrated using a He-based standard mixture containing 5% of CO.

6.3.5. Temperature Programmed Oxidation (TPO)

O_2-TPO simply measures oxidation of the Fe carbide, as well as any coke formation on the catalysts. O_2-TPO was applied to the same samples after the CO-TPD experiment. Accordingly, the catalyst-bed was first cooled down to room temperature under pure He flowing at 50 cm^3/min, and then the sample was heated in a gas mixture of 5%O_2/He flowing at 50 cm^3/min with a ramping rate of 5°C/min from room temperature to 950°C. All the TPO profiles were recorded in an on-line mass spectrometer (MS, Dycor ProMaxion, Ametek Process Instruments) located down-stream of the reactor. To enable the quantitative measurement of coke formation, the CO and CO_2 mass signal intensities were calibrated using a He-based standard mixture containing 5% of CO and 10% of CO_2.

6.3.6. Raman Microscope Spectrometer

Raman spectra were recorded with a Renishaw inVia Raman Microscope spectrometer equipped with a laser beam emitting at 532 nm, and 100 mW output power. The photons scattered by the sample were dispersed by an 1800 lines/mm grating monochromator and simultaneously collected on a CCD camera. The collection optic was set at 50x objective. The samples selected for the Raman study were both calcined and used samples after FTS reaction. The calcined samples were directly mounted into the analysis chamber of the Raman Microscope spectrometer without further treatment, whereas the used samples, recovered from the FTS reactor, were kept in hydrocarbon material to avoid exposure to air-oxidation while being transferred from the FTS reactor to the analysis chamber. Therefore, the used samples were pretreated in a special cell to dry them from hydrocarbon products before recording the Raman spectra. The pretreatment procedure consisted of a 20 cm^3/min H_2 flow over the catalyst, increasing the temperature from ambient temperature to 300°C at a ramping rate of 10°*C*/min and holding it for 30 min at 300°C.

6.3.7. In situ X-ray absorption near edge structure (XANES)

In-situ TPR XANES measurements for Fe K-edge were collected on the Double Crystal Monochromator (DCM) beamline at LSU's synchrotron facility (The J. Bennett Johnston, Sr. Center for Advanced Microstructures and Devices (CAMD), Baton Rouge, Louisiana, USA). The samples were prepared to obtain the optimum step-size [ln (μ_0/μ) = 1.0-1.4], which was found to be approximately 20 mg of the catalysts mixed well with 40 mg of amorphous SiO_2 (99.9% metals basis, amorphous, Alfa Aesar) and loaded into a Lytle cell. The mixed sample was placed between two pieces of Kapton tapes, which was then made gas-tight after aluminum spacers were screwed into place. The syngas flow was maintained by rotameters (Model FM-1050, Matheson Trigas), the sample temperature was controlled by a Variac (10 amp, Model 3PN1010B, Staco) with a custom-built temperature controller (Omega CN7500 PID controller). To prevent the heating element from burning out, the furnace was purged by He. The syngas (16.5% CO, 33.0% H_2, 5.00% Ar, and balance He, Airgas) was caused to flow through the Lytle cell of approximately 12 cm^3 (using an ADM2000 Agilent flowmeter to measure the gas exit from the Lytle cell), whereas the exhaust gas was vented. The temperature was increased from room temperature to 362ºC at a ramping rate of 2ºC/min.

The XANES scans were collected during the ramping temperatures by using specific parameters summarized in Table 1. The DCM is used with Ge (220) crystal calibrated with a 7.5 μm thick α-Fe foil and to maintain the calibration, the foil reference of the element being measured was placed in the beam path after the transmission chamber while the scanned was in transmission mode. The synchrotron operates its storage ring with an electron energy of 1.3 GeV and a current typically between 100 mA and 230 mA.

Table 1. Fe K-edge XANES scanning parameters during TPR ramping temperature

	Fe K-edge
Fe K-edge energy	7.122 eV
Scan interval relative to edge	-50, -15, 50, 100
Energy step size (eV)	1, 0.5, 1
Integration time (s)	1

X-ray absorption spectra were obtained at the Fe K-edge of Fe/Mg/Cu. The Fe XANES were measured for reference compounds with known local structures, such as Fe_2O_3 (99.99% metals basis, Alfa Aesar), FeO (99.5% metals basis, Alfa Aesar), Fe_3O_4 (99.95% metals basis, Alfa Aesar), and a 7.5 μm thick α-Fe foil positioned after the transmission chamber for calibration purposes, and θ-Fe_3C standard which was synthesized using a similar procedure described elsewhere [12]. In brief, Fe_2O_3 (99.99% metal basis, Alfa Aesar) was pretreated during temperature programmed reduction by 99% CO from room temperature until 700°*C* at a ramping rate of 10°*C*/min. Prior to removing the resulting sample of θ-Fe_3C from the TPR reactor, the sample was passivated at room temperature by flowing 1% O_2/He for 1 h.

Athena software (v. 0.8.061) as well as IFEFFIT software was used to process and analyze the transmission data and linear combination fitting of the derivative of the normalized XANES spectra [16]. Prior to linear combination fitting (LCF), the K-edge energy of Fe foil reference (using the maximum of the first derivative of the Fe foil spectrum which was measured independently in each run) was shifted to Fe foil value (7122 eV). Each spectrum (including the standards) was calibrated according to the maximum of the first derivative of the Fe foil spectrum shift. After edge identification, the spectra were processed by subtraction of the pre-edge and determining the normalizing range. Then, we identified and quantified each spectra by comparing the LCF of its derivative against the reference standard derivative spectrum.

6.4. Catalytic Activity

The catalysts were tested in the CO hydrogenation reaction using a fixed-bed microreactor (stainless steel 316, 165 mm long and 8.5 mm ID). The reaction temperature was measured with a K-type thermocouple buried in the catalytic bed. The reactor was held within a furnace equipped with a temperature controller. All pipes after reactor outlet were kept at 130ºC. The reaction system was equipped with a stainless steel hot trap set at 110ºC in order to collect the heavier products (C_m hydrocarbons). Flow rates were controlled using Bronkhorst High-Tech Series mass flow controllers.

The calcined samples (500 mg, 0.212–0.315 mm particle size) were diluted with 1.5 g of silicon dioxide (sand SiO_2, Sigma Aldrich material) to avoid hot spots. First, the catalysts were activated *in situ* at 270°C (the temperature was increased at an initial rate of 10°C/min from room temperature to 150°C, reducing the heating rate to 1°C/min beyond 150°C until reaching the activation temperature of 270°C) and kept for 24 h in syngas ($31CO/62H_2/7N_2$, GHSV = 0.0083 L/g.s) at atmospheric pressure. The reactor was then cooled down under synthesis gas atmosphere to the reaction temperature (250ºC) and pressurized at 2.02 MPa. When the reactor reached the desired pressure, the ratio of the reactant was set based on the reaction condition required: either decreasing the H_2/CO ratio to 1/1 or keeping it similar to the synthesis gas ratio during activation process. CO hydrogenation then followed and catalyst performance was tested under steady-state conditions.

Analysis of reactant gases and products was performed on-line with a gas chromatograph (HP 6890 Plus). A Porapak Q (1/8" x 3 m) packed column connected to a thermal conductivity detector (TCD) was used to analyze the inorganic gases (H_2, N_2, CO, and CO_2) and water. Hydrocarbons and oxygenated compounds were analyzed with a DB-1 capillary column (60 m x 0.25 mm x 0.25 μm) connected to a flame ionization detector (FID). The following temperature program was used: -50ºC hold for 10 min, then a ramping of 10ºC/min up to 230ºC, and then keeping at this temperature for 20 min. Nitrogen was used as internal standard for chromatographic analyses. [15, 17, 18]

6.5. Results and Discussion

6.5.1. Textural Analysis.

The nitrogen adsorption-desorption isotherms of all copper promoted catalysts, including unpromoted catalysts, are shown in Figure 1. All samples displayed type IV isotherms, characteristic of mesoporous materials, in accordance with the IUPAC.[19, 20]

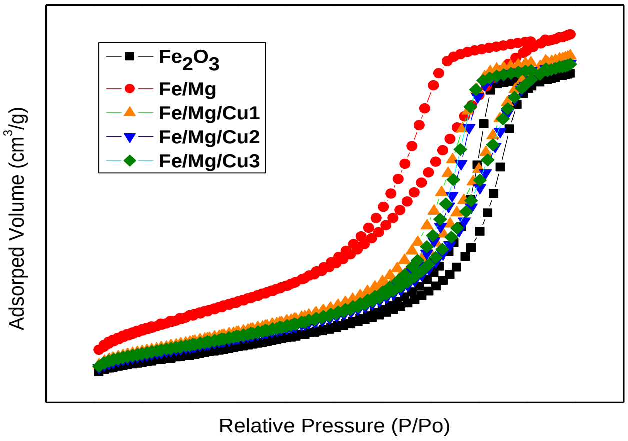

Figure 1. Nitrogen adsorption-desorption isotherms of the Fe_2O_3-MgO catalysts with different copper content also the precipitated pure iron oxide are included.

The BET surface area, pore volume, and pore diameter of the precipitated Fe_2O_3 and iron-magnesium promoted with different copper contents are shown in Table 2. The addition of magnesium to iron-based catalysts increases the BET area, whereas the addition of copper to Fe_2O_3-Mg catalysts decreases the BET area of the iron magnesium oxide catalyst. The effect of Mg for increasing the specific surface area in our study is consistent with others.[7, 21, 22] The BET surface areas of all the copper promoted catalysts are decreased from 120 m^2/g for Fe/Mg and fall in the range between 76 and 83 m^2/g. The decrease in the specific BET surface area after the addition of Cu could be due to possible agglomeration of iron precursor in the course of Cu incorporated and/or the calcination conditions. The Fe particle size increases with copper content.

Table 2. Textural properties of the Fe_2O_3-MgO catalysts with different copper content, also the precipitated pure iron oxide are included

Catalyst	**BET Surface Area (m^2/g)**	**Pore volume ($cm^3\ g^{-1}$)[a]**	**Pore diameter (nm)**	**Fe oxide particle size (nm)[b]**
Pure Fe	65.3	0.191	11.7	14.1
Fe/Mg	120	0.215	7.2	11.6
Fe/Mg/Cu1	82.7	0.202	9.7	14.0
Fe/Mg/Cu2	76.0	0.197	10.4	14.4
Fe/Mg/Cu3	77.7	0.197	10.1	14.3

[a] values of pore volume were calculated by BHJ method from desorption isotherm

[b] values of iron particle size were obtained from XRD by Scherrer equation

6.5.2. H_2-Temperature Programmed Reduction (TPR)

For Fe/Mg, Figure 2 shows two expected main reduction peaks at about 325ºC and 500ºC. The 325ºC peak can be deconvoluted into three peaks located at about 250ºC and 300ºC and one main peak located at 325ºC. The 250ºC peak probably corresponds to the reduction of surface Fe^{3+} to mixture of Fe^{3+} and Fe^{2+} (Fe_3O_4) while that at 300ºC corresponds to the reduction of α-Fe_2O_3 which interacts directly with MgO to Fe_3O_4. The 325ºC peak can be attributed to reduction of tridimensional α-Fe_2O_3 to Fe_3O_4.[7, 8, 23-25]

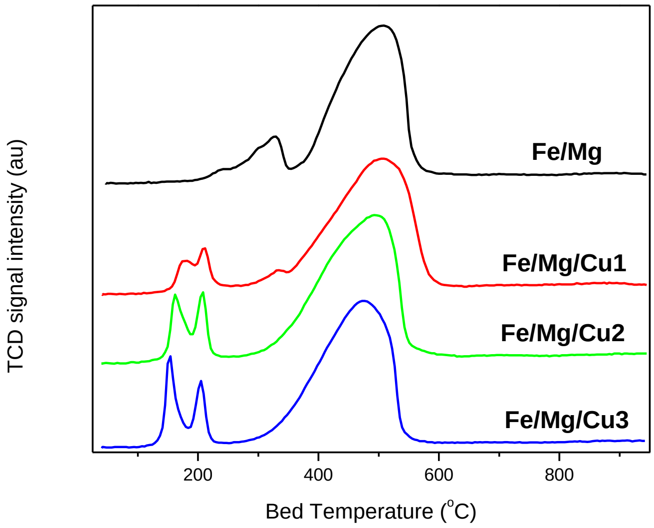

Figure2. H_2-TPR profiles of the Fe_2O_3-MgO catalysts with different copper content.

Figure 2 clearly shows that the each three Cu-promoted catalysts showed a twin TPR peak below 300ºC (at 175ºC and 210ºC) and one peak at around 500ºC. The 175ºC peak is attributed to the reduction of the solid solution of CuO and part of α-Fe_2O_3 to Cu and Fe_3O_4.[7, 26] The consistently increasing greater 175ºC peaks correspond to the higher copper content. The 210ºC peak is attributed to the reduction of the residual α-Fe_2O_3 to Fe_3O_4 which decreases from about 325ºC for unpromoted Fe/Mg (without Cu promotion) to 210ºC with Cu promotion, consistent with results shown by others.[7, 27] As copper crystallites nucleate during reduction of CuO and provide H_2 dissociation sites that lead to reactive hydrogen species capable of reducing iron oxides at a relatively lower temperature, the presence of Cu in the catalysts shifts the reduction of α-Fe_2O_3 to Fe_3O_4 at lower temperatures.[24, 28]

The 500ºC peak is attributed to the reduction of magnetite iron oxide (Fe_3O_4) to metallic iron (Fe^0).[7, 29] This shows that the concentration and reducibility of Fe_3O_4 to Fe^0 is also dependent of copper content since this peak at 500°C shifts toward lower reduction temperature values with increase Cu content. But the effect of copper on the reduction of Fe_3O_4 is rather low. This may be due to the formation of a solid solution of Fe_3O_4 and MgO inhibits the effect of copper to facilitate the reduction of Fe_3O_4 to metallic state.[7]

6.5.3. X-ray Diffraction (XRD)

Figure shows the XRD patterns for freshly calcined catalysts. XRD for the fresh calcined Fe/Mg showed only the well crystallized rhombohedral hematite iron oxide (α-Fe_2O_3) phase, which has characteristic diffraction peaks at 2θ values of 24.3°, 33.3°, 35.8°, 40.9°, 49.6°, 54.2°, 57.6°, 62.4° and 64.1°.[23] There was no diffraction peak for crystalline Mg or $MgFe_2O_4$ phase due to the low concentration of magnesium that appears to be well dispersed in α-Fe_2O_3. Such results indicate that the addition of Mg to the iron catalyst can promote the dispersion of α-Fe_2O_3 crystallite, which is in agreement with the BET surface area results mentioned above. Also, no X-ray powder diffraction patterns were detected for copper oxides in the Cu-promoted catalysts, indicating that Cu-promoted precursors do not affect the α-Fe_2O_3 oxide crystalline phases. The hematite iron oxide structures, once formed, remain stable during subsequent thermal treatment, and aqueous impregnation.[8] The effects of adding magnesium and copper oxides to the crystallite on iron oxide particle size were calculated by Scherrer's equation and depicted in Table 2. The Mg-promoted catalysts show smaller crystalline size than α-Fe_2O_3, while Cu-promoted catalysts for the Fe_2O_3-MgO show crystallite size comparable to of α-Fe_2O_3. Our results are consistent with the recently reported study by Park *et al.* [8] who indicate that iron particle size decreases with increased Mg content.

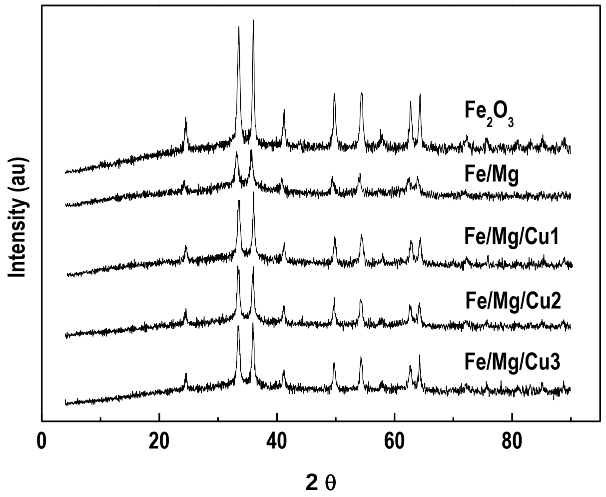

Figure 3. XRD patterns of the Fe_2O_3-MgO catalysts with different copper content, also the precipitated pure iron oxide are included.

6.5.4. Temperature Programmed Desorption (TPD)

Figure 4 shows the CO-TPD on CO-carburized Fe/Mg/Cux, (x = 1, 2, or 3) catalysts. Table 3 shows the corresponding amount of CO desorption for all catalysts (mmol CO/g catalyst). For all catalysts, the main CO desorption peaks fall within the temperature range between 350 and 650°C. The unpromoted catalyst has two groups of desorption peaks: the first peak below 200°C is ascribed to weak CO adsorption, while the main peak located at higher temperatures of around 475°C and overlapped with small peaks at higher temperature (600°C) corresponds to the strong CO adsorption. There are numerous papers dealing with the desorption of CO from clean single-crystal iron (Fe (100)) surfaces.[30-33] As reported in these studies, the CO desorbs from a clean Fe (100) surface to produce four CO desorption peaks, which were designated as three desorption peaks at temperature of -23, 67, and 157°C and are ascribed to the desorption of CO molecular states, while the fourth peak at ~ 527°C is attributed to desorption of dissociative CO adsorbed and recombined to desorb at this temperature.[34] The temperatures of the main CO desorption peaks in this study from carburized iron surfaces on all catalysts studied herein are far higher than those of the molecular CO on the Fe (100) surface and fall in the temperature range of dissociative CO desorption.[30, 35] Therefore, the temperatures for the main CO desorption peaks are located in the dissociative CO desorption temperature range. Accordingly, these CO desorption peaks, which fall in the temperature range between 350 and 650°C, could correspond to the recombination of surface-adsorbed carbon and oxygen species. Figure 4 shows that the addition of Cu promoter produces new CO desorption peaks apparent at higher temperatures. The Fe/Mg/Cu1 and Fe/Mg/Cu3 catalysts, in particular, show a multi-peak overlapped curve with the maximum peak position at 730°C and 745°C, respectively. In the catalyst samples containing a mixture of iron carbide and iron oxide phases under the applied pretreatment conditions, CO-TPD can be regarded as a temperature programmed desorption of carbon and oxygen species in the catalysts. Both of these carbon and oxygen species, which are desorbed from the mixture of iron carbides and iron oxides, recombine from both the surface-adsorbed carbon and oxygen species and those in the crystal lattices of iron carbides and iron oxides. This may due to surface adsorbed carbon and oxygen atoms recombining relatively easily into CO molecules, which would be desorbed at relatively low temperature. However, the desorption of CO molecules which are produced from the reaction of O and C atoms in the crystal lattices of iron oxides and carbides would, at least, require higher temperatures to overcome the additional transfer barriers from the bulk of the catalyst to catalyst surfaces. Therefore, the lower temperature peak centered at ~ 475°C could be ascribed to desorption of surface and/or near surface C and O species. On the other hand, the higher temperature peak (above 700°C) could be attributed to desorption of bulk iron carbides with neighboring iron oxides. In addition, the desorption temperature of CO species increases with increasing copper content, especially for Fe/Mg/Cu1 and Fe/Mg/Cu3. The results indicate that C and O adsorption or Fe-C and Fe-O bonds are strengthened by copper incorporation.[34, 36-38]

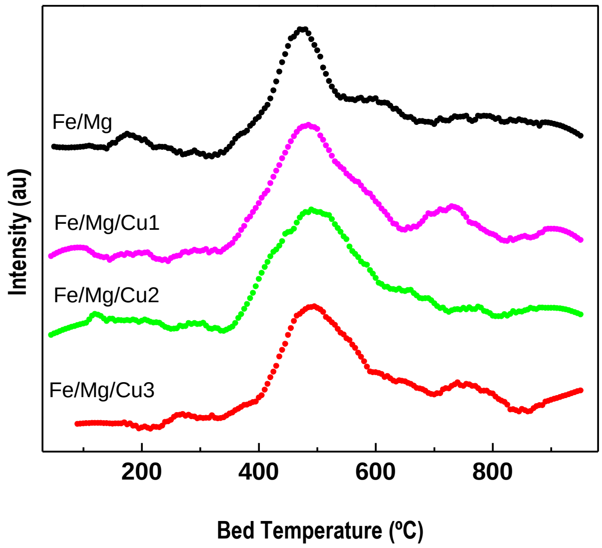

Figure 4. CO desorption profiles during the CO-TPD experiments for the Fe_2O_3-MgO catalysts with different copper content. Cu/Fe atomic ratio = 0, 0.01, 0.02, and 0.03 for Fe/Mg, Fe/Mg/Cu1, Fe/Mg/Cu2, and Fe/Mg/Cu3, respectively.

Table 3. Amounts of CO desorption during the CO-TPD experiments for the Fe_2O_3-MgO catalysts with different copper content

Catalyst	**mmol of CO/g cat**
Fe/Mg	3.52
Fe/Mg/Cu1	3.71
Fe/Mg/Cu2	3.62
Fe/Mg/Cu3	3.88

6.5.5. Temperature Programmed Oxidation (TPO)

Temperature Programmed Oxidation was used to have a measure the oxidizable carbon on the reduced catalysts surfaces. Figures 5 a,b shows the O_2-TPO profiles of CO_2 and CO, respectively. Table 4 shows the total amount of COx in the TPO test. The

O_2-TPO pattern for Fe/Mg exhibits a broad single peak between 500-800°C, whereas, the main TPO peak is shifted toward lower temperatures for the three Cu-promoted catalysts.

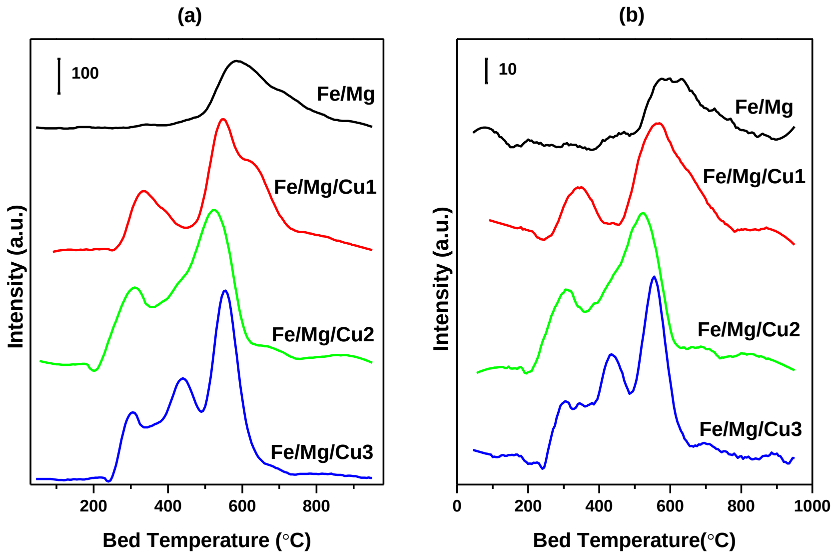

Figure 5. CO_x profiles during the O_2-TPO experiments for the Fe_2O_3-MgO catalysts with different copper content: (a) CO_2 profiles; (b) CO profiles.

Correspondingly, these O_2-TPO profiles obtained for promoted samples are shifted toward lower oxidation temperatures with increased copper content, and provide extra peaks. Our results are consistent with a recent report that shows that the oxidation of Cu-Fe-CeO_2/ZrO_2 occurred at a lower temperature compared to Cu-free catalysts such as pure iron oxide and Fe-CeO_2/ZrO_2.[39] In the same report, experimental results showed that there were no significant changes depending on Cu additive content, whereas our results show that the Cu content has an effect on the number and shape of the oxidation peaks. These differing conclusions are generally believed to be due to features such as different experimental conditions and catalyst formulation. Different positions of CO_2 generated in the TPO measurements suggest that different graphite and iron carbide species were formed.[40] As shown in Table 4, the total amount of COx increases for the Cu-containing catalysts; increases slightly with incremented copper loading; and reaches a maximum at the Cu/Fe atomic ratio of 0.02. Above this copper content (in the scope of this study), no significant change in the amount of COx was observed.

Accordingly, both graphite and carbide phases increase once Cu is incorporated. Numerous studies show that the effect of Cu on the extent of reduction and carburization in Fe oxides increases the rate of reduction and carburization of Fe oxide components and leads to the formation of FeC_x.[12, 13, 23, 41]

Table 4. Amounts of the reforming CO and CO_2 during the O_2-TPO experiments for the Fe_2O_3-MgO catalysts with different copper content

Catalyst	mmol of CO/g cat(MS28)	mmol of CO_2/g cat(MS44)	Total mmol of CO_x/g cat
Fe/Mg	3.26	14.0	17.3
Fe/Mg/Cu1	5.42	28.7	34.1
Fe/Mg/Cu2	6.91	33.2	40.1
Fe/Mg/Cu3	6.766	32.5	39. 3

6.5.6. Formation of carbonaceous compounds during FTS reaction

The influence of carburization on surface carbonaceous species was investigated by using laser Raman spectroscopic technique. Raman spectra of the calcined catalysts (Figure 6) indicate mainly the peaks of the hematite phase (α-Fe_2O_3),[42, 43] consistent with the results shown herein (Figure 3). As expected, there were no Raman spectra due to Mg, most likely owing to the low Mg loading. Similarly, no Raman spectra were detected for copper for the treatment of the Cu promoted catalyst precursors. These observations are consistent with the above results observed by XRD (Figure 3). The Raman spectra for the catalysts used during FTS reaction after 72 h in a fixed-bed reactor (FBR) are shown in Figure 7. It can be seen that Raman spectra profiles of the spent catalysts show a weak peak at 669 cm^{-1} and two broad peaks at 1320 and 1600 cm^{-1}. The weak peak appearing at 669 cm^{-1} is ascribed to the magnetite iron oxide (Fe_3O_4) phase,[42] and the band at around 1320 cm^{-1} is usually attributed to the appearance of the breathing mode of A_{1g} symmetry (D band) of graphitic carbon. This mode becomes active in the presence of disordered graphite structures. The band at around 1600 cm^{-1} can be assigned to the in-plane bond-stretching motion of pairs of C

sp^2 atoms. This mode usually becomes active in the presence of ordered graphite (G band) carbonaceous species.[44, 45] The Raman spectra profile of the graphite reference (data not shown) shows a broad band and a sharp band at 1360 and 1580 cm^{-1}, respectively. Raman bands associated with Fe carbide appear at a much lower frequency region.[46] The carbon species on the carburized catalysts based on Raman result analysis are mostly amorphous carbonaceous compounds because the higher frequency band compared with the graphite reference[46] was much weaker and broader. The Raman spectra of all the Cu-promoted catalysts show similar carburization profiles. Apparently, in the present study, copper does not affect the carbonaceous species formation after 72 h time on stream, and only affects the carburization rate at the beginning of the reaction as proved by FTS activity results.

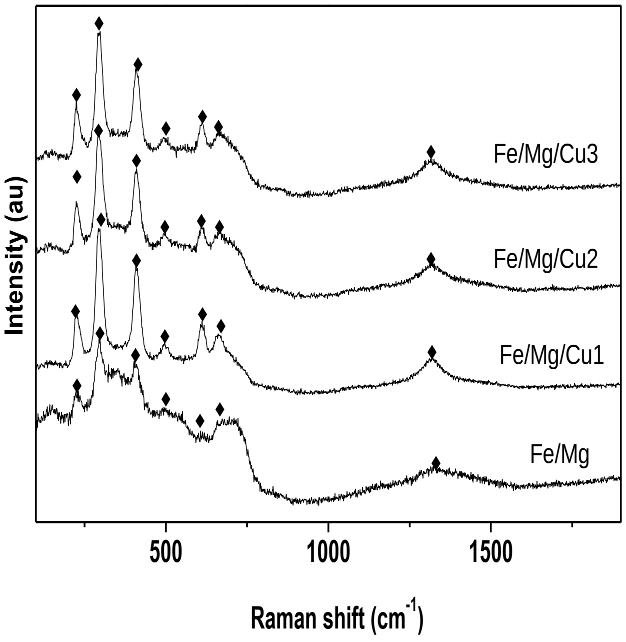

Figure 6. Laser Raman spectra for the Fe_2O_3-MgO catalysts with different copper content: (♦) hematite α-Fe_2O_3.

It has been also noted that the spent catalysts' Raman spectra do not show any peaks related to α-Fe_2O_3 (data not shown), indicating that all the hematite iron oxide species are completely reduced during FTS reaction. The presence of a weak Raman spectra appearing at 669 cm^{-1} ascribed to the magnetite phase of the Raman spectra profiles is due to exposed iron carbide becoming air-oxidized during the transfer of the sample from the fixed-bed reactor to the analysis cell of the Raman spectroscopy instrument.

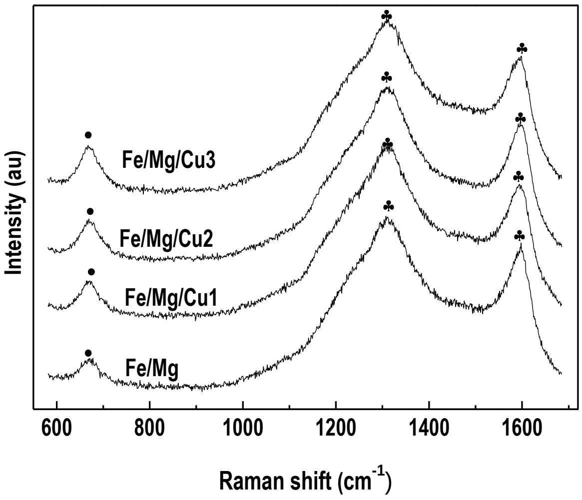

Figure 7. Laser Raman spectra of the spent catalysts after 72 hours time on stream during FTS. Reaction condition: T = 250 °C, P = 2.02 MPa, SV = 7.5 g h/mol, and H_2/CO = 1: (●) magnetite Fe_3O_4; (♣) carbonaceous species.

To further investigate the influence of reactant ratio (H_2/CO ratio) on the surface carbonaceous species, the spent catalysts after 72 h (time on stream) which used different H_2/CO ratios during FTS reaction were investigated by laser Raman spectroscopy (LRS) and spectra profiles shown in Figure 8. The Raman spectra of the two catalysts used with different H_2/CO ratios (1/1 or 2/1) show similar carburization profiles. Apparently, in the present study, the synthesis gas composition does not affect the carbonaceous species formation after 72 h time on stream and the H_2/CO composition ratio only affects the carburization rate at the beginning of the reaction as proved by FTS activity results.

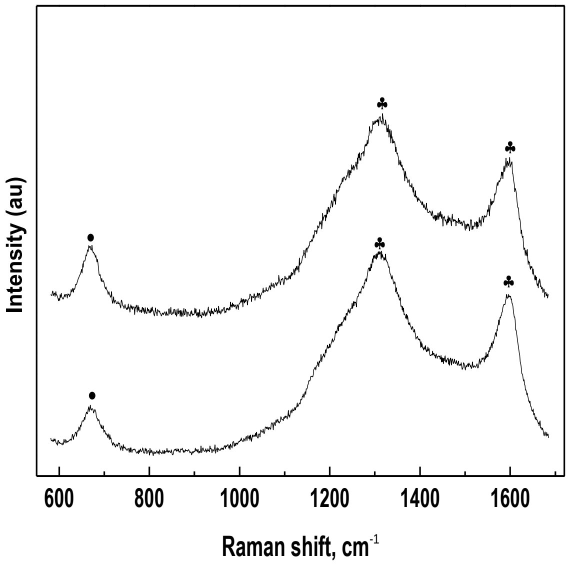

Figure 8. Laser Raman spectra of the spent catalysts (Fe/Mg/Cu2) after 72 hours time on stream during FTS. Reaction condition: T = 250 °C, P = 2.02 MPa, SV = 7.5 g h/mol, and (H_2/CO = 1 (lower) H_2/CO = 2 (upper)): (●) magnetite Fe_3O_4; (♣) carbonaceous species.

6.5.7. X-ray Absorption near Edge Spectroscopy

In situ XANES measurements for Fe K-edge of Fe/Mg/Cu1, Fe/Mg/Cu2, and Fe/Mg/Cu3 catalysts were collected to study the effect of copper loading content on the extent of reduction and carburization of iron oxide species during TPR under synthesis gas, and their spectra are shown in Figures 9, 11, and 13, respectively. The LCF at the Fe K-edge of these catalysts was also analyzed and is shown in Figures 10, 12, and 14, respectively. In the LCF, the hematite and magnetite phases (Fe_2O_3 and Fe_3O_4) were modeled as a single phase because these two phases (Fe_2O_3 and Fe_3O_4) cannot be distinguished owing to the amorphous structure and similarities in the XANES spectra of these two phases (Fe_2O_3 and Fe_3O_4) [47]. A comparison of these two spectra (Fe_2O_3 and Fe_3O_4) is shown in Figure 15.

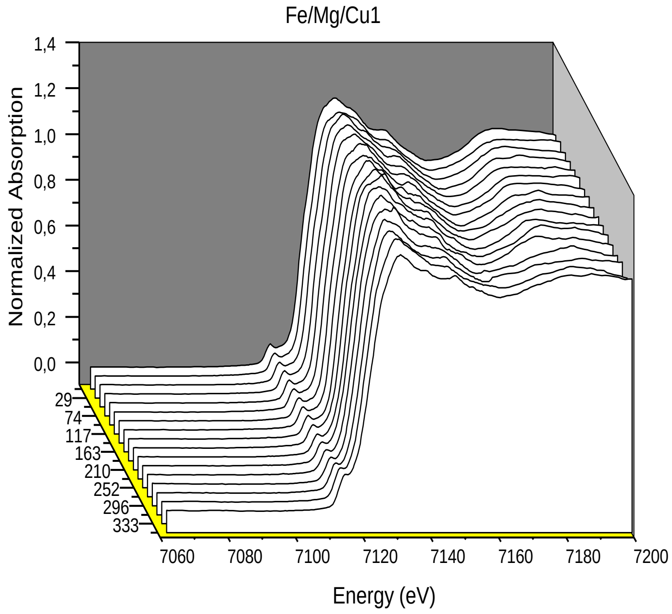

Figure 9. In-situ XANES spectra for the Fe K-edge for the Fe/Mg/Cu1 catalyst during Temperature Programmed Reduction ramping at 2 °C in syngas (H_2/CO = 2).

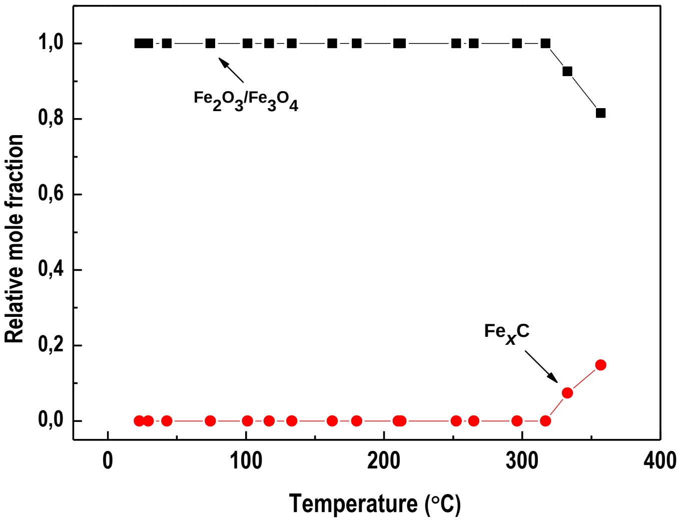

Figure 10. Composition of the iron oxide and carbide phases in the Fe/Mg/Cu1 catalyst, from Linear combination fitting (LCF) as a function of temperature.

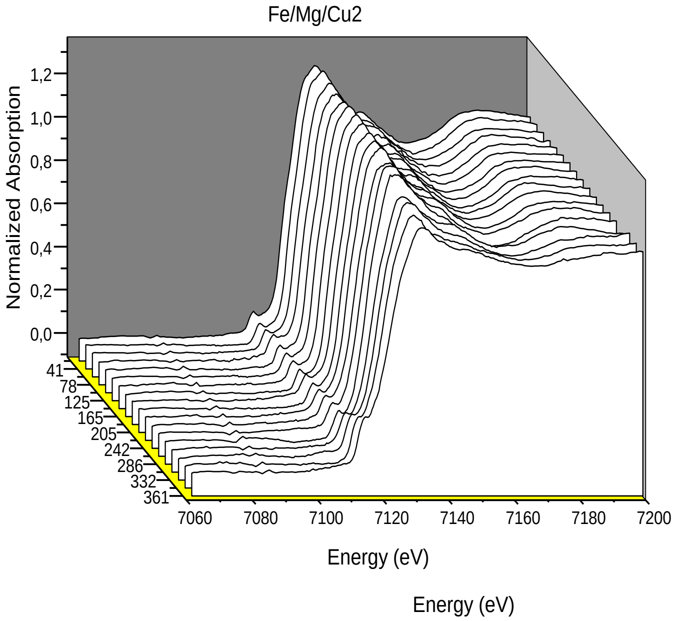

Figure 11. *In-situ* XANES spectra for the Fe K-edge for the Fe/Mg/Cu2 catalyst during Temperature Programmed Reduction ramping at 2 °C in syngas (H_2/CO = 2).

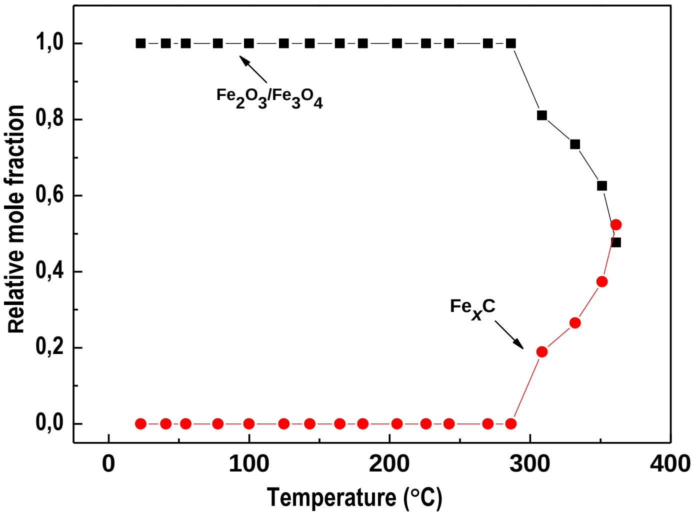

Figure 12. Composition of the iron oxide and carbide phases in the Fe/Mg/Cu2 catalyst, from Linear combination fitting (LCF) as a function of temperature.

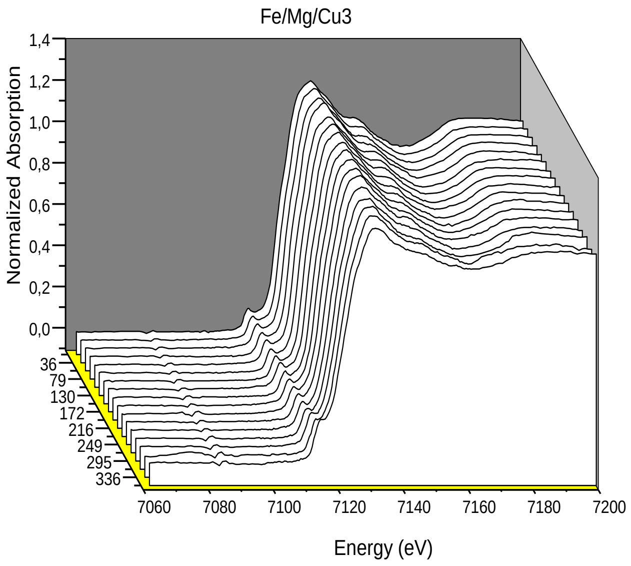

Figure 13. *In-situ* XANES spectra for the Fe K-edge for the Fe/Mg/Cu3 catalyst during TPR ramping at 2 °C in syngas ($H_2/CO = 2$).

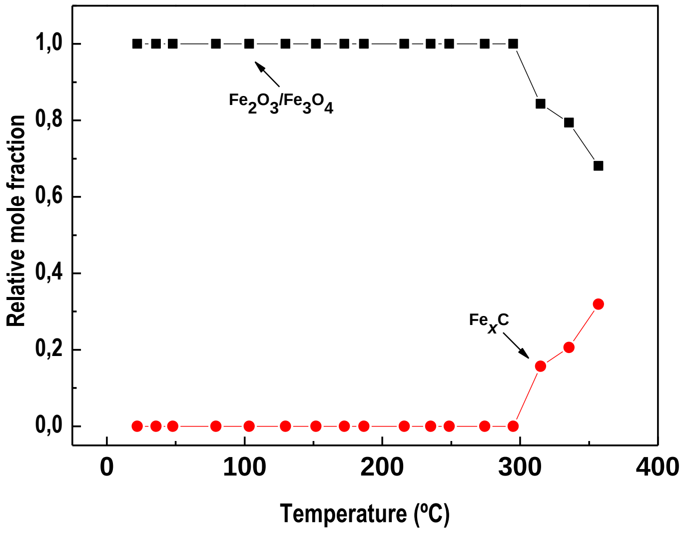

Figure 14. Composition of the iron oxide and carbide phases in the Fe/Mg/Cu3 catalyst, from Linear combination fitting (LCF) as a function of temperature.

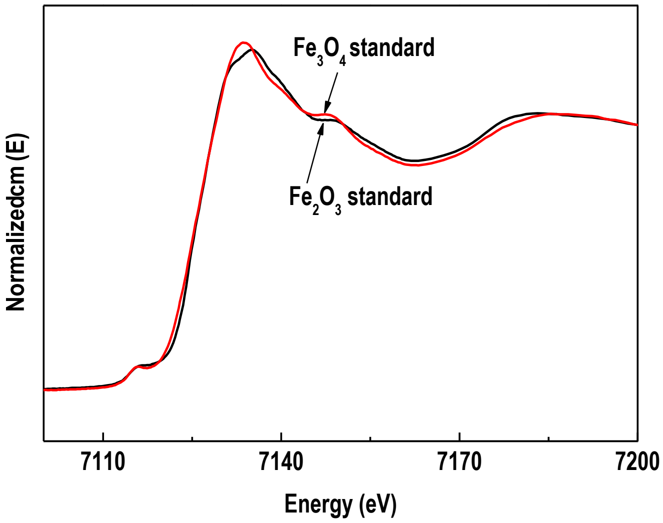

Figure 15. Normalized Fe K-edge XANES spectra of the Fe_2O_3 and Fe_3O_4 standards.

The Fe K-edge X-ray absorption spectra for Fe/Mg/Cux oxides (x = 1, 2 and 3) confirm that the hematite and magnetite phases (Fe_2O_3 and Fe_3O_4) are the starting iron phases at low temperatures. In XANES spectra for the Fe/Mg/Cu1 catalyst (Figure 9), no detectable change in the spectra is observed below 317°C. After about 330°C, a slight change is seen in the white line shape of the spectrum and shoulder at the edge, corresponding to the iron carbide appearance at this temperature, which is confirmed by the appearance of Fe_xC in the LCF profile as shown in Figure 10.

Figure 11 shows the Fe K-edge X-ray absorption spectra for the catalyst promoted by 2 atomic mole percentage of copper (Fe/Mg/Cu2). In this spectrum, no significant change is observed below 300°C. Gradual changes in the white line intensity and growth of a shoulder at the edge occurred at temperatures around 300°C. Thus, it appears that the carburization process of iron oxide in this catalyst starts to occur at 300°C, around 30°C lower than for the catalyst promoted by 1 atomic mole percentage of copper, which is confirmed by the appearance of iron carbide (Fe_xC) in the LCF profile as shown in Figure 12.

In situ Fe K-edge X-ray absorption spectra for higher copper loading in this study (Fe/Mg/Cu3) and LCF profiles are shown in Figures 13 and 14, respectively. In this catalyst, the conversion of iron oxide into Fe_xC (carburization process) begins at about 315°C as shown in the LCF profile. The carburization process in this catalyst occurred at around 15°C lower than that for the lowest copper-promoted catalyst (Fe/Mg/Cu1), whereas it is around 15°C higher than that for the medium copper-promoted catalyst (Fe/Mg/Cu2).

The evolution of Fe K-edge X-ray absorption spectral features technique in Fe/Mg/Cu*x* (x = 1, 2 and 3) oxide catalysts during the TPR process under synthesis gas was used as a technique to characterize the effects of copper loading in the extent of carburization process rates. From the Fe K-edge spectra and LCF profiles, it is clear that copper promotes the carburization extent of iron oxide. This result is consistent with the results reported by Li *et al.*[12] The TPR of Fe/Mg/Cu*x* (x = 1, 2 and 3) oxide catalysts in pure hydrogen prove that copper promotes the reduction of iron oxides. The catalyst promoted by 2 atomic mole percentage of copper (Fe/Mg/Cu2) starts to become carburized at about 30°C and 15°C lower than the temperatures corresponding to carburization of Fe/Mg/Cu1 and Fe/Mg/Cu3, respectively. Thus, the Cu/Fe atomic mole ratio of 0.02 was shown to be the optimum copper loading. Numerous studies have been performed to probe the effect of Fe-carbide formation by the secondary metal (promoter) and its effects on catalytic properties.[12, 48-51] Li *et al.*[12] investigated the structure and site evolution of iron oxide catalyst precursors during the FTS reaction and found that the initial rate and extent of carburization, and the FTS rate at steady-state, were higher for Fe_2O_3 precursors containing either Cu or K.

6.6. Catalytic Activity

The influence of copper content on the catalytic activities and product selectivity on iron magnesium catalysts during FTS reaction were studied. The CO conversion of these catalysts is shown in Figure 16. All catalysts in this study showed a CO conversion increase with time on stream (TOS), and reached the maximum CO conversion after about 2.5 h on stream, and subsequently the activity decreased with TOS. The catalytic activity of the catalyst promoted by one atom gram percentage of copper (Fe/Mg/Cu1) is similar to that for the unpromoted catalyst (Fe/Mg). When the catalyst is promoted by more than one atom gram of copper, CO conversion increases significantly with the increase of copper content and reaches its maximum at Cu/Fe = 0.02 (Fe/Mg/Cu2). With an increase in Cu/Fe atomic mole ratio from 0.02 to 0.03, there is no significant change in the CO conversion. This is a clear observation that a Cu/Fe atomic ratio of 0.02 leads to the optimum FTS catalytic activity. Combining the results from FTS activities and XANES data, it can be stated that there is an obvious relationship between the catalytic activity and the extent of carburization.[52, 53] A Cu/Fe atomic ratio of 0.02 gives a greater carburization extent, as proved by XANES results.

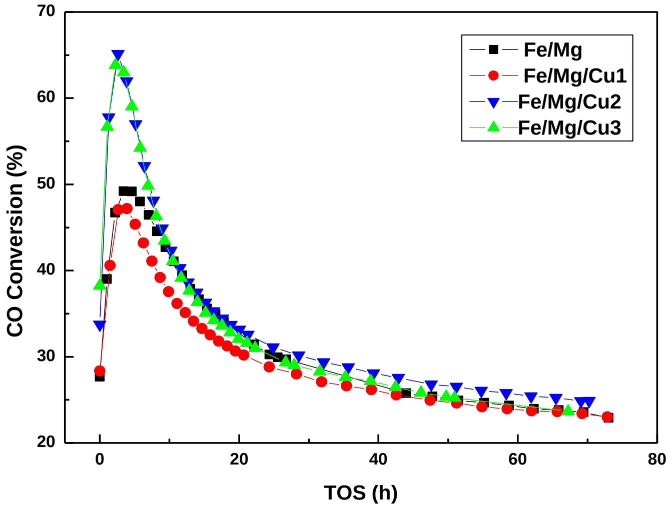

Figure 16. CO conversion of the Fe_2O_3-MgO catalysts with different copper content. Reaction condition: T = 250 °C, P = 2.02 MPa, SV = 7.5 g h/mol, and $H_2/CO = 1$.

The effects of reactant concentration (syngas ratio) on the catalytic activities, CO_2 selectivity, and hydrocarbon distribution during FTS reaction were also studied for the optimal catalyst in the present study (Fe/Mg/Cu2) and the results are summarized in Table 5. The CO conversion of Fe/Mg/Cu2 at 1.25 h on stream is 56.7% and 63.6% for H_2/CO ratio of 1/1 and 2/1, respectively. The catalytic activity of Fe/Mg/Cu2 at around 28 h on stream is 29% and 57.9% for H_2/CO ratio 1/1 and 2/1, respectively. It is clear that the richer hydrogen content in the reactant ($H_2/CO = 2/1$) led to increased FTS catalytic activity in iron-based catalysts. The CO_2 selectivity of the catalyst at 1.25 h on stream is 29.8% and 25.8% for the syngas ratio $H_2/CO = 1/1$ and 2/1, respectively. The decline in the CO_2 selectivity when H_2 content increases in the reactant composition is probably because the abundance of hydrogen content on the catalytic surface led to a reverse water-gas shift reaction. In contrast, the CH_4 increases from 13.7 to 18.7 when the H_2 content increases in the reactant composition ratio from H_2/CO = 1/1 and 2/1, respectively. It can be seen that the synthesis gas composition richer in H_2 (H_2/CO = 2/1) leads to an increase in the lower molecular weight hydrocarbons selectivity, such as CH_4 and (C_2-C_4), and decreases the higher molecular weight hydrocarbons (C_5^+) and oxygenates selectivity. The olefin-to-paraffin selectivity ($C2^=$- $C_4^=/C_2$-C_4) decreases as a result of higher hydrogen content in the syngas ratio (H_2/CO) from 1/1 into 2/1. These results lead us to conclude that the abundance of hydrogen content on the catalytic surface (as a result of the increase in H_2/CO ratio) not only favors termination of chain growth, with more lower molecular weight hydrocarbons such as methane, but also promotes the secondary hydrogenation of olefins to paraffins. Some studies have been performed to investigate the effect of H_2/CO ratio on hydrocarbon products distribution during FTS reaction on Fe-based catalysts.[54-57] Hao *et al.*[54] reported that high H_2/CO is preferred to the chain termination probabilities, and suppresses the chain growth probabilities, which results in a selectivity shift toward lower molecular weight hydrocarbons.

Table 5. FTS Catalytic Activities of the Fe/Mg/Cu2 catalysts. Reaction condition: *T* = 250 °C, *P* = 2.02 MPa, SV = 7.5 g h/mol, and different syngas ratios H_2/CO = 1 or 2

H_2/CO ratio	**TOS/h**	**CO conv. (%)**	**Selectivities (%)**					**Olefin/Parafin**
			CO_2	**CH_4**	**C_2-C_4**	**C_5+**	**C_{oxy}**	
1/1	1.25	56.7	29.8	13.7	39	14.8	2.7	2.1
2/1	1.25	63.6	25.8	18.7	41.6	11.6	2.3	1.1
1/1	28.00	29	27.6	10	37.4	21.5	3.5	1.5
2/1	28.28	57.9	25	13.9	43.7	14.3	3.1	0.9

The CO conversion, hydrocarbon distribution and CO_2 selectivity obtained at 2.5 and 28 h on stream for these catalysts are summarized in Tables S1 and 2, respectively. The selectivity of low molecular weight hydrocarbons decreases with time on stream and shifts toward higher hydrocarbons (C_5^+). Table S1 illustrates that CO_2 selectivity is affected by copper content promoters. The CO_2 selectivity of unpromoted catalysts is 24.7%. All Cu-containing samples showed higher CO_2 selectivity than unpromoted Fe/Mg. The CO_2 selectivity of the promoted catalysts increased with higher copper content and reached a maximum at the Cu/Fe atomic ratio of 0.02. Beyond this copper content, a slight decrease in the selectivity of CO_2 was observed as copper content was raised further. As shown in Table S1, the CO_2 selectivity approaches and follows a similar trend to the CO conversion for copper-promoted catalysts. This is consistent with the CO conversion level that has a strong impact on relative FTS activity and WGS reaction on Fe-based catalysts. The increase of CO_2 selectivity in Cu-promoted catalysts comes from the positive effect of copper on the WGS reaction. CO can be converted either into hydrocarbons by FTS reaction or with H_2O, which forms FTS primary products on Fe-based catalysts, to produce CO_2 via secondary water-gas shift reaction. The results of CO_2 selectivity, in this study, led us to conclude that the addition of copper promotes the WGS reaction. This is consistent with the study conducted by Li *et al.*[23]

As shown in Supporting Information Table S1, the methane selectivity of these catalysts was relatively high at around 11.5%, which was acceptable since no K promoter was introduced in the present study.[23, 58] There is no significant effect in the selectivity of methane when the Fe-Mg oxide is promoted by copper oxide. The selectivity of high molecular weight hydrocarbons (C_5^+) for catalysts with a Cu/Fe atomic ratio of 0.01 (Fe/Mg/Cu1) is similar to that of unpromoted catalysts. However, beyond this copper loading (Cu/Fe atomic ratio of 0.01), a decrease in high molecular weight hydrocarbons selectivity was observed. The addition of copper to Fe/Mg catalysts slightly decreases the ability of the catalysts toward chain growth to form higher molecular weight hydrocarbons (C_5^+). This result is consistent with the result of Li *et al.*[23] The effect of copper content on the olefin-to-paraffin ratio $[(C_2^=-C_4^=)/(C_2-C_4)]$ is shown in Table S1. It is clear that appropriate amounts of copper can inhibit olefin selectivity by improving the hydrogenation reaction of olefins to paraffins. The olefin selectivity of the catalysts decreases with the increase of copper content and reaches a minimum at the Cu/Fe atom ratio of 0.02. Beyond this copper content, a slight increase in the selectivity of olefin was observed.

6.7. Conclusions

The addition of magnesium to iron-based catalysts leads to increased BET specific area and smaller iron oxide particle size. The XRD of the promoted and unpromoted calcined precursors showed only a crystalline hematite iron oxide (α-Fe_2O_3) phase, and no XRD diffraction peaks due to Mg or Cu were recorded, probably because their low concentration in the samples and full dispersion on hematite iron oxide. The extent of hematite iron oxide reduction increases and shifts toward lower reduction temperatures due to incorporation with Mg and Cu species; in addition, the extent of reduction increases with higher Cu loading. The content of iron carbide phases during the TPR process in the synthesis gas first increases with the increase of copper content and reaches a maximum for the Cu/Fe atom ratio of 0.02. The FTS catalytic activity is promoted with copper because Cu promotes the formation of the iron carbide, which is the active phase. The maximum catalytic activity was obtained at the Cu/Fe atom ratio of 0.02. Then, at higher copper levels, there is a decrease in the catalytic activity. A maximum in the catalytic activity and methane selectivity was obtained for the synthesis gas ratio of 2 ($H_2/CO = 2$).

ASSOCIATED CONTENT

Supporting Information

FTS catalytic activities of the Fe_2O_3-MgO catalysts with different copper content in Table S1 and S2.

Table S1. FTS catalytic activities of the Fe_2O_3-MgO catalysts with different copper content. Reaction condition: T = 250 °C, P = 2.02 MPa, SV = 7.5 g h/mol, and H_2/CO=1

Catalysts	Fe/Mg	Fe/Mg/Cu1	Fe/Mg/Cu2	Fe/Mg/Cu3
CO conversion (%)	46.7	47	65.1	63.8
Time on stream (h)	2.23	2.68	2.25	2.62
CO_2 Selectivity (%)	24.7	25.9	33.4	32.7
HC Selectivity (%)				
CH_4	11.4	11.7	11.5	11.3
C_2-C_4	41.9	40.5	38	38.7
C_5^+	18.9	18.9	14	14.2
Coxy	3.1	3	3.1	3.1
Olefin-to-paraffin				
($C_2^=$-$C_4^=$/C_2-C_4) ratio	3.2	2.7	2	2.2

Table S2. FTS catalytic activities of the Fe_2O_3-MgO catalysts with different copper content. Reaction condition: T = 250 °C, P = 2.02 MPa, SV = 7.5 g h/mol, and $H_2/CO=1$

Catalysts	Fe/Mg	Fe/Mg/Cu1	Fe/Mg/Cu2	Fe/Mg/Cu3
CO conversion (%)	29.9	28	30.2	29
Time on stream (h)	25.55	28.25	28.0	28.57
CO_2 Selectivity (%)	21.5	21.9	30.7	27.6
HC Selectivities (%)				
CH_4	8.8	9.8	9.6	10
C_2-C_4	41.1	40.2	35.7	37.4
C_5^+	24.4	24.4	20.7	21.5
Coxy	4.2	3.7	3.3	3.5
Olefin/Paraffin				
$(C_2^=-C_4^=/C_2-C_4)$ ratio	2.4	2.1	1.4	1.5

- **Acknowledgments**

This material is based upon work funded by the U.S. Department of Agriculture, under Award Number 11-DG-11221636-187. The XRD, Raman, textural properties analysis, and catalytic performance were obtained in ICP-CSIC, Madrid, Spain. The assistance of Dr. Nitin Kumar, Dr. Miranda Smith, Mr. Devendra Pakhare and Ms. Pratibha Sharma is gratefully appreciated. We also acknowledge the help of Mr. Gregory Merchan, CAMD beamline scientist with XANES experiments.

6.8. References

(1) de Smit, E.; Weckhuysen, B. M. The renaissance of iron-based Fischer-Tropsch synthesis: on the multifaceted catalyst deactivation behaviour. *Chem. Soc. Rev.* **2008,** *37*, 2758-2781.

(2) Liu, K.; Suo, H.; Zhang, C.; Xu, J.; Yang, Y.; Xiang, H.; Li, Y. An active Fischer–Tropsch synthesis FeMo/SiO2 catalyst prepared by a modified sol–gel technique. *Catal. Commun.* **2010,** *12*, 137-141.

(3) Lohitharn, N.; Goodwin Jr, J. G.; Lotero, E. Fe-based Fischer–Tropsch synthesis catalysts containing carbide-forming transition metal promoters. *J. Catal.* **2008,** *255*, 104-113.

(4) Tijmensen, M. J. A.; Faaij, A. P. C.; Hamelinck, C. N.; van Hardeveld, M. R. M. Exploration of the possibilities for production of Fischer Tropsch liquids and power via biomass gasification. *Biomass Bioenerg.* **2002,** *23*, 129-152.

(5) Özçimen, D.; Karaosmanoğlu, F. Production and characterization of bio-oil and biochar from rapeseed cake. *Renew. Energy* **2004,** *29*, 779-787.

(6) Sharma, P.; Elder, T.; Groom, L. H.; Spivey, J. J. Effect of structural promoters on Fe-based fischer-tropsch synthesis of biomass derived syngas. *Top. Catal.* **2014,** *57*, 526-537.

(7) Yang, J.; Sun, Y.; Tang, Y.; Liu, Y.; Wang, H.; Tian, L.; Wang, H.; Zhang, Z.; Xiang, H.; Li, Y. Effect of magnesium promoter on iron-based catalyst for Fischer–Tropsch synthesis. *J. Mol. Catal. A-Chem.* **2006,** *245*, 26-36.

(8) Park, M.; Kang, J. S.; Na, K. P.; Lee, S. D.; Awate, S. V.; Moon, D. J. Studies on Nanosized Iron Based Modified Catalyst for Fischer-Tropsch Synthesis Application. *J. Nanosci. Nanotechnol.* **2011,** *11*, 1447-1450.

(9) Gallegos, N. G.; Alvarez, A. M.; Cagnoli, M. V.; Bengoa, J. F.; Marchetti, S. G.; Mercader, R. C.; Yeramian, A. A. Selectivity to Olefins of Fe/SiO2–MgO Catalysts in the Fischer–Tropsch Reaction. *J. Catal.* **1996,** *161*, 132-142.

(10) Jun, K.-W.; Roh, H.-S.; Kim, K.-S.; Ryu, J.-S.; Lee, K.-W. Catalytic investigation for Fischer–Tropsch synthesis from bio-mass derived syngas. *Appl. Catal. A-Gen.* **2004,** *259*, 221-226.

(11) Riedel, T.; Claeys, M.; Schulz, H.; Schaub, G.; Nam, S.-S.; Jun, K.-W.; Choi, M.-J.; Kishan, G.; Lee, K.-W. Comparative study of Fischer–Tropsch synthesis with

H2/CO and H2/CO2 syngas using Fe- and Co-based catalysts. *Appl. Catal. A-Gen.* **1999,** *186*, 201-213.

(12) Li, S.; Meitzner, G. D.; Iglesia, E. Structure and site evolution of iron oxide catalyst precursors during the fischer-tropsch synthesis. *J. Phys. Chem. B* **2001,** *105*, 5743-5750.

(13) Li, S.; Krishnamoorthy, S.; Li, A.; Meitzner, G. D.; Iglesia, E. Promoted Iron-Based Catalysts for the Fischer–Tropsch Synthesis: Design, Synthesis, Site Densities, and Catalytic Properties. *J. Catal.* **2002,** *206*, 202-217.

(14) Luque, R.; de la Osa, A. R.; Campelo, J. M.; Romero, A. A.; Valverde, J. L.; Sanchez, P. Design and development of catalysts for Biomass-To-Liquid-Fischer-Tropsch (BTL-FT) processes for biofuels production. *Energy Environ. Sci.* **2012,** *5*, 5186-5202.

(15) Herranz, T.; Rojas, S.; Pérez-Alonso, F. J.; Ojeda, M.; Terreros, P.; Fierro, J. L. G. Carbon oxide hydrogenation over silica-supported iron-based catalysts: Influence of the preparation route. *Appl. Catal. A-Gen.* **2006,** *308*, 19-30.

(16) Ravel, B.; Newville, M. ATHENA, ARTEMIS, HEPHAESTUS: data analysis for X-ray absorption spectroscopy using IFEFFIT. *J. Synchrot. Radiat.* **2005,** *12*, 537-541.

(17) Herranz, T.; Rojas, S.; Pérez-Alonso, F. J.; Ojeda, M.; Terreros, P.; Fierro, J. L. G. Hydrogenation of carbon oxides over promoted Fe-Mn catalysts prepared by the microemulsion methodology. *Appl. Catal. A-Gen.* **2006,** *311*, 66-75.

(18) Pérez-Alonso, F. J.; Granados, M. L.; Ojeda, M.; Herranz, T.; Rojas, S.; Terreros, P.; Fierro, J. L. G.; Gracia, M.; Gancedo, J. R. Relevance in the fischer-tropsch synthesis of the formation of Fe-O-Ce interactions on iron-cerium mixed oxide systems. *J. Phys. Chem. B* **2006,** *110*, 23870-23880.

(19) Fischer, F.; Tropsch, H. Über die Entwicklung unserer Benzinsynthese aus Kohlenoxyd und Wasserstoff bei gewöhnlichem Druck. Brennstoff – Chemie: 1930, Vol. 11.

(20) Berg, F. R. V. d. Utrecht University, The Netherlands, 2001.

(21) Shen, J.; Guang, B.; Tu, M.; Chen, Y. Preparation and characterization of Fe/MgO catalysts obtained from hydrotalcite-like compounds. *Catal. Today* **1996,** *30*, 77-82.

(22) Sádaba, I.; Ojeda, M.; Mariscal, R.; Fierro, J. L. G.; Granados, M. L. Catalytic and structural properties of co-precipitated Mg–Zr mixed oxides for furfural valorization via aqueous aldol condensation with acetone. *Appl. Catal. B-Environ.* **2011,** *101*, 638-648.

(23) Li, S.; Li, A.; Krishnamoorthy, S.; Iglesia, E. Effects of Zn, Cu, and K Promoters on the Structure and on the Reduction, Carburization, and Catalytic Behavior of Iron-Based Fischer–Tropsch Synthesis Catalysts. *Catal. Lett.* **2001,** *77*, 197-205.

(24) Noichi, H.; Uddin, A.; Sasaoka, E. Steam reforming of naphthalene as model biomass tar over iron–aluminum and iron–zirconium oxide catalyst catalysts. *Fuel Process. Technol.* **2010,** *91*, 1609-1616.

(25) Zhang, C.-H.; Wan, H.-J.; Yang, Y.; Xiang, H.-W.; Li, Y.-W. Study on the iron–silica interaction of a co-precipitated Fe/SiO2 Fischer–Tropsch synthesis catalyst. *Catal. Commun.* **2006,** *7*, 733-738.

(26) Pour, A. N.; Housaindokht, M. R.; Tayyari, S. F.; Zarkesh, J. Fischer-Tropsch synthesis by nano-structured iron catalyst. *J. Nat. Gas Chem.* **2010,** *19*, 284-292.

(27) Valente, J. S.; Hernandez-Cortez, J.; Cantu, M. S.; Ferrat, G.; López-Salinas, E. Calcined layered double hydroxides Mg–Me–Al (Me: Cu, Fe, Ni, Zn) as bifunctional catalysts. *Catal. Today* **2010,** *150*, 340-345.

(28) Zhang, C.-H.; Yang, Y.; Teng, B.-T.; Li, T.-Z.; Zheng, H.-Y.; Xiang, H.-W.; Li, Y.-W. Study of an iron-manganese Fischer–Tropsch synthesis catalyst promoted with copper. *J. Catal.* **2006,** *237*, 405-415.

(29) Nakhaei Pour, A.; Shahri, S. M. K.; Bozorgzadeh, H. R.; Zamani, Y.; Tavasoli, A.; Marvast, M. A. Effect of Mg, La and Ca promoters on the structure and catalytic behavior of iron-based catalysts in Fischer–Tropsch synthesis. *Appl. Catal. A-Gen.* **2008,** *348*, 201-208.

(30) Benziger, J.; Madix, R. J. The effects of carbon, oxygen, sulfur and potassium adlayers on CO and H2 adsorption on Fe(100). *Surf. Sci.* **1980,** *94*, 119-153.

(31) Cameron, S. D.; Dwyer, D. J. Charge transfer effects on CO bond cleavage: CO and potassium on Fe(100). *Surf. Sci.* **1988,** *198*, 315-330.

(32) Amenomiya, Y.; Pleizier, G. Chemisorption of gases on a promoted iron catalyst: I. Hydrogen, nitrogen, carbon monoxide and carbon dioxide. *J. Catal.* **1973,** *28*, 442-454.

(33) Moon, D. W.; Dwyer, D. J.; Bernasek, S. L. Adsorption of CO on the clean and sulfur modified Fe(100) surface. *Surf. Sci.* **1985,** *163*, 215-229.

(34) Zhang, C.; Zhao, G.; Liu, K.; Yang, Y.; Xiang, H.; Li, Y. Adsorption and reaction of CO and hydrogen on iron-based Fischer–Tropsch synthesis catalysts. *J. Mol. Catal. A-Chem.* **2010,** *328*, 35-43.

(35) Seip, U.; Tsai, M. C.; Christmann, K.; Küppers, J.; Ertl, G. Interaction of Co with an Fe(111) surface. *Surf. Sci.* **1984,** *139*, 29-42.

(36) Wan, H.; Wu, B.; Zhang, C.; Xiang, H.; Li, Y. Promotional effects of Cu and K on precipitated iron-based catalysts for Fischer–Tropsch synthesis. *J. Mol. Catal. A-Chem.* **2008,** *283*, 33-42.

(37) Suo, H.; Wang, S.; Zhang, C.; Xu, J.; Wu, B.; Yang, Y.; Xiang, H.; Li, Y.-W. Chemical and structural effects of silica in iron-based Fischer–Tropsch synthesis catalysts. *J. Catal.* **2012,** *286*, 111-123.

(38) Zhang, H.; Ma, H.; Zhang, H.; Ying, W.; Fang, D. Effects of Zr and K Promoters on Precipitated Iron-Based Catalysts for Fischer–Tropsch Synthesis. *Catal. Lett.* **2012,** *142*, 131-137.

(39) Kim, H.-S.; Cha, K.-S.; Yoo, B.-K.; Ryu, T.-G.; Lee, Y.-S.; Park, C.-S.; Kim, Y.-H. Chemical hydrogen storage and release properties using redox reaction over the Cu-added Fe/Ce/Zr mixed oxide medium. *J. Ind. Eng. Chem.* **2010,** *16*, 81-86.

(40) Zhang, J.-l.; Ma, L.-h.; Fan, S.-b.; Zhao, T.-S.; Sun, Y.-h. Synthesis of light olefins from CO hydrogenation over Fe–Mn catalysts: Effect of carburization pretreatment. *Fuel* **2013,** *109*, 116-123.

(41) Li, S.; Iglesia, E.; Meitzner, G. D. Fischer-Tropsch synthesis catalysts based on Fe oxides modified by Cu and K: Structure and catalytic requirements. **2000,** *45*, 221-224.

(42) de Faria, D. L. A.; Venâncio Silva, S.; de Oliveira, M. T. Raman microspectroscopy of some iron oxides and oxyhydroxides. *J. Raman Spectrosc.* **1997,** *28*, 873-878.

(43) Ding, M.; Yang, Y.; Wu, B.; Xu, J.; Zhang, C.; Xiang, H.; Li, Y. Study of phase transformation and catalytic performance on precipitated iron-based catalyst for Fischer–Tropsch synthesis. *J. Mol. Catal. A-Chem.* **2009,** *303*, 65-71.

(44) Urbonaite, S.; Hälldahl, L.; Svensson, G. Raman spectroscopy studies of carbide derived carbons. *Carbon* **2008,** *46*, 1942-1947.

(45) Ferrari, A. C.; Robertson, J. Interpretation of Raman spectra of disordered and amorphous carbon. *Phys. Rev. B* **2000,** *61*, 14095-14107.

(46) Ning, W.; Koizumi, N.; Chang, H.; Mochizuki, T.; Itoh, T.; Yamada, M. Phase transformation of unpromoted and promoted Fe catalysts and the formation of carbonaceous compounds during Fischer–Tropsch synthesis reaction. *Appl. Catal. A-Gen.* **2006,** *312*, 35-44.

(47) Schimanke, G.; Martin, M. In situ XRD study of the phase transition of nanocrystalline maghemite (γ-Fe2O3) to hematite (α-Fe2O3). *Solid State Ion.* **2000,** *136–137*, 1235-1240.

(48) Campos, A.; Spivey, J. J.; Roy, A.; Lohitharn, N.; Goodwin, J.; Lotero, E.; Lamb, H. Characterization of Mo additions in iron-based Fischer-Tropsch catalysts using X-ray absorption spectroscopy and X-ray diffraction. *Nucl. Instrum. Methods Phys. Res. Sect. A-Accel. Spectrom. Dect. Assoc. Equip.* **2007,** *582*, 236-238.

(49) Vasireddy, S.; Campos, A.; Miamee, E.; Adeyiga, A.; Armstrong, R.; Allison, J. D.; Spivey, J. J. Study of attrition of Fe-based catalyst supported over spent FCC catalysts and their Fischer-Tropsch activity in a fixed bed reactor. *Appl. Catal. A-Gen.* **2010,** *372*, 184-190.

(50) Campos, A.; Lohitharn, N.; Roy, A.; Lotero, E.; Goodwin Jr, J. G.; Spivey, J. J. An activity and XANES study of Mn-promoted, Fe-based Fischer-Tropsch catalysts. *Appl. Catal. A-Gen.* **2010,** *375*, 12-16.

(51) Campos, A. A.; Lohitharn, N.; Roy, A.; Goodwin Jr, J. G.; Spivey, J. J. In *Using in-situ Fe and Mn K-edge XANES to study a Mn-promoted Fe/Cu/SiO 2 catalyst during H 2 reduction and during the Fischer-Tropsch synthesis*, ACS National Meeting Book of Abstracts, 2010.

(52) Herranz, T.; Rojas, S.; Pérez-Alonso, F. J.; Ojeda, M.; Terreros, P.; Fierro, J. L. G. Genesis of iron carbides and their role in the synthesis of hydrocarbons from synthesis gas. *J. Catal.* **2006,** *243*, 199-211.

(53) Al-Dossary, M.; Ismail, A. A.; Fierro, J. L. G.; Bouzid, H.; Al-Sayari, S. A. Effect of Mn loading onto MnFeO nanocomposites for the CO2 hydrogenation reaction. *Appl. Catal. B-Environ.* **2015,** *165*, 651-660.

(54) Hao, Q.; Bai, L.; Xiang, H.; Li, Y. Activation pressure studies with an iron-based catalyst for slurry Fischer-Tropsch synthesis. *J. Nat. Gas Chem.* **2009,** *18*, 429-435.

(55) Bai, L.; Xiang, H.-W.; Li, Y.-W.; Han, Y.-Z.; Zhong, B. Slurry phase Fischer–Tropsch synthesis over manganese-promoted iron ultrafine particle catalyst. *Fuel* **2002,** *81*, 1577-1581.

(56) Ji, Y.-Y.; Xiang, H.-W.; Yang, J.-L.; Xu, Y.-Y.; Li, Y.-W.; Zhong, B. Effect of reaction conditions on the product distribution during Fischer–Tropsch synthesis over an industrial Fe-Mn catalyst. *Appl. Catal. A-Gen.* **2001,** *214*, 77-86.

(57) Li, T.; Yang, Y.; Tao, Z.; Zhang, C.; Xiang, H.; Li, Y. Study on an iron–manganese Fischer–Tropsch synthesis catalyst prepared from ferrous sulfate. *Fuel Process. Technol.* **2009,** *90*, 1247-1251.

(58) Qing, M.; Yang, Y.; Wu, B.; Wang, H.; Wang, H.; Xu, J.; Zhang, C.; Xiang, H.; Li, Y. Effect of the zirconia addition manner on the modification of Fe–SiO2 interaction. *Catal. Today* **2012,** *183*, 79-87.

Chapter 7: Effect of Mn loading onto MnFeO nanocomposites for the CO_2 hydrogenation reaction

7

Effect of Mn loading onto MnFeO nanocomposites for the CO_2 hydrogenation reaction

M. Al-Dossary1, J.L.G. Fierro1*, Adel A. Ismail2,3**, Houcine Bouzid2,4 and S.A. Al-Sayari2,5

1Institute of Catalysis and Petroleum Chemistry, CSIC, Marie Curie 2, Cantoblanco, 28049 Madrid, Spain

2Promising Centre for Sensors and Electronic Devices (PCSED), Advanced Materials and Nano-Research Centre, Najran University, P.O. Box 1988, Najran 11001, Saudi Arabia

3Nanostructured Materials and Nanotechnology Division, Central Metallurgical Research and Development Institute (CMRDI), P.O. Box 87 Helwan, Cairo 11421, Egypt

4Laboratoire des Matériaux Ferroélectriques, Faculté des Sciences de Sfax, Route Soukra Km 3,5, BP 802, F-3018 Sfax, Tunisia
5College of Science and Arts-Sharoura, Najran University, Saudi Arabia
E-mail address: jlgfierro@icp.csic.es; adelali141@yahoo.com

Abstract

This work describes the preparation of mesoporous xMnFe oxide (x = 0, 0.05, 0.1, 0.2, 0.3 and 0.5 molar ratios) nanocomposites through a one-step sol-gel process in the presence of a triblock copolymer as a structure-directing agent. The prepared oxides were used as catalysts in the CO_2 hydrogenation via Fischer-Tropsch reactions for the production of valuable hydrocarbons. Among the catalysts, the 0.05MnFe catalyst performed best under the selected reaction conditions: a reaction temperature of 340 °C, overall pressure of 20 bar, reactant mixture of 23% CO_2/69% H_2/8% N_2 and flow rate of 20 mL min^{-1}. This catalyst provided a much higher conversion of CO_2 to hydrocarbons (63.2% C_2-C_5, 3.9% to C_{6+} and 3.6% to oxygenates) and the lowest levels of CO and methane formation among the xMnFe series. Moreover, 0.05MnFe was the only catalyst with a mesoporous structure, and it had a substantially lower reduction temperature than did the other members of the series. The enhanced catalytic activity of the 0.05MnFe catalyst, which contains only a small amount of Mn, appears to result primarily from its high specific area and relatively easy reduction

Keywords: Fischer-Tropsch synthesis (FTS); CO_2 hydrogenation; Mn promotion; Fe-based catalysts; Fe-based FTS catalysts.

7.1. Introduction

Carbon dioxide emissions into the atmosphere from fossil fuel combustion are progressively increasing, with obvious effects on the climate. As fossil fuels will remain the world's primary energy source for decades to come, the stabilization of CO_2 levels in the atmosphere is one the greatest challenges faced by the scientific community [1].

At the present, recycling CO_2 to produce liquid renewable or sustainable hydrocarbons is one of the most interesting catalytic alternative options [2-8]. This conceptual approach offers the possibility of converting CO_2 into high-density transportation fuels compatible with our current storage and distribution network. A simple conversion route is the Fischer-Tropsch synthesis (FTS), which provides clean synthetic fuels when starting with CO_2-rich feeds [9-14].

FTS is a key technology employed over the last 90 years for the production of chemicals and clean transportation fuels from carbon sources alternative to unsustainable crude oil [15-17]. Alternative C-containing sources, such as biomass or coal, offer the possibility of producing H_2-deficient or CO-rich syngas feeds. CO_2 hydrogenation comprises two reaction steps: the reverse water-gas shift (RWGS) reaction (Eq. 1) and the Fischer–Tropsch (FT) reaction (Eq. 2):

$$CO_2 + H_2 \rightarrow CO + H_2O \qquad \Delta H_{298} = +41\ \text{kJ/mol} \qquad [1]$$

$$CO + 2\ H_2 \rightarrow (\text{-}CH_2\text{-}) + H_2O \qquad \Delta H_{298} = -152\ \text{kJ/mol} \qquad [2]$$

Compared with the traditional FT synthesis, twice as much hydrogen is needed in this two-step reaction, and more water is formed as a byproduct. Thermodynamically, as it is a slightly endothermic reaction, the conversion of CO_2 by RWGS is limited at the low temperatures used in the traditional FT reaction: at an H_2/CO_2 ratio of 3 (stoichiometric ratio for CO_2 hydrogenation to $-CH_2-$) only 13-23% of CO_2 is converted to CO at temperatures between 220 and 300 ºC [18]. The exothermic FT reaction is not thermodynamically limited in the above temperature regime; thus, it is possible to achieve higher CO_2 conversion for the overall reaction because of the consecutive RWGS reaction, which forms CO.

Iron-based catalysts have been used for the hydrogenation of CO_2 to C_{2+} hydrocarbons [19-24]. For these systems, it is generally accepted that, instead of the direct hydrogenation of CO_2, the RWGS (Eq. 1) proceeds over these catalysts, followed by the hydrogenation of CO to hydrocarbons (Eq. 2) via the FT synthesis reaction. Fe-based catalysts can catalyze both the RWGS reaction [25] and the hydrogenation of CO and are thus expected to show good performance for the hydrogenation of CO_2.

Compared to other metal catalysts employed for FTS, the iron-based catalysts provide higher conversion, selectivity to lower olefins and flexibility in terms of the process parameters [26-28]. However, catalysts containing Fe alone do not solve the problem of low selectivity to lower olefins, a general limitation of the FTS process. Manganese has been widely used as a promoter of FTS on iron catalysts, particularly for producing low olefins [29-32]. The individual effect of manganese promotion on supported or unsupported iron catalysts has also been the focus of much research effort [22,33-36].

Lohitharn and Goodwin have indicated improved activity and/or selectivity upon the addition of transition metals to Fe-based FTS catalysts [37]. It has been reported that the incorporation of various transition metals other than Cu, such as Zr, Cr, Mo, Mn, Ta and V, greatly increased the catalyst activities for both CO hydrogenation and WGS to varying degrees [38]. Among the promoted iron-based catalysts, the Fe-Mn catalyst is of industrial interest and has been described extensively in recent years due to its higher olefin and middle distillate selectivity. For instance, Mn-promoted Fe catalysts with Mn loadings up to 15 wt% demonstrated greater light olefin (C_2-C_4) formation than their Mn-free counterpart [35,39-41]. In most studies, Mn-Fe oxides were prepared by the conventional co-precipitation of the hydroxides, which were then subjected to air-calcination. Recently, Mn-Fe binary oxides have been synthesized by a template-free controlled thermal decomposition approach from single-phase Mn-Fe binary oxalate, which was prepared by precipitation from a Mn^{2+}-Fe^{2+} solution mixed with oxalic acid [42].

Mesoporous materials are considered promising for high-efficiency catalysts due to their high surface areas and large pore sizes. Therefore, our approach in the present work consisted of the preparation of mesoporous Mn-Fe nanocomposites through a simple one-step sol-gel process in the presence of a triblock copolymer as a structure-directing agent and their use for the CO_2 hydrogenation via FT synthesis for the production of higher hydrocarbons. This paper presents the results of our recent studies on the effects of manganese addition to MnFeO nanocomposites for the CO_2 hydrogenation reaction. The catalysts were investigated using different characterization techniques to establish the relationship between catalyst structure and performance.

7.2. Experimental

7.2.1. Materials

The block copolymer surfactant EO_{106}-$PO_{70}EO_{106}$ (F-127, EO = -CH_2CH_2O-, PO=-$CH_2(CH_3)CHO$-, MW 12600 g/mol), iron(III) acetylacetonate (97%, $Fe(C_5H_7O_2)_3$), manganese(II) acetate tetrahydrate (99.99%, $(CH_3COO)_2Mn.4H_2O$), HCl, C_2H_5OH and CH_3COOH were purchased from Sigma-Aldrich.

7.2.2. Preparation of mesoporous Mn-Fe-O nanocomposites

Mesoporous Mn/Fe oxides were synthesized through a simple one-step sol-gel process in the presence of the F127 triblock copolymer as a structure-directing agent. To homogenously distribute manganese nanoparticles into the Fe_2O_3 framework, we utilized a multicomponent assembly approach, wherein the surfactant, Mn and Fe_2O_3 were assembled in a single-step process. First, 2.4 g of F127, 2.3 mL of CH_3COOH and 0.74 mL of HCl were dissolved in 30 mL of ethanol, to which 2.28 g of $Fe(C_5H_7O_2)_3$ was added under magnetic stirring for 60 min. Next, the appropriate amounts of $(CH_3COO)_2Mn.4H_2O$ were added to the F127-$Fe(C_5H_7O_2)_3$-CH_3COOH mesophase to obtain manganese-to iron molar ratios of 0, 0.05, 0.1, 0.2, 0.3 and 0.5. The mixture was continuously stirred for 2 h and then transferred into a Petri dish. The ethanol was evaporated at 40 °C and a relative humidity of 40% for 12 h, followed by the transfer of the sample into a 65 °C oven and aging for an additional 24 h. The as-made mesostructured hybrids were calcined at 450 °C in air for 4 h at a heating rate of 1 °C/min and a cooling rate of 2 °C/min to remove the surfactant and to obtain mesostructured manganese-iron oxides at different molar ratios (x). The samples are hereafter referred to as xMnFe, where x = 0, 0.05, 0.1, 0.2, 0.3 and 0.5.

7.2.3. Characterization techniques

7.2.3.1. N_2 adsorption–desorption isotherms

Nitrogen adsorption-desorption isotherms were obtained with an Autosorb apparatus (Quantachrome Instruments) at liquid nitrogen temperature (-196 ºC). Prior to analysis, the samples were subjected to vacuum (10^{-5} mbar) at 200 ºC for 22 h to ensure a clean surface. The surface areas were calculated by the Brunauer-Emmett-Teller (BET) method using the adsorption data within the P/P_0 range from 0.05 to 0.30. The pore volumes were measured at a relative pressure P/P_0 of 0.95. The pore size distribution was analyzed using the Barrett-Joyner-Halenda (BJH) model.

7.2.3.2. High-resolution transmission electron microscopy (HRTEM)

Transmission electron microscopy **(**TEM) was conducted at 200 kV with a JEOL JEM-2100F-UHR field-emission instrument equipped with a Gatan GIF 2001 energy filter and a 1k CCD camera to record the EEL spectra. An energy dispersive X-ray microanalysis (EDX) system was used to verify the semi-quantitative composition of the supported phases. The prepared catalysts were ultrasonically dispersed in acetone at room temperature and then spread over a holey carbon-copper microgrid. At least ten representative images were recorded for each sample. To obtain statistically reliable information, the lengths of ca. 300 particles were measured.

7.2.3.3. X-ray diffraction (XRD)

X-ray diffraction (XRD) data were acquired on a Bruker AXS D4 Endeavour X diffractometer using Cu $K\alpha_{1/2}$, $\lambda\alpha_1$=154.060 pm, $\lambda\alpha_2$ = 154.439 pm radiation.

7.2.3.4. Temperature-programmed reduction (TPR)

TPR experiments were performed on powder samples. The samples (30 mg) were loaded in a U-shaped tubular quartz reactor heated by an electrical furnace on-line with a Micromeritics TPD/TPR 2900 apparatus. The calcined precursors were reduced with 50 mL(STP)/min of a 10 vol% H_2/Ar reducing mixture. The temperature was progressively increased from room temperature to 900 °C at a linear programmed rate of 10 °C/min. A cold trap was placed at the outlet of the reactor to collect the water. H_2

was used as a reference gas, and the consumption of hydrogen was measured by comparison of the thermal conductivity difference between the reference and the product gas.

7.2.3.5. X-ray photoelectron spectroscopy (XPS)

X-ray photoelectron spectra (XPS) were obtained using a VG Escalab 200R electron spectrometer equipped with a MgKα (hν = 1253.6 eV, 1 eV = 1.6302 x 10^{-19} J) X-ray source powered at 100 W. The kinetic energies of photoelectrons were measured using a hemispherical electron analyzer working in constant-pass-energy mode. High-resolution spectra were recorded by scanning narrow kinetic energy windows (20-35 eV) at a pass energy of 50 eV. The linearity of the energy scale was calibrated against the Au $4f_{7/2}$ (84.0 eV) and Cu $2p_{3/2}$ (932.6 eV) photoemission lines by standard procedures. The background pressure in the analysis chamber was kept below 2 x 10^{-9} mbar during data acquisition. The XPS signals were recorded in increments of 0.07 eV with dwell times of 40 ms. The binding energies (BE) were calibrated relative to adventitious carbon (C-C/C-H) using the C 1s peak at 284.8 eV. The peak intensities were estimated by calculating the integral of each peak after smoothing and subtraction of the Shirley background and fitting the experimental peak by a least-squares routine using Gaussian and Lorentzian lines (90G/10L). The atomic ratios were computed from the intensity ratios normalized by the atomic sensitivity factors [43].

7.2.4. Catalytic activity

The catalysts were tested in the CO_2 hydrogenation reaction using a fixed-bed stainless-steel reactor. The reactor temperature was measured with a K-type thermocouple buried in the catalytic bed. All pipes after the reactor outlet were kept at 130 °C. The reaction system was equipped with a stainless-steel hot trap set at 120 °C to collect the heavier products. The flow rates were controlled using a Brooks 5850 TR series mass flow controller. To facilitate the heat transfer and to prevent hot spots resulting from the exothermal character of the reaction, the calcined catalysts (200 mg) were diluted with SiO_2 (ca. 1.8 g). First, the catalysts were activated *in situ* at 400 °C (heating rate of 10 °C min^{-1}) for 5 h in pure hydrogen at atmospheric pressure. The reactor was then cooled to the reaction temperature (340 °C), after which the reactant gas mixture (23% CO_2/69% H_2/8% N_2) was flowed through the activated catalyst at a flow rate of 20 mL min^{-1} and the system was pressurized to 20 bar. This moment was considered the initial time of the reaction. Product analysis was performed on-line with a gas chromatograph (HP 6890 Plus). A Porapak Q (1/8" x 3 m)-packed column connected to a thermal conductivity detector was used to analyze the inorganic gases (H_2, N_2, CO, CO_2) and water. Hydrocarbons and oxygenated compounds were analyzed with a DB-1 capillary column (60 m x 0.25 mm) connected to a flame ionization detector. The following temperature program was used: -50 °C for 10 min, a 10 °C min^{-1} ramp up to 230 °C, and holding at this temperature for 20 min. N_2 was used as the internal standard for chromatographic analyses.

CO_2 conversion and selectivity to a given product are defined as follows:

$$X_{CO2} = [(\text{moles } CO_2)_{in} - (\text{moles } CO_2)_{out}]/(\text{moles } CO_2)_{in}] \text{ x } 100 \qquad [3]$$

$$S_i\ (\%) = \text{moles of } i \text{ product}/(\text{moles } CO_{2\ in} - \text{moles } CO_{2\ out}) \text{ x } 100 \qquad [4]$$

where X_{CO2} is the conversion of CO_2, S_i is the selectivity to product *i* and (moles $CO_2)_{in}$ and (moles $CO_2)_{out}$ are the number of moles of CO_2 at the reactor inlet and outlet, respectively.

7.3. Results

7.3.1. Textural properties

The nitrogen adsorption-desorption isotherms and the BJH desorption pore size distribution plots of xMnFe are shown in Figure 1, and the pore structure parameters are summarized in Table 1. Sample 0.05MnFe presented type IV isotherm patterns with an H3-type hysteresis loop, which are characteristic of mesoporous materials with cylindrical pores formed in gallery regions [44]. This proves that the 0.05MnFe sample exhibits a mesoporous structure. For this sample, the onset of the hysteresis loop occurs at high relative pressure (P/P_0 = 0.62), which corresponds to the beginning of capillary condensation in the pores. The upper closure point of the hysteresis loop, at which the pores are completely filled with liquid, is approximately P/P_0 = 0.99. In contrast, the other xMnFe (x = 0.1-0.5) samples show type IV isotherms with very thin H4 hysteresis loops, and the desorption branch of the isotherms of these samples extended to a lower pressure, suggesting a partial loss of structural organization and the formation of some narrower slit-shaped pores [45]. In addition, the 0.05MnFe displays a relatively narrow pore size distribution with maximum at 19.1 nm, however the pore size distribution for the other xMnFe samples are flat without any maximum (Figure 1C). Both the BET areas and pore volumes are approximately one order of magnitude lower than those of the parent 0.05MnFe sample. It is also emphasized that the pore size of the 0.05MnFe sample is only slightly higher (19.1 nm) than that of the other members of the series (11.1-17.4 nm) (Table 1).

Table 1. BET area, pore volume and pore size of mesoporous xMnFe samples

Catalyst	**BET area (m^2/g)**	**Pore vol (cm^3/g)**	**Pore size (nm)**
Fe_2O_3	4.0	0.021	17.4
0.05MnFe	34.4	0.179	19.1
0.1MnFe	1.5	0.004	11.7
0.2MnFe	7.6	0.031	13.3
0.3MnFe	2.9	0.009	11.1
0.5MnFe	4.1	0.019	15.2

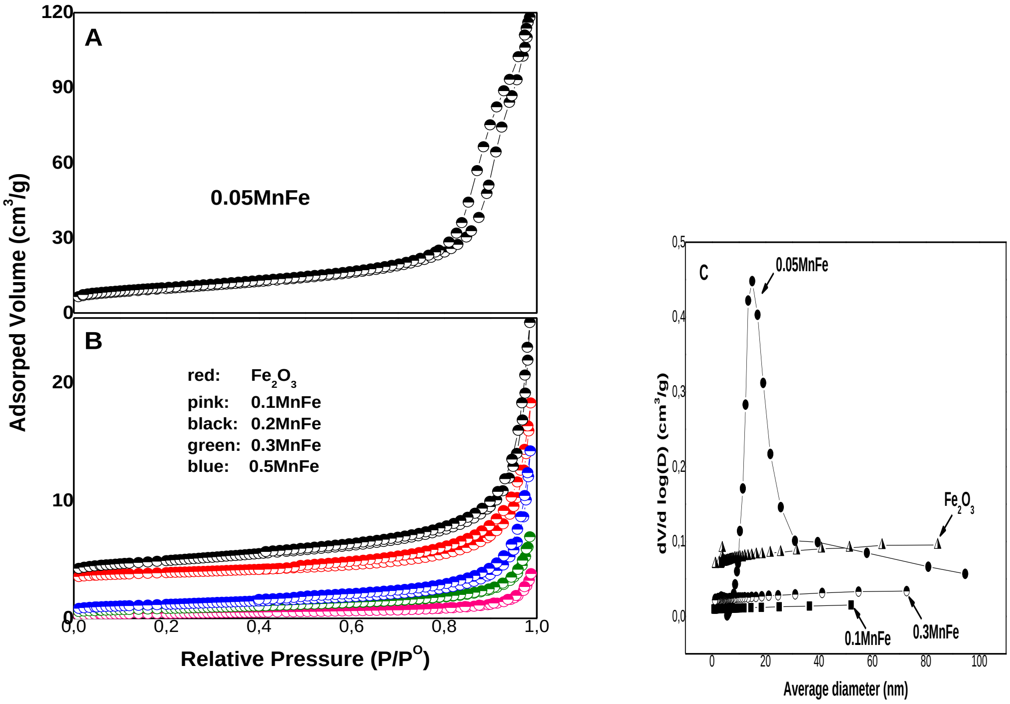

Figure 1. Nitrogen adsorption-desorption isotherms of (A) 0.05MnFe, (B) Fe_2O_3 and xMnFe samples with x = 0.10, 0.20, 0.30 and 0.50, and (C) Pore size distributions.

7.3.2. Morphology

The TEM images illustrate the morphology of the prepared mesoporous α-Fe_2O_3 and xMnFe nanocomposites at different molar ratios of 0.05 and 0.3 Mn/Fe oxides (Fig. 2). The TEM images revealed that α-Fe_2O_3 is comprised of uniform granular crystals with a particle size of ~15 nm, and a worm-like disordered arrangement of the mesoporous α-Fe_2O_3 nanoparticles was obtained (Fig. 2a). At high magnification, the α-Fe_2O_3 nanoparticles are quite uniform in size and spherical in shape (Fig. 2b). Selected area electron diffraction (SAED) pattern (Fig. 2c, inset) further confirms that α-Fe_2O_3 nanocrystals are progressively formed. When Mn was added to α-Fe_2O_3 nanoparticles at molar ratio of 0.05, TEM images at low and high magnification show worm-like pore shapes and consist of uniform nanoparticles with sizes of about 20 nm (Fig. 2d and e). With increasing Mn/Fe molar ratio to reach 0.3, TEM images show assembled agglomerations of nanoparticles with mesoporosity structure (Fig. 2g) as confirmed by the observation of solid irregular elliptical α-Fe_2O_3 nanoparticles (Fig. 2h) with an average diameter of ~40-50 nm (Fig. 2g and h). It is clearly seen that the particle sizes gradually increases with increasing Mn/Fe molar ratio. Energy dispersive X-ray (EDX) spectra of the α-Fe_2O_3 and 0.3MnFe samples, with the latter being consistent with the Mn:Fe ratio used in the starting sol mixtures (Fig. 2j and k). The atomic planes of the α-Fe_2O_3 nanoparticles are separated by 3.7 Å, which agrees with the (012) crystallographic planes of α-Fe_2O_3 in the obtained composites (Fig. 2c, f and i).

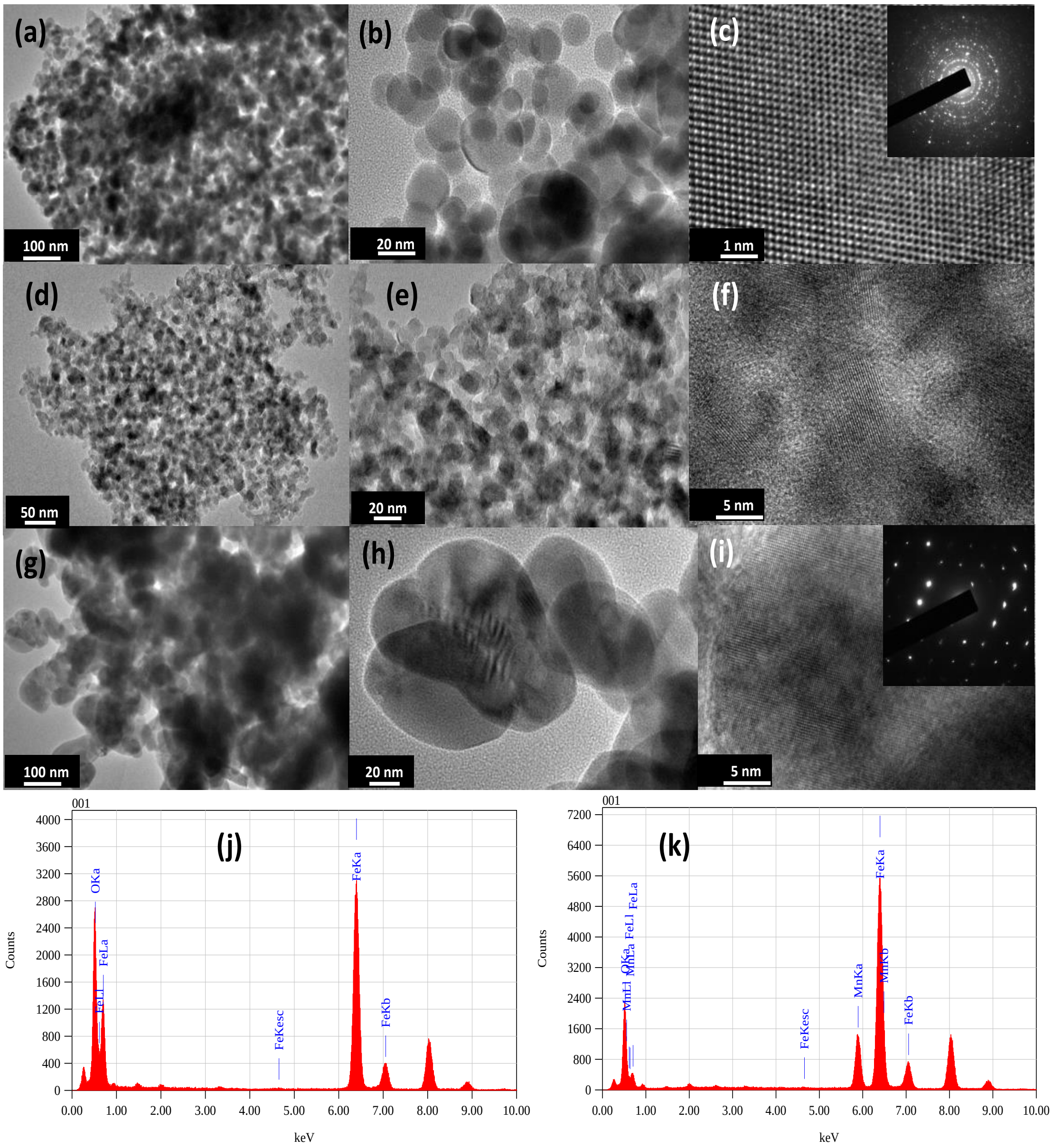

Figure 2. TEM images of mesoporous α-Fe_2O_3 at low and high magnifications (a,b); HRTEM image of α-Fe_2O_3 and the insets show the SAED patterns for the α-Fe_2O_3 (c); 0.05MnFe nanocomposites at low and high magnifications (d,e); HRTEM image of 0.05 MnFe nanocomposite (f), 0.3MnFe nanocomposite at low and high magnifications (g,h); HRTEM image of 0.3MnFe nanocomposites and the insets show the SAED patterns for the α-Fe_2O_3 (i). EDX spectra of α-Fe_2O_3 and 0.3 xMnFe (j,k).

7.3.3. Structural characteristics

Figure 3 shows the X-ray diffraction patterns of the synthesized α-Fe_2O_3 and xMnFe nanocomposites at different molar ratios of x = 0.05, 0.1, 0.2, 0.3 and 0.5. The XRD patterns of the α-Fe_2O_3 and xMnFe nanocomposites correspond to a hexagonal structure of α-Fe_2O_3 with structural parameters of a = b = 5.038 Å, c = 13.772 Å, which are in good agreement with the recorded values of JCPDS File Card No. 33-0664. The obvious peaks at (012), (104) and (110) suggest that the obtained α-Fe_2O_3 that the obtained α-Fe_2O_3 was well-crystallized. The intensity of the (104) peak was higher than that of the (110) peak in all prepared samples, as shown in Figure 3. It clearly seen that the prepared samples can be mainly investigated as α-Fe_2O_3, trace amount of maghemite and amorphous Mn oxides (Fig. 3). In addition, there is no trace maghemite at 0.05 Mn/Fe sample. This is explained by at low Mn content, the prepared sample is almost magnetite and amorphous Mn oxides, however, maghemite phase appeared as a result of a trace phase transformation. No manganese oxide phases can be observed, suggesting that the manganese oxides are highly dispersed in the α-Fe_2O_3 network. However, XPS investigation (see below) confirmed that an amorphous MnOx phase covers the α-Fe_2O_3 nanoparticles.

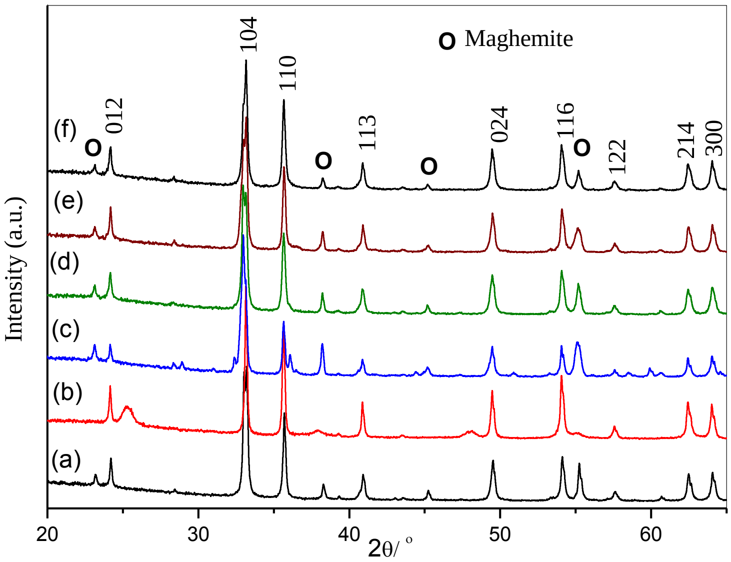

Figure 3. XRD of α-Fe_2O_3 and xMnFe nanocomposites at different molar ratios of 0.05 (b),0.1(c), 0.2(d), 0.3(e) and 0.5(f) calcined at 450 °C for 4 h. Shifted for sake of clarity.

7.3.4. Reducibility

The reducibility of the calcined xMnFe samples was investigated by TPR experiments, and the reduction profiles are displayed in Figure 4. The reduction profile of the Mn-free Fe_2O_3 sample shows only an asymmetric reduction peak with a maximum at approximately 730 °C. The TPR profiles of 0.2MnFe, 0.3MnFe and 0.5MnFe are quite similar to one another but somewhat different from that of Fe_2O_3: they show a very small H_2 consumption peak at approximately 610 °C, associated to reduction of Mn^{4+} into Mn^{3+}, and a very intense peak at approximately 710 °C, with a tail extending toward higher temperatures in the cases of 0.2MnFe and 0.5MnFe. However, the reduction profile of sample 0.05MnFe is quite different, being rather broad with a maximum at approximately 570 °C (150 °C below that observed for the Mn-free sample).

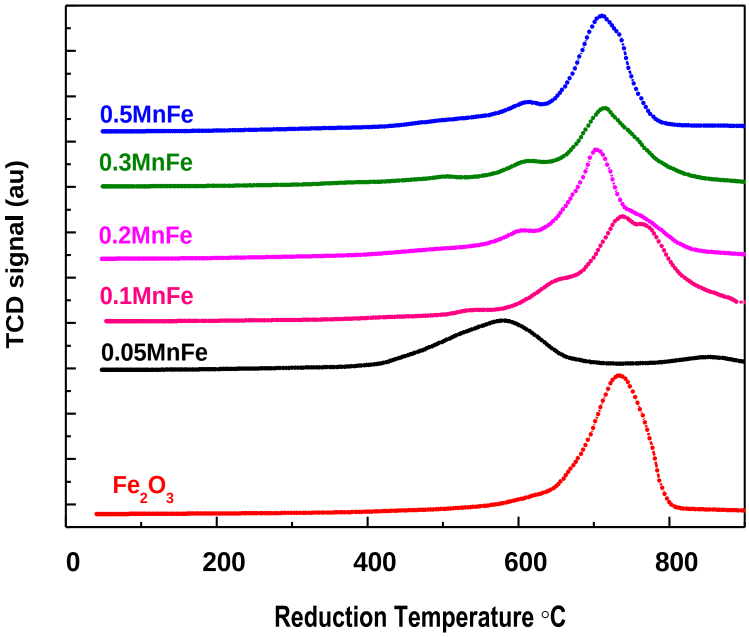

Figure 4. TPR profiles of xMnFe nanocomposites at different Mn/Fe ratios.

To quantify the extent of sample reduction up to a maximum reduction temperature of 900 °C, the TCD was calibrated, and the H_2 consumption was evaluated for all the xMnFe (x = 0-0.5) samples. Table 2 presents the H_2 consumption during reduction for all these samples. The maximum H_2 consumption occurs for the Fe_2O_3 sample (1.70 x

10^{-4} mol), decreasing somewhat for samples 0.5MnFe (1.53 x 10^{-4} mole), 0.3MnFe (1.32 x 10^{-4} mole) and 0.2MnFe (1.59 x 10^{-4} mole). Sample 0.05MnFe exhibited the lowest H_2 consumption (0.94 x 10^{-4} mole). To determine the reduction extent, the theoretical H_2 consumption values were evaluated assuming that Fe_2O_3 is completely reduced to Fe metal and that the initial manganese oxide is a spinel Mn_3O_4 that is reduced to MnO according to the following equations:

$$Fe_2O_3 \rightarrow Fe_3O_4 \rightarrow FeO \rightarrow Fe \quad [5]$$

$$Mn_3O_4 \rightarrow MnO \quad [6]$$

The theoretical H_2 consumptions expected for complete reduction according to these two equations are also compiled in Table 2. The comparison of the experimental H_2 consumption with the theoretical values indicates that metallic Fe is not reached up to a maximum temperature of 900 ºC in any of the cases. This is clearly illustrated by the relatively low extent of reduction observed for the Mn-free sample (Fe_2O_3), in which the reduction progressed only up to FeO and no metallic Fe was formed.

Table 2. H_2 consumption during TPR experiments

Catalyst	**Theor. H_2 consumption (mol x 10^{-4})**	**Exp. H_2 consumption (mol x 10^{-4})**
Fe_2O_3	2.82	1.7
0.05MnFe	2.74	0.94
0.1MnFe	2.66	1.09
0.2MnFe	2.48	1.59
0.3MnFe	2.28	1.32
0.5MnFe	1.82	1.53

7.3.5. Surface analysis

Photoelectron spectroscopy was employed to reveal the chemical states and the relative concentrations of Mn and Fe on the surface of calcined xMnFe samples. For all the samples, high-resolution Fe 2p, Mn 2p and O 1s spectra were recorded, and that of the representative 0.3MnFe sample is displayed in Figure 5. Moreover, the corresponding binding energies of the Fe $2p_{3/2}$, Mn $2p_{3/2}$ and O 1s core levels are summarized in Table 3.

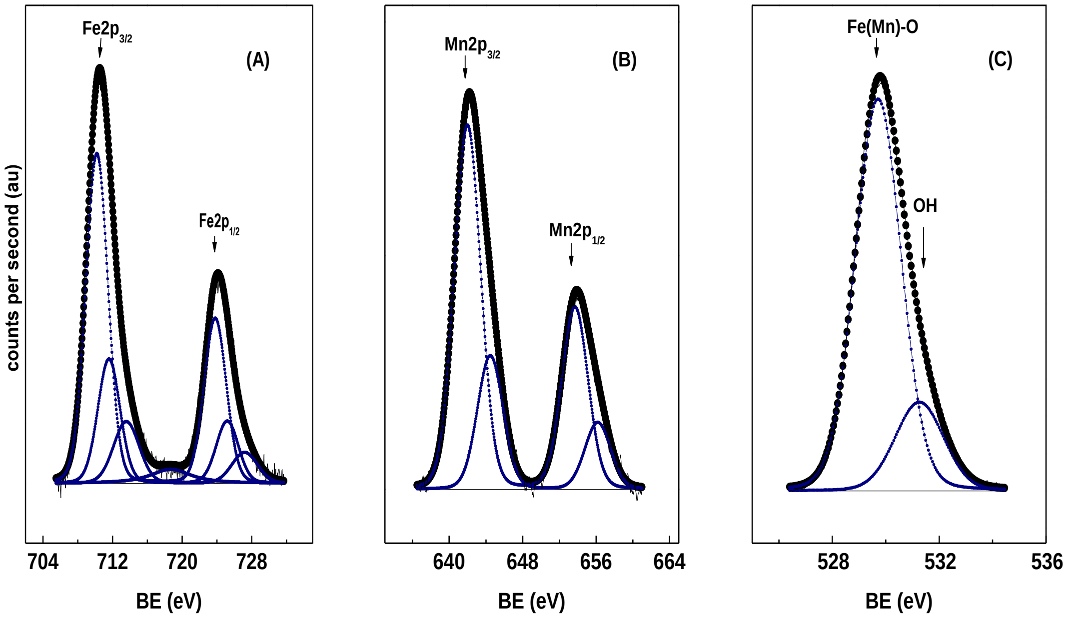

Figure 5. Fe 2p (A), Mn 2p (B) and O 1s (C) core-level spectra of the representative 0.3MnFe sample.

The binding energy of the most intense Fe $2p_{3/2}$ component of the Fe 2p doublet of the Mn-free sample (Fe_2O_3) appears at 710.9 eV, which is typical of Fe^{3+} ions in an environment of oxide ions [46]. In addition, this sample and all other xMnFe samples show a small satellite line situated at approximately 718.9 eV, which is the fingerprint of Fe^{3+} ions. The data collected in Table 3 also indicate that the BE of the Fe $2p_{3/2}$ peak of the other xMnFe samples is slightly lower (710.1-710.4 eV) than that of the Mn-free sample. For these xMnFe (x = 0.05-0.50) samples, the most intense Mn $2p_{3/2}$ peak of the doublet showed a similar BE value of 641.7-642.0 eV regardless of Mn content. Regarding the Fe 2p peaks, the Mn 2p lines show an asymmetric shape on the high-binding-energy side, which is associated with final state effects and therefore ignored. The BEs values of the Mn $2p_{3/2}$ component (Table 3) suggest that manganese could be present in the oxidation state Mn^{3+}; however, due to the close proximity of the BEs of Mn^{3+} and Mn^{4+}, precise assignment is not possible by considering only the energies recorded for the 2p core levels. Unambiguous assignment of the oxidation state of manganese oxides can be obtained by recording the Mn 3s level. Therefore, the multiplet Mn 3s core-level spectrum was also recorded for all Mn-containing xMnFe samples (spectra not shown here). This spectrum arises from the exchange interaction between the core level electron (Mn 3s) and the unpaired electrons in the valence band level (Mn 3d) by photoelectron ejection [47]. The splitting energy (ΔE) of the Mn 3s level of the xMnFe samples is in the range 5.5-5.4 eV. According to [48,49], these values allow the calculation of the average oxidation state of Mn in the xMnFe samples as 2.6-2.7, which suggests that both Mn_2O_3 and Mn_3O_4 coexist on the surface region of the xMnFe catalysts.

The binding energies of the O 1s core level spectra of xMnFe samples are also summarized in Table 3. The O 1s spectra consist of two O-containing bonds: metal oxide (Mn-O-Mn and Fe-O-Fe) at 529.3-530.3 eV and hydroxyl groups (Mn(Fe)-OH) at 531.5-531.7 eV [50]. No peak was detected at a binding energy somewhat above 533.0 eV, characteristic of adsorbed molecular water, indicating that the samples are completely dried. The hydroxyl content was rather low (16-23% of total oxygen). Quantification of surface species was also achieved using the XPS spectra. From the intensity ratios (I_{Mn}/I_{Fe}) of the spectra, which were normalized by atomic sensitivity factors [43], atomic Mn/Fe ratios were computed, and the values are collected in Table 3 (last column). These values clearly indicate that Mn is strongly segregated toward the surface. Thus, the iron oxide nanoparticles are likely covered, at least to some extent, by an amorphous MnO_x phase.

Table 3. Binding energies (eV) of the core levels of xMnFe samples

Sample	**Fe $2p_{3/2}$**	**Mn $2p_{3/2}$**	**O 1s**	**Mn/Fe at**
Fe_2O_3	710.9	-	530.3 (79) 531.7 (21)	-
0.05MnFe	710.3 (70) 711.6 (30)	641.9	529.7 (77) 531.5 (23)	0.246
0.1MnFe	710.2 (74) 711.6 (26)	642.0	529.7 (81) 531.5 (19)	0.318
0.2MnFe	710.3 (57) 711.5(43)	642.0	529.7 (80) 531.4 (19)	0.561
0.3MnFe	710.4 (68) 711.6 (32)	642.0	529.7 (84) 531.5 (16)	0.712
0.5MnFe	710.1 (45) 711.6 (55)	641.7	529.6 (83) 531.2 (17)	0.795

Values in parentheses are peak percentages

7.3.6. Catalytic performance

The CO_2 hydrogenation performances were investigated for xMnFe catalysts with different Mn loading to study the effect of Mn loading in the hydrogenation of CO_2 toward valuable products. Moreover, the CO_2 hydrogenation reaction was performed with the Mn-free (pure Fe_2O_3) catalyst for comparison. Figure 6 illustrates the CO_2 conversion as a function of time on stream for the xMnFe catalysts. It is apparent that for all the catalysts tested under the selected reaction conditions (340 °C, 20 bar and a 23% CO_2/69% H_2/8% N_2 reactant mixture), a pseudo-stationary state is reached after approximately 5 h on stream. Nevertheless, the CO_2 conversion profiles differ by the value of x. The catalyst with the lowest Mn content (0.05MnFe) once activated maintains essentially constant CO_2 conversion over the time on-stream of 48 h. However, the other catalysts, with atomic ratios x higher than 0.05, show a complex behavior in which the CO_2 conversion drops slightly at times on-stream in the range 5-

15 h and then progressively increases without reaching a plateau by the end of the duration test (48 h). These observations suggest that catalyst activation involves three different processes: (i) a fast initial activation; (ii) a subsequent slight drop in the FTS rate, due very likely to slower FTS rate as compared to the carbidation rate; and (iii) slow increase of the FTS rate as a consequence of the higher concentration of active C* species available on the surface when carbidation level is high. The activity profiles also indicate that a small amount of Mn (as used in the 0.05MnFe catalyst) drastically improves the performance (30% CO_2 conversion) with respect to the Fe_2O_3 catalyst (ca. 12% CO_2 conversion). However, a further increase in the Mn/Fe molar ratio (0.2MnFe and 0.5MnFe catalysts) inhibited CO_2 hydrogenation activity. This is illustrated by the CO_2 conversions of 16.5 and 10% achieved by the 0.2MnFe and 0.5MnFe catalysts, respectively.

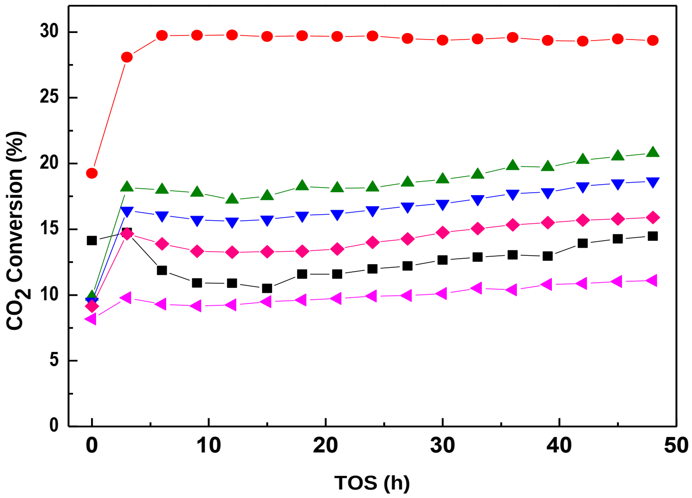

Figure 6. Percentage of CO_2 conversion of different xMnFe catalysts as a function of time on-stream (reaction conditions: 340 °C, 20 bar, CO_2:H_2:N_2 = 23:69:8 (molar)). (■) Fe_2O_3; (●), 0.05MnFe; (▲) 0.1MnFe; (▼) 0.2MnFe; (♦) 0.3MnFe; and (◀) 0.5MnFe.

It is worth mentioning that the CO_2 conversion obtained using the 0.5MnFe catalyst is lower than that using the Mn-free (Fe_2O_3) catalyst. Based on these results on the effect of the Mn/Fe molar ratio in the range x = 0.05-0.50, it is evident that only a very small amount of Mn (as used in the 0.05MnFe catalyst) strongly promoted the CO_2

hydrogenation toward hydrocarbon formation and led to the optimum activity. The drop in catalytic activity with increasing Mn content in the catalyst formulation could be due to partial coverage of the active sites, i.e., Fe carbide phases, by the amorphous Mn oxide/carbide phases, which in turn prevent the reactant from making contact with the active centers.

Figure 7 shows the CO and hydrocarbon selectivities including oxygenated components, and Table 4 compiles the product selectivities, including the olefins/paraffins ratio. It is worth mentioning that the hydrocarbon selectivities (HC) are reported here on a CO-free basis. Compared to the Mn-free (Fe_2O_3) catalyst, the 0.05MnFe catalyst inhibited CH_4 formation to some extent. For the 0.05MnFe catalyst, the CO selectivity was approximately 8%, which is much lower than the value of 32% recorded for the Fe_2O_3 catalyst.

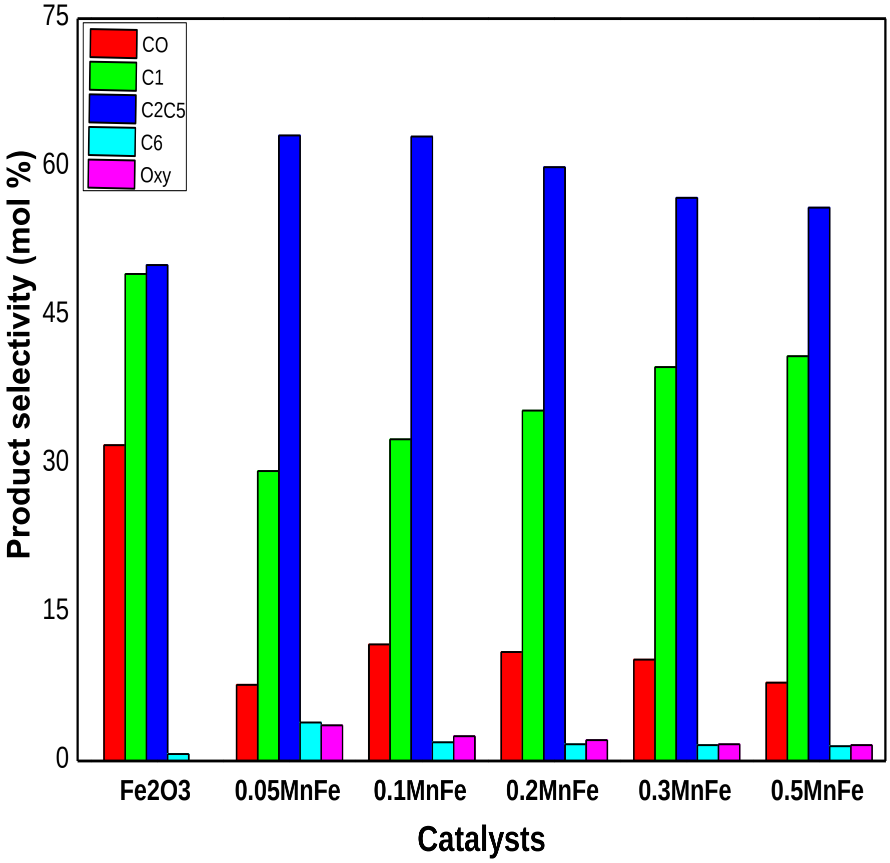

Figure 7. CO, hydrocarbon and oxygenate selectivity for all the xMnFe catalysts (reaction conditions as in Figure 6).

Table 4. Product selectivity and olefin/paraffin ratio of the xMnFe catalysts

Catalyst	**Fe_2O_3**	**0.05MnFe**	**0.1MnFe**	**0.2MnFe**	**0.3MnFe**	**0.5MnFe**
CO	31.9	7.7	11.8	11	10.2	7.92
C_1	49.2	29.3	32.5	35.4	39.8	40.9
C_2-C_5	50.1	63.2	63.1	60	56.9	55.9
C_{6+}	0.7	3.9	1.9	1.7	1.6	1.5
Oxy	0	3.6	2.5	2.1	1.7	1.6
O/P	0.31	0.37	0.40	0.49	0.7	0.79

Reaction conditions as in Figure 6. Carbon balance was in all cases between 93 and 99 %.

Moreover, this catalyst promoted the formation of valuable hydrocarbons, such as C_2-C_5, higher-molecular-weight hydrocarbons (C_{6+}) and oxygenated products. From the data compiled in Table 4, it is clear that the Mn loadings higher than x = 0.05 are detrimental to the production of useful products. In those catalysts, the selectivity to CH_4 increases at the expense of valuable product formation, such as C_2-C_5, C_{6+} and oxygenates. The only advantage of the xMnFe (x > 0.05) catalysts is their higher effectiveness for increasing the olefin/paraffin ratio.

Chain growth probability (α) was calculated (Figure S1) and its values of some representative catalysts are summarized in Table S1. The lowest α value (0.30) was recorded for the Mn-free (x = 0) catalyst, then increased for 0.05MnFe (0.43) and finally decreased for 0.2MnFe (0.35) and 0.5MnFe (0.33). It has been reported that since CO_2 hydrogenation follows a reaction mechanism similar to that of CO hydrogenation (with a previous CO_2 shift reaction) [53,54], the product distribution for both reactions should be very similar when using the same catalyst and reaction conditions. The relatively low values of chain growth probability measured in this work can be explained in terms of the low residence time employed in the reaction tests.

7.3.6.1. Structural and surface characteristics of used catalysts

The nature of surface species in Fe-based catalysts changes dramatically when exposed to the reaction employed in the CO_2 hydrogenation reaction. Characterization of both surface and bulk structures by XPS and XRD techniques demonstrated that α-Fe_2O_3 is the principal crystalline phase present in xMnFe catalyst precursors (cf. Figures 3 and 5). However, this α-Fe_2O_3 phase disappeared completely and new ones were developed in the xMnFe catalysts exposed to the reactant mixture (23% CO_2/69% H_2/ 8% N_2) at 300 ºC, 20 bar overall pressure for a time on-stream of 48 h.

The XRD patterns of some representative used xMnFe catalysts are displayed in Figure 8. These patterns show diffraction lines at 39.3°, 40.9°, 43.9°, 44.9° and 47.2° assigned to iron carbide (Hägg carbide, χ-Fe_5C_2) [51] and other diffractions at 30.1°, 35.5°, 37.1°, 57° and 62.6° typical of magnetite (Fe_3O_4) [53]. It is known that magnetite is responsible for the RWGS reaction, whereas iron carbide is highly catalytically active for FTS [53]. In addition, diffraction lines belonging to graphitic carbon together with lines of an unidentified species are clearly distinguished. It is also observed in Figure 8 that the number and intensity of the diffraction lines increase with the value of x. This indicates that the extent of formation of iron carbide(s) and phases depend of the Mn content of the catalysts. As the diffraction lines of crystalline χ-Fe_5C_2 were almost absent in the Mn-free (Fe_2O_3) catalysts, it is suggested that manganese oxide accelerates the generation of the χ-Fe_5C_2 phase in the catalysts maintained for 48 h on-stream [54].

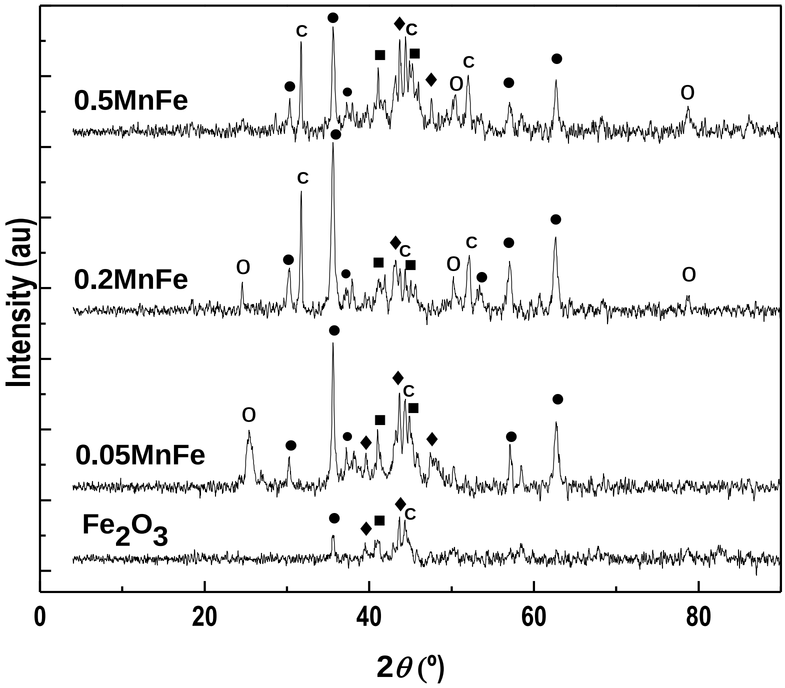

Figure 8. XRD patterns for the used catalysts with different manganese contents. Reaction conditions: 340 °C, 20 bar, CO_2:H_2:N_2 = 23:69:8 (molar) for 48h. (●) magnetite; (♦) carbide; (■) magnetite and carbide; (c) carbon; (○) unknown phase.

The nature of surface species of used xMnFe catalysts was investigated by XPS . The binding energies of core-levels and surface atomic ratios are summarized in Table S2. The Fe 2p spectra of used xMnFe catalysts were satisfactorily fitted to two components: a major one at a binding energy of 710.5-710.7 eV associated to Fe_3O_4 and a minor one at 708.1-708.3 eV which is characteristic of the Hägg carbide (χ-Fe_5C_2). The Fe 2p spectra of some representative catalysts are displayed in Figure 9A. These spectra show clearly that the intensity of the Fe 2p doublet of carbide species is maximum for the Mn-free sample and then decreases progressively upon increasing x. Moreover, the C ls core-level spectra of used xMnFe catalysts exhibited three components (Figure 9B) at binding energies of: 284.8 eV due to sp^3 C from contamination, 283.1-283.4 eV associated to carbidic carbon and at ca. 281.3 eV originated by graphitic carbon [55, 56].

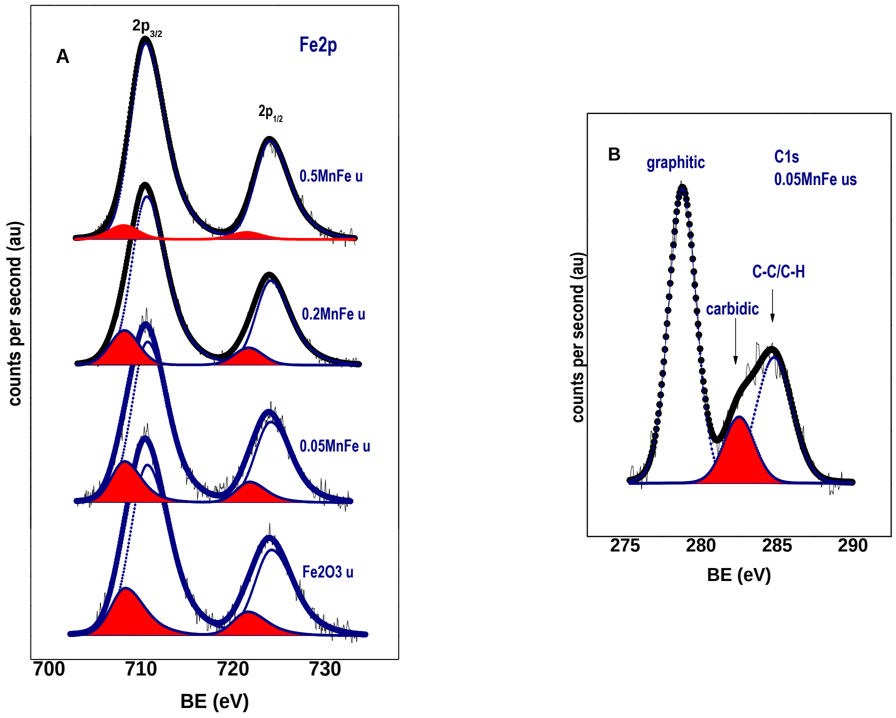

Figure 9. (A) Fe 2p core-level spectra of some used xMnFe catalysts. The minor Fe 2p doublet in red color refers to iron carbide species. (B) C 1s spectrum of the representative 0.05MnFe used catalyst. The different carbon species are indicated by arrows.

Atomic C/Fe ratios were also computed from the C 1s and Fe 2p core-level spectra and results are also compiled in Table S2. In this calculation, only carbidic iron and carbidic carbon components were selected for such calculations. It can be noted that the average C/Fe ratio of carbidic species is 0.49, slightly higher than the nominal value expected for the Hägg carbide (χ-Fe_5C_2) whose nominal value is 0.40. This result suggests that the most abundant iron carbide phase in used xMnFe catalyst is the χ-Fe_5C_2 phase. Table S2 also summarizes the Mn/Fe atomic ratios of used catalyst. The values of these ratios are higher than that reported in Table 3 for the fresh (oxidic) samples, suggesting than additional segregation of manganese oxides toward the surface occurs during the carbidation of the catalysts during on-stream operation.

7.4. Discussion

7.4.1. Catalysts structure

As prepared, the xMnFe catalysts consist of a crystalline α-Fe_2O_3 phase and amorphous Mn oxides. The EDX spectra indicated the presence of Fe and Mn elements and confirmed that the final xMnFe nanocomposite structures are consistent with the nominal Mn/Fe ratios. Notwithstanding, the highly sensitive XPS technique demonstrated that all the catalyst surfaces became Mn-enriched. There is no contradiction between the information provided by the EDX and XPS techniques, but the latter is surface-sensitive and thus obtains structural information from a low number of atomic layers beneath the surface layer, typically approximately 3 nm, whereas the X-rays recorded in the EDX technique originate from depth of a few micrometers. Therefore, Mn enrichment is only confined to a few atomic layers (surface and sub-surface layers).

Perhaps the most relevant differences among the xMnFe catalyst series are the much higher BET area and easier reduction of the 0.05MnFe catalyst. The lower BET area for the other xMnFe catalysts with $x > 0.05$ suggests that the template approach employed here is not appropriate for high Mn loading. It is emphasized that the ease with which the 0.05MnFe catalyst is reduced compared to the other catalyst members of the series is essential, as it could favor the carbidation of Fe oxide phases. As will be shown in the next section, the 0.05MnFe catalyst is fully activated during the first 5 h on stream, and its performance remains stable throughout the 48-h duration of the test.

7.4.2. Effect of Mn on performance

It is known that the formation of hydrocarbons from CO_2 takes place via the two-step mechanism of the RWGS reaction and FT reaction [57]. Over Fe catalysts, CO is an important reaction intermediate in the conversion of CO_2 to higher hydrocarbons over Fe-based catalysts [58]. However, the unpromoted Fe-based catalysts are not selective for the desired FT products. Manganese is one of the promoters of Fe catalysts investigated in some detail because it influences the selectivity to higher hydrocarbons. From a mechanistic viewpoint, manganese not only improves the reducibility of iron oxide but also modifies the distribution of iron species and catalyst basicity [22,41]. The data shown in Figure 7 and Table 3 indicate unambiguously that the positive effect of Mn is only valid in a limited concentration range. Manganese-to-iron ratios higher than 0.05 appear detrimental for the production of useful C_2-C_5, C_{6+} and oxygenated products due to increasing CH_4 formation (cf. Table 3) and decreasing CO_2 conversion. A possible reason for this effect may be that high manganese loadings and particularly the highly segregated manganese oxide on the surface (cf. Tables 3 and S2) limit the accessibility of reactants to the active Fe phase. Thus, to maintain the performance of the Fe active phases, it is essential to avoid or minimize the coverage/blockage of such phases by the amorphous MnO_x phases.

In the course of CO_2 hydrogenation, it was demonstrated that CO formation is the essential step for producing C_{2+} hydrocarbons with high conversion and selectivity. The higher performance of the 0.05MnFe catalyst for the RWGS reaction would certainly contribute to the increase in the C_{2+} hydrocarbon formation from CO_2 under 20 bar of overall pressure. The selectivity to CH_4 in hydrocarbons decreases greatly for the 0.05MnFe catalyst, while the selectivity to C_2-C_5 hydrocarbons follows an opposite trend. This could be associated to the preference for the adsorption of CO_2 rather than H_2 on this catalyst; however, H_2 is expected to diffuse better than CO_2 toward the active phase when higher amounts of Mn are incorporated ($x > 0.05$). For these catalysts, the relative low CO_2/H_2 ratio on the active sites would most likely favor methane formation. It is reported that olefins are formed as a primary product over paraffins and undergo hydrogenation in the secondary steps [59]. Although it is expected that the CO_2/H_2 ratio reaching the active sites is relatively high, the overall H_2 concentration should be lower than for its 0.05MnFe counterpart, a favorable olefin formation condition. This tendency was observed in the finding of an improved selectivity toward olefins in the C_2-C_5 fraction for high values of x.

7.4.3. Insights into the nature of the active phase

It is generally accepted that iron carbides, rather than metallic iron or iron oxides, are the active species in FT synthesis reactions [60-63]. Under FTS reaction temperatures as high as the one employed in this work (340 ºC), many reports agreed that the active phase is χ-Fe_5C_2 carbide, whereas θ-Fe_3C carbide is a deactivation or spectator phase [64]. According to a volcano plot for metal-CO bond strength versus FT activity for Fe (and Co) catalysts, increasing the carbon content in iron carbide will weaken the Fe-CO bonding and therefore enhance catalyst activity.

The results reported here allow to firm conclusions to be drawn on the type of iron carbide developed on catalyst surface. The Fe 2p spectra of representative catalysts used in CO_2 hydrogenation for 48 h on-stream (Figure 9A) unambiguously demonstrate that the Hägg carbide (χ-Fe_5C_2) is the major carbide phase developed on the catalyst surface. However, very likely other iron carbide phases may be also present as one would infer from the plethora of diffraction lines observed in used catalysts, and specially for the catalysts with $x > 0.05$. Moreover, other iron carbides different from χ-Fe_5C_2 are expected to display very similar binding energies of the most intense Fe $2p_{3/2}$ line of the Fe 2p doublet, The data displayed in Figure 6 clearly indicate that the catalyst 0.05MnFe became carbided in approximately 5 h using the $H_2/CO_2/N_2$ mixture under 20 bar overall pressure and maintained stationary-state conversion for the duration of the test (48 h on stream). In contrast, the other xMnFe catalysts, including Fe_2O_3, were initially carbided over the first 5 h but were then slowly deactivated for approximately 10 additional hours, very likely by the accumulation of carbon. At longer times, another slow carbidation process took place. It is also noted that no stationary state could be reached during the testing period (48 h). As noted above, with the exception of 0.05MnFe catalyst, all catalysts displayed very low specific areas, which might impede carbon diffusion and therefore make carbidation an extremely slow process.

7.5. Conclusions

Manganese-iron oxide (xMnFe, x = 0-0.5) catalysts were prepared by a template approach and then tested in the hydrogenation of CO_2 into hydrocarbons/oxygenate products. The results obtained lead to the following conclusions. (i) Only the 0.05MnFe catalysts exhibited a mesoporous structure and moderately high BET area. (ii) Surface analysis by XPS showed a Mn-enriched surface (in a ca. 3-nm region). (iii) The 0.05MnFe catalyst was found to be reduced at much lower temperatures (maximum at 570 ºC) than the other members of the series (maximum at approximately 730 ºC) and was also easily carbided during the activation step. (iv) Under fixed reaction conditions (20 bar, 340 ºC, CO_2:H_2:N_2 = 23:69:8 (molar)), the Mn loading was found to exert a strong influence on CO_2 conversion and selectivity to different products. (v) The 0.05MnFe catalyst displayed the best performance with reduced CO and CH_4 formation and improved selectivity to C_2-C_5 and C_{6+} hydrocarbons as well as the formation of some oxygenates.

ASSOCIATED CONTENT

Supplementary Information

ASF Product Distribution

The product distribution of hydrocarbons in FTS can be described by the Anderson-Schulz-Flory (ASF) equation:

$$Wn/n = (1-\alpha)^2 \cdot \alpha^{n-1} \qquad \text{[Eq S1]}$$

where Wn is the mass fraction of a hydrocarbon (HC) with chain length n and the growth probability factor α is assumed to be constant. α determines the total carbon number distribution of the FT products. Experimental values are displayed in Figure S1. According to Eq S1, a plot of the logarithm of Wn/n versus n results in a straight line plot whose slope is related to α.

Eq S1 has been linearized nad the experimental results are collected in Figure S1. In addition, chain growth probability values were calculated from the linear part of the plots and they are compiled in Table S1 (last column). In addition, Table S1 summarizes the major crystalline phases detected in the xMnFe catalysts used in CO_2 hydrogenation reaction for 48 h under fixed reaction conditions.

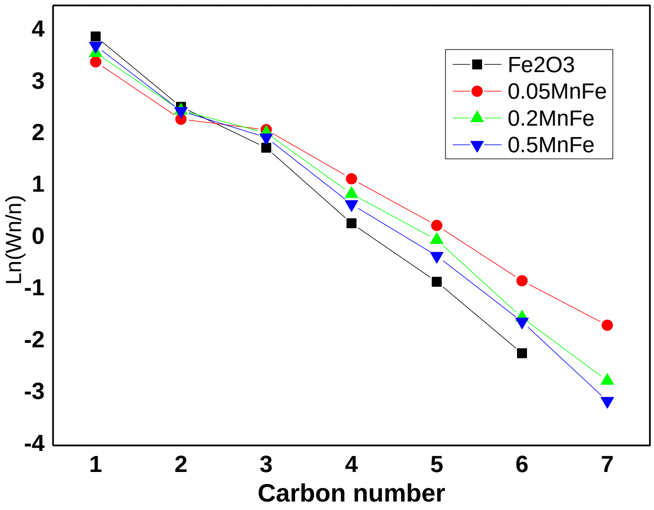

Figure S1. Anderson-Schulz-Flory distribution of the hydrocarbons obtained during the CO_2 hydrogenation under fixed reaction conditions: 340 °C, 20 bar, CO_2:H_2:N_2 = 23:69:8 (molar).

Table S1. Main crystalline phases and chain probability growth of some representative catalysts used on stream for 48 h

catalyst (used 48 h on-stream)	**main crystalline phases**	**chain growth probability (α)**
Fe_2O_3	graphite C, Fe_3O_4, χ-Fe_5C_2,	0.30
0.05MnFe	graphitic C, Fe_3O_4, χ-Fe_5C_2, unknown phase	0.43
0.2MnFe	graphitic C, Fe_3O_4, χ-Fe_5C_2, unknown phase	0.35
0.5MnFe	graphitic C, Fe_3O_4, χ-Fe_5C_2, unknown phase	0.33

XPS Analysis of used catalysts

Table S2 summarizes the bindig energies (eV) and C/Fe and Mn/Fe surface atomic ratios of xMnFe catalysts used in the CO_2 hydrogenation reaction for 48 h on-stream.

Table S2. Binding energies of core-level spectra and surface atomic ratios of some representative xMnFe catalysts used in the CO_2 hydrogenation reaction

	Fe $2p_{3/2}$	**Mn $2p_{3/2}$**	**C1s**	**O1s**	**C/Fe at***	**Mn/Fe at**
Fe2O3 us	708.3 (18) 710.7 (82)	-	281.5 (7) 283.4 (12) 284.8 (81)	529.6 (21) 532.4 (79)	0.51	-
0.05MnFe us	708.3 (14) 710.7 (86)	640.8	281.3 (10) 283.5 (11) 284.8 (79)	529.4 (26) 532.4 (74)	0.49	0.628
0.2MnFe us	708.2 (10) 710.6 (90)	641.0	281.4 (14) 283.6 (9) 284.8 (77)	529.6 (33) 531.8 (67)	0.46	0.849
0.5MnFe us	708.1 (8) 710.5 (92)	640.8	281.5 (15) 283.6 (8) 284.8 (77)	529.7 (30) 532.0 (70)	0.49	0.952

Only carbidic C and iron carbide species were considered in this calculation

Acknowledgments

This research was supported by Najran University, Najran, The Kingdom of Saudi Arabia.

7.6. Referencesç

[1] Z. Jiang, T. Xiao, V.L. Kuznetsov, P.P. Edwards, Philosophical Transactions of the Royal Society A 368 (2012) 3343.

[2] M. Aresta, A. Dibenedetto, Dalton Transactions 28 (2007) 2975.

[3] G. Centi, S. Perathoner, Catalysis Today 148 (2009) 191.

[4] G.A. Olah, Angewandte Chemie-International Edition 44 (2005) 2636.

[5] Q. Wang, J. Luo, Z. Zhong, A. Borgna, Energy and Environmental Science 4 (2011) 42.

[6] A.J. Hunt, E.H.K. Sin, R. Marriott, J.H. Clark, ChemSusChem 3 (2010) 306.

[7] A. Goeppert, M. Czaun, G.K.S. Prakash, G.A. Olah, Energy Environmental Science 5 (2012) 7833.

[8] R. Ladera, F.J. Perez-Aonso, J.M. Gonzalez-Carballo, M. Ojeda, S. Rojas, J.L.G. Fierro, Applied Catalysis B: Environmental 142-143 (2013) 241.

[9] L.M. Chew, H. Ruland, H.J. Schulte, W. Xia, M. Muhler, J. Chem. Sci. 126(2) (2014) 481.

[10] X.Y. Quek, Y. Guan, R.A. van Santen, E.J.M. Hensen, ChemCatChem 3 (2011) 1735.

[11] Q. Zhang, J. Kang, Y. Wang, ChemCatChem 2 (2010) 1030.

[12] M. Feyzi, A. Hassankhami, Journal of Natural Chemistry 20 (2011) 677.

[13] W. Wang, S.P. Wang, X.B. Ma, J.L. Gong, Chem. Soc. Rev. 40 (2011) 3703.

[14] Z. You, W. Deng, Q. Zhang, Y. Wang, Chinese Journal of Catalysis 34 (2013) 956.

[15] A.Y. Khodakov, W. Chu, P. Fongarland, Chemical Review 107 (2007) 1692.

[16] H.M.T. Galvis, J.H. Bitter, C.B. Khare, M. Ruitenbeek, A.I. Dugulan, K.P. de Jong, Science 335 (2012) 835.

[17] V.R. Calderone, N.R, Shiju, D. Curulla-Ferré, S. Chambrey, A. Khodakov, A. Rose, J. Thiessen, A. Jess, G. Rothenberg, Angewandte Chemie-International Edition 52 (2013) 4397.

[18] U. Rodemerck, M. Holena, E. Wagner, Q. Smejkal, A. Barkschat, M. Baerns, ChemCatChem 5 (2013) 1948.

[19] S.S. Nam, H. Kim, G. Kishan, M.J. Choi, K.W. Lee, Applied Catalysis A: General 179 (1999) 155.

[20] M.L. Cubeiro, H. Morales, M.R. Goldwasser, M.J. Pérez-Zurita, F. González-Jiménez, G. Urbina, Applied Catalysis A: General 189 (1999) 87.

[21] T. Riedel, H. Schulz, G. Schaub, K.W. Jun, J.S. Hwang, K.W. Lee, Topics in Catalysis 26 (2003) 41.

[22] T. Herranz, S. Rojas, F.J. Pérez-Alonso, M. Ojeda, P. Terreros, J.L.G. Fierro, Applied Catalysis A: General 311 (2006) 66.

[23] R.W. Dorner, D.R. Hardy, F.W. Williams, B.H. Davis, H.D. Willauer, Energy and Fuels 23 (2009) 4190–4195.

[24] R.W. Dorner, D.R. Hardy, F.W. Williams, H.D. Willauer, Applied Catalysis A: General 373 (2010) 112–121.

[25] Q. Zhang, J. Kang, Y. Wang, ChemCatChem 2 (2010) 1030.

[26] C. Pirola, M. Scavini, F. Galli, S. Vitali, A. Comazzi, F. Manenti, P. Ghigna, Fuel 132 (2014), in press.

[27] N. G. Hamilton, R. Warringham, I.P. Silverwood, J. Kapitán, L. Hecht, P.B. Webb, R.P. Tooze, W. Zhou, C.D. Frost, S. F. Parker, D. Lennon, Journal of Catalysis 312 (2014) 221.

[28] J. Lu, L. Yang, B. Xu, Q. Wu, D. Zhang, S. Yuan, Y. Zhai, X. Wang, Y. Fan, Z. Hu, ACS Catalysis 4(2) (2014) 613.

[29] B. H. Davis, Catalysis Today 84 (2003) 83.

[30] S. Soled, E. Iglesia, Catalysis Letters 7 (1990) 271.

[31] Y. Jin, A.K. Datye, Journal of Catalysis 196 (2000) 8.

[32] A.P. Steynberg, M.E. Dry, Eds., Fischer-Tropsch Technology, in Studies in Surface Science and Catalysis, No. 152, Elsevier, Amsterdam, 2004.

[33] G.P. van der Laan, A.A.C.M. Beenackers, Catalysis Reviews-Science and Engineering 41(3-4) (1999) 255.

[34] Y. Liu, B.-T. Teng, X.-H. Guo, Y. Li, J. Chang, L. Tian, X. Hao, Y. Wang, H.W. Xiang, Y.Y. Xu, Y. Wang, Journal of Molecular Catalysis A: Chemical 272(1-2) (2007) 182.

[35] T. Li, Y. Yang, C. Zhang, X. An, H. Wan, Z. Tao, H. Xiang, Y. Li, F. Yi, B. Xuet, Fuel 86(7-8) (2007) 921.

[36] Y. Yang, H.-W. Xiang, L. Tian, H. Wang, C.-H. Zhang, Z.-C. Tao, Y.-Y. Xu, B. Zhong, Y.-W. Li, Applied Catalysis A: General 284(1-2) (2005) 105.

[37] N. Lohitharn, J.G. Goodwin, Journal of Catalysis 260 (2008) 7.

[38] R.W. Dorner, H.D. Willauer, D.R. Hardy, F.W. Williams, Report NRL/MR/ 6180-09-9200, 2009.

[39] R. Malessa, M. Baerns, Industrial Engineering Chemistry Research 27 (1988) 279.

[40] L. Bai, H.W. Xiang, Y.W. Li, Y.Z. Han, B. Zhong, Fuel 81 (2002) 1577.

[41] N. Lohitharn, J.G. Goodwin Jr., E. Lotero, Journal of Catalysis 255 (2008) 104.

[42] Z. Shu, Y. Chen, W. Huang, X. Cui, L. Zhang, H. Chen, G. Zhang, X. Fan, Y. Wang, G. Tao, D. He, J. Shi, Applied Catalysis B: Environmental 141-142 (2013) 42.

[43] C.D. Wagner, L.E. Davis, M.V. Zeller, J.A. Taylor, R.H. Raymond, L.H. Gale, Surface and Interface Analysis 3 (1981), 211.

[44] F. Rojas, I. Kornhauser, C. Felipe, J.M. Esparza, S. Cordero, A. Dominguez, J.L. Riccardo, Physical Chemistry and Chemical Physics 4 (2002) 2346.

[45] B.C. Gagea, Y. Lorgouiloux, Y. Altintas, P.A. Jacobs, J.A. Martens, Journal of Catalysis 265 (2009) 99.

[46] P. Li, E.Y. Jiang , H.L. Bai, Journal of Physics D: Applied Physics 44 (2011) 075003.

[47] M. Chigane, M. Ishikawa, Journal of Electrochemical Society 147 (2000) 2246.

[48] M. Toupin, T. Brousse, D. Bélanger, Chemistry of Materials 14 (2002) 3946.

[49] C.H. Liang, C.S. Hwang, Journal of Alloys Compounds 500 (2010) 102.

[50] F. Xiao, Y. Xu, International Journal of Electrochemical Science 7 (2012) 7440.

[51] H. Wang; Y. Yang; J. Xu; H. Wang; M. Ding; Y. Li, Journal of Molecular Catalysis A: Chemical 326 (2010) 29.

[52] H. Suo; S. Wang; C. Zhang; J. Xu; B. Wu; Y. Yang; H. Xiang; Y.-W. Li, Journal of Catalysis 286 (2012) 111.

[53] P. Prasad P, J.W. Bae, K.W. Jun, K.W. Lee, Catalysis Surveys from Asia 12 (2008) 170.

[54] C. Yang, H.B. Zhao, Y.L. Hou, D. Ma, Journal of the American Chemical Society 134 (2012) 15814.

[55] D.J. Dwyer, J.H. Hardenbergh, J. Catalysis 87 (1984) 66.

[56] C.S. Kuivila, J.B. Butt, P.C. Stair, Applied Surface Science 32(1988) 99.

[57] W. Wang, S. Wang, X. Ma, J. Gong, Chemical Society Reviews 40 (2011) 3703.

[58] R.W. Dorner, D.R. Hardy, F.W. Williams, H.D. Willauer, Energy and Environmental Science 3 (2010) 884.

[59] R.A. Dictor, A.T. Bell, Journal of Catalysis 97 (1986) 121.

[60] D.B. Bukur, L.Nowicki, R.K.Manne, X.S. Lang, Journal of Catalysis 155 (1995) 366.

[61] S.Z. Li, W.P. Ding, G.D. Meitnzer, E. Iglesia, Journal of Physical Chemistry B 106 (2002) 85.

[62] H. Schulz, T. Riedel, G. Schaub, Topics in Catalysis 32 (2005) 117.

[63] J.F. Bengoa, A.M. Alvarez, M.V. Cagnoli, N.G. Gallegos, S.G. Marchetti, Applied Catalysis A: General 325 (2007) 68.

[64] J. Xu, C.H. Bartholomew, Journal of Physical Chemistry B 109 (2005) 2392.

Chapter 8: General Conclusions

8

General Conclusions

Several studies with Fe-based catalysts for the Fischer-Tropsch synthesis have been carried out in this PhD Thesis whose main conclusions are described next:

Syngas Conversion to Hydrocarbons on Zirconia-Supported Iron Catalysts

The Zr-Fe-O catalyst precursors that were prepared using Fe-loadings of 0 to 100% were calcined at 450 °C to obtain well-crystallites of Fe_2O_3. Then, these precursors were activated in the H_2/CO mixture and tested using Fischer Tropsch Syntheses. The main conclusions of this study include the following: (i) CO conversion was strongly dependent on the surface iron concentration, in agreement with the XPS measurements; (ii) CO_2 selectivity was lower than 10% and nearly constant in the Fe-rich catalysts but decreased as a function of increasing zirconium, which agreed with the expected influences of the water gas-shift reaction on iron sites; (iii), for the Fe-poor catalysts (15Fe and 5Fe) in which no crystalline iron phases were observed by XRD and a strong Zr-enrichment was revealed by XPS, the lowest CO conversion was attained by the Zr-rich catalyst (15Fe and 5Fe) with activities of less than 5% (CO conversion), indicating that the reaction mechanism is different from the reactions involving the Fe-rich catalysts; and (iv) the highest CO conversion occurred in the Zr-free (100Fe) catalyst. Because the active phases of these catalysts in the target reaction are iron carbides, we normalized the CO conversion levels to the iron content (Fe at.g). Based on this calculation, we noted that the 95Fe and 85Fe catalysts displayed better performance. Indeed, the performance of the pure iron oxide appeared to be better but its activity profile decreased slightly with time on-stream, which indicated that this catalyst becomes progressively deactivated. The rather low performance of the other Zr-rich catalysts (15Fe and 5Fe) can be explained as follows: (i) when iron oxides are the minor phase, the small Fe_2O_3 crystallites likely interact strongly with the zirconia surface and make the carburization process more difficult relative to the Fe-rich compositions; and (ii) when zirconia is the major phase in this Zr-rich composition region, partial coverage of Fe_2O_3 crystallites by zirconia is expected, which may induce a loss of active iron sites and a subsequent drop in performance.

Effect of high-temperature pre-reduction in Fischer-Tropsch synthesis on Fe/ZrO_2 catalysts

The Fe/ZrO_2 catalysts prepared by conventional incipient wetness impregnation method were investigated for the FTS. It is noticed that size of iron oxide particles play an important role in the catalyst reduction degree due to the effect that particle size of iron oxide has on the interaction strength between the support and iron catalyst. We have found that Fischer-Tropsch synthesis reaction with Fe-based catalysts is very significantly affected by iron oxide particle size. In the range of iron particle size in this study, the CO conversion rate during FTS increases as a function of the increase in particle size, reaching a maximum value for mean Fe particle size of approximately 7 nm.

Cu-promoted Fe_2O_3/MgO-based Fischer-Tropsch catalysts of biomass-derived syngas

The addition of magnesium to iron-based catalysts leads to increased BET specific area and smaller iron oxide particle size. The XRD of the promoted and unpromoted calcined precursors showed only a crystalline hematite iron oxide (α-Fe2O3) phase, and no XRD diffraction peaks due to Mg or Cu were recorded, probably because their low concentration in the samples and full dispersion on hematite iron oxide. The extent of hematite iron oxide reduction increases and shifts toward lower reduction temperatures due to incorporation with Mg and Cu species; in addition, the extent of reduction increases with higher Cu loading. The content of iron carbide phases during the TPR process in the synthesis gas first increases with the increase of copper content and reaches a maximum for the Cu/Fe atom ratio of 0.02. The FTS catalytic activity is promoted with copper because Cu promotes the formation of the iron carbide, which is the active phase. The maximum catalytic activity was obtained at the Cu/Fe atom ratio of 0.02. Then, at higher copper levels, there is a decrease in the catalytic activity. A maximum in the catalytic activity and methane selectivity was obtained for the synthesis gas ratio of 2 ($H_2/CO = 2$).

Effect of Mn loading onto MnFeO nanocomposites for the CO_2 hydrogenation reaction

Manganese-iron oxide (xMnFe, x = 0-0.5) catalysts were prepared by a template approach and then tested in the hydrogenation of CO_2 into hydrocarbons/oxygenate products. The results obtained lead to the following conclusions. (i) Only the 0.05MnFe catalysts exhibited a mesoporous structure and moderately high BET area. (ii) Surface analysis by XPS showed a Mn-enriched surface (in a ca. 3-nm region). (iii) The 0.05MnFe catalyst was found to be reduced at much lower temperatures (maximum at 570 ºC) than the other members of the series (maximum at approximately 730 ºC) and was also easily carbided during the activation step. (iv) Under fixed reaction conditions (20 bar, 340 ºC, CO_2:H_2:N_2 = 23:69:8 (molar)), the Mn loading was found to exert a strong influence on CO_2 conversion and selectivity to different products. (v) The 0.05MnFe catalyst displayed the best performance with reduced CO and CH_4 formation and improved selectivity to C_2-C_5 and C_{6+} hydrocarbons as well as the formation of some oxygenates.

En esta Tesis Doctoral se han realizado varios estudios con catalizadores de hierro usados en la síntesis de hidrocarburos mediante el proceso Fischer-Tropsch. Las conclusiones más importantes que se han derivado de tales estudios se resumen a continuación:

Conversión de gas de síntesis a hidrocarburos en catalizadores de hierro soportados en ZrO_2

Los precursores de los catalizadores del tipo Zr-Fe-O se prepararon con contenido de Fe entre 0 y 100%, y se calcinaron a 450 ºC para obtener el óxido Fe_2O_3 bien cristalizado. Después, estos precursores se activaron en la mezcla H_2/CO y se ensayaron en la reacción de síntesis Fischer-Tropsch. Las conclusiones más importantes de este estudio incluyen: (i) la conversión de CO depende marcadamente de la concentración de hierro en la superficie de los catalizadores, en concordancia con las medidas de XPS; (ii) La selectividad de CO_2 resultó inferior a 10% y permaneció aproximadamente constante en los catalizadores ricos en hierro pero decreció en función del aumento del contenido de Zr, lo que está de acuerdo con la influencia esperada de la reacción del gas de agua ($CO + H_2O \rightarrow CO_2 + H_2$) sobre los centros de hierro; (iii) en los catalizadores con bajo contenido de hierro (15Fe y 5Fe) en los que no aparecieron fases cristalinas de hierro mediante la técnica de difracción de Rayos X se observó un fuerte enriquecimiento de ZrO_2 mediante la técnica XPS al mismo tiempo que mostraron una baja conversión de CO, inferior al 5% indicando que el mecanismo de reacción es diferente al que ocurre en los catalizadores ricos en hierro; y (iv) la máxima conversión de CO se observó sobre el catalizado sin Zr (100Fe). Debido a que las fases activas de estos catalizadores en la reacción FT son los carburos de hierro, los niveles de conversión se normalizaron por el contenido de hierro (Fe at.g). Este cálculo mostró que los catalizadores 95Fe y 85Femuestran eñ mejor comportamiento catalítico. En verdad, el comportamiento catalítico del catalizador 100Fe resultó ser el mejor si bien su perfil de actividad decreció ligeramente con el tiempo en reacción lo que indica que este catalizador se desactiva progresivamente. La baja actividad de los catalizadores ricos en Zr (15Fe y 5Fe) puede explicars como sigue: (i) cuando los óxidos de hierro constituyen la fase minoritaria, las pequeñas nanopartículas de Fe_2O_3 interaccionan fuertemente con la superficie del ZrO_2 hacen que el proceso de carburización resulte más difícil que en aquellos que son ricos en hierro; y (ii) cuando el ZrO_2 es la fase mayoritaria es posible que una parte de las nanopartículas de Fe_2O_3 resulten recubiertas por el ZrO_2, lo que puede induciruna pérdida de de centros activos de hierro y por consiguiente una pérdida de actividad catalítica.

Efecto de la pre-reducción a elevada temperatura de los catalizadores Fe/ZrO_2 en la actividad en la reacción de síntesis Fischer-Tropsch

Se estudió el comportamiento delos catalizadores Fe/ZrO_2 preparados por el método convencional de impregnación a humedad incipiente en la síntesis Fischer-Tropsch. Se puso de relieve que el tamaño de las nanopartículas de Fe_2O_3 desempeña un papel importante en la extensión de reducción debido a que el tamaño de partícula del óxido de hierro determina la interacción entre el óxido y el sustrato (ZrO_2). Se ha puesto de relieve que la reacción de síntesis Fischer-Tropsch sobre catalizadores de hierro está afectada de forma significativa por el tamaño de las partículas de óxido de hierro. En el rango de tamaños de particular alcanzado en los catalizadores usados en esta Tesis, la velocidad de hidrogenación de CO aumenta conforme lo hace el tamaño de partícula, alcanzando un máximo para tamaños medios de partícula de aproximadamente 7 nm.

Catalizadores Fe_2O_3/MgO promovidos con Cu para la reacción de síntesis Fischer-Tropsch con gas de síntesis producido a partir de biomasa

La incorporación de MgO a los catalizadores basados en hierro produce un incremento de la superficie específica y una disminución del tamaño de las partículas de Fe_2O_3. Los perfiles de difracción de rayos X delos precursores calcinados promovidos y no promovidos mostraron solamente la presencia de la fase hematita cristalina (α-Fe_2O_3), pero en ningún caso difracciones asociadas a MgO u óxidos de cobre debido probablemente a a la baja concentración de tales fases en las muestras y a la elevada dispersión de la fase hematita. La extensión de la reducción de la fase hematita aumenta y se desplaza a bajas temperaturas de reducción como consecuencia de la incorporación de especies MgO y Cu. Además, la extensión de la reducción aumenta con el contenido de Cu. El contenido de fases de carburo de hierro durante el proceso de activación de los catalizadores en atmósfera de gas de síntesis primero aumenta con el incremento del contenido de Cu y alcanza un máximo para la relación atómica Cu/Fe de 0.02. La actividad catalítica en la reacción de síntesis FT está promovida por el Cu debido a que el Cu favorece la formación de la fase de carburo de hierro que es la fase activa en la reacción. El máximo de actividad catalítica se alcanzó en el catalizador cuya relación atómica Cu/Fe es 0.02. Para contenidos de Cu superiores la actividad catalítica decae. El máximo de la actividad catalítica y máximpo de la selectividad a metano se obtiene con un gas de síntesis cuya relación molar H_2/CO es 2.

Efecto del contenido de Mn en los sistemas MnFeO para a reacción de hidrogenación de CO_2

Los catalizadores de óxido de manganeso-hierro (xMnFe, x = 0-0.5) se prepararon conforme a la metodología de templado y después se ensayaron en la reacción de hidrogenación de CO_2 a productos hidrocarburos/oxigenados. Los resultados obtenidos han permitido extraer las conclusiones siguientes: (i) solamente el catalizador 0.05MnFe presentó una estructura mesoporosa y superficie específica moderada. (ii) El análisis de la superficie mediante la técnica XPS mostró un enriquecimiento en manganeso (en la región de la superficie de unos 3-nm). (iii) El catalizador 0.05MnFe se redujo a temperatura mucho más baja (570 ºC) que los demás catalizadores de la serie (730 ºC). Igualmente se carburizó más fácilmente que los otros catalizadores durante su activación. (iv) Bajo condiciones fijas de reacción (20 bar, 340 ºC, CO_2:H_2:N_2 = 23:69:8, molar), el contenido de Mn ejerce una influencia decisiva en la conversión de CO_2 y la selectividad a diferentes productos. (v) El catalizador 0.05MnFe mostró el mejor comportamiento catalítico, con menor selectividad hacia CO y CH_4 and selectividad mejorada a hidrocarburos C_2-C_5 y C_{6+} así como hacia la formación de algunos oxigenados.

Appendix

I. Symbols and abbreviates

List of Symbols

d Distance between two consecutive planes

E_b Binding energy of the excited electron

E_C Kinetic energy

$h\upsilon$ photon energy

I Intensity

m/z Mass / ion charge number

n number of carbon atoms in a chain

N_A Avogadro number

P Pressure

P_0 Saturation pressure of N_2 at -196°C

q_1 Adsorption heat

q_c Condensation heat of adsorbed gas

R Gas constant

S_{BET} Catalyst specific surface area calculated by applying the BET method to the adsorbed isotherm of N_2 at -196°C

S_i Product i selectivity

T Experimental temperature

V Adsorbed gas volume

V_m Monolayer volume

Wn Mass fraction of chain with n carbon atoms

X Conversion

α Growth probability factor

θ Incidence angle

λ Incident wavelength

σ Cross-sectional area covered by N_2 molecule

Φ Spectrometer work function

List of abbreviates

ASF	Anderson-Schulz-Flory
BE	Binding Energy
BET	Brunauer-Emmett-Teller
BTL	Biomass-to-Liquids
CBTL	Coal and Biomass-To-Liquid
CCD	Charge coupled device
CG	Gas chromatograph
CTL	Coal-to-Liquids
EDX	Energy dispersive X-ray
FBR	Fixed-bed reactor
FID	Flame ionization detector
FT	Fischer Tropsch
FTS	Fischer Tropsch synthesis
GHSV	Gas hourly space velocity
GTL	Gas-to-Liquids
H_2-TPR	Temperature programmed reduction
HRTEM	High resolution transmission electron microscopy
JCPDS	Joint Committee on Powder Diffraction Standards
LCF	Linear combination fitting
MFC	Mass flow controller
MS	Mass spectrometer
PC	Pressure controller
TCD	Thermal conductivity detector
TEM	Transmission electron microscopy
TPA	Temperature programmed analysis
TPD	Temperature programmed desorption
TPO	Temperature programmed oxidation
WGS	Water-Gas Shift reaction
XANES	X-ray absorption near edge structure
XPS	X-ray photoelectron spectroscopy
XRD	X-ray diffraction

II. Tables index

III. Figures index

IV. Publications derived from the Doctoral Thesis

Syngas Conversion to Hydrocarbons on Zirconia-Supported Iron Catalysts

M. Al-Dossary, M. Ojeda, J.L.G. Fierro

Catalysis Letters (2015) in press

Abstract

The hydrogenation of CO to hydrocarbons is investigated over zirconia iron-based catalysts prepared by co-precipitation. These catalysts, in which the Fe-content varied between 0 and 100%, were tested in the CO hydrogenation reaction under fixed reaction conditions (H_2/ CO = 2, T = 250 ºC, P = 20 bar, GHSV = 0.0083 L/g.s.). The resulting activity data indicated that CO conversion is strongly dependent on the iron contents of the catalysts. The lowest CO conversion (< 5%) was obtained using Zr-rich catalysts (15Fe and 5Fe), and the highest CO conversion was obtained using Zr-free (100Fe) catalysts. For this catalyst, the CO conversion level reaches 38.5%, with selectivities for the C_2-C_4 and C_5+ hydrocarbons of 49.7 and 27.7%, respectively. However, the activity profile of this catalyst slightly decreases with the time on-stream, indicating that it is progressively deactivated. If the activity is normalized to the iron content, the 95Fe and 85Fe catalysts display slightly better performances and are relatively stable for on stream periods of at least 48 h.

Effect of high-temperature pre-reduction in Fischer-Tropsch synthesis on Fe/ZrO_2 catalysts

M. Al-Dossary and J.L.G. Fierro

Applied Catalysis A: General (2015) in press

Abstract

Fischer-Tropsch synthesis of low molecular weight (C_2-C_4) olefins is a valuable alternative process for the production of key chemicals from non-petroleum precursors such as a renewable C source like biomass. The influence of the H_2 treatment temperature of zirconia-supported iron catalysts on the conversion of synthesis gas has been investigated. The CO conversion rate, based on steady-state, increased with the pretreatment temperature up to a maximum and then decreased at higher temperatures. Moreover, methane selectivity was found to decrease slightly from the lowest H_2 treatment temperatures (46%) to the highest ones (34%), while C_2-C_4 and C_5^+ hydrocarbons followed an opposite trend. Presumably, methane formation takes place at highly active low coordination sites residing at corners and edges, which are more abundant on small iron carbide particles. Lower hydrocarbons are mainly produced at terrace sites that are available and active, quite independent of the iron crystallite size.

Cu-Promoted Fe_2O_3/MgO-Based Fischer-Tropsch Catalysts of Biomass-Derived Syngas

M. Al-Dossary, J.L.G. Fierro, and J.J. Spivey

Industrial Engineering Chemistry Research 54(3) (2015) 911-921.

Abstract:

A series of precipitated Fe_2O_3/MgO catalysts incorporated with the copper promoter were prepared by the combination of coprecipitation and incipient witness impregnation methods. The catalysts were characterized by N_2-adsorption-desorption isotherms, X-ray diffraction (XRD), H_2 temperature programmed reduction (H_2-TPR), CO temperature programmed desorption (CO-TPD), O_2 temperature programmed oxidation (O_2-TPO), laser Raman spectroscopy (LRS), and X-ray absorption near edge structure (XANES). The Fischer-Tropsch (FT) synthesis reaction of the catalysts was also performed in a fixed bed reactor using different H_2/CO ratios ($H_2/CO = 1$ or 2). The characterization results indicated that Mg increases the BET surface area of precipitated oxide precursors by inhibiting sintering during thermal treatment, and leads to the formation of the relatively smaller iron crystallite size. Cu increases the rate of Fe_2O_3 reduction by providing H_2 dissociation sites. The content of iron carbide phases during TPR process in the synthesis gas increases with the increase of copper content and reaches a maximum for the Cu/Fe atom ratio of 0.02. The optimal catalyst with Cu/Fe = 0.02 has high activity. A maximum in the catalytic activity and methane selectivity was obtained for the synthesis gas ratio of 2 ($H_2/CO = 2$).

Effect of Mn loading onto MnFeO nanocomposites for the CO_2 hydrogenation reaction

Applied Catalysis B: Environmental 165 (2015) 651-660.

Abstract

This work describes the preparation of mesoporous xMnFe oxide (x = 0, 0.05, 0.1, 0.2, 0.3 and 0.5 molar ratios) nanocomposites through a one-step sol-gel process in the presence of a triblock copolymer as a structure-directing agent. The prepared oxides were used as catalysts in the CO_2 hydrogenation via Fischer-Tropsch reactions for the production of valuable hydrocarbons. Among the catalysts, the 0.05MnFe catalyst performed best under the selected reaction conditions: a reaction temperature of 340 °C, overall pressure of 20 bar, reactant mixture of 23% CO_2/69% H_2/8% N_2 and flow rate of 20 mL min^{-1}. This catalyst provided a much higher conversion of CO_2 to hydrocarbons (63.2% C_2-C_5, 3.9% to C_{6+} and 3.6% to oxygenates) and the lowest levels of CO and methane formation among the xMnFe series. Moreover, 0.05MnFe was the only catalyst with a mesoporous structure, and it had a substantially lower reduction temperature than did the other members of the series. The enhanced catalytic activity of the 0.05MnFe catalyst, which contains only a small amount of Mn, appears to result primarily from its high specific area and relatively easy reduction.

V. Curriculum vitae

MOHAMMED ALI M. ALDOSSARY

PHONE : 0034 915 854773
MOBILE : 0034 603 137934
E-MAIL : ma99sa@htmail.com

Date of Birth	29-01-1981, Saudi Arabia
Gender	Male

EDUCATION

- 2002 A Bachelor's Degree in Chemistry Department, College of Science at King Saud University(KSU) with GPA : **4.22 / 5**

  http://www.ksu.edu.sa/Pages/default.aspx
- 2009 A Master Degree in Hetrogeuious Catalysis (oxidative and non-oxidative conversion of light paraffins into olefins on chromite-based catalysts). In Institute of Catalysis and Petrochemistry, CSIC – at Autonoma University of Madrid, Spain. with **8.83 / 10**

  http://www.icp.csic.es/

WORK EXPERIENCE

- I have joined SABIC (Saudi Arabia Basic Industrial Corporation) in Research and Technology Center (R&T) as a researcher chemist in (2002) until now.
- On Job Training (OJT).
- Assigned as a team member on technical support to evaluate and characterize many catalysts for dehydrogenation of ethyl benzene to styrene and propane to propylene and aromatization of isobutene at SABIC R&T (2002- 2007).

TRAINING &SKILLS

- I attended many general and catalyst training courses:

  • Catalyst Preparation & Characterization course 21.05.2005 - 25.05.2005

  • Heterogeneous Catalysis course at Cardiff university, UK. 03.07.2006 - 21.07.2006

  • Advance Heterogeneous Catalysis course at Institute of Catalysis and Petrochemistry,(ICP- CSIC) Spain. 06.082007-17.08.2007

  • NIOK Course “Characterization in Catalysis Research” at the Eindhoven University of Technology, The Netherland, 24. 01. 2011-26. 01. 2011.

  • Safe Work Practices course at SABIC, Saudi Arabia

  • Lab Safety course course at SABIC, Saudi Arabia

  • Dealing with Hazardous Chemicals course at SABIC, Saudi Arabia

  • The Quality Advantage (TQA) course at SABIC, Saudi Arabia

  • Design of Experiments (DOE) course at SABIC, Saudi Arabia

  • Technical Communication and Report Writing course at SABIC, Saudi Arabia

  I attended international catalyst conferences inside and outside Saudi Arabia.

- I attended various courses in computer skills.

TECHNICAL SKILES AND COMPETENCES

- Designing and build-up of catalytic reactor

- Synthesis of catalysts based on metallic nanoparticles
- Characterization techniques such as, XRD, XPS, XANES, Temperature-Programmed Analysis
- Evaluation of catalytic performance and product analysis by GC

STAY OF FOREIGN LABORATORIES

- 23. 01. 2012 – 20. 07. 2012

Department of Chemical Engineering

Louisiana State University (LSU)

United States of America (USA)

Supervisor: Professor James J. Spivey

Acknowledgments

First of all, thanks are due to ALLAH the almighty, for his bounties throughout my life.

Then, I would like to express my gratitude to my supervisor and promoter Prof. Jose Luis Garcia Fierro. I will always be thankful to you for giving the great opportunity to becoming a scientist under your guidance. From the very beginning I felt your confidence in me and my capabilities, what was an immense support during the whole period. Your enthusiasm and effort are remarkable and became for me a continuous motivation. Prof. Fierro, I want to thank you for all your useful advices and for your continuous guidance. I appreciate your meticulous revisions and I find very inspiring the grate love for science that you always transmit. Also, I would like to express my sincere thanks to Dr. Manuel Ojeda for your guidance, freedom to perform research, encouragement and scientific discussions, which were always stimulating new ideas.

Thanks are also due to the management of SABIC (Saudi Arabia Basic Industries Corporation) for granting me a scholarship to study for a doctorate at Institute of Catalysis and Petrochemistry (ICP-CSIC) in Spain.

Doing a PhD is very much like a trip. A trip that makes the PhD student not only educated, but also wiser, more experienced and stronger. For me this journey started when I got approval from SABIC that selected me as best candidate for higher education program and acceptance letter from Prof. J.L.G Fierro for a PhD position in his group. I am very grateful for giving me the opportunity to become a member of the Sustainable Energy and Chemistry (EQS) group at Institute Of Catalysis and

Petrochemistry, Consejo Superior de Investigaciones Científicas (ICP-CSIC), Madrid, Spain.

I strongly believe without technical support of our group, it would not have been possible to complete my research. My special thanks to Dr. Noelia Mota who introduced to me different experimental setup’s in our Laboratories, which enabled me to work on them independently. I also want to take the opportunity to say my thanks to Javier Arenales, Fernando Vaquero, Maria Consuelo, Vanesa del Villar Garrachon, Inmaculada Murillo Leo and Rut Lopez for your usual support and it was nice to share my office with you. I had enjoyed our time together in the same office and laboratory. I acknowledge the help of Dr. Barbara Garcia. Barbara, you have been very helpful and always used to find time for me to discuss.

In addition to the scientific and professional experiences I gained during the PhD period, those of relationships with all staff members of the Sustainable Energy and Chemistry (EQS) group. Furthermore, I highly appreciate and thank for their great assistance on my work.

I appreciate the opportunity to work with Prof. James Spivey’s research group at Louisiana State University. I had a very nice time working in the group as a guest PhD. I also want to take the opportunity to thank the beam scientist that assisted us in our XANES experiments at LSU’s synchrotron facility (CAMD, Baton Rouge, Louisiana), in particular, Gregory Merchan.

The last but not least, I would like to express my appreciations and respect to my family that are thoroughly ‘the stars of my life’: my mother, father, wife, brothers, sisters and sons for their infinite love they have for me. I strongly believe that without their support and encouragement I could not have managed to pursue higher education. Although all in my family are very dear to me but my parents have been a role model

for me for their patience and understanding. My parents, I owe my wellbeing to you and will always do… my achievement, if any, will always be yours and words are not capable to describe how I am grateful for that. Many thanks to my close family for fun activities we had together in Madrid. My wife has been an unfailing source of support to me during my stay in Spain and my beloved sons Ali, Hatim and Khalid are always bright candles in my life. They bring me endless joy.

If I do a post analysis of myself, I see myself as a person who has gained experience and knowledge both scientifically and personally, although my social features have partly deactivated in this period. I hope I can regenerate these features. It has been a very steep learning curve and I enjoyed working in the Sustainable Energy and Chemistry (EQS)